High sensitivity solid-state NMR spectroscopy of catalytic surfaces

Ribal Jabbour

Numéro National de thèse : 2020LYSE1200

THESE de DOCTORAT DE L'UNIVERSITE DE LYON

opérée au sein de

l'Université Claude Bernard Lyon 1

Ecole Doctorale 206

Ecole Doctorale de Chimie de Lyon

Spécialité : Résonance Magnétique Nucléaire

Discipline : Chimie

Soutenue publiquement le 09/11/2020, par :

Ribal JABBOUR

High-Sensitivity Solid-State NMR of Catalytic Surfaces

Devant le jury composé de :

Frederic Blanc	Professeur Université de Liverpool, Royaume Uni	Rapporteur
Christel Gervais	Professeure Université de Sorbonne, Paris	Rapporteur
Michel Bardet	Directeur de Recherche Université de Grenoble, Grenoble	Examinateur
Franck Fayon	Directeur de Recherche CEMHTI - UPR3079 CNRS, Orléans	Examinateur
Maggy Hologne	Maître de Conférences ISA - UMR5280, Lyon	Examinatrice
Chloé Thieuleux	Directrice de Recherche CNRS C2P2 - UMR5265, Lyon	Examinatrice
Anne Lesage	Ingénieure de Recherche CNRS CRMN - FRE2034, Lyon	Directrice de thèse

Contents

Acknowledgements

First and foremost, I would like to thank all the people that made this work possible, directly and indirectly.

Specifically, I would like to thank the jury : Prof. Blanc, Prof. Gervais, Dr. Bardet, Dr. Fayon, Dr. Hologne and Dr. Thieuleux, for accepting to be part of my PhD, for taking the time to read the manuscript, their presence in the defense and the fruitful discussions and suggestions made through the defense.

I would also like to thank my supervisor Dr Anne Lesage for her confidence, for the liberty she gave me throughout this work, for the exceptional level of equipment at my disposition and for all her suggestions and guidance throughout different projects presented in this manuscript. I would like to thank you for choosing me to be in charge of this project and the possibility of important scientific collaboration that made this work the most robust possible. Anne, I would like to thank your almost every day guidance during these three years, the quality of your explanations and your infinite patience when things were tough.

I would also like to thank Dr. David Gajan for his practical and chemistry expertise and for diffusing his knowledge about the equipment and how this operate in the spectrometer hall. David, Thank you for your patience, your guidance and suggestions.

The projects in this thesis were always part of a passionate collaboration. On this occasion, I would like to thank Pr. Christophe Copéret and his group at ETH Zurich. I would also like to thank Dr. Chloé Thieuleux, Dr. Marc Renom-Carrasco, Dr. Clément Camp and Sébastien Lassalle at the C2P2 Lyon, and also Dr. Aaron Rossini and Dr. Amrit Venkatesh at Ames laboratory with whom I had the opportunity to collaborate. I would like to thank Dr. Olivier Ouari of the University of Aix-Marseille for providing all the polarizing agents that are vital for every DNP experiment. I would like to thank Dr. Alicia Lund with whom i had the opportunity to learn about the Platinum NMR during the weekdays and weekends ! Finally, I would like to thank Dr. Pierrick Berruyer who initiated and taught me everything to know on the structural characterization to be able to take on this project.

I would like to thank all the people of the CRMN that I had the chance to know during these 3 years : Monu, Georges, Jasmine, Emeline, Sirine, Loic, Hubert, Cécile C., Andrea, Kevin, Tobias, Jan S., Jan B., Dorothéa, Daniella, Guido, Diane, Olivier, Ladislav, Giacomo, Quentin, Samuel, Stuart, Théo, Morgan, Sami ... A special thank you for Adrian and Arthur with whom these 3 years wouldn't be as enjoyable !

I would like to thank all my friends in France and abroad that I met or already know during

these three years.

Finally, I would like to thank my family : my mother, Father, my brother Rami and my sister Rouba but also every other member of the family for all their support ...
Wishing you a pleasant reading!

Abstract

The vast majority of chemical reactions used today in industry relies on heterogenous catalysts. Over the last three decades, many efforts were devoted at preparing well-defined, single-site supported organometallic catalysts that would combine the advantages of molecular complexes in terms of productivity, rates and selectivity, with an ease of separation and recyclability. The rational design of such systems depends on our ability to characterize with a high level of certainty their atomic-scale structure. Among the panoply of analytical techniques that can be applied to get a detailed knowledge of the active center, solid-state Nuclear Magnetic Resonance (NMR) spectroscopy under Magic Angle Spinning (MAS) plays an essential role. This spectroscopy suffers however from one key drawback, its inherently low sensitivity. This sensitivity issue is further exacerbated when the substrate of interest is located on a surface. The recent advent of hyperpolarization techniques and more specifically of Dynamic Nuclear Polarization (DNP) opens new opportunities for a highly detailed structural characterization of active sites in heterogeneous catalysts.

The core of my PhD has concerned the implementation of advanced NMR methods of high sensitivity, namely DNP enhanced NMR spectroscopy and proton NMR spectroscopy, to unravel the atomic-scale structure of single-site, well defined heterogeneous catalysts. Three systems were investigated, all involved in key catalytic reactions. First, I elucidated the three-dimensional structure of an Iridium-NHC complex supported onto mesoporous silica. DNP enhanced NMR was applied to determine the structure of the surface species at various steps of the synthetic pathway. I showed that the implementation of conventional and selective REDOR (Rotational Echo Double Resonance) experiments between ^{29}Si, ^{13}C and ^{15}N nuclei enables the measurement of distance constraints corresponding specifically to the Ir-NHC complex despite the presence of unreacted spectator species. The result is a well-defined structure where the Ir atom points to the porous cavity. This unexpected feature was interpreted by the residual presence of a cyclooctadiene (COD) ligand, coordinating the molecular Ir complex which could be confirmed by Extended X-Ray Absorption Fine Structure (EXAFS). I also demonstrated the use of static DNP-enhanced wide-line ^{195}Pt NMR spectroscopy in combination with room-temperature proton-detected experiments to provide unique insight into the surface structure of a Platinum organometallic complex, representative of Pt single-site catalysts. Finally, I implemented proton double- and triple-quantum NMR experiments to unravel the structure of a new family of hetero-bimetallic surface complexes. The approach allowed the unambiguous determination of the number of hydride protons surrounding the metal centers. Different synthetic pathways yielded distinct surface structures that were elucidated by NMR in combination with IR spectroscopy and X-ray methods. Overall, several

groundbreaking NMR methodologies were developed that are expected to become more widely implemented to guide the rational design of immobilized catalyst.

Résumé de la thèse

La grande majorité des réactions chimiques utilisées aujourd'hui dans l'industrie repose sur des catalyseurs hétérogènes. Au cours des trois dernières décennies, de nombreux efforts ont été consacrés à la préparation de catalyseurs organométalliques supportés bien définis, qui allient les avantages des complexes moléculaires en termes de rendement et de sélectivité, avec une facilité de séparation et de recyclage. La conception rationnelle de tels systèmes dépend de notre capacité à caractériser avec un haut niveau de certitude leur structure à l'échelle atomique.

Parmi la panoplie de techniques analytiques qui peuvent être appliquées pour obtenir une connaissance détaillée du centre actif, la spectroscopie par résonance magnétique nucléaire (RMN) à l'état solide sous rotation à l'angle magique (MAS) joue un rôle essentiel. Cette spectroscopie souffre cependant d'un inconvénient majeur, sa sensibilité intrinsèquement faible. Ce problème de sensibilité est encore exacerbé lorsque le substrat d'intérêt est situé sur une surface. L'avènement récent des techniques d'hyperpolarisation et plus particulièrement de la Polarisation Dynamique Nucléaire (DNP) ouvre de nouvelles opportunités pour une caractérisation structurale très détaillée des sites actifs dans des catalyseurs hétérogènes.

Le cœur de ma thèse a porté sur la mise en œuvre de méthodes RMN avancées de haute sensibilité, à savoir la spectroscopie RMN améliorée par DNP et la spectroscopie RMN du proton, pour démêler la structure à l'échelle atomique de catalyseurs hétérogènes bien définis en un seul site. Trois systèmes ont été étudiés, tous impliqués dans des réactions catalytiques clés.

Tout d'abord, j'ai élucidé la structure tridimensionnelle d'un complexe Iridium-NHC supporté sur de la silice mésoporeuse. La RMN améliorée par DNP a été appliquée pour déterminer la structure des espèces de surface à différentes étapes de la voie de synthèse. J'ai montré que la mise en œuvre d'expériences REDOR (Rotational Echo Double Resonance) sélectives entre les noyaux ^{29}Si, ^{13}C et ^{15}N permet de mesurer des contraintes de distance correspondant spécifiquement au complexe Ir-NHC malgré la présence d'espèces spectatrices n'ayant pas réagi. Le résultat est une structure bien définie, où l'atome d'iridium pointe vers la cavité poreuse. Cette caractréstique inattendue a été interprété par la présence résiduelle d'un ligand cyclooctadiène (COD), coordonnant le centre métallique, ce qui a été confirmé par les données Extended X-Ray Absorption Fine Structure (EXAFS) et les analyses chimiques. J'ai également démontré l'utilisation de la spectroscopie RMN statique du ^{195}Pt améliorée par DNP qui combinée avec des expériences de détection des protons à température ambiante permet de confirmer la structure de surface d'un complexe organométallique de platine, représentatif de catalyseurs bien défini de Pt. Enfin, j'ai mis en œuvre des expériences de RMN proton double et triple quanta pour démêler la structure d'une nouvelle

famille de complexes de surface bimétalliques. L'approche a permis de déterminer sans ambiguïté le nombre de protons hydrure entourant les centres métalliques. Différentes voies de synthèse ont donné des structures de surface distinctes qui ont été élucidées par RMN en combinaison avec de la spectroscopie infrarouge et des méthodes de diffraction des rayons X. Plusieurs méthodologies RMN innovantes ont été développées qui devraient devenir plus largement utilisées pour guider la conception rationnelle de catalyseurs hétérogènes.

Chapter 1

Introduction

1.1 A brief overview on heterogeneous catalysis

According to the encyclopedia Britannica catalysis can be defined as " the modification of the rate of a chemical reaction, usually an acceleration, by addition of a substance not consumed during the reaction " [1]. The term catalysis was first used in 1835 by the Swedish chemist Jöns Jacob Berzelius to refer to a series of experimental evidences made in the late-18th and early-19th centuries relative to the modification of chemical reactions induced the presence of small amounts of foreign substances. For example, Sigismund Constantin Kirchhoff discovered in 1811 the conversion of starch into sugar in the presence of sulfuric acid. In 1817, Sir Humphry Davy described the combustion of gaseous mixtures of coal gas and air in the presence of platinum or palladium wires [2]. These pioneering observations and many others were at the origin of a new and exciting field of investigation, catalysis. The first Nobel prizes in catalysis were awarded at the beginning of the 20th century, first in 1900 to Wilhelm Ostwald for providing a fundamental understanding of catalytic reactions and revealing that a catalyst was affecting a reaction's speed without being included in its end-products, and later, in 1912, to Paul Sabatier for the discovery that many metals, such as nickel or platinum, were active catalysts for hydrogenation of organic molecules. After more than a century of advances, catalysis today is of paramount importance in many aspects of our day-to-day life in fields as diverse as energy, medicine, plastics, environment ... It is indeed estimated that 85 % of all products manufactured involves catalysis somewhere in their production chain, and that over 90 % of all industrial chemicals are produced with the help of catalysts (from plastics to pharmaceuticals and fertilizers) [3].

Catalysts can be gases, liquids or solids. Generally, catalysts are classified depending on their physical state or the nature of the reactions that they catalyze. In homogeneous catalysis, the catalyst is of the same physical state as the reacting substance (generally liquid or gas). The vast majority the catalytic reactions used today in chemical industry rely on heterogeneous catalysts. By contrast to homogeneous catalysis, in heterogeneous catalysis, the catalyst act in a different phase than the reacting substrates (the catalyst is typically a solid and the reactants and the products are in a liquid or gaseous phase). The great benefit of heterogeneous catalysis is the ease of separation of the catalyst from the reaction mixture, for example by filtration or decantation. Heterogeneous catalysts can thus be readily and effectively recovered, which is a key aspect in industrial manufacturing processes. A historical perspective on heterogeneous catalysis, reviewing key discoveries over the last couple of hundred years can be found in reference [4].

Over the last three decades, many efforts were devoted at designing catalytic materials with a controlled structure of the active site as well as a controlled dispersion in order to improve their catalytic activity and selectivity [5]. Porous materials of high specific surface areas (and therefore hosting a large number of active sites per nm^2) have attracted a lot of interest as catalysts or catalyst supports. This encompasses oxides (zeolites, mesoporous alumina or aluminosilicates, aluminophosphates, layered double hydroxides), but also carbon nanotubes or metal-organic frameworks (MOFs) [6–10]. Silica-type mesoporous materials have also emerged as an attractive class of heterogeneous catalysts and catalytic supports. Among them, the Mobil Composition of Matter No. 41 (MCM-41) [11] and Santa Barbara Amorphous-15 (SBA-15) [12] introduced in 1998 are broadly employed. They both display a hexagonal arrangement of one-dimensional pores of diameter between 2 nm and 10 nm for MCM-41 materials, and of up to 30 nm for SBA-15, with micropores connecting the channels for this latter. Heteroatoms such as aluminum, metal nanoparticles or catalytically active ligands can be incorporated within these mesoporous networks by impregnation,

substitution or chemical grafting.

1.2 Preparation of well-defined heterogenous catalysts

Well-defined, single-site (i.e. identical catalytic sites) supported organometallic catalysts prepared from molecular complexes and oxides have long been considered as the ideal heterogeneous catalysts as that would combine the advantages of molecular complexes in terms of productivity, rates and selectivity, with ease of separation and recyclability. The two most common strategies to prepare well-defined supported catalysts are Supported Homogeneous Catalysis (SHC) and Surface Organometallic Chemistry (SOMC). Reviews on these topics can be found in references [13–17]. Figure 1.1 summarizes these two approaches.

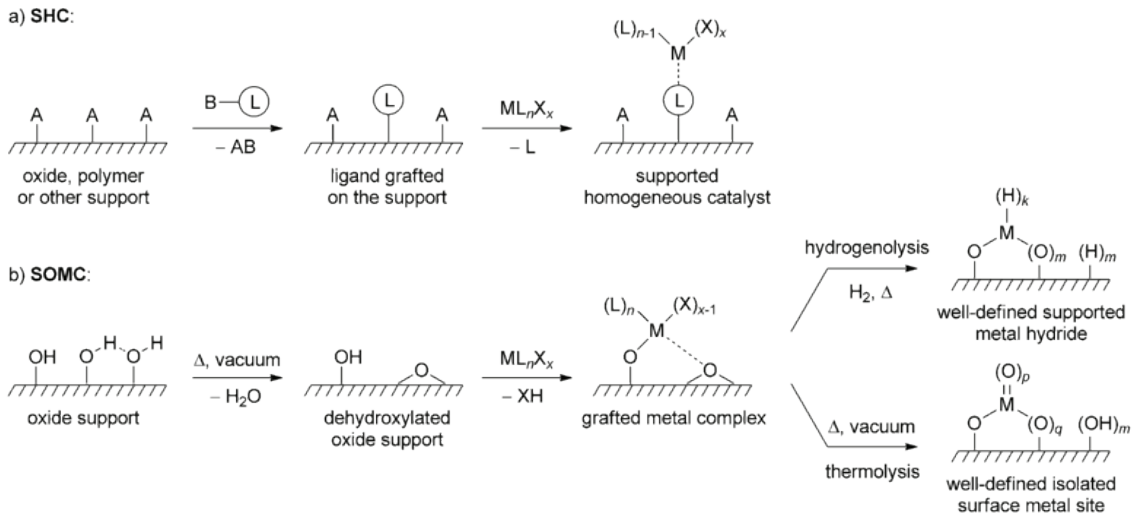

Figure 1.1: Key concepts for the preparation of well-defined supported catalysts by: a) Supported homogeneous catalysis (SHC) and b) surface organometallic chemistry (SOMC). Reprinted with permission from [15]. Copyright 2020 Wiley and Sons.

In **SHC**, an organic ligand is first incorporated in a material, and the metal sites are subsequently grafted to this ligand. This leads to the generation of surface species whose structure is extremely similar to that of the corresponding homogeneous catalyst. However, this approach often yields materials that are less active than their homogeneous counterparts, because the distribution of the catalytic sites embedded in the support is not uniform, their accessibility is limited and the interaction between the metal center and the surface is usually uncontrolled. Strategies have been proposed to overcome these limitations, such as the use of structure-directing agents to improve the distribution of organic ligands in the matrix. Along these lines, Thieuleux and co-workers have recently shown that mesostructured hybrid organic-silica materials represented ideal supports to prepare well-defined heterogeneous catalysts, offering high molecular diversity [18]. Other attractive supports include periodic mesoporous silicas [19] or organic frameworks such as conjugated microporous polymers [20].

In **SOMC**, the metal site is anchored directly at the surface of the support, usually a high surface area oxide, via its oxygen atoms. The density of the OH groups is usually controlled by dihydroxylation at elevated temperatures, and various neutral (L) or anionic (X) ancillary ligands are chosen " by design " so as to modulate the reactivity of the metal sites. After post-treatment isolated metal

hydrides or metal sites can be produced. This strategy has a solid-track record with success stories in key chemical reactions, such as olefin and alkane metathesis or Ziegler-Natta polymerization [21]. Figure 1.2 illustrates the variety of structures that can be engineered by SOMC and the extent of their catalytical capacities. Limitations concern the possible presence of multiple grafted metal species, as well as the requirement of having an oxygen ligand in the first coordination sphere.

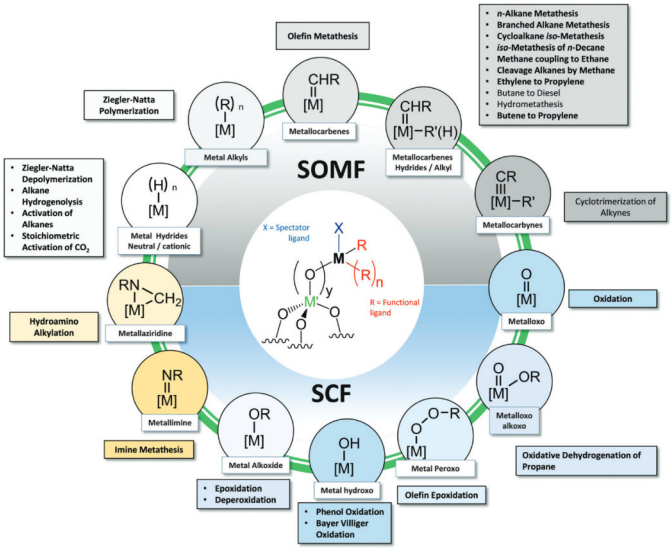

Figure 1.2: Examples of surface Organometallic Fragments (SOMFs) and Surface Coordination Fragments (SCFs) that can be anchored onto an oxide support, together with the corresponding catalytic reactions in which one fragment is part of the presumed catalytic mechanism. Reprinted with permission from [22]. Copyright 2020 Royal Chemical Society.

1.3 Structure elucidation of well-defined heterogeneous catalysts

Both Supported Homogeneous Catalysis and Surface Organometallic Chemistry aim at preparing well-defined single-site catalysts to bridge the gap between homogeneous and heterogenous catalysis. The rational design of well-defined heterogeneous catalysts with improved activity and selectivity depends on the ability to characterize with a high level of certainty their atomic-scale structure. Many modern analytical techniques can be combined to get a detailed knowledge of the spatial surroundings of the active center, as commonly done to characterize the coordination sphere of homogeneous catalysts. Among them, surface microanalysis, Infrared (IR) spectroscopy, Ultraviolet (UV) visible spectroscopy, X-ray absorption-based technique such as EXAFS (extended X-ray absorption fine structure), XANES (X-ray absorption near edge structure) and XPS (X-ray Photoelectron Spectroscopy) or Atomic Force Microscopy (AFM). Among this panoply of techniques, solid-state NMR spectroscopy under Magic Angle Spinning (MAS) plays an essential role. Indeed, besides its versatility (NMR can be applied to any solid substrate, whether crystalline or amorphous) and its non-destructive application, the key advantage of NMR spectroscopy is that it provides atomic-scale structural and dynamics information by probing local environments around nuclei, via measurement of isotropic chemical shifts, anisotropic chemical shift tensors, homonuclear and heteronuclear dipolar interactions, or quadrupolar couplings. The large majority of nuclei

have NMR-active isotopes that can be (more or less easily) observed, which is another advantage of NMR. This spectroscopy suffers however from one key drawback, its inherently low sensitivity. This is because NMR involves transition between energy levels that are almost equally populated. This adds to the low natural abundance of many interesting nuclei such as ^{13}C (1.1 %), ^{15}N (0.364 %) or ^{17}O (0.038 %) among others. This sensitivity issue is further exacerbated when the substrate of interest is located on a surface, i.e. represents only a tiny fraction of the sample volume. This drastic reduction in concentration is illustrated schematically on the following figure.

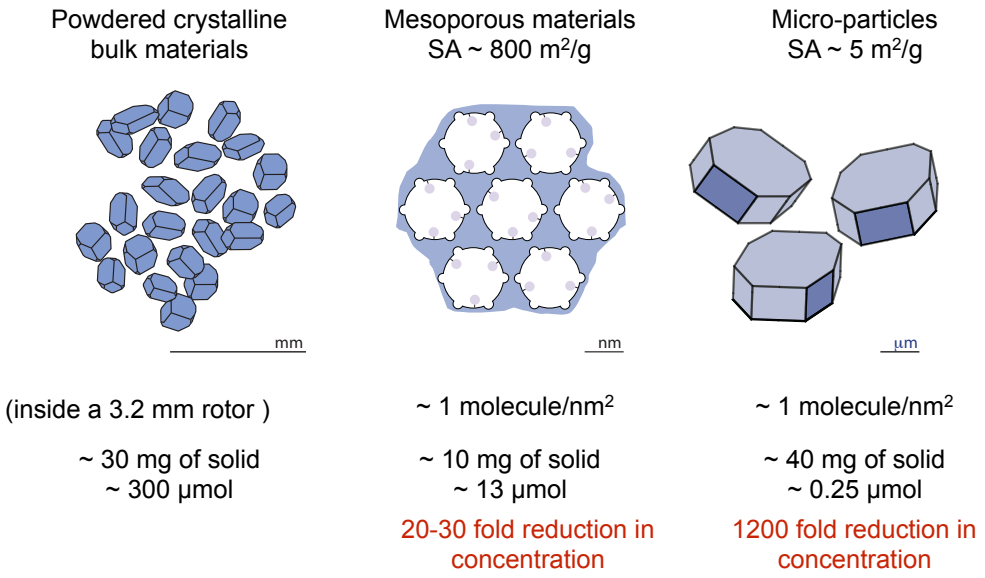

Figure 1.3: Scheme illustrating the drop in concentration of the nuclei of interest from bulk solids to high- and low surface area materials [22]. Courtesy of Dr. Aaron Rossini.

Cross-polarization from surface protons was the first approach proposed to observe selectively and with relatively high sensitivity the NMR signal of heteroatoms at surfaces. Thus, Maciel and Sindorf reported the first NMR signature of a surface in 1980 with the ^{29}Si CPMAS spectrum of silica gels [23]. Three resonances were identified corresponding to the Q_2, Q_3 and Q_4 species (Figure 1.4-(a),(b)). The first MAS NMR spectra of supported metal complexes were reported by Wasylishen and co-workers [24] as reported in Figure 1.4-(c) and (d).

As well-defined organometallic catalysts often include a metal-hydrogen or metal-carbon bond, these complexes are typically characterized by ^{1}H and ^{13}C solid-state NMR spectroscopy, although other NMR probes can be considered such as ^{31}P [25] or ^{17}O [26]. Proton because of its high sensitivity, represents a unique NMR probe, and as will be described later in this manuscript has been widely employed for structure characterization of single site heterogeneous catalysts. Carbon-13 NMR is much more challenging and has often been applied in combination with isotopic labelling. The recent advent of hyperpolarization techniques and more specifically of Dynamic Nuclear Polarization has opened new opportunities for a highly detailed structural characterization of these materials.

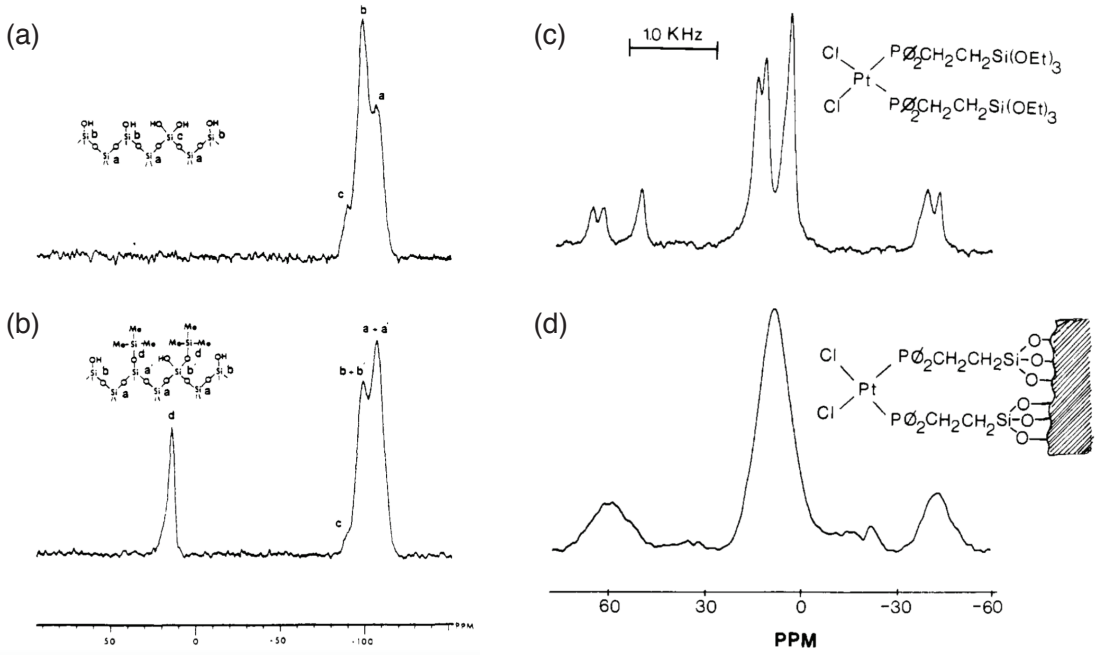

Figure 1.4: ^{29}Si CPMAS spectra of S-157 silica gel at 11.88 MHz (a) before and (b) after trimethylsilylation with trimethylchlorosilane. ^{31}P CPMAS spectra of *cis*-[$PtCl_2(Ph_2PCH_2CH_2Si[OEt]_3)_2$) (c) before and (d) after immobilization on silica gel. Adapted with permission from [23] and [24]. Copyright 2020 ACS.

1.4 Outline of the PhD manuscript

The core of my PhD has concerned the implementation of NMR methods of high sensitivity, namely DNP enhanced NMR spectroscopy and proton NMR spectroscopy, to unravel the atomic-scale structure of single-site well defined heterogeneous catalysts. Three systems were investigated whose structure is depicted in Figure 1.5. They all correspond to well-defined single-site complexes that have been prepared either by the SHC or SOMC approaches described above. Namely, the Ir-NHC and the Pt catalysts were generated by respectively SHC and SOMC strategies, while the synthesis of the bimetallic complexes took advantage of both methods. The Ir-NHC and the Ta=Ir complexes correspond to highly active heterogeneous catalysts, while the Pt complex represents a model for single site Pt catalysts. In chapter 2 and 3, we will review literature on respectively

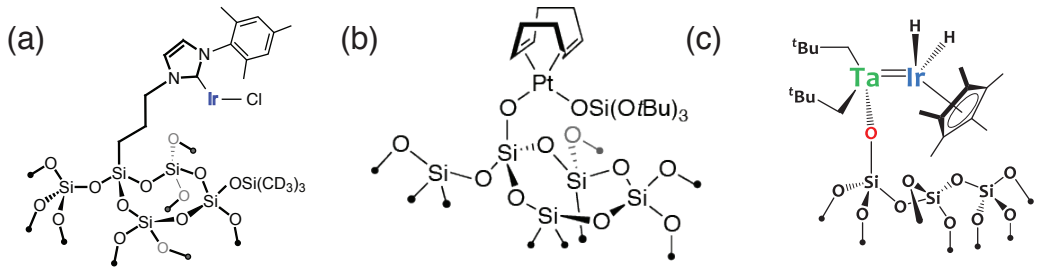

Figure 1.5: (a) Iridium-NHC supported on a silica suface and used for alkene hufrogenation reactions, (b) [(COD)Pt($OSi(O^tBu)_3)_2$] grafted on a silica surface and used in alkane dehydrogenation, CO oxidation, the water-gas shift reaction ... and (c) [≡SiOTa-($CH_2^tBu)_2IrH_2(Cp^*)$] hetero-bimetallic complex grafted on a silica surface and used for example for the deuteration of fulorobenzene.

surface DNP enhanced solid-state NMR spectroscopy and proton multiple-quantum NMR spec-

troscopy, with a special focus on applications in catalysis relevant to the research project. Chapter 4 will summarize our research efforts devoted to the structural elucidation of the Iridium-NHC (Figure 1.5-(a)). DNP enhanced NMR was applied to determine the three-dimensional structure of the surface species at several steps of the synthetic pathway. We showed that the implementation of conventional as well as selective Rotational Echo-DOuble Resonance (REDOR) experiments between ^{29}Si,^{13}C and ^{15}N nuclei enabled one to probe distance constraints corresponding specifically to the Ir-NHC despite the presence of unreacted " spectator " species. The final surface structure points towards the residual presence of a COD (1,5-CycloOctaDiene) ligand, coordinating the molecular Ir complex. The relevance of this structure is discussed with respect to EXAFS and other analytical data. In chapter 5, we show how the implementation of DNP enhanced wide-line ^{195}Pt NMR spectroscopy in combination with room-temperature proton-detected experiments HMQC (Heteronuclear Multiple Quantum Coherence) experiments provides unique insight into the surface structure of the Pt(COD) complex of Figure 1.5-(b). Finally, in chapter 6, we describe the implementation of proton double- and triple-quantum spectroscopy to unravel the structure of a new family of heterobimetallic surface complexes (Figure 1.5-(c)). The approach allowed the unambiguous determination of the number of hydrides surrounding the metal centers. We also demonstrated that different synthetic pathways yielded distinct surface structure that are elucidated by NMR in combination with IR spectroscopy and X-ray methods.

Chapter 2

Dynamic Nuclear Polarization Surface Enhanced NMR Spectroscopy

2.1 Introduction

Over the last two decades, solid-state NMR spectroscopy under Magic Angle Spinning (MAS) has developed as an essential analytical technique for the characterization of a broad range of crystalline and amorphous substrates, ranging from organic molecular compounds to inorganic or hybrid materials. Besides its versatility, the key advantage of NMR spectroscopy is that it provides atomic-scale structural and dynamics information by probing local environments around nuclei, via the measurement of isotropic chemical shifts, anisotropic chemical shift tensors, homonuclear and heteronuclear dipolar interactions, or quadrupolar couplings. This spectroscopy suffers however from one key drawback, its inherently low sensitivity, which prevents NMR to be applied in many of the most exciting areas of modern materials science. Throughout the years, several hyperpolarization techniques were developed to investigate solid substrates that could not be studied using conventional NMR spectroscopy, such Parahydrogen Induced Polarization (PHIP) [27] or hyperpolarized ^{129}Xe NMR [28]. Both were successfully applied to heterogeneous catalytic materials [29–32]. Among these approaches, Dynamic Nuclear Polarization (DNP) has recently emerged as an elegant, efficient, robust and versatile way to circumvent the sensitivity limitation of solid-state NMR spectroscopy, allowing signal enhancements by several orders of magnitude. In this chapter we will focus on the description of DNP enhanced Magic Angle Spinning (MAS) NMR spectroscopy and its application on surfaces in materials science. A review on other hyperpolarization methods can be found for example in reference [33].

2.2 DNP-enhanced solid-state NMR spectroscopy

2.2.1 A brief overview

DNP relies on a polarization transfer from electron to nuclear (coupled) spins upon the continuous saturation of electron paramagnetic resonance (EPR) transitions by microwaves (μw). The maximum enhancement (ε) that can be achieved thus correlates with the gamma ratios of the electron (γ_e) and of the polarized nucleus (γ_n) which is $\varepsilon \approx 658$ for protons. The theory of DNP was first developed by Overhauser in 1953 [34] and then experimentally demonstrated by Carver and Slichter on metallic lithium, who reported an enhancement of 100 [35]. The saturation of the conducting electrons at their Larmor frequency ω_e, followed by (zero- and double-quantum) relaxation processes involving the simultaneous inversion of the electron and nuclear spins led to a 100-fold enhancement of the ^{7}Li NMR spectrum. This effect, which requires mobile electrons, is nowadays known as the Overhauser Effect (OE) and is mostly exploited in DNP of liquids. Several other polarization transfer schemes from electrons to nuclei were subsequently described and exploited in the solid-state. In 1958, Abragam discovered the Solid Effect (SE) [36]. This two-spin process relies on zero- or double-quantum transitions upon irradiation at ω_{e+} ω_n or ω_{e-} ω_n, and is effective at moderate magnetic field for narrow EPR line radical. A third process, involving two dipolar coupled electrons and a nucleus, the Cross-Effect (CE) process, was described in 1963 by Kessenikh *et al* [37]. In this mechanism, the EPR frequencies of the two unpaired electrons must differ by the nuclear Larmor frequency, i.e. ω_{e1} - ω_{e2}= ω_n in order to allow a polarization transfer from the electrons to the nucleus upon saturation of one of the EPR frequencies. This process is particularly efficient for nitroxide radicals for which the CE matching conditions is fulfilled by the anisotropy of the g-tensor. After these proofs of principles, DNP solid-state NMR went through a phase of extinction, before experiencing a real renaissance in the 90s, thanks to the ongoing

work by Griffin and co-workers that made MAS DNP NMR compatible with high magnetic fields (> 5 T). The development of gyrotron sources capable of delivering high-power high-frequency continuous waves (CW), the advent of MAS probes operating at cryogenic temperatures (< 100 K) or the design of ever more efficient polarizing agents (the source of free electrons) like AMUPol or TEKPol were key milestones, which, in combination with suitable sample formulations, allow one to achieve today signal enhancement factors ε_H (defined as the intensity ratio measured in mw on and off spectra) of up to 300 (at 9.4 T and ~100 K) in a broad range of bulk solvent solutions. Over the last two decades, this approach has been successfully applied to a wide range of complex materials and biomolecular solid-state assemblies yielding details on atomic-level surface structures that had been previously inaccessible. One detrimental aspect of CW DNP MAS NMR is the need

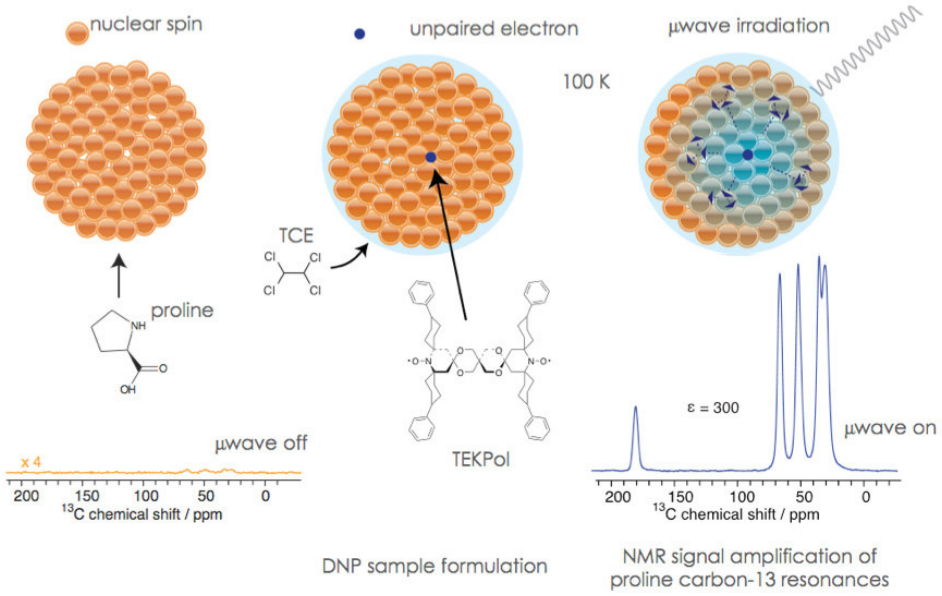

Figure 2.1: Schematic representation of the principle of DNP-enhanced solid-state NMR spectroscopy. The polarization of the unpaired electrons in TEKPOL radical is transferred upon microwave irradiation to the carbon-13 spins of a particulate material (e.g. powdered proline) wetted by a solution of 1,1,2,2-tetrachloroethane (TCE). A 300-fold signal amplification of the carbon-13 resonances is achieved at 100 K and 9.4 T. (Courtesy of Dr. M. Kaushik)

to work at cryogenic temperatures, around or below 100 K, in order to benefit from long electron relaxation times and to effectively saturate the EPR line of the polarizing agent, as will be detailed in the next sections. As a result, the enhancement factor decreases significantly with increasing temperatures. To overcome this limitation, alternative strategies are currently being developed, based on photo-excited triplet states using pentacene and other light-activated radicals, [38] or on pulsed DNP [39] with the recent introduction of time domain techniques such as Nuclear Orientation Via Electron Spin Locking (NOVEL) [40] or Time-Optimized DNP (TOP) [41]. These approaches require however non-standard equipment to generate microwave pulses, and will not be discussed in this thesis.

2.2.2 Continuous-wave DNP polarizing schemes

Several polarizing schemes have been described and implemented to transfer in solids and under continuous microwave irradiation the electron polarization to nearby nuclei, the performances of

which depend on the chemical structure, concentration and electronic properties of the polarizing agent, on the strength of the magnetic field, on the spinning frequency or on sample temperature.

The Solid Effect (SE) is a two-spin process, and proceeds via the hyperfine dipolar coupling between the electron and the nuclear spin. A nominally forbidden electron transition at the frequency of $\omega_{mw} = \omega_{0I} \pm \omega_{0S}$ is irradiated (ω_{mw}being the microwave frequency, ω_{0I} the electronic and ω_{0S} the nuclear Larmor frequency). Eigenstate mixing leads to double quantum (DQ) and zero quantum (ZQ) transitions, resulting to positive or negative enhancements, respectively. The solid effect is effective for polarizing agents with homogeneous and inhomogeneous EPR linewidth both smaller than the nuclear Larmor frequency ("narrow line" radicals). This is for instance the case for trityl or 1,3-bis-diphenylene-2-phenylallyl (BDPA) radicals. The interest of SE DNP is however limited as the probabilities for DQ and ZQ transitions scale with $1/B_0^2$, and modest SE enhancements are usually obtained at high field.

The Cross Effect (CE) involves three coupled spins, two electrons and a nucleus. When the so-called matching condition is fulfilled, i.e., when the EPR frequencies of two dipolar coupled electrons $\omega_{0,e1}$ and $\omega_{0,e2}$ match the Larmor frequency of the nucleus, a degeneracy in the energy levels of the three-spin system occurs, which, upon irradiation at one of the two electron frequencies, leads to an enhancement of the nuclear polarization. The condition ω_{e1} - ω_{e2}= ω_n is the so-called Cross-Effect matching condition. The population distribution at thermal equilibrium for a general three-spin system in the eight different energy levels, and after saturation of the allowed EPR transitions and CE transition is depicted in Figure 2.2. . The saturation of the electron

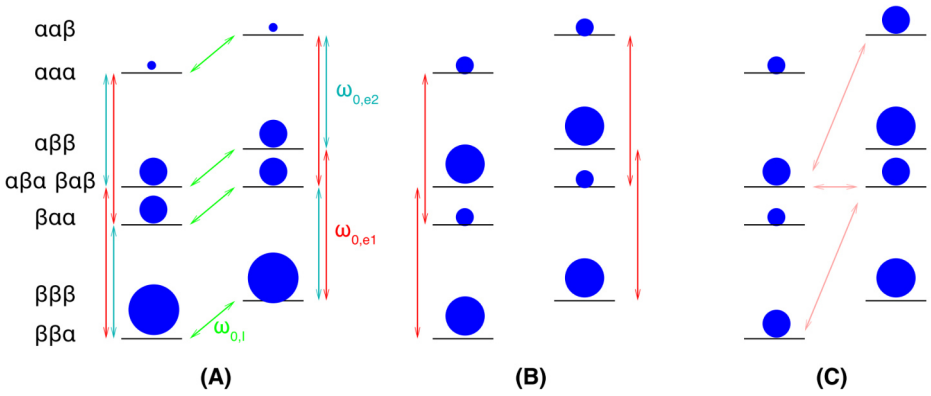

Figure 2.2: Depiction of the energy levels for a three-spin system (e_1, e_2 and nucleus I). Each level corresponds to one eigenvector $| m_{e_1} m_{e_2} m_1 >$. When levels $| \alpha\beta\alpha >$ and $| \beta\alpha\beta >$ are degenerated, the CE matching condition occurs. The single quantum transitions are represented by the red, blue and green arrows for e_1, e_2 and I. (A) Is the distribution of the population at thermal equilibrium. (B) Saturation effect of the EPR transition of e_1 at ω_{0,e_1}. (C) Shows the population distribution after the CE. Adapted from [42].

of the highest EPR frequency will lead to a negative enhancement while the saturation of the other electron will lead to a positive enhancement. CE DNP is especially efficient for radicals having a large inhomogeneous EPR line, like is the case for TEMPO-based radicals, for which the matching condition is permitted by the anisotropy of the g-tensor between nitroxides of different orientation. The EPR line broadening scales with B_0 for nitroxides, and thus the probability of CE frequency matching decreases with the field. As a result, the CE enhancement factors scale

with $1/B_0$. The theory of CE under MAS has been described in two landmark papers by Thurber *et al.* [43] and by Mentik-Vigier *et al* [44]. The authors presented analytical results based on the Landau-Zener theory of adiabatic transitions and described CE under MAS as a series of spin transitions at avoided crossings of the energy levels (LACs for level anti-crossings), with varying degrees of adiabaticity. Three main LACs are considered: (i) electron-microwave crossing, when the microwave frequency crosses the EPR frequency of one electron, $\omega_m \sim \omega_{e1,2}$; (ii) three-spin crossing, when the difference of the EPR frequencies crosses the NMR frequency, ω_{e1} - $\omega_{e2} \sim \pm\omega_n$; (iii) electron-electron crossing, when $\omega_{e1} \sim \omega_{e2}$. Several series of such events (or several LACs) happen during the rotor period is schematically represented in the figure below for two electrons with a g-anisotropy. The system starts with the two electron resonances that are well-separated

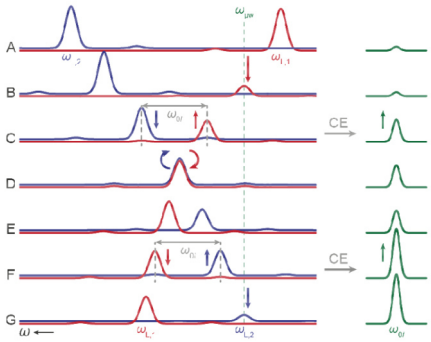

Figure 2.3: Schematic representation of CE events under MAS. Reprinted with permission from [45]. Copyright 2020 AIP.

(A). In the course of the rotation, the electron frequencies vary over the anisotropic pattern of the g-tensor. At some point, the frequency of one of the two electrons matches the microwave irradiation frequency (B, microwave LAC). This leads to a partial saturation of the concerned electron (electron 1 in red in this scheme). When the CE condition is matched (C, CE LAC), the polarization difference of the electrons is transferred to the nucleus. An increase in nuclear polarization is observed. The frequencies of the two electrons then cross. The dipolar coupling between the two electrons (D, dipolar LAC) induces a mixing of the electron spin states and an exchange of electron polarization if the process is adiabatic. As rotation continues, another CE LAC event may happen and more polarization is transferred to the nucleus.

The Overhauser effect (OE) a third mechanism has recently received renewed attention. The Overhauser Effect (OE) is a two-spin process. In contrast to the SE, the microwave irradiation is applied at the single quantum EPR transitions and the enhancement is generated by zero-quantum and double-quantum relaxation. In solids, the OE is based on a stochastic modulation of the scalar hyperfine couplings between electron and nuclear spins. In a landmark paper, Griffin and co-workers have observed significant OE DNP in insulating solids using the narrow line polarizing agent BDPA dispersed in polystyrene, and sulfonated-BDPA (SA-BDPA) dissolved in glassy glycerol/water matrices. Importantly, their experimental data indicate that OE scales favorably with increasing magnetic fields [46].

2.2.3 Polarization sources for high field MAS DNP NMR

A significant number of stable radicals have been developed as polarization sources to enable ever more efficient solid-state DNP. They mostly belong to three main families: trityl radicals (for SE DNP), nitroxides (for CE DNP) and BDPA-derived molecules (for SE and OE DNP). Here, we will focus on radicals for CE DNP, as this latter is still the dominant and most commonly exploited mechanism for DNP MAS NMR. Initial CE high-field DNP experiments were performed with solutions doped with high concentrations of monoradical species. Thus, in 1995, TEMPO (2,2,6,6-tetramethylpiperiinl-1oxyl) nitroxide was the first radical to be used for DNP enhanced solid-state NMR [47]. Griffin and co-workers then demonstrated that biradical polarizing agents, having a short distance between the two unpaired electrons, yielded significant improvements in the DNP process [48, 49]. To do so, two TEMPO radicals were tethered by a poly-(ethylene glycol) chain of variable length to control the electron-electron dipolar coupling [48]. An enhancement factor of 3.9 larger than the one obtained with TEMPO (namely 250 at 90 K and 5 T) was achieved with the shortest radical in the series. This subsequently led to the introduction of TOTAPOL in 2006, which has been largely used by the DNP community for more than a decade [49]. Rigid tethers constraining the orientation of the TEMPO moieties in a nearly orthogonal conformation were later proposed with the introduction of bTbK (bis-TEMPO-bisketal) that yielded a further improvement in the enhancement factors (325 at 80 K and 5 T) [50]. More recently, the importance of having long electronic relaxation times was highlighted with the development in 2012 and 2013 of highly efficient, slowly relaxing, binitroxides by Zagdoun *et al* [51, 52]. These advances in the design of nitroxide polarization sources has led to the introduction of TEKPol [52] and later AMUPol [53] radicals. Longer electron relaxation times indeed facilitate the saturation of the EPR lines and prevents a too fast recovery of the electron magnetization towards equilibrium [54]. TEKPol and AMUPol remains the gold standard radical at intermediate magnetic fields, providing enhancement factors of around 300 at 100 K and 9.4 T in respectively organic and aqueous solutions. Variants were proposed like TEKPol-2, a slighly bulkier version of TEKPol [55] or like bcTol [56]. Figure 2.4 shows some of the most important nitroxide-based polarizing agents discussed above and that act as efficient polarizing sources at low and intermediate magnetic fields (below 9. 4 T).

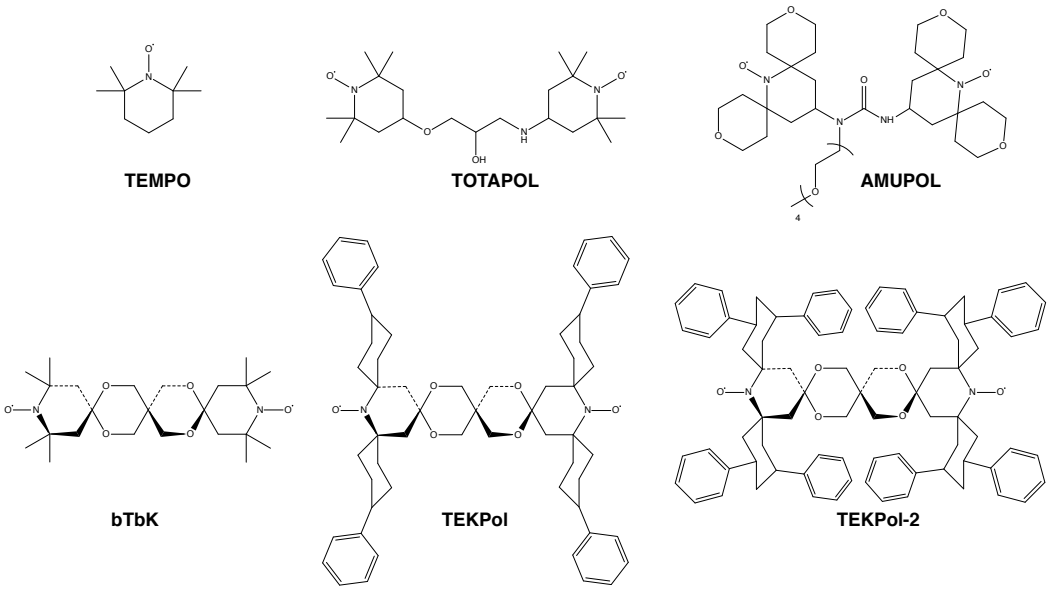

Figure 2.4: Nitroxide based radicals for DNP at intermediate magnetic fields.

The design of efficient polarizing agents is an active field of research. Very recently, the efforts have shifted towards the development of polarizing agents having high DNP performance at very high magnetic fields (18.8 T and above). Indeed, the performance of AMUPol or TEKPol radicals significantly decreases with increasing magnetic fields. Thus, in a 3.2 mm rotor, the proton enhancement of a frozen solution of 10 mM AMUPol in d8-glycerol/D_2O/H_2O 60/30/10 (v/v/v) typically drops from 300 at 9.4 T to about 140 at 14.1 T, 48 at 18.8 T and 20 at 21.1 T. This decrease in enhancement factor is in line with theoretical analysis and with numerical simulations of CE DNP with binitroxides. One approach to obtain high enhancement at high field consists in investigating CE DNP using narrow line biradicals, or mixture of narrow line radicals. In 2013, Michaelis *et al.* reported direct ^{13}C enhancement at 5 T using a mixture of SA-BDPA and trityl radicals, and observed significant CE DNP upon saturation of the slowly relaxing SA-BDPA moiety [57]. In this work, the difference between the narrow EPR line of trityl and the maximum of the EPR line of the TEMPO was shown to perfectly match the ^{13}C Larmor frequency for the direct carbon-13 CE DNP. Enhancements of 600 were reported on a 5 T magnet at 82 K.

In 2015, Mathies *et al.* introduced a new class of biradicals in which a nitroxide and a narrow-line radical, namely trityl, were chemically tethered [58]. TEMTriPol-1 (Figure 2.5), which displays a strong coupling interaction between the two electrons, yields proton NMR signal enhancements of 65 at 18.8 T (two times more than AMUPol in a similar formulation). In contrast to broad line binitroxide radicals, TEMTriPols show a remarkable field dependence, with DNP enhancements increasing with the field. This work notably highlighted the key role of the sum of the dipolar and exchange electron-electron coupling in the design of radicals for very high field DNP. Recently, Wisser *et al.* presented a new series of hybrid radicals consisting of a BDPA moiety tethered to a nitroxide and reported DNP enhancements of up to 180 at 18.8 T and 60 at 21.1 T with HYTEK2, the best radical in the series. Hybrid radicals show a favorable spinning frequency dependence as well as no or little depolarization (i.e. their absolute sensitivity gain does not decrease with increasing spinning frequencies as is the case for AMUPol or TEKPol radicals) [59].

Following on from the idea that relatively high magnetic interactions led to improved DNP performances at very high magnetic fields, the structure of six-membered nitroxide ring biradicals were recently revisited and new water-soluble binitroxides, dubbed AsymPols [60] and TinyPols [61] were introduced. With the best radical in the TinyPol series, DNP enhancement factors as high as 90 and 38 at respectively 18.8 T and 21.1 T were reported in aqueous solutions and 40 kHz MAS frequency.

As a conclusion, while bi-nitroxides are still the gold-standard polarizing agents for DNP MAS NMR at low and intermediate magnetic fields, hybrid radicals appear to be more efficient at higher field and fast MAS. We note that despite the huge amount of work that has been done to develop these radicals, the enhancements achieved with those polarizing sources are still far from the theoretical maximum amplification factor of 658. Future developments in the radical design, but also in the probe hardware (with for example a better distribution of the μw in the rotor) are expected to further improve the efficiency of CE DNP using exogeneous eletronc sources. Figure 2.5 shows the structure of three well-performing radicals at high fields. Another solution to achieve high enhancements at very high fields is to exploit the favorable field dependence of OE DNP. This mechanism has recently received renewed attention after the discovery that it may be active in insulating solids in solid state DNP using BDPA (1,3-bisdiphenylene-2-phenylallyl) radicals [46] and have a favorable field dependence. It has been recently shown at the host institution that enhancement of up to 100 could be obtained for BDPA in OTP (ortho-terphenyl), a rigid glassy

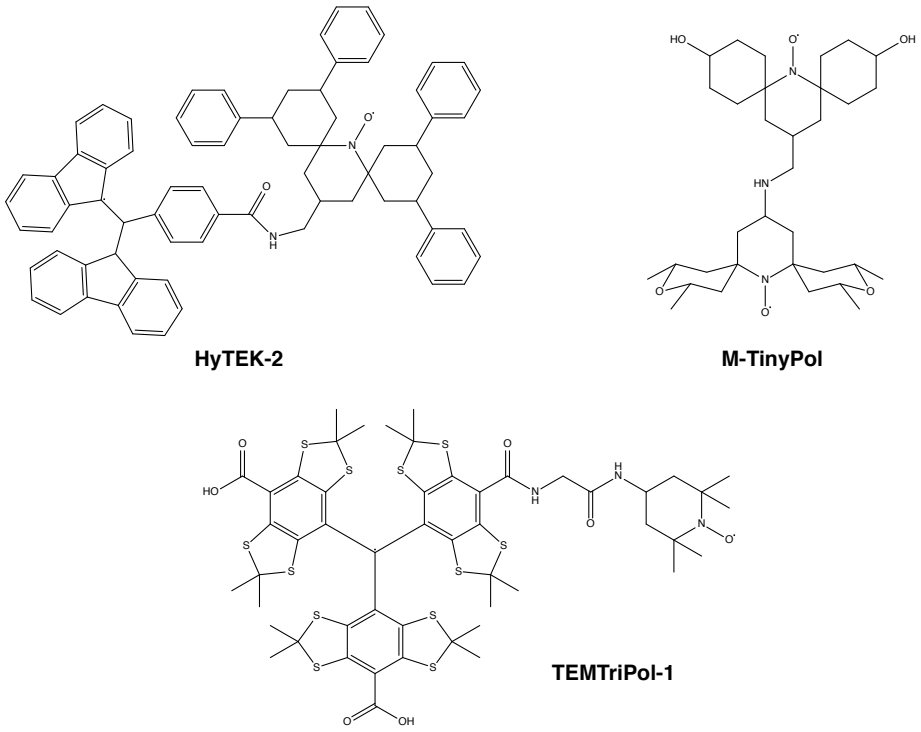

Figure 2.5: Best-performing bi-radicals at high magnetic fields, namely, hybrid biradicals HyTEK-2 and TEMTriPol-1 that are soluble in organic solvents, as well as di-nitroxide and water-soluble M-TinyPol.

solvent [62, 63]. We note however, the OE currently requires build-up times on the order of 40 s that mitigate to some extent the gain in overall sensitivity.

All the polarizing agents mentioned can be classified under the exogeneous polarzing sources. Antoher type of polarizing agents exist dubbed endogeneous PA. Those consist of metal complexes such as Gd(III). Specifically, biradicals made of two Gd(III) attached to one another. Direct DNP was used with these PA on ^{1}H, ^{13}C and ^{15}N [64]. Another metal complex used is Mn(II) and was used to polarize ^{7}Li nuclei [65]. In recent developments, Fe(III) was used as a polarizing agent making the probing of ^{17}O spectra at natural abundance possible [66]. More information about paramagnetic ions used for DNP can be found in reference [67]. Moreover, defects in materials can also be used to hyperpolarize the sample. In particular, surface defects in silicon micro- and nanoparticles can be used for direct ^{29}Si nuclear polarization enhancement [68]. Finally, γ-rays can be used to create stable radicals in inorganic solids, such as fused quartz and borosilicate glasses, as well as organic solids, such as glucose, cellulose, and a urea/polyethylene polymer that can be used to polarize the sample. Enhancements of 400 and 30 can be observed on quartz and glucose respectively by probing the ^{29}Si and ^{1}H [69].

2.2.4 DNP MAS NMR Instrumentation

DNP MAS NMR was not accessible to high magnetic fields until the 90s, when Griffin *et al.* proposed the use of high frequency and high-power gyrotrons to generate the microwave irradiation. In parallel, they designed and developed low temperature (LT) magic angle spinning triple-resonance probes, [70–72] operating at temperatures as low as 80 K, so as to carry out experiments in cryogenic conditions and improve the saturation of the electrons. We note here that another advantage of running DNP experiments at low temperatures is that frozen solutions can be used as polar-

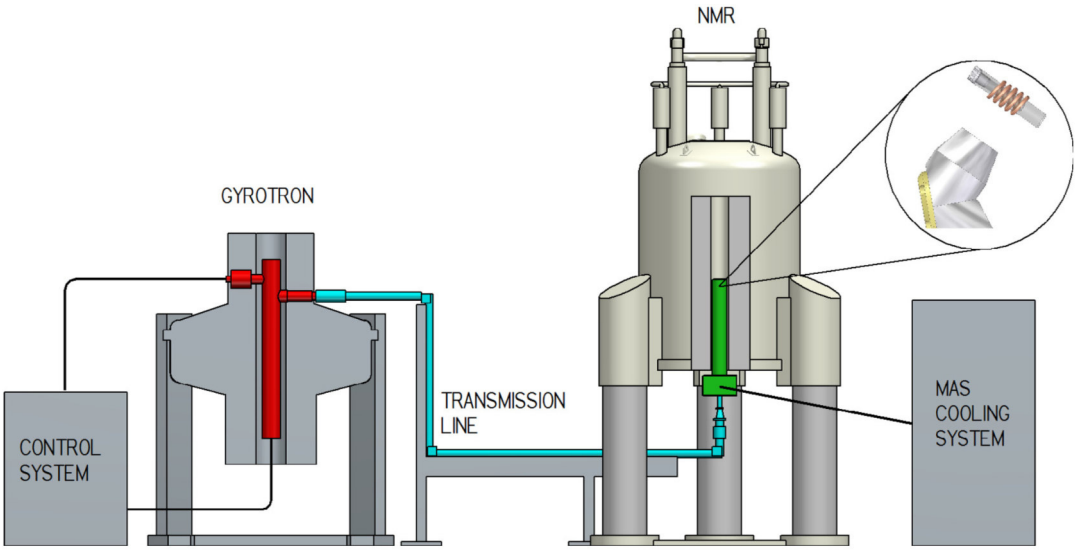

Figure 2.6: Commercial MAS DNP instrumentation composed of a gyrotron, an NMR magnet, a waveguide and a cryocabinet. Reprinted with permission from [73]. Copyright 2020 Elsevier Inc.

ization matrices that benefit from an intense dipolar-coupled network of protons that efficiently transport the enhanced polarization throughout the sample by spin diffusion. The commercial instrumentation currently available from the manufacturer Bruker and that has been used during this PhD has been built according to the design initially introduced by the Griffin's group. Figure 2.6 describes this instrumentation. The microwaves are generated by a frequency-fixed gyrotron, and the beam is transmitted to the NMR probe via a transmission line and irradiate continuously a 3.2 or 1.3 mm sapphire or zirconia rotor. The NMR magnet is equipped by the sweep coil, whose current can be tuned so as to reach the optimal CE condition for the different radicals. The probe cooling is ensured by cooling down three independent nitrogen gas channels bearing, drive, and variable temperature through a liquid nitrogen heat exchanger. A temperature of around 110 K is achieved that can be measured by inserting microcrystalline KBr in the sample. Sample spinning frequencies of respectively 14 and 40 kHz are reached with the 3.2 and 1.3 mm LT MAS probes. Here we note that the distribution of the microwave is dependent on the probe design and of the probe diameter as illustrated in Figure 2.7. Moreover, DNP MAS experiments can be performed at ultra-low temperature ($\sim$ 30 K) if the helium is used as a cooling gas instead of nitrogen. This will generally be advantageous in terms of the total sensitivity. However, it will be disadvantageous due to the slower polarization buildup at lower temperature and lower DNP efficiency at higher field [74, 75].

2.3 DNP enhanced NMR spectroscopy of surfaces

2.3.1 Principle

Over the last decade DNP has developed as a key approach to boost the NMR sensitivity of surfaces in functional materials. Enhancement of NMR signals by DNP appears indeed particularly relevant for characterization of surfaces of inorganic and hybrid materials for which isotope labeling is usually impossible or difficult, and where the active sites conferring its properties to the sample are

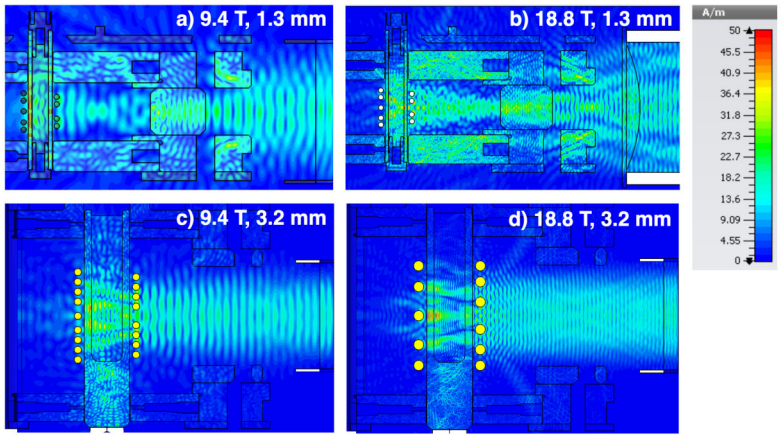

Figure 2.7: Numerical electromagnetic simulation of microwave magnetic field for two MAS geometries at two frequencies; central cuts through MAS stator are shown in each case. Input power is 0.5 W, microwave beam incoming from the right side. 1.3 mm and 3.2 mm plots are not drawn to scale with respect to each other. Reprinted with permission from [59]. Copyright 2020 ACS.

often dilutes. A key experimental strategy to transpose the high enhancement factors observed for bulk frozen solutions to surfaces and materials that are intrinsically free of paramagnetic radicals is to the use incipient wetness impregnation (IWI). In this approach, the powdered materials are wetted by a minimal amount of a solution containing a radical. For porous materials the polarizing solution will penetrate the pores by capillary action, while for non-porous materials it will simply wet the surface. The polarization of the unpaired electrons is then transferred from the radical to the ^{1}H nuclei on the surface either directly or via proton spin diffusion through the surrounding solvent molecules. Cross-polarization is applied to polarize surface low-gamma nuclei such as ^{13}C, ^{29}Si, ^{15}N, ^{31}P, ^{27}Al... This methodology (indirect DNP) is especially effective to selectively enhance the NMR signals of surface entities in an approach called DNP SENS (DNP surface enhanced NMR spectroscopy) [76–78]. Alternative strategies to IWI have been used, some of which will be discussed in section 2.3.6. If the first proofs of concepts were reported in 2010 and 2011 on model mesoporous silica matrices of high surface area [79, 80], recent applications concern a large range of chemical systems as will be described below. Using this sample preparation protocol, high DNP enhancement factors are usually obtained on the surface nuclei, which makes it possible to record rapidly multi-dimensional and multi-nuclear experiments (such as homo- and hetero-nuclear correlations or dipolar recoupling experiments) that are needed to get access to structural information and that are extremely challenging, if not impossible, on dilute species with conventional NMR. Alternatively, the polarization can can be transferred directly from the unpaired electrons of the polarizing agent to the low-gamma nuclei of interest at the surface using a single pulse experiment (direct DNP). Both DNP SENS methods are described schematically in Figure 2.8. While the enhancement is usually much lower with direct DNP, this approach allows probing both surface and sub-surface/bulk nuclei. Complementary spectra are usually detected with the two methods as illustrated in Figure 2.9. Alternative methods to transfer the polarization from one nucleus to another are being used and are shown to be more effective than the cross-polariaztion in some cases. Specifically, in the case of quadrupolar nuclei, the INEPT scheme with adiabatic recoupling is shown to improve the sensitivity of detection of quardupolar nuclei greatly [82, 83]. This method is currently being used for all quadrupolar nuclei. Another method of transfer used for

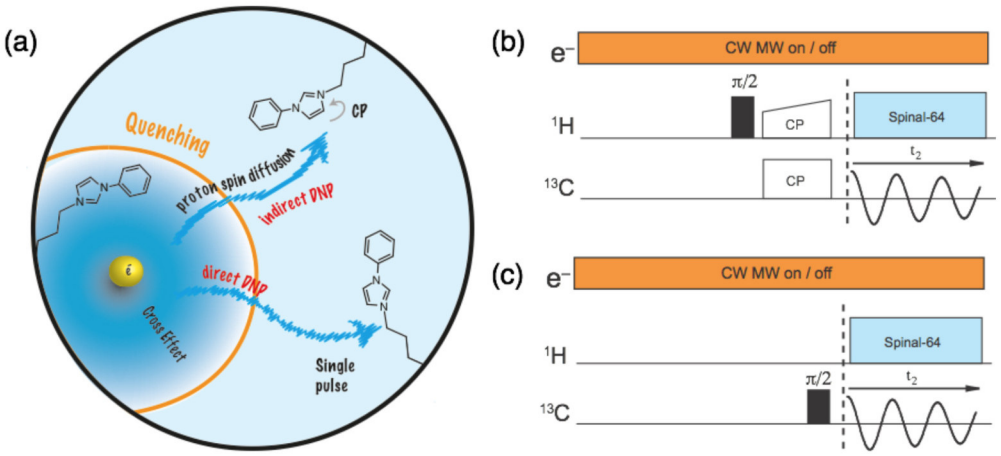

Figure 2.8: a) Description of the DNP SENS experiment. b) Pulse sequence used for 1D CP MAS NMR spectroscopy. c) Single pulse sequence used for 1D MAS NMR spectroscopy. MW is switched on continuously.

quadrupolar nuclei is the PRESTO (Phase-shifted Recoupling Effects a Smooth Transfer of Order) scheme [84, 85]. In general, when DNP is performed, the matrix contains a pool of protons that facilitates the polarization diffusion from one nucleus to another. Usually, it is done via proton-proton spin diffusion and then by cross-polarization to other nuclei. However, Björgvinsdóttir *et al.* showed recently that a bulk of proton-free inorganic solids can be hyperpolarized [86]. This is achieved through homonuclear spin diffusion between low-γ nuclei. This is possible by direct excitation or by pulse cooling, a repetitive bursts of cross polarization [87]. The authors showed a gain of 50 in overall sensitivity for an inorganic solid of $^{119}SnO_2$. This method also applied for Ga^{31}P, ^{113}CdTe and α-quartz.

2.3.2 Some practical aspects

Sample preparation is an essential part of DNP experiment. It involves selecting a chemically inert polarizing agent at the right concentration, and selecting a polarizing matrix that forms an amorphous glass at cryogenic temperatures with or without an added cryoprotectant. It is imperative that the polarizing agent as well as the matrix are compatible with the surface of interest, and are therefore chosen case-by-case basis. Polarizing agents are often selected according from the radicals listed in Figure 2.4 and 2.5, depending on the magnetic field and of the polarizing medium. Some of these aspects are discussed below.

2.3.3 The polarizing matrix

For all the work described in this thesis, Incipient Wetness Impregnation was used to formulate the DNP samples [88]. The approach consists in wetting the dry powdered material with a solution containing the polarizing agent. The solvent is chosen to i) be compatible with the surface and ii) to form a good glass at cryogenic temperature so as to ensure a balanced distribution of the radical within the sample. Aqueous solutions containing a mixture of glycerol or dimethylsulfoxide (DMSO) and water (also known as the "DNP juices") can be employed with water-soluble radicals. For surfaces that cannot be impregnated with water (e.g. water-sensitive surfaces or hydrophobic surfaces), organic solvents such as 1,1,2,2 Tetrachloroethane (TCE) are commonly used [89]. The proton content of the matrix is an important parameter and deuteration may be used to channel

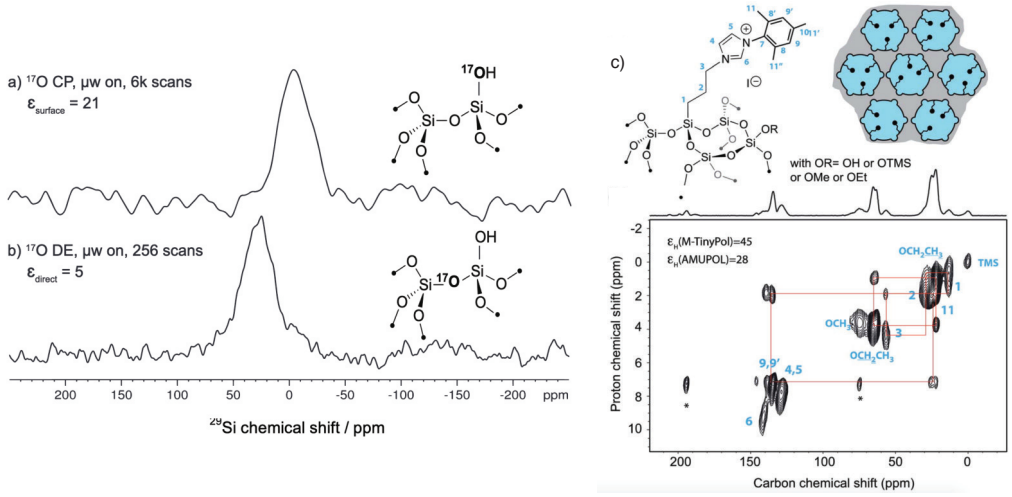

Figure 2.9: a) ^{17}O CP and b) Direct Excitation spectra of $Si^{17}O_2$(∼ 20 % ^{17}O enrichment) impregnated with a 16 mM solution of HyPTEK in TCE obtained at 18.8 T (527 GHz electron Larmor frequency) with a 12 kHz MAS frequency in a 3.2 mm rotor. Both spectra are recorded under μw irradiation. c) Contour plot of a 2D DNP SENS ^{1}H-^{13}C HETCOR spectrum of the surface compound recorded at 18.8 T and 12.5 kHz MAS frequency using a 3.2 mm rotor. The sample was impregnated with a 10 mM solution of TinyPol in H_2O. The contact time was 500 ms. During $t_{1,e}$ DUMBO homonuclear decoupling was applied. [81] The one-dimensional carbon-13 cross-polarization spectrum is shown above the 2D map. The red lines show the various correlations. Reprinted with permission from [59, 61]. Copyright 2020 ACS and RSC.

more efficiently the polarization form the electrons to the surface nuclei [90–92]. A similar effect has been observed by Perras and co-workers upon deuteration of the radical [93]. This latter increases the radicals' relaxation time, thus contributing to a higher saturation factor and larger DNP enhancement. The rigidity of the matrix is also a key factor to ensure long electronic relaxation times, and along these lines it has been shown that ortho-terphenyl (OTP) represents a performant matrix for solid-state DNP [62, 94]. Alternative strategies have been used for nanoparticles that form colloidal suspensions aggregating at low temperatures. In 2017, Viger-Gravel *et al.* proposed to use frozen acrylamide gels as an alternative DNP medium to the widely used glycerol/water or DMSO/water matrix, and reported enhancements of around 200 with AMUPol at 3.8 mM in pure water at 9.4 T and 100 K [95]. This matrix was also shown to be well-adapted for disperse nanoparticles. More recently Hanrahan *et al.* showed that by impregnating the NPs and adding dielectric particles i.e Boron Nitride (*h*-BN), higher enhancement factors can be achieved [96].

2.3.4 The radical concentration

The concentration of the polarizing agent is a crucial factor as it will determine not only the signal enhancement directly measured from μw on and off experiments and the build-up time of the polarization, but also the paramagnetic bleaching factor (i.e. the fraction of surface that will be invisible by NMR due to strong paramagnetic effects). In 2012, Zagdoun *et al.* determined the optimal radical concentration for mesoporous silica materials. To do so, the overall sensitivity factor Σ_{Si} was considered, defined as the product of the ε_H by the contribution factor θ, where this latter corresponds to the fraction of nuclei that contributes to the NMR signal. θ encompasses both the paramagnetic bleaching and losses due to depolarization [51]. Figure 2.10 shows the enhancement

ε_H (a), the contribution factor (b) and the absolute sensitivity factor (c) as a function of radical concentration, here bTbK in TCE. The optimal concentration that yields the highest Σ_{Si} and $\Sigma^{\dagger}_{Si}$ (that takes into account the temperature factor) was found to be 16 mM [51]. The optimal radical

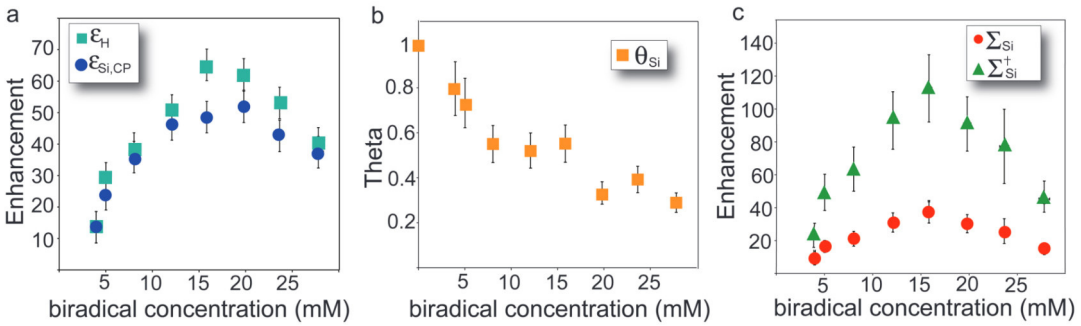

Figure 2.10: (a) ^{1}H enhancement (ε_H) and ^{29}Si enhancement via CP ($\varepsilon_{Si,CP}$) as a function of the biradical concentration. (b) The quenching factor θ_{Si} recorded as function of the radical concentration and (c) The overall sensitivity $\Sigma^{\dagger}_{Si}$ and Σ_{Si}. $\Sigma^{\dagger}_{Si}$ is defined as Σ_{Si} multiplied by T_{rt}/T_{DNP}. Reprinted with permission from [51]. Copyright 2020 ACS.

concentration will however depend on the DNP mechanism, on the radical used and on the surface properties, and therefore 16 mM is not a universal concentration for DNP SENS. In 2018, Perras *et al.* showed that a universal concentration for all kind of materials should be avoided and suggested that materials with high surface area requires higher concentrations for better perfomances. This is due to the interactions between the radicals and the surface [97].

2.3.5 Tuning the surface to improve the DNP performance

In some cases, the substrate or the surface can be tuned to improve the performance of DNP SENS without modifying its properties. Notably, it has been shown that the presence of methyl groups drastically affect the DNP performance. This is because methyl groups act as relaxation sinks due to their rotation that still occurs at cryogenic temperature, and prevent an effective transport of the polarization [98,99]. For the materials that will be discussed in chapter 4, the silica surface has to be passivated, i.e. the hydroxyl groups have to be replaced by passive groups that will not react with the reagents during the grafting step of the metallic complexes. In reference [98], different passivating groups were investigated. Enhancement of 9 was found in such a case, whereas if the passivating group was trimethylsilyl an improvement was observed and enhancement of 73 was recorded on a propylazide ligand grafted on the surface. It has been shown that optimizing and improving the DNP conditions to ensure high efficiency and high sensitivity has been and is always a work in progress.

2.3.6 Dedicated strategies for reactive surfaces

While DNP SENS has emerged as a versatile approach to investigate the atomic-scale structure of surfaces by NMR, its application to reactive surfaces remains challenging. Indeed, the presence of highly reactive species (e.g. Lewis acidic metal center in heterogeneous catalysts) may lead to the degradation / reduction of the exogenous polarizing agent, and/or to a modification of the properties of the material (e.g. deactivation of the catalyst by coordination of the free radical). In such cases, no or little signal enhancement is obtained. In addition, the resonances of the reduced

radicals may be observed, which complicates spectral analysis [100]. Several approaches have been proposed to overcome this issue and prevent a close approach of the polarizing agent to the surface sites. Although not implemented in this PhD work, they are described below, as they could be of potential interest in the future for the investigation of the surface catalysts described in chapter 6.

Dendritic polarizing agents

Dendritic polarizing agents and more specifically carbosilane-based dendritic polarizing agents have been proposed by Copéret *et al.* in 2016 to investigate sensitive surfaces [101]. This approach involves the encapsulation of the radical in hydrophobic carbosilane dendrimers that inhibit direct contact and therefore interaction between the surface of materials and the PA. Dendrimers of various sizes were considered. Two critical points were investigated in this study. First, as a homogeneous distribution of the PAs in the matrix is essential to obtain high enhancement factors, the authors showed by EPR spectroscopy that the dendritic radicals did not aggregate and that the distribution of radicals in the matrix was similar to that obtained with non-dentritic analogues. Second, the DNP efficiency of the encapsulated radicals was evaluated by NMR. The dendritic polarizing agent with the bulkiest and most rigid structure (Figure 2.11-(a)) was shown to yield the highest DNP SENS enhancement factor and to preserve long coherence life times on surface species. Using this polarizing agent, a carbon-13 CPMAS enhancement of around 10 was reported on a highly reactive single-site tungsten-based heterogeneous catalyst for which conventional binitroxide radicals did not yield to any DNP effect (Figure 2.11-(b) and (c)).

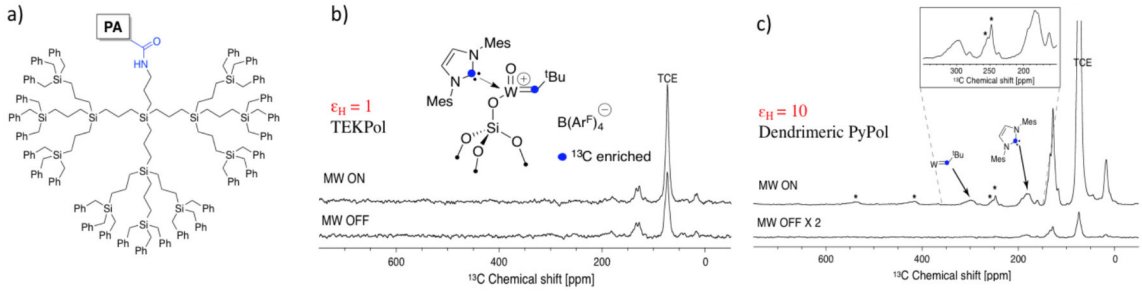

Figure 2.11: a) Dendritic polarizing agents with 3 dendritic wedges. DNP enhanced 13C CPMAS spectra of $W^{13}C@SiO_2$ impregnated with (b) 16 mM TEKPol solutions and (c) 16 mM of the dendrimeric radical in TCE with MW on (top) and off (bottom). The inset shows the enlarged region between 250 and 350 ppm). Asterisks mark the spinning side bands. Reprinted with permission from reference [101]. Copyright 2020 RSC.

Large-sized radicals and porous materials with small pore sizes

This approach, suggested by Basset and co-workers in 2017, is tuned to confined active sites in porous materials with suitably small windows so that the penetration of a bulky radical is sterically prevented [100]. Two conditions are required: i) fairly small pores (typically 2.5-3.0 nm) and ii) a relatively large-sized radical (typically a binitroxide such as TEKPol that has a diameter of about 2 nm). Thus, this strategy is based on the design of a porous system with a pore size that will avoid direct contact between the radical and the active site but let solvent molecules diffusing into the cavities so as to allow efficient spin diffusion within reasonable build-up times, and that will still be large enough to accommodate the surface species of interest. The method has been successfully

applied on highly reactive complexes such as [(≡Si-O-)W(Me)$_5$] supported on MCM-41 of pore diameter 2.5 or 3 nm as illustrated in Figure 2.12.

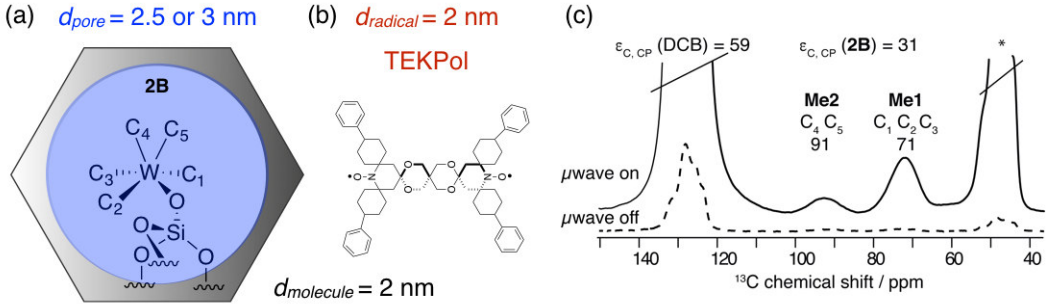

Figure 2.12: a) Chemical structure and size ($d_{molecule}$) of W(Me)$_6$ anchored into mesoporous silica (2B) with a pore size of 2.5 or 3 nm (drawing not to scale). (b) TEKPol structure and size ($d_{radical}$). (c) ^{13}C CPMAS DNP SENS (100 K, 400 MHz, 263 GHz gyrotron) of **2B** anchored in MCM-41 of pore diameter 3 nm, impregnated with 16 mM TEKPol 1,2-dichlorobenzene (DCB) solution. Reprinted with permission from [100]. Copyright 2020 RCS.

Hydrophilicity effects to promote self-aggregation and -protection

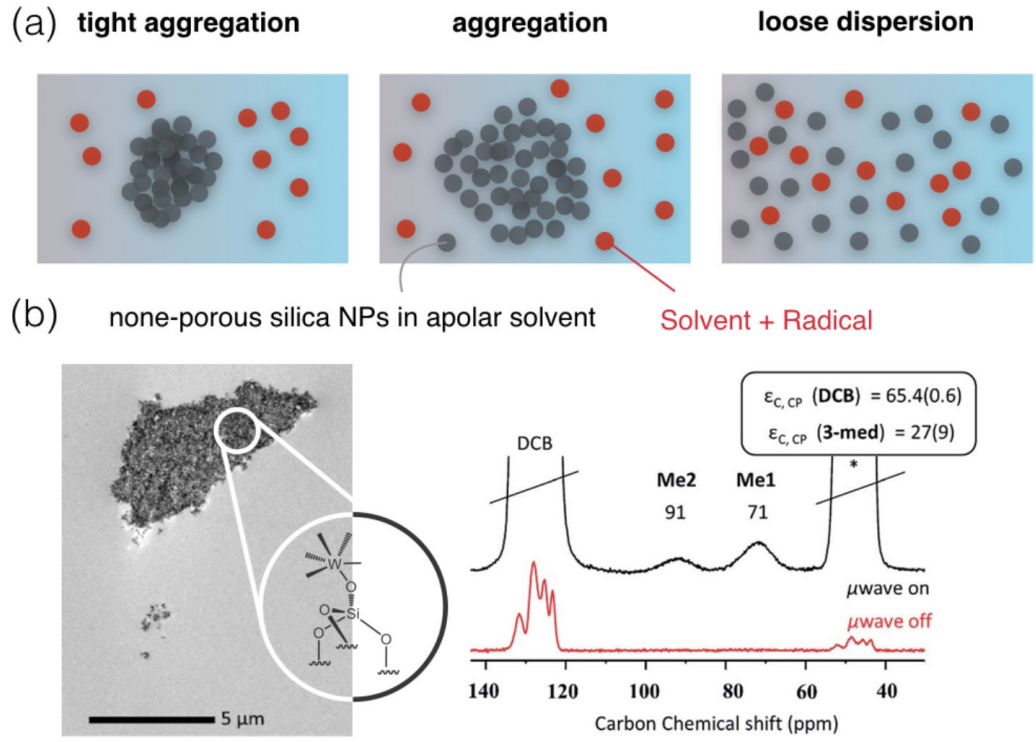

Figure 2.13: Schematic model representing silica nanoparticles aggregation or dispersion when covered with a fragment at high, moderate or low concentration in a non-polar medium. The radical is excluded from the aggregates or dispersed (Courtesy of Dr J. Viger-Gravel). (b) TEM micrograph of the distribution of particles and structure of the W-based organometallic complex grafted at their surface, together with the μw on and off carbon-13 spectra (in black and red respectively). Reprinted with permission from reference [102].Copyright 2020 RSC.

The following strategy is suitable for non-porous materials, and has been proposed by Basset

et al, a year later. In this approach, the radical-surface interactions are prevented by the aggregation of the particles that leads to a partial protection of the reactive surface species inside the interparticle space, thereby preventing reaction with the polarization agents. The concept consists in tuning the surface, here of silica nanoparticles, by modifying their hydrophilicity, as a function of the nature of the surface organometallic fragments and of their concentration, thus promoting their aggregation or their dispersion in an apolar solvent, as illustrated in Figure 2.13-(a). In particular, correlations were established between the hydrophilicity of the support on one hand, and the concentration of surface functional groups and its carbon content on the other hand. High concentration and carbon content promote self-aggregation in non-polar solvents, which in turn prevents a (bulky) radical from diffusing between particles while allowing the solvent molecules to penetrate the inter-granular space [102]. The concentration of silanols (as the aggregation of the particles occurs mainly through the formation of inter-particle hydrogen bonds) as well as the size of the surface groups (bulky fragments reduce aggregation due to steric hindrance) are other key parameters in this approach. Enhancements as high as 64 have been reported for [(≡Si-O-)W(Me)$_5$] (the same surface complex as in the previous section but grafted here on non-porous silica nanoparticles) as shown in Figure 2.13.

Protecting the reactive surface by pyridine adsorption

Copéret *et al.* have very recently introduced a new formulation for DNP SENS of reactive surfaces that could in principle be broadly applied [103]. This strategy consists of adsorbing pyridine molecule on the surface of the material prior to sample impregnation. Pyridine is a well-known probe molecule to detect the presence of Lewis and Brønsted acid sites on alumina or silica-alumina surfaces, as well as a widely-used ligand in coordination chemistry to stabilize reactive metal sites. Pyridine was thus used as a passivating molecule to cover the surface and subsequently prevent a close proximity between the radicals and the reactive acid sites. Investigations made on Ziegler-Natta (ZN) catalysts where pyridine had been adsorbed before impregnation with TEKPol in TCE solution have shown a 10-fold enhancement at 14.4 T (Figure 2.14).

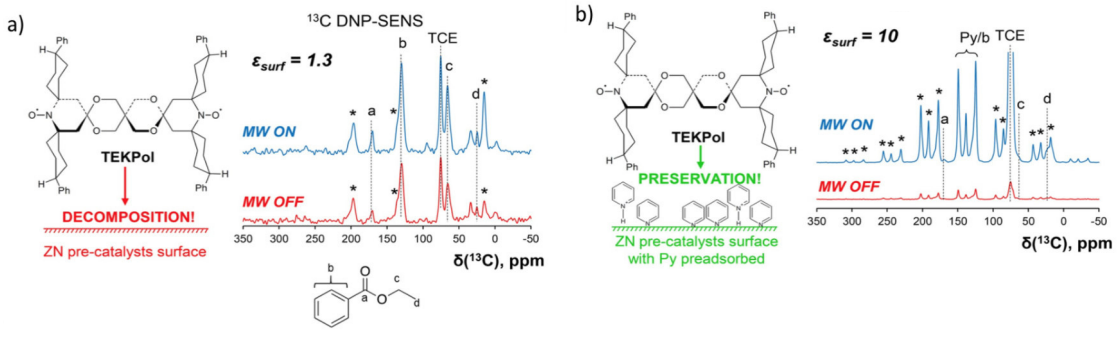

Figure 2.14: ^{13}C DNP enhanced spectra of ZN surface without (a) and with (b) pre-adsorbed pyridine. Reprinted with permission from reference [103].Copyright 2020 RSC.

Alternatives approaches

Finally, for the sake of completeness, we mention alternative approaches that have never been exploited to polarize reactive surfaces, but which could be potentially extremely useful in such a context. The first concept is similar to the one of the dentritic radicals. In 2014, Lelli *et al*

proposed to incorporate hydrophobic radicals into micelles formed by neutral amphiphiles [104]. Relatively high enhancement factors were reported in bulk frozen solutions of d_8-glycerol:D_2O:H_2O for bTbK or TEKPol embedded in surfactants. Such assemblies could be used to polarize reactive surfaces compatible with water. We also note that many materials have endogenous radicals that could be used as a source of electrons to polarize reactive species. For example, the surface of silica nanoparticles could be polarized from dangling bonds or paramagnetic defects at the surface of the particles [105]. Alternatively, porous silica supports that incorporate polarizing agents inside the walls of the material have been designed and exploited for MAS or dissolution DNP [106–108]. To the best of our knowledge however, none of the above-mentioned strategies have been investigated for DNP SENS of reactive catalysts.

2.4 Applications in heterogeneous catalysis

If the first demonstration experiments were reported on model mesoporous silica matrices of high surface area [79, 80], recent applications concern a large range of chemical systems such as high performance organometallic heterogeneous catalysts, doped silicon surfaces, metal-organic frameworks, ligand-capped nanoparticles, cementitious materials, quantum dots or zeolites. In most of these examples, the enhanced proton polarization is transferred to dilute and (moderately) low-gamma spin I = 1/2 nuclei (^{13}C, ^{31}P, ^{29}Si, ^{119}Sn or ^{15}N) located at the surface of the materials. The signal of surface quadrupolar nuclei, of interest for many modern inorganic or hybrid materials, can be similarly enhanced. Several ^{27}Al DNP SENS NMR spectra have been reported on a variety of systems, including of surface species having relatively large quadrupolar broadening. Some investigations were also successfully conducted by exploiting the DNP enhanced NMR signature of extremely low-gamma and/or low abundance nuclei such as ^{17}O (I = 5/2, natural abundance 0.0438%, resonance frequency at 9.4 T 54 MHz) [109–114] , ^{43}Ca (I = 7/2, natural abundance 0.135 %, resonance frequency at 9.4 T 26 MHz) [115], ^{89}Y (I = 1/2, natural abundance 100 %, resonance frequency at 9.4 T 19.6 MHz) [116], ^{95}Mo (I = 5/2, natural abundance 15.92 %, resonance frequency at 9.4 T 26.6 MHz), ^{47}Ti (I = 5/2, natural abundance 7.44 %, resonance frequency at 9.4 T 22.56 MHz) or ^{49}Ti (I = 5/2, natural abundance 5.41 %, resonance frequency at 9.4 T 22.56 MHz) [82], or of nuclei with extremely broad CSA patterns ranging from several hundred kHz to tens of MHz such as ^{195}Pt (I = 1/2, natural abundance 33 %, resonance frequency at 9.4 T 86 MHz) [117, 118] or ^{35}Cl (I = 3/2, natural abundance 75 %, resonance frequency at 9.4 T 39 MHz). [119, 120] Without being exhaustive, some recent applications on heterogeneous catalytic materials will be reviewed in the following. Many studies concern the catalytic support itself and will not be mentioned here. In most of the studies described below, DNP SENS is applied in combination with other surface techniques. We also note that a review on this topic was proposed by Pruski and co-workers in 2015 [121].

2.4.1 Organometallic catalysts immobilized onto oxide supports

Several groups reported DNP SENS experiments on well-defined organometallic complexes grafted on the surface of porous or non-porous inorganic frameworks, mostly silica, but also alumina, titania or mixed oxides. The work done by Copéret *et al.* and by Basset *et al.* on metal-NHC surface complexes immobilized on mesoporous silica, will be described in a dedicated section. A few studies done on other systems are highlighted here. In 2015, Gutmann *et al.* investigated

a bi-rhodium complex covalently linked to a bi-functionalized SBA-15 support [122] by ^{13}C and ^{15}N DNP SENS experiments at natural abundance. They were able to distinguish the different binding modes of the catalyst. On the same year, Pruski and co-workers applied 1D ^{15}N and 2D ^{1}H-^{15}N DNP enhanced NMR experiments to confirm the surface structure and chemical bonding of $\equiv SiOZr(NMe_2)_3$ obtained by reacting $Zr(NMe_2)_4$ with mesoporous silica nanoparticles [123]. In 2014, Conley *et al.* applied ^{119}Sn DNP experiments on materials obtained by grafting tin complex on silica dehydroxylated at 700 °C, and demonstrated the presence of minor surface species at extremely low concentration (< 0.1 molecule / nm^2), formed after reaction of the molecular precursor onto isolated Q_2 silanols and surface rearrangement. ^{13}C-^{119}Sn REDOR experiments were applied to confirm the surface structures [124]. More recently, Aljuhani *et al.* applied ^{15}N DNP SENS to charaterize the coordination sphere of a well-defined hafnium complex grafted catalyst on a silica surface [125]. In 2015, Ong *et al.* reported the DNP investigation of a well-defined tungsten complex immobilized on $SiO_{2-(700)}$ particles. Two-dimensional ^{13}C-^{13}C dipolar correlation experiments were performed to quantitatively measure carbon-carbon distances in metallacycles, which are intermediates in the alkene metathesis catalytic cycle [126]. More recently, two-dimensional ^{13}C-^{1}H and ^{29}Si-^{1}H DNP enhanced experiments were implemented to investigate tantalum complexes, formed by grafting $TaMe_5$ and dimeric $Ta_2(OMe)_{10}$ onto a silica support, that were used as precursors for the synthesis of catalytically active and air-stable tantalum nitride nanoparticles, and to unravel the chemistry at the surface of the support. Finally, we mention the recent work by Camacho-Bunquin *et al.* on organometallic Pt-complexes supported on silica. ^{13}C and ^{195}Pt DNP NMR spectroscopy were performed to determine the structure of the Pt-complex [127].

2.4.2 Metal organic Frameworks (MOFs)

Metal-organic Frameworks (MOFs) are one of the most attractive families of solid supports for heterogeneous catalysis as their topology and pore sizes can be tuned with a high degree of flexibility, and as their structure can be functionalized by catalytic sites [128]. As is the case for other

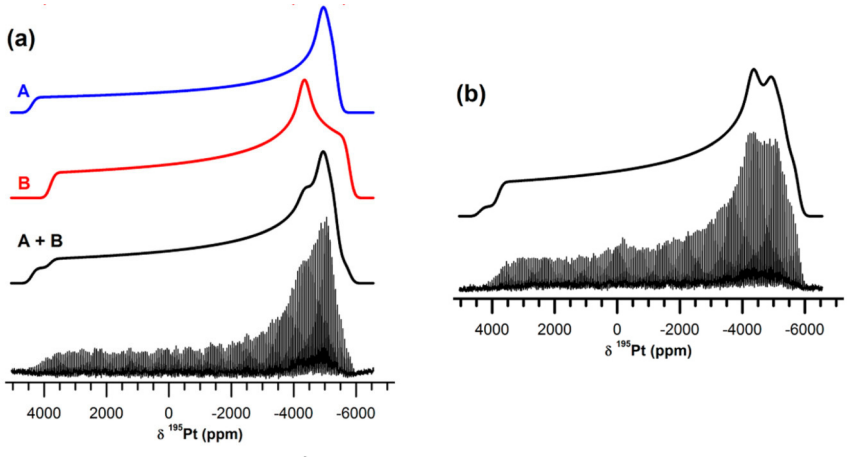

Figure 2.15: DNP-enhanced ultrawideline ^{195}Pt-^{1}H spectra of Pt^{2+}/UiO-66-NH_2 before (a) and after (b) reductive treatment for 30 min at 150°C in 10 % H_2/Ar. Simulated powder patterns for the cis (A) and trans (B) sites, as well as their sum (A + B), are shown at the top. Adapted with permission from reference [117]. Copyright 2020 ACS.

classes of solid catalysts, establishing structure-activity relationships is essential to understand and improve their catalytic properties. In 2012, Rossini *et al.* presented the first application of DNP

SENS on functionalized MOFs. The authors showed that the radical (bCTbK in this case, $d_{radical}$ = 1.5 nm) was slowly diffusing inside the pores (d_{pores} = 1.6 nm), leading to an increase of the DNP enhancement with time, and that this diffusion was blocked in proline-functionalized MOF compounds. Despite these difficulties to make the polarizing agent penetrate the network, sizable amplification factors were reported (between 5 and 16 at 9.4 T) that enabled the fast acquisition of ^{13}C and ^{15}N NMR spectra with high S/N ratio [129]. Later, Pourpoint *et al.* measured ^{13}C-^{27}Al correlations and proximities by DNP SENS on aluminum-based MOFs, using the TOTAPOL radical that was shown to penetrate the framework, and obtained distances in agreement with the expected topology of the material [130]. UltraWideline NMR was also used to characterize MOFs in 2016 by Kobayashi *et al.* [117]. UltraWideline ^{195}Pt spectra were used to differenciate the cis and trans conformation of the Pt^{2+}/UiO-66-NH_2 MOF as shown in Figure 2.15.

2.4.3 Microporous Organic Polymers (MOPs)

Miroporous Organic Polymers (MOPs) are also attracting much interest in heterogeneous catalysis. The first DNP SENS study of MOP was reported by Blanc and co-workers in 2013 [110]. Relatively high enhancement (of the order of 13 at 9.4 T) were obtained using bCTbK that was shown to fully penetrate the porous network despite the small pore size (d_{pores}= 1.6 nm), which was attributed to the swelling of the material upon impregnation. ^{13}C and ^{15}N spectra could be acquired at natural abundance within tens of minutes, opening the way to high-throughput investigations on libraries of materials. Blanc and co-workers also exploited DNP to characterize conjugated microporous polymers (CMPs) and recorded with high-sensitivity one- and two-dimensional ^{13}C NMR spectra on a wide variety of structures, including quantitative data that were used to establish the polymer composition [131]. More recently, Wisser *et al.* reported DNP SENS data on CMPs which were post-synthetically modified with a rhodium complex and which were used as macroligands for heterogeneous photocatalysis [132]. The bipyridine-based porous polymers and the rhodium-functionalized catalysts were characterized by ^{13}C CPMAS and ^{1}H-^{13}C HETCOR spectra. As part of my PhD work and as a side project, I have been involved in a more in-depth structural study on these materials. The publication is in preparation, and the results will not be detailed in the PhD manuscript. However, they will be quickly summarized here. In order to get access to the porous structure of the rhodium-modified CMPs, we implemented DNP enhanced ^{13}C-^{15}N REDOR experiments, that enabled to probe the distance between the rhodium complex and ^{15}N-labelled amino groups incorporated into the framework (Figure 2.16).

2.4.4 Alumina and aluminosilicates

Alumina and aluminosilicates (including zeolites) are widely used as catalysts or as catalytic supports. Solid-state NMR spectroscopy is one of the most versatile and applied technique to investigate their atomic-scale structure. The recent development of DNP has opened new opportunities to selectively probe with an unprecedented level of details, not only their surface structure, but also host-guest interactions, acidities and catalytic cycles. The first ^{27}Al DNP SENS experiments on γ-alumina were reported in 2011 by Vitzthum *et al.* Aluminum-27 enhancements of around 20 were obtained at 9.4 T using TOTAPOL and multiple-quantum (MQ-MAS) experiments were recorded [133], highlighting the resonances of Al(IV) and Al(VI) sites. Later, Lee *et al.* observed the presence of pentacoordinated Al in mesoporous alumina and reported surface-selective ^{27}Al-^{27}Al dipolar correlation spectra that probed proximities between the various surface sites [134]. In

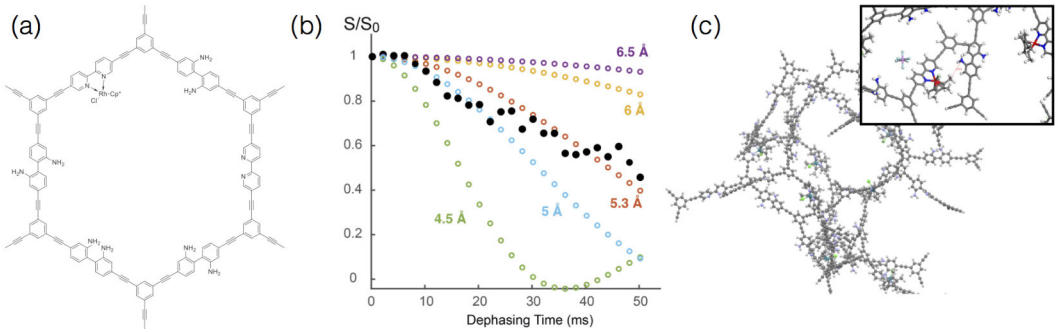

Figure 2.16: (a) Schematic structure of the rhodium-functionalized CMP. The porous polymer is composed of 25 % of bipyridine monomer and 75 % of di-amino-biphenyl (100 % 15N-labeled). (b) Intensity ratio S/S_0 as a function of the recoupling times. The signal intensities were measured on the carbon-13 resonance of the methyl groups of the Rhodium complex. As the nitrogen atoms of the bipyridine motifs bearing the metal center are not ^{15}N-labelled, the dephasing of the CH_3 signal will only arise from spatial proximities with amino groups in neighboring bipyridine units. The slope of the dephasing curve reflects the size of the dipole−dipole interactions and can be interpreted in terms of average ^{13}C-^{15}N internuclear distance. (c) DFT-calculated structure, showing proximities between the CH_3 of the rhodium complex and the amino groups at the crossing of two polymer chains.

2015 Valla *et al.* applied DNP to enhanced the ^{27}Al and ^{29}Si signals of aluminosilicates, and get an atomic-level description of the interface between silica and alumina in these materials. Notably, proximities between these two heteronuclei were probed by comparing dipolar- and scalar-based correlation experiments [135]. A few DNP NMR studies have been reported on zeolites, either to follow reaction mechanisms [136–138], to reveal new features of the framework topology [139] or of the active sites [140–144] , or to investigate the host-guest interaction [145]. In particular DNP was exploited in mechanistic studies of zeolites to observe and identify the NMR signature of naturally abundant [138] or ^{13}C-labelled reactants [136, 137] over reaction times.

2.4.5 Functionalized metal nanoparticles and quantum dots

The benefits of DNP enhanced NMR have also been exploited to investigate the surface structure of catalytically active metal nanoparticles and of quantum dots for photocatalysis. In 2013, Pruski and co-workers applied DNP SENS to enhance the signal for organic molecules adsorbed with low surface coverages on γ-Al_2O_3-supported Pd nanoparticles [146]. More than 2500-fold time savings (at 9.4 T using TEKPOL) were reported, enabling the rapid acquisition of scalar- and dipolar-based ^{13}C-^{13}C correlations experiments on Methionine-impregnated particles. This led to the elucidation of the binding and breakdown of this amino acid on the nanoparticle surface and the identification of the key sites on the adsorbate undergoing the attack in a catalytic reaction. Surfaces of quantum dots were also studied by DNP using dedicated formulation protocols, as mentioned earlier. Piveteau *et al.* reported enhancements between 40 and 80 on oleate-capped CdSe quantum dots by dispersing them into porous SiO_2, and probed surface interactions by ^{13}C-^{111}Cd dipolar HMQC experiments [147]. Later, DNP enhanced PASS experiments were implemented on CdSe quantum dots coated with a CdS shell and NMR signals from different atomic and magnetic environment in the cores and at the surfaces were distinguished [148]. A thorough review on nanoparticles has been recently published and more details can be found in reference [149]. In 2017, Hope *et al.* showed the first Surface-selective direct ^{17}O DNP on CeO_2 nanoparticles [150]. (Sub-)Surface sites can only be detected with direct DNP with high selectivity generated from the slow diffusion from

radicals in the vicinity of the surface. Indirect DNP can be used to identify -OH terminations and adsorbed water on the CeO_2 surface. More recently, Nagashima *et al.* used the INEPT scheme to probe the ^{17}O signal at natural abundance from an Al-doped ZnO NPs impregnated with TEKPol solution [82].

2.5 DNP SENS on NHC Supported Catalysts

2.5.1 NHC heterogeneous catalysts

The synthesis, reactivity and stability of a five-membered ring N-heterocyclic carbenes (NHCs) as well as their application as ligands for metal complexes were reported by Wanzlick *et al.* in the 60s [151,152]. Arduengo *et al.* revived the interest of NHCs as ligands in transition metal chemistry in 1991 with the characterization of the first crystalline carbene, a N-heterocyclic carbenes [153]. NHCs have an extraordinary thermal and air stability, low toxicity and electron-rich, σ-donors, forming very strong bonds with the majority of metals, making them ideal ligands for metal complexes in homogeneous catalysis. N- heterocyclic carbene (NHC) for heterogeneous catalysis is still a relatively nascent area and the potential of these systems has been reviewed recently by Ranganath *et al* [154].

Homogeneous catalysts are usually well-defined and well-characterized single-site compounds. Imitating this level of definition is an on-going challenge of heterogeneous catalysis. This is essential to obtain the high performance and selectivity found in homogeneous catalysts. Surface organometallic chemistry (SOMC) has developed as an established approach to design, prepare and characterize well-defined heterogeneous catalysts, thus leading to the development of active and selective heterogeneous catalysts for many key chemical transformations. Silica has attracted much attention as a support because covalent bonds can be established with surface OH groups, the density of which can be controlled by dehydroxylation at elevated temperatures. Thus, silica nanoparticles dehydroxylated at 700 °C will contain approximately 0.8 silanol groups per nm^2. While metals can be directly grafted on the silica support, methods where an organic ligand is first introduced are preferable as they offer more flexibility in terms of design. They are notably well suited for the preparation of supported NHC catalysts.

In the following we will briefly describe two possibilities to introduce organic ligands and prepare immobilized NHC complexes: the so-called indirect and direct grafting processes. The indirect method consists in post-grafting functionalized organosilane precursors onto the oxide support. Although convenient and simple, this approach presents some limitations. Specifically, this procedure does not allow an accurate control of the ligand distribution and of the nature of the final active site (multiply ligated metal centers can be formed after coordination). In addition, some variability is introduced in the nature of the surface species (formation of mono-, di-, and tripodal species), which leads to a gradient of stability towards leaching [18]. The direct method also known as the sol-gel process, is the method of choice to prepare supported functionalized metallic complexes with organic linkers regularly distributed along the silica surface. This approach relies on the co-hydrolysis followed by the co-condensation of tetraethylorthosilicate (TEOS) and of an organotriethoxysilane ($RSi(OEt)_3$) in the presence of a structure-directing agent (SDA) and leads to the formation of ordered mesoporous silica materials directly functionalized by the organic precursor (R). This ensures a homogeneous distribution along the inner surface pore channels of the organic fragments (with a distance of typically 1 nm between them) [155–157] as well as its attachment

to a silicon atom belonging to the silica network and bound by three Si-O linkages. The metallic complex is then grafted onto the organic linker after a series of surface reactions.

This strategy is illustrated in Figure 2.17 for the synthesis of Ru-NHC heterogeneous catalysts. The sol-gel process yields to the formation of iodine or chlorine precursors at the surface of the mesoporous silica, that are transformed into imidazolium ligands before reaction with Ru complexes. The surface is passivated before reaction with the metal complex to remove all residual alkoxy/silanol groups. This protocol yields highly active and stable (with minimum bleaching) single site catalysts. It requires however the optimization of the initial fragment concentration to enhance the catalytic performance and facilitate the diffusion of the reactant during the catalytic reaction [156]. In addition, the choice of the counterion is crucial, as demonstrated for homogeneous systems for example by Wappel *et al* [158].

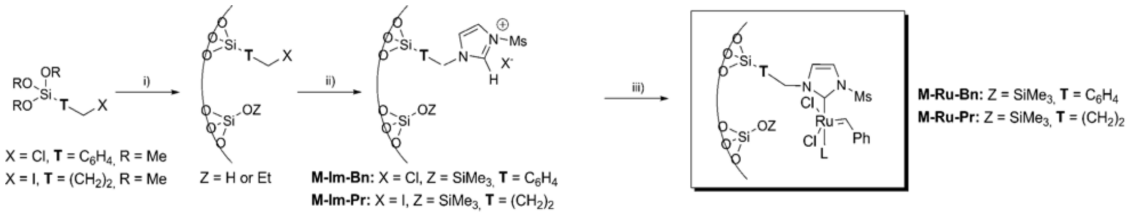

Figure 2.17: Stepwise preparation of supported Ru-NHC catalysts by the sol-gel method followed by a series of post-reactions on the surface. Reprinted with permission from [159]. Copyright 2020 Wiley and Sons.

2.5.2 Structural characterization of NHC catalysts by DNP SENS

Several of these NHC catalysts have been investigated by DNP SENS. In 2013, Conley *et al.* applied this approach to investigate palladium-NHC catalysts incorporated within mesoporous silica [160]. Both the imidazolium precursor and the actual catalyst were studied (Figure 2.18-(a)). The authors reported DNP enhancements of 25 and 15 on the two surface compounds respectively, upon impregnation with a 16 mM solution of bCTbK in TCE (Figure 2.18-(b) and Figure 2.18-(c). The one-dimensional ^{13}C spectra were fully assigned from a series of ^{1}H-^{13}C 2D HETCOR NMR experiments recorded with various CP contact times. The appearance of a new signal at 181 ppm notably confirmed the conversion from the precursor to the catalyst. Additionally, two-dimensional ^{1}H-^{29}Si HETCOR spectra showed spatial proximities between the allyl and mesityl groups of the Pd-NHC fragment the and the surface deuterated TMS (trimethylsilyl) surface groups, suggesting that the organometallic ligand is bent, interacting with the surface. DNP SENS studies were also

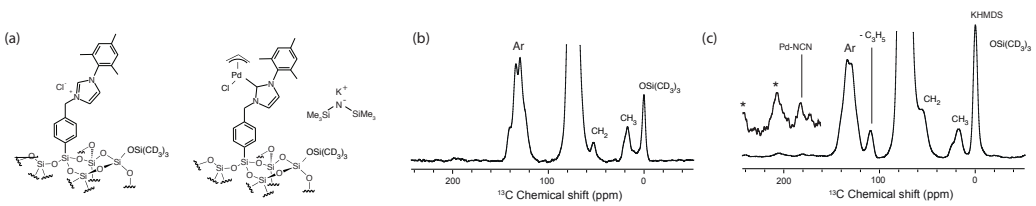

Figure 2.18: (a) Structures of Mat-Im and Mat-Pd. (b) 1D carbon-13 CPMAS spectra of Mat-Im with microwaves on and off. (c) carbon-13 CPMAS spectra of Mat-Pd with microwaves on and off. Adapted with permission from [160]. Copyright 2020 Wiley and Sons.

reported by Samantaray *et al.* on Ru-NHC catalysts [155].

Two systems were investigated, anchored to the silica surface via either a rigid (mesitylphenyl) or flexible (propyl) organic linker. DNP enhanced 2D ^{1}H-^{29}Si HETCOR spectra (Figure 2.19) provided key information on the orientation of the two ligands with respect to the surface. Namely, the 2D spectrum of flexible precursor clearly showed correlations between the Q_3 and Q_4 silicon-29 resonances and the methyl protons of the mesityl ligands. On the contrary, this correlation did not appear in the spectrum of rigid precursor. This was a clear indication that the flexible linker promoted the folding of the ligand towards the surface, allowing a stabilization by the interactions with the surface. In contrast the organic linker points towards the exterior of the surface in the case of a rigid linker. No DNP enhanced NMR experiments could be conducted on the Ru-NHC catalysts, likely because of the deactivation (reduction) of the exogenous radical (here TOTAPOL) by the highly reactive Ru metallic centers. Nevertheless, conventional ^{31}P NMR displayed evidence for the presence of PCy_3 coordinated to the Ru center when attached to the rigid arm. Such coordination is absent when the Ru complex is grafted on the flexible linker. All the observations are thus consistent with the formation of a NHC-Ru alkylidene species stabilized by surface oxygen atoms when the metal center is attached to the surface via the propyl group, and explain the higher catalytic activity of the flexible complex. The flexibility of the linker enables the active site to either react with the substrate or relax, reversibly, to the surface. Similarly,

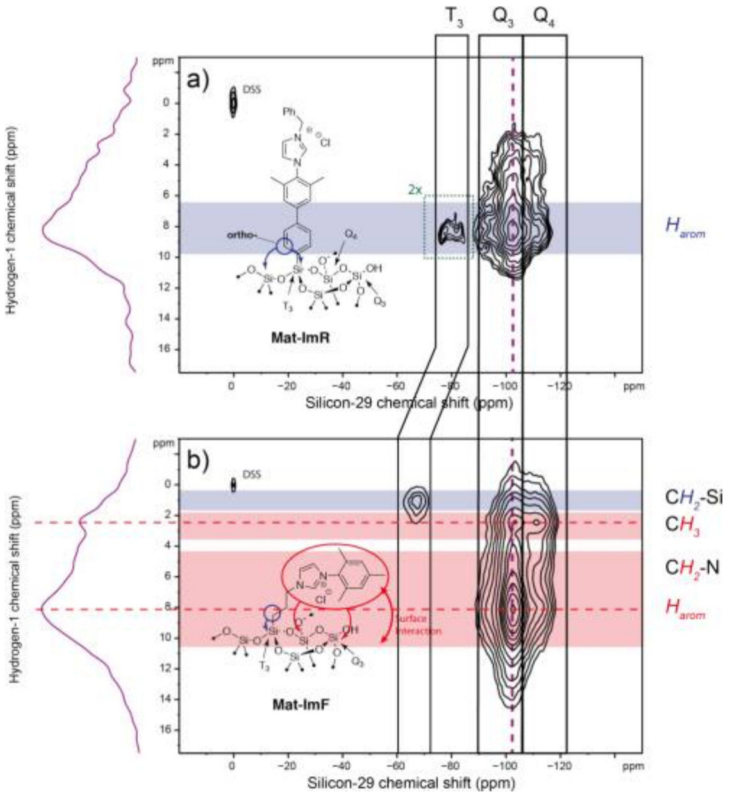

Figure 2.19: (a) ^{1}H-^{29}Si HETCOR experiments for the materials with a rigid linker. No sign of interaction between ligand and surface is observed. (b)^{1}H-^{29}Si HETCOR experiments for the materials with a flexible linker. A clear correlation between the ^{29}Si sites and the CH_3 of the mesityl as well as the proton of the carbene. Reprinted with permission from [161]. Copyright 2020 ACS.

correlations were found in conventional and DNP enhanced ^{1}H-^{13}C HETCOR spectra between the NMR resonances of the protons of the TMS groups and the aromatic carbon atoms of the mesityl for an Ir-NHC material, anchored to the silica with a flexible propyl tether, suggesting that the

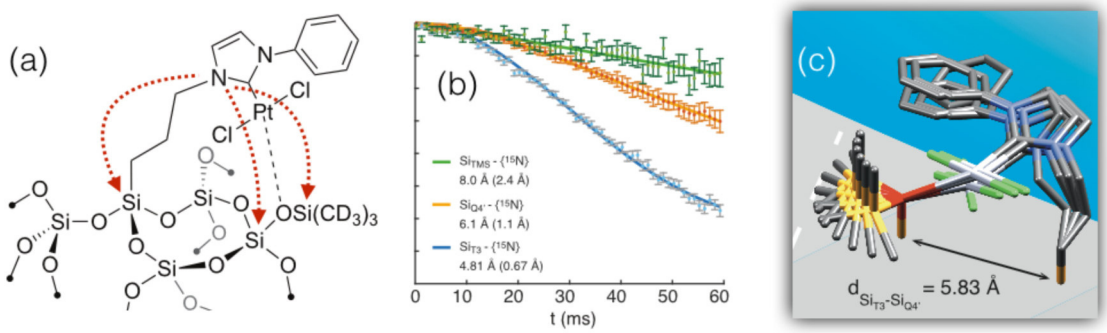

Figure 2.20: (a) Chemical structure of the Pt supported catalyst, and examples of ^{15}N-^{29}Si structural constraints that were measured. (b) The corresponding experimental DNP SENS REDOR data. (c) Structure ensemble obtained for the material. Reprinted with permission from [163]. Copyright 2020 ACS.

fragment is stabilized and folded towards the surface [162]. This material is at the core of the study reported in chapter 4.

More recently, Berruyer *et al.* went one step further with the demonstration that the full three-dimensional structure of a Pt-NHC complex anchored on an amorphous silica surface could be determined by DNP SENS [42]. The 200-fold increase in the NMR sensitivity of the surface fragment provided by DNP enabled the implementation of a series of multidimensional and multinuclear NMR correlation experiments providing quantitative structural restraints. A total of 12 ^{13}C-^{15}N and ^{29}Si-^{15}N distances were obtained under rotational echo double resonance (REDOR) experiments on ^{15}N-labeled samples. The result, in combination with EXAFS, was a detailed structure for the surface complex, determined with a precision of 0.71 Å, as illustrated in Figure 2.20. In chapter 4, we will show how this approach could be extended to multiple-site surfaces.

Chapter 3

Proton NMR : Exploiting the High Abundance and High γ of this Nucleus

3.1 High-resolution proton solid-state NMR spectroscopy

Because it has a high gyromagnetic ratio, a natural abundance of 99.99 % and is present in many molecular systems, proton is a nucleus of choice in NMR spectroscopy. Thus, proton NMR is a key tool for the investigation of substrates in solution where the molecular tumbling averages out the anisotropic part of the NMR interactions and where resolved proton spectra are usually detected. These interactions are listed in the table below together with their order of magnitude. In the solid-state, complications arise mainly due to the presence of anisotropic interactions, and

Homonuclear dipolar coupling Hamiltonian	$\hat{H}_D^{homo} = -(\frac{\mu_0}{4\pi})\frac{\gamma_I^2}{r_{IS}^3}\bar{h}\frac{(3cos^2\theta - 1)}{2}(3I_{1Z}I_{2Z} - I_1I_2)$	0 - 20 kHz
Heteronuclear dipolar coupling Hamiltonian	$\hat{H}_D^{hetero} = -(\frac{\mu_0}{4\pi})\frac{\gamma_I\gamma_S}{r_{IS}^3}\bar{h}(3cos^2\theta - 1)I_ZS_Z$	0 - 20 kHz
Chemical Shift Anisotropy (CSA) Hamlitonian	$\hat{H}_{CS} = \sigma_{iso}\gamma B_0 + \frac{1}{2}\delta_{CS}[3cos^2\theta - 1 - \eta_{CS}sin^2\theta cos(2\varphi)]I_Z$	0 - 2000 ppm

Figure 3.1: List of the relevant Hamiltonians for proton NMR spectroscopy with the range of amplitude. γ_I and $\gamma_S$are the gyromagnetic ration of spins I and S respectively, r_{IS} is the internuclear distance between the two spins. σ_{iso} is the isotropic chemical shift, η the asymmetry parameter, and δ the anisotropy parameter. B_0 is the magnetic field and μ_0 is the vacuum permeability. θ and φ are the polar angles of the B_0 field.

in particular due to the presence of strong homonuclear dipolar couplings that drastically broaden the NMR lines.

A standard approach to average out these interactions is magic angle spinning (MAS) [164]. However, because the homonuclear dipolar coupling Hamiltonian does not commute with itself at any time, i.e. is a homogeneous interaction according to the definition given in the seminal paper by Maricq and Waugh [165], spinning the sample around the magic angle at a frequency smaller that the size of the homonuclear dipolar interaction, does not fully average out this interaction, which leads to a substantial residual line broadening. This residual broadening progressively decreases with increasing spinning frequencies. This is in contrast to what happens for inhomogeneous interactions (for which the Hamiltonian commutes with itself at each point of the rotation), as is the case for the anisotropic chemical shift (CSA) or the dipolar coupling interaction between unlike spins that will split into sharp spinning side bands as soon as the rotation starts. Today, rotor diameter as small as 0.7 mm or 0.6 mm enables spinning samples at frequencies as high as respectively 110 and 126 kHz. Studies of proton NMR lines as a function of the spinning frequency on microcrystalline samples have shown that the homogeneous residual linewidth has a linear dependence [166]. At the spinning frequencies achievable today, this residual broadening becomes comparable to chemical shift distributions and susceptibility effects even for crystalline systems.

Figure 3.2-(a) illustrates the resolution improvement in the proton spectrum of powdered microcrystalline solids as a function of the spinning frequency. Even at the highest spinning frequencies available today, the residual line widths have a significant contribution from homogeneous interactions [167]. For surface complexes, where molecular dynamics helps averaging out dipolar interactions, only a modest enhancement in resolution is observed at very fast MAS, as shown in Figure 3.2-(b), and the linewidth are usually dominated by chemical shift distributions.

Magic Angle Spinning can be combined with the application of homonuclear decoupling schemes in an approach called CRAMPS (Combined Rotation and Multiple Pulse Sequence). This concept was introduced by Waugh *et al.* [169]. Progress in this area has been rapid [170],

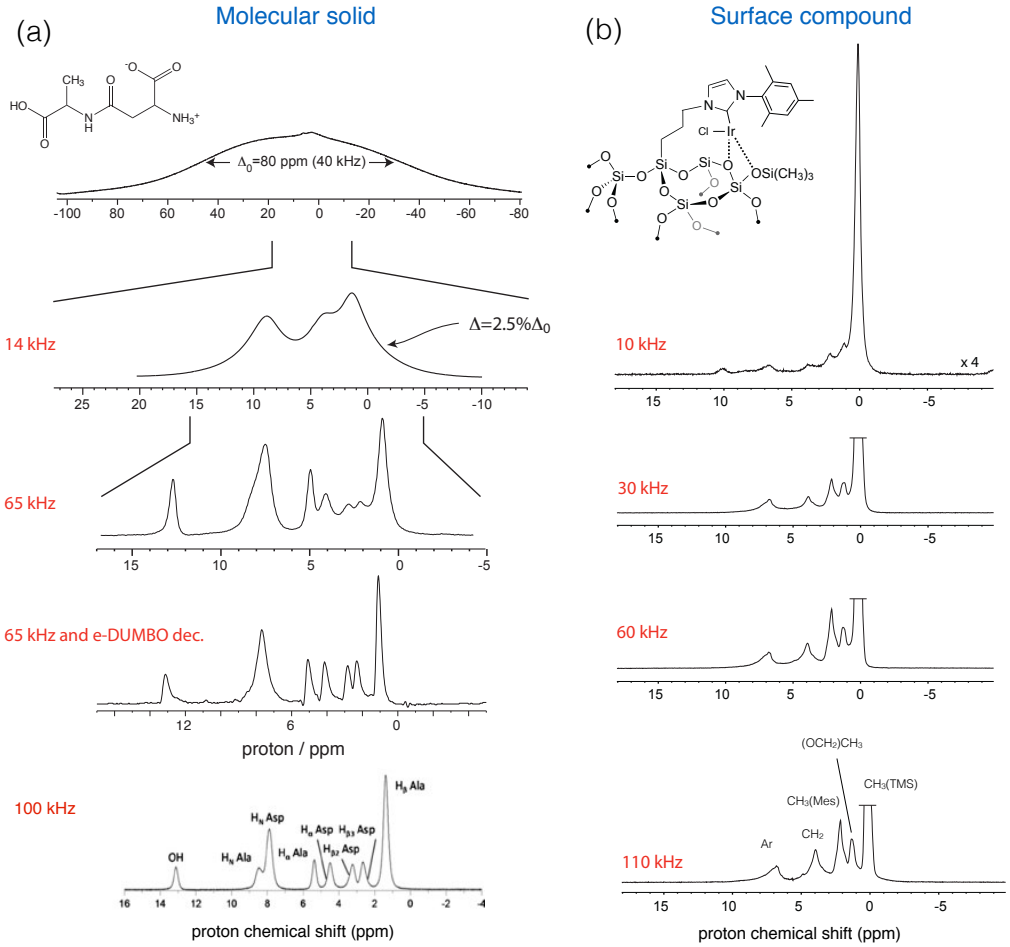

Figure 3.2: (a) Scheme illustrating the resolution improvement in proton spectra of powdered molecular solids upon fast MAS and/or homonuclear decoupling. Spectra of the β-Asp-Ala dipeptide are shown. The spectra at 65 and 100 kHz were adapted from references [168] and [167] respectively. (b) Proton spectra of a surface organometallic complex, as a function of the spinning frequency (unpublished results acquired during the PhD thesis of P. Berruyer).

with the introduction of phase-modulated efficient DUMBO family [171, 172], and the PMLG scheme [173–179].. A recent paper on the different decoupling schemes has been published by Paruzzo and Emsely [180]. Although CRAMPS approaches require a higher level of technical expertise than MAS alone on powdered molecular solids, they usually provide better spectral resolution as shown in Figure 3.2-(a), for powdered β-Asp-Ala dipeptide.

The approaches described above aim at improving spectral resolution in proton solid-state NMR spectroscopy by removing dipolar couplings and retrieving chemical shift information. Dipolar coupling interactions are however directly correlated to inter-nuclear distances, and therefore are informative about spatial proximities when they can be measured or observed. Proton multiple-quantum (MQ) spectroscopy has been widely used, first in the static case and then under MAS, to probe proton-proton contacts or achieve spin counting experiments, thus enabling to retrieve essential structural information.

3.2 Proton multiple-quantum NMR spectroscopy

3.2.1 Multiple-Quantum experiments in static solids

The first MQ experiments in solids were demonstrated under static conditions by the group of Pines in the mid-80s [181–184], who described a time-resolved experiment, where multiple-quanta among dipolar-coupled spins are created over time. The number of correlated spins, and therefore the proton spin cluster size, can be extracted from the intensity distribution of MQ orders. The approach was demonstrated to determine the number of protons in adamantane, liquid crystal molecules, as well as in clustered monohydrides present in hydrogenated amorphous silicon. The multiple quantum experiment proposed by Baum *et al.* is divided into four parts as shown in figure 3.3. All the MQ experiments follow this indirect detection scheme.

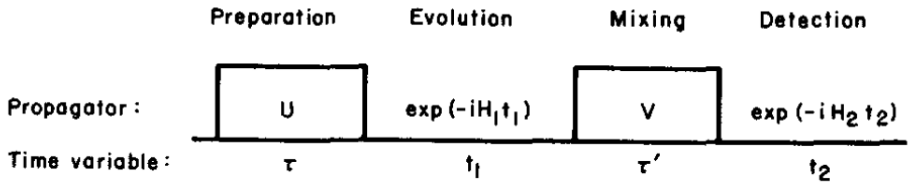

Figure 3.3: General scheme for a multiple experiment. The multiple coherences are generated in the preparation period, react to the local field during t_1, then transfered to single coherences in the mixing period to be detected during t_2. Reprinted with permission from [182]. Copyright 2020 AIP Publishing

Excitation (or preparation) period: Experimentally, the MQ coherences are generated during a preparation period of duration τ where a sequence of pulses creates a two-quantum average Hamiltonian. Even order coherences develop at a rate that reflect the distribution of dipolar couplings. Baum *et al.* proposed to apply a eight-pulses sequence that creates the following two-quantum average Hamiltonian:

$$\tilde{H}(0) = \frac{1}{3}(H_{yy} - H_{xx}) = -\frac{1}{2}\sum_{i<j} D_{ij}(I_{i+}I_{j+} - I_{i-}I_{j-}) \tag{3.1}$$

where $I_{j\pm} = I_{jx} \pm iI_{jy}$. Pulse imperfections lead to the generation of odd ordered coherences that are eliminated by the phase cycling.

Evolution Period: Different multiple-quantum orders (2, 4, 6 ...) are separated by incrementing the phases of the preparation pulses for each t_1 point according to the time proportional phase incrementation (TPPI) method. The number of orders ($\pm n_{max}$) is calculated from the phase increment $\Delta\phi = \pi/n_{max}$. Adjacent orders of coherences acquire a different offset frequency $\Delta\phi\ /\Delta t_1$ where Δt_1 is the time increment. A Fourier Transform of the resulting interferogram separate the MQ orders in the frequency domain [182].

Reconversion (or mixing) Period: After the evolution period, and since the MQ coherences cannot be detected directly, a reconversion or mixing period is applied to convert them into observable single quantum coherences. The reconversion is accomplished by implementing a 90° phase shift to the preparation period pulses, so as to time-reverse the effect of the double-quantum Hamiltonian.

Detection Period: After the mixing period, a delay is inserted to dephase unwanted transverse magnetization. A $(\pi/2)_x$ pulse is then applied to detect the desired signal in t_2. Figure 3.4 shows an example of a multiple quantum experiment [181].

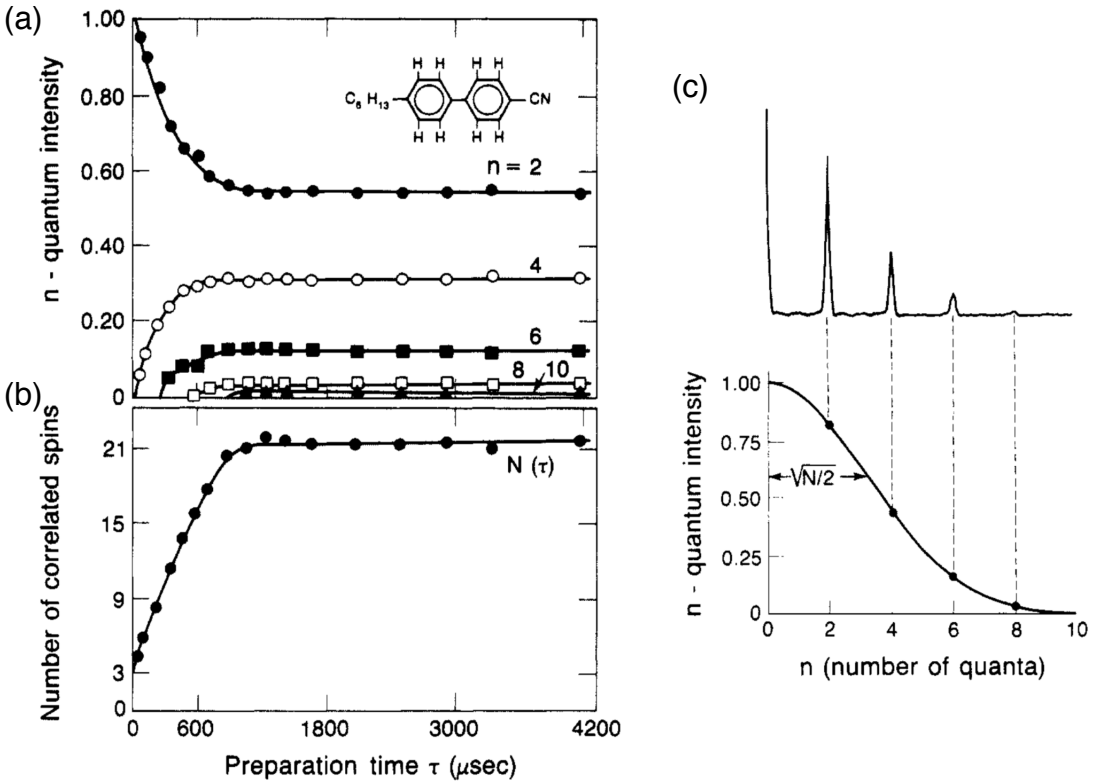

Figure 3.4: (a) n-Quantum intensity vs. preparation time for the liquid crystal, p-hexyl-p'-cyanobiphenyl. The intensity of each multiple-quantum order has been normalized to the two-quantum intensity, and smooth curves have been drawn through the data points to aid the eye. (b) Number of correlated spins N(τ) vs. the preparation period τ. After an induction period, the effective system size N(τ) levels off at 21, indicating that the number of interacting spins is limited to the size of the individual liquid crystal molecules which contain 21 protons. (c) 180-MHz ^{1}H multiple-quantum spectrum of the liquid crystal, p-hexyl-p'-cyanobiphenyl for a preparation of 660 μs. The data points are measured from the spectrum by integrating each peak corresponding to each multiple-quantum order. The effective system size N characterizes the number of correlated spins, in this case 20, at each preparation time and is obtained by fitting the intensities to a Gaussian distribution. Reprinted with permission from [181]. Copyright 2020 AIP Publishing

We note that another version of this experiment, called "spin-counting" experiment where no evolution during t_1 takes place ($t_1 = 0$ in Figure 3.4), has been proposed a few years later [185], which offers enhanced sensitivity. This experiment has been applied for example to probe proton densities on various silica gel catalytic supports [186].

3.2.2 Multiple-Quantum in spinning solids: general principle

Proton multiple-quantum experiments have limited interest in static conditions as chemical shifts are usually unresolved. Several strategies have been proposed to combine MQ experiments with magic angle spinning. If the spinning frequency is fast enough to average out dipolar interactions, the multiple-quantum scheme used in the static case (as the eight-pulse scheme described above) cannot be implemented without adjustment. Indeed, MAS causes a self-time reversal of the dipolar

Hamiltonian during the excitation and reconversion period, which leads to a disappearance of the MQ coherences after each rotor period. In 1986, Meier and Earl [187] introduced a new strategy for rotating solids. They suggested to switch the phase of the radio-frequency pulses in the excitation and reconversion blocks every half rotor period so as to change the sign of the spatial part of the Hamiltonian synchronously with the modulation of its spatial part. The effectiveness of this approach was demonstrated on adamantane (with the generation of ^{1}H MQ coherences) [187] on ^{13}C-labeled Zinc-acetate (^{13}C DQ coherences) [188]. However, this method is limited to slow spinning frequencies, for which the rotation period can accommodate at least two cycles of the MQ pulse sequence, and therefore to samples with small anisotropic interactions.

An alternative solution is to excite MQ coherence at fast MAS frequencies is to use rotor-synchronized pulse sequences where the cycle of the recoupling sequence is a whole number of the rotor period and that will counteract the effect of MAS (these sequences are referred to as dipolar recoupling sequences). DRAMA (Dipolar Recovery at the Magic Angle) proposed by R. Tycko and G. Dabbagh was the first pulse sequence proposed to recouple dipolar coupling in fast rotating solids [189]. Several variants were then proposed of increasing complexity and efficiency, including towards the very fast MAS frequencies that can be achieved today. Reviews on dipolar recoupling sequences can be found in references [190, 191].

3.2.3 Proton double-quantum spectroscopy

In the early 2000s, proton double-quantum NMR spectroscopy has emerged as a unique approach to probe proton-proton proximities in solid substrates. The general pulse sequence, transfer pathway and schematic two-dimensional DQ-SQ spectrum is shown in Figure 3.5 (a), (b) and (c). The

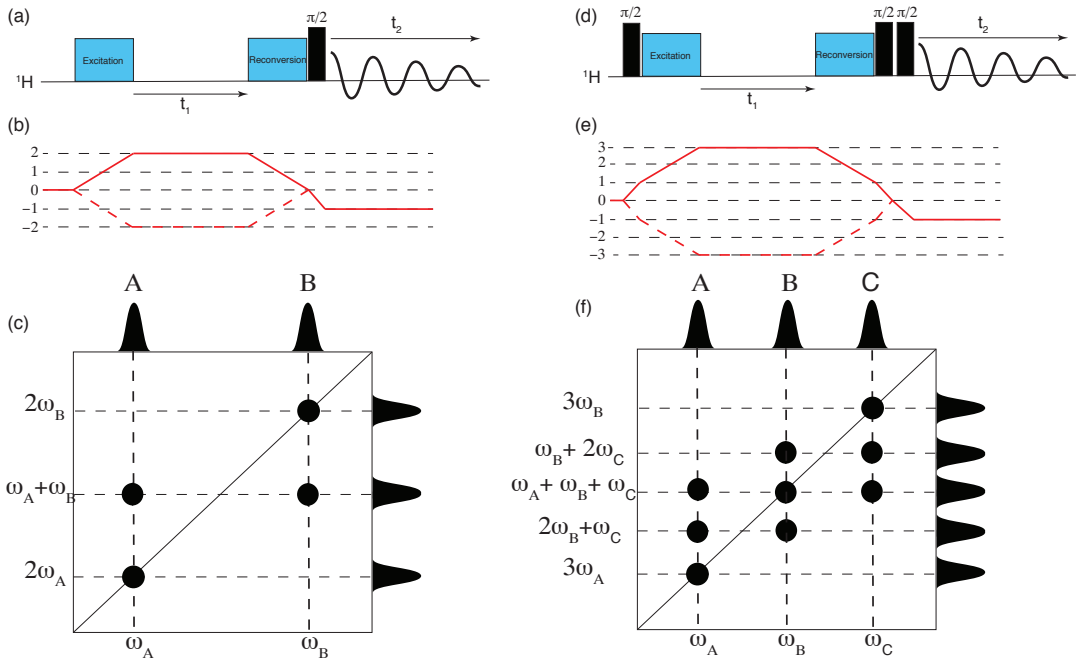

Figure 3.5: General pulse sequence to generate (a) DQ coherences and (d) TQ coherences. (b) Represents the transfer pathway for the DQ-SQ experiment and (e) for the TQ-SQ experiment. (c) and (f) shows schematically some of the expected correaltions in a DQ and TQ correlation experiment. For (c) we considered dipolar coupling between protons A, protons B, and protons A and B. For (f) we considered a dipolar coupling between protons A, protons C, protons A and B, and protons B and C.

double-quantum coherences are created during the excitation period during which a dipolar recoupling pulse sequence is applied. Their evolution during t_1 is correlated with that of the (observable) single-quantum coherences that will be generated during the reconversion period. A schematic representation of the DQ-SQ correlation spectrum is shown in 3.5-(c). The DQ coherence will evolve during t_1 at the sum of the individual SQ frequencies. Two dipolar-coupled protons A and B yield correlation peaks AB at (ω_A,ω_A+ω_B) and (ω_B, ω_A+ω_B). Auto-correlation peaks along the ω_1=2ω_2 diagonal (AA and BB) arise when there is a dipolar coupling between two protons of the same isotropic chemical shift. The intensity of a DQ signal depends on the coupling between the two protons.

The **BABA sequence** introduced by Spiess and co-workers in 1995 [192], is one of the methods of choice to reintroduce dipolar couplings among protons. Its name is derived from the presence of BAck-to-BAck pulses (Figure 3.6). The evolution period is bracketed by two 90° pulses whose phases in adjacent segments of $\tau_R/2$ are shifted by 90°. This shift enables to change the sign of the spatial part by of the DQ Hamiltonian and to compensate the negation of the spatial part by MAS. The sequence thus generates a pure double-quantum average Hamiltonian. Its amplitude depends on the Euler angle γ (relating the principal axes of the dipolar coupling tensor in the crystallite frame to the reference frame fixed in the rotor). The BABA sequence was first demonstrated to generate heteronuclear ^{1}H-^{13}C multiple-quantum coherences [192]. The first application for proton DQ NMR was reported by Schnell *et al.* in 1998 with two-dimensional DQ-SQ proton spectra of L-Alanine at 35 kHz MAS in a 2.5 mm probe [193].

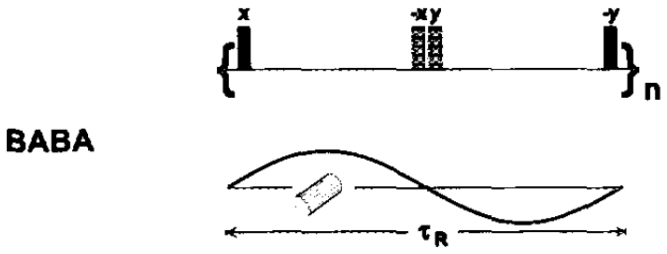

Figure 3.6: BABA pulse sequence. Adapted with permission from [192]. Copyright 2020 Elsevier.

For γ amplitude-modulated recoupling sequences as is the case for BABA, besides the fact that the excitation and reconversion efficiency is not uniform for all crystallite orientations, a spinning side-band pattern is observed in the DQ dimension when the t_1 increment is not set to the rotor period. Thus, they are two ways of recording BABA DQ-SQ spectra, either in a rotor-synchronized mode where all the spinning side-bands fold on the centerband, or in a non-synchronized mode. The first mode offers enhanced sensitivity and employs States quadrature detection [194] (the time increment Δt_1 is equal to the indirect spectral width, i.e. to the spinning rate). For an isolated spin pair and short recoupling times, the efficiency (inversely proportional to r^6, where r is the internuclear distance) of the excitation and reconversion of DQ coherences is proportional to the dipolar coupling constant, and thus, semi-quantitative information about proton-proton proximities can be extracted [195]. In the synchronized fashion, the DQ spectral width is however limited to the MAS frequency, which may represent a limiting factor especially at magnetic high fields. For example, at a MAS frequency of 20 kHz, the achievable proton spectral width on a 800 MHz magnet is 25 ppm. The non-synchronized version yields sideband patterns in the DQ dimension.

The origin of the sideband pattern has been investigated by Geen *et al.* [196], who demonstrated that this effect was linked to the modulation of the reconversion DQ Hamiltonian by the rotor frequency due to the t_1 incrementation. This mechanism was called Reconversion Rotor Encoding (RRE) [197]. For an isolated spin pairs, quantitative proton-proton distances can be extracted from the spinning side-band pattern. Examples where spinning sideband patterns were used to extract distance information can be found in [198]. Non-synchronized experiments usually require the acquisition of a large number of t_1 increments and are thus time-consuming. Recoupling sequences in which the Eurler angle γ is appears in the phase rather than in the amplitude of the Hamiltonian (γ-encoded recoupling sequence) are attractive alternatives to BABA in cases where rotor synchronization is a limitation. Indeed, no rotor synchronization is needed. In addition, they offer an improved dependence of the DQ excitation and reconversion with respect to crystallite orientation.

The **C7 recoupling sequence** introduced by Lee *et al.* in 1995 [199] and its improved POST-C7 variant [200] are some of the most popular γ-encoded schemes. Figure 13.7 shows the pulse scheme of the C7 and POST-C7 sequence. Like many other recoupling schemes, they are based on symmetry principles defined by Levitt and co-workers [201]. They are composed of a basic element Cϕ repeated seven times with a phase increment of $2\pi/7$. The length of each basic element is set to 4π, and the duration of the full cycle is two rotation periods. Therefore, the radio-frequency amplitude is 7 times the spinning frequency. The POST-C7 was introduced to improve the robustness C7 pulse sequence with respect to the shift offsets and radio-frequency inhomogeneity. The C7 basic element consists in two 2π pulses with opposite phases $(2\pi)_\phi(2\pi)_{\phi+\pi}$ denoted $C4\bar{4}$, where $\bar{4}$ indicates the flip angle in units of $\pi/2$. In the POST-C7 sequence the basic element corresponds to $C_\phi^{1\bar{4}3}$, i.e. three pulses $(\pi/2)_\phi(2\pi)_{\phi+\pi}(3\pi/2)_\phi$. This modification enables broader recoupling and increased efficiency. On a more practical level, as mentioned above and unlike the BABA scheme, C7 and POST-C7 experiments do not require to synchronize the t_1 increment with the rotor period. However, the RF amplitude of sequence is constrained to 7 times the spinning speed. This is a strong limitation in particular towards very fast MAS frequencies, as those permitted today by small volume rotors. Today, BABA is still the preferred option under those spinning conditions [202].

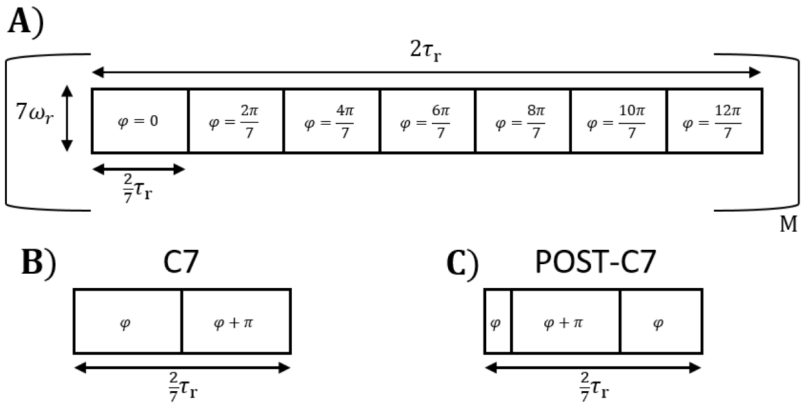

Figure 3.7: A schematic representation of the C7 pulses. It consists of repeating 7 times the basic phase element defined by incrementing each time with a factor of $2\pi/7$. Each pulse has an rf amplitude equal to 7 times the spinning frequency. The basic element can either be the B) C7 or C) POST-C7 with the corresponding element $C_\phi^{4\bar{4}}$ and $C_\phi^{1\bar{4}3}$ respectively. Reprinted with permission from [203].

3.2.4 Proton triple-quantum spectroscopy

Triple-quantum coherences can also be generated using the same principle to get information about triplets of dipolar-coupled protons. The coherence pathway selection as well as the corresponding 2D plot are shown schematically in Figure 3.5 e) and f) respectively. Correlations will appear (ω_A, $\omega_A+\omega_B+\omega_B$), ($\omega_B$, $\omega_A+\omega_B+\omega_C$) and ($\omega_C$, $\omega_A+\omega_B+\omega_C$) for three coupled protons A, B and C. Auto-correlation peaks along the $\omega_1=3\omega_2$ diagonal arise for three protons of the same isotropic chemical shift. One way to generate TQ correlations is to use DQ recoupling schemes bracketed by a 90° pulse at the beginning of the excitation period to prepare an initial state in the transverse plane, and by a 90° pulse at the end of the reconversion period as reported and demonstrated on L-Alanine at 35 kHz MAS by Spiess and co-workers in 1998 [204]. In analogy to the DQ case, the TQ spinning-sideband pattern contains information on spin topologies as formalized by Friedrich *et al.*, using a simple 90°-τ_R/2-90° pulse sequence for the excitation and reconversion of TQ coherence [205]. Spiess and co-workers used BABA to excite TQ coherences, but alternative schemes can be employed like C7 as demonstrated by Eden and Levitt in the context of carbon-13 NMR spectroscopy [206]. An efficiency of 8 % in the excitation of TQ coherences was reported in this study. Homonuclear recoupling pulse scheme producing an average dipolar Hamiltonian comprising three-spin triple-quantum operators and therefore specifically designed for highly efficient TQ excitation were later introduced [207, 208]. They had however not been investigated for proton spectroscopy. In 2009, Leskes and Vega proposed to apply the phase modulated Lee Goldburg sequence in a non-synchronous mode to generate proton TQ coherences [209].

3.3 Application on surface organometallic complexes

High-resolution proton solid-state NMR spectroscopy is an extremely useful approach to characterize surface organometallic catalysts. Proton spectra of such complexes are usually reasonably resolved even at moderate spinning frequencies as illustrated in Figure 3.2, as the number of protons around the metal center is usually limited as is the case for the support itself (overall low proton density) and molecular dynamics often helps to partially average out the dipolar coupling network. Thus, the application of CRAMPS approaches are usually not needed. In addition, the high NMR sensitivity of proton counteracts the low concentration of surface sites. One-dimensional proton NMR spectroscopy as well as two-dimensional ^{1}H-^{1}H or ^{1}H-X (with X= ^{13}C, ^{15}N, ^{31}P...) correlation experiments are thus commonly employed to characterize surface organometallic catalysts. In the following, we will briefly review some key examples of proton MQ NMR spectroscopy reported on supported organometallic complexes, in particular for the characterization of metal hydrides. Proton multiple-quantum spectroscopy is a central technique is the solid-state NMR toolkit to probe proton-proton proximities and many other applications of proton MQ NMR spectroscopy concern systems such as supramolecular organic assemblies, polymers, oxide supports or functionalized surfaces. A relatively recent review on this topic can be found for example in reference [212].

The first example of this type of spectroscopy on an organometallic complex was reported by Rataboul *et al.* in 2004 [210], in order to identify and distinguish mono-hydrides and dihydride zirconium species, namely [(≡SiO)$_3$Zr-H] and [(≡SiO)$_2$Zr-H$_2$] on a silica surface. Two proton resonances were observed for the hydrides. The lower-field resonance led to a strong autocorrelation

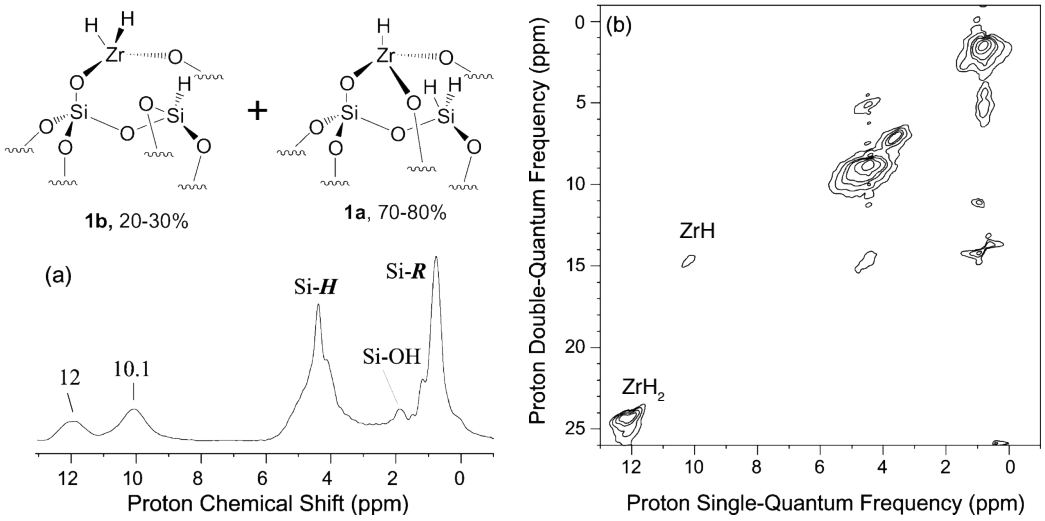

Figure 3.8: (a) 1D proton spectrum of the [Zr-H] species shown above. (b) ^{1}H DQ correlation spectrum. No homonuclear decoupling was applied in t_1 and t_2 as the averaging of the anisotropic interactions by MAS (here 14 kHz) was sufficient to yield resolved proton spectra. BABA recoupling was applied. Reprinted with permission from [210]. Copyright 2020 ACS.

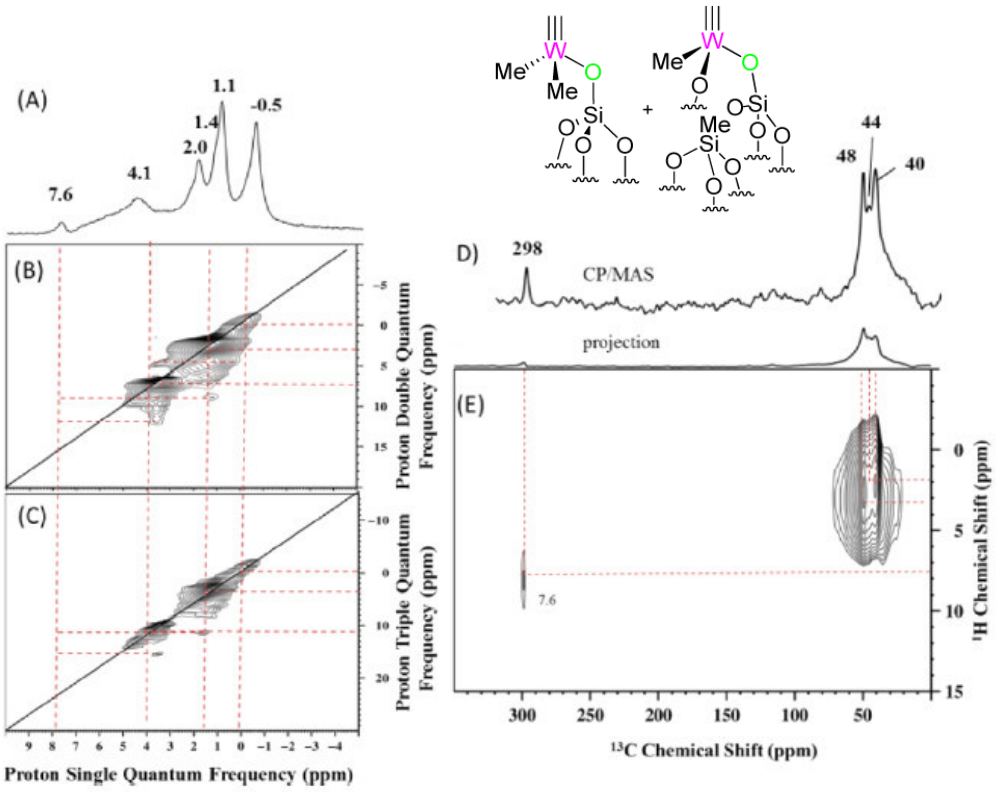

Figure 3.9: (A) 1D proton spectrum of the (≡SiO-)W(≡CH)Me_2] and [(≡SiO-)$_2$W(≡CH)Me] species. (B) ^{1}H DQ correlation spectrum. (C) ^{1}H TQ correlation spectrum. (D) ^{13}C CP-MAS NMR spectrum. (E) 2D CP-MAS HETCOR NMR spectrum acquired with short contact times of 0.2 ms. Reprinted with permission from [211]. Copyright 2020 ACS.

in DQ spectrum, and therefore could be readily assigned to the dihydrides. The second resonance correlating with SiH protons was assigned to the monohydride species as shown in Figure 3.8. While proton DQ NMR spectroscopy has later been applied quite broadly to characterize organic ligands around supported metal centers, only few studies were carried out on to identify the NMR signature of metal hydrides. Basset and co-workers reported proton DQ NMR spectra of silica surface hafnium hydrides [213–215], as well as on titanium hydrides [216]. In 2007, Avenier *et al.* implemented DQ and TQ NMR experiments to characterize imido amido tantalum surface species and demonstrate the reactivity of tantalum hydrides with respect to N-H bond cleavage of ammonia [217] and dinitrogen dissociation [218]. The resonances of Ta=NH and Ta-NH_2 protons were identified indirectly by the absence of autocorrelation in respectively two-dimensional DQ and TQ spectra. Triple-quantum experiments have then been applied in a few cases on supported organometallic complexes, for example to identify CH_3 groups attached to the metal. In 2014, Basset and co-workers unambiguously assigned the resonances of methyl groups bonds to various W complexes, namely [(≡SiO-)W(≡CH)Me_2] and [(≡SiO-)$_2$W(≡CH)Me], by combining proton DQ and TQ NMR experiments with ^{1}H-^{13}C HETCOR spectra [211] as showed in Figure 3.9. In particular, the proton signal at 4.1 ppm was assigned to the methyl groups of the bipodal species while the other signal at 1.4 and 1.1 ppm to the nonequivalent methyl groups in monopodal species.

However, to the best of our knowledge, TQ experiments were so far never implemented to directly assess the number of protons attached to a supported metal center. In chapter 6 of this manuscript, we will describe the implementation of DQ and TQ experiments on bimetallic surface complexes to unambiguously identify the number of (or "count") the hydride protons surrounding the metal centers.

Chapter 4

Atomic-Scale Surface Structure of a Highly Active Iridium N-Heterocyclic Carbene Catalyst

4.1 Introduction

Over the last twenty years, strong efforts have been devoted towards the development of supported organometallic catalysts as a new route to deliver highly efficient catalytic systems that would combine the advantages of molecular complexes with ease of separation and recyclability [15, 17, 219]. However, despite enormous attempts to reach these goals, most supported systems do not meet the expectations, often yielding similar catalytic performances to their homogeneous homologues, without avoiding deactivation phenomena frequently encountered in solution. This lack of benefits severely limits their interest for industrial use [220]. One major limitation in the development of more efficient immobilized metal complexes is the absence of any reliable analytical approach that provides a detailed atomic-scale description of their structure at the surface of the solid support. As mentioned in the introduction, a wide range of techniques are in principle available to characterize the surface of catalytic materials such as Infrared (IR) spectroscopy, EXAFS (Extended X-ray Absorption Fine Structure), XPS (X-ray Photoelectron Spectroscopy) or AFM (Atomic Force Microscopy). However, these approaches lead only to an incomplete description of the spatial arrangement, atom by atom, around the active site, and do not enable the visualisation of its structure in three dimensions. Thus, the detailed surface structure of supported organometallic catalysts often remains unknown: do they adopt well-defined conformations or in contrast form a bundle of disordered structures, do they interact with the solid support, what are the ligands stabilizing the metal centers, do their structure evolve in the course of the catalytic reaction? This lack of detailed molecular picture is currently a strong barrier to establish fine structure-activity, stability, selectivity relationships and to design in a rational way supported organometallic catalysts with enhanced productivity.

In this context, a major step forward has been achieved with the demonstration that the full three-dimensional structure of a Pt organometallic complex bound to an amorphous silica surface could be determined by DNP SENS [42]. This was done by implementing a series of ^{29}Si-{^{15}N} and ^{13}C-{^{15}N} REDOR experiments that provided a set of 8 structural restraints. The structures of the organic precursor and of the Pt complex were determined from these distance constraints. As no experimental NMR data was available on the orientation of the imidazole ring, this latter was determined using a Pt-O distance of approximately 2.68 Å obtained from EXAFS analysis. A structure was therefore proposed where a noncovalent interaction between Pt and the oxygen atom of the trimethylsiloxy group was stabilizing the surface complex (see Figure 2.20 in Chapter 2). The same orientation was then used for the supported organic precursor. This prototypical surface site was not catalytically relevant. The objective of this project was to extend the methodology implemented by Berruyer *et al.*, to the investigation of a more complex catalytic surface, namely a silica-supported hybrid Iridium-N-heterocyclic carbene (Ir-NHC) material, involved in alkyne hydrogenation. The catalytic activity of this material had been investigated in detailed by Romanenko *et al.* in 2015, who demonstrated much higher conversion rates in trans-stilbene hydrogenation respect to the molecular analog [162]. A relatively detailed NMR investigation was performed. Notably, correlations between the aromatic protons and the surface silicons on one hand and between the aromatic protons and the carbons of the surface passivating groups on the other hand, jointly with the absence of NMR resonances that would correspond to the cyclooctadiene (COD) ligand, suggesting that the organic spacer was folded toward the surface so as the iridium species were stabilized by surface oxygen atoms. However, no direct evidence for such a folding was available.

Here, by combining a new labeling strategy with the implementation of REDOR experiments that selectively probed the proximity of the imidazole ring to the surface, the structure of the Ir-NHC material, as well as those of the synthesis intermediates were determined.

4.2 Sample preparation and DNP formulation

The materials were prepared and provided by the group of Dr Chloé Thieuleux (C2P2 laboratory in Lyon). They were obtained by co-condensation of tetraethylorthosilicate (TEOS) with an organotriethoxysilane in a sol-gel process in the presence of a structure-directing agent. This approach ensures a regular distribution of the organic ligands [157] inside one-dimensional pores of diameter ∼6 nm and length ∼1 μm, that display a hexagonal arrangement. Starting from a propyliodide flexible linker, a series of reactions yielded the imidazolium functionalities. The surface silanol groups were transformed into trimethylsiloxane (the so-called surface passivation), in order to avoid any complexation onto the silanols. This material will be referred to as Mat-Im. An Ag-NHC material (Mat-NHC-Ag) was then prepared by the addition of a soluble silver source. The Ir-NHC material was finally obtained upon transmetalation with the [IrCl(COD)$_2$] molecular complex (Mat-NHC-Ir). A detailed description of the synthesis can be found in reference [162]. Figure 4.1 illustrates schematically the synthetic pathways and shows the various surface species produced during the preparation of the catalytic material.

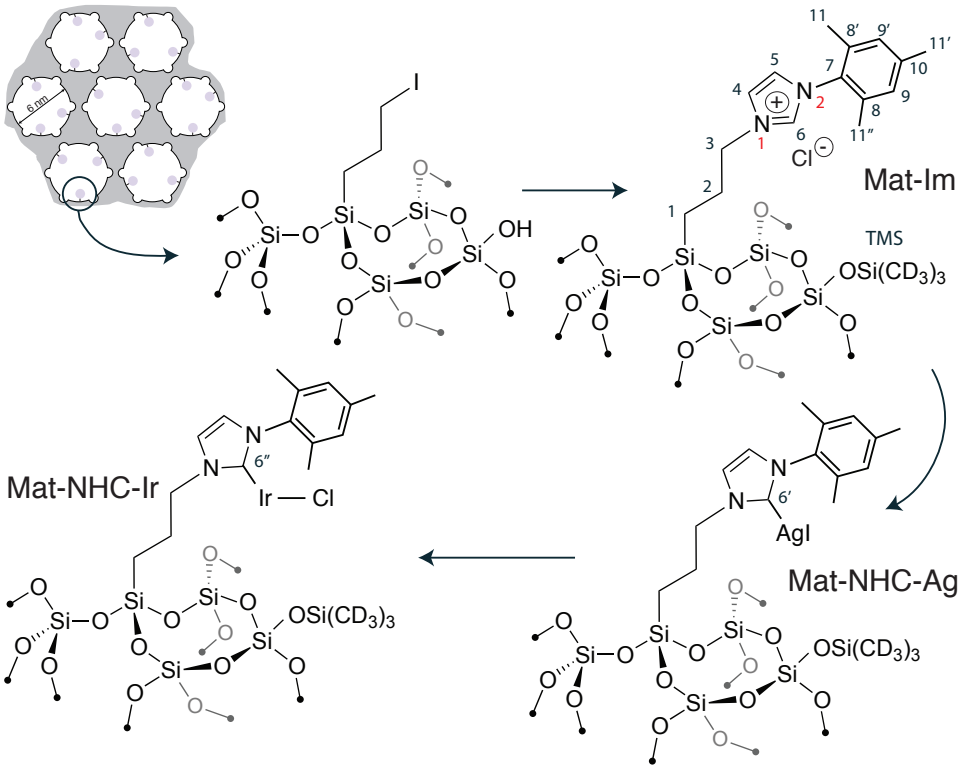

Figure 4.1: Synthesis of the Ir catalyst. More details can be found in reference [221]

Six isotopically-labelled materials were prepared and investigated, with ^{15}N labels at the first (N_1) or second (N_2) position of the imidazole ring, Mat(1)-Im, Mat(1)-NHC-Ag, Mat(1)-NHC-Ir, Mat(2)-Im, Mat(2)-NHC-Ag, Mat(2)-NHC-Ir. In all of them, the carbene (at position C_6) was

^{13}C-labeled. This was intended to provide information on the orientation of the imidazole ring. The trimethylsiloxane (TMS) groups as well as the mesityl group were deuterated in order to ensure long DNP build-up times and high enhancement factors, as described in chapter 2. Here we note that the concentration of the organic or organometallic ligands at the surface was higher than that in the materials published by Romanenko *et al.* in 2015, as the complexes investigated here were prepared with a TEOS: organotriethoxysilane ratio of 19 versus 30. It was checked that the catalytic activity of the Mat-NHC-Ir material prepared for this study was unchanged. All the NMR measurements were done under DNP conditions. Typically, 20 mg of the powdered materials were impregnated with 30 μL of a 16 mM solution of TEKPol in TCE using the incipient wetness impregnation method. The wet powder was then packed inside a 3.2 mm sapphire rotor with a Vespel cap. Proton enhancement factors of between 30 and 100 were typically measured at 9.4 T and 100 K.

The diffusion of the radical inside the pores of organic-inorganic mesostructured materials prepared by a sol-gel process, as those discussed here, has been investigated in detail by Pierrick Berruyer during his PhD thesis, who demonstrated that this diffusion was dependent on the size of the polarizing agent. The contribution factor θ as defined in reference [222] was measured for different radicals, and the results clearly suggested that large-sized radicals such as TEKPol or partially enter the pores of the silica matrix, while this was not the case for smaller radicals such as bCTbK [223]. Contribution factors of 82 % and 18 % were indeed measured for TEKPol and bCTbK respectively. The fact that TEKPol will only penetrate in the first ∼10 % of the pore volume in the materials investigated here is a key feature. Indeed, this implies that relatively long transverse relaxation times T_2' will be preserved for the surface species that are not in contact with the radical, which will in turn enable the implementation of sensitive REDOR experiments. In parallel, solvent suppression methods based on the application of a spin echo block prior to signal acquisition could be implemented [224]. Figure 4.2 shows the effect of solvent suppression on Mat(1)-Im. The resonance of the solvent molecules in contact with the radical at the exterior or at the entrance of the pores will quickly dephase, while the NMR lines corresponding to the surface species are hardly attenuated.

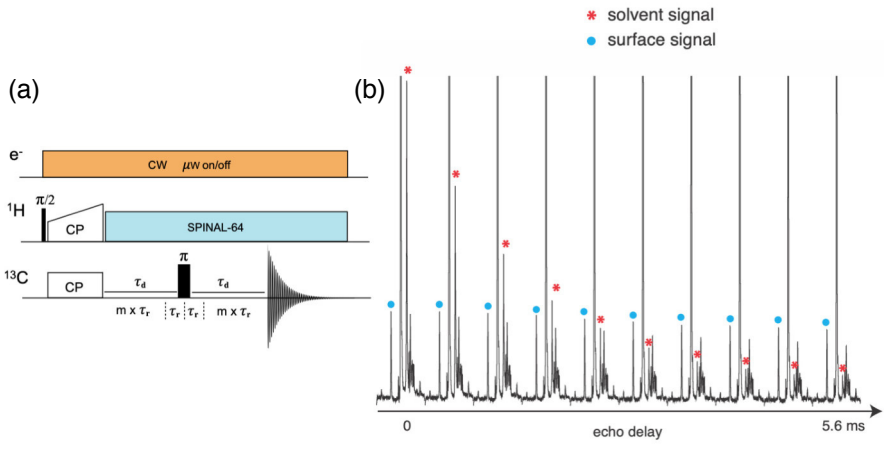

Figure 4.2: (a) Solvent suppression pulse sequence. (b) One-dimensional carbon-13 spectra recorded on Mat-Im(1) for increasing delays of the echo period. The resonance of the solvent (here TCE) is indicated by red dots, while those of the surface species by blue dots. With increasing echo-delays the solvent signal decrease and the surface signal remains the same.

4.3 Resonance assignment and evidences for multiple surface species

The ^{1}H, ^{13}C, ^{15}N and ^{29}Si resonances of the NHC precursor and of the silver and iridium complexes were assigned from one-dimensional (1D) DNP-enhanced cross-polarization (CP) and two-dimensional (2D) heteronuclear correlation (HETCOR) spectra. Figure 4.3 shows the ^{13}C and ^{15}N CPMAS spectra of Mat(1)-Im, Mat(1)-NHC-Ag and Mat(1)-NHC-Ir. The 2D ^{1}H-^{13}C HETCOR spectra are reported in Figure 4.4, while Figure 4.5 displays the ^{29}Si NMR data. The NMR chemical shifts are reported in Table 4.1. The assignment is also indicated above the 1D spectra. The analysis of the spectra allowed one not only to identify the resonances of each surface species,

		Mat-Im	Mat-NHC-Ag	Mat-NHC-Ir
^{1}H	H_1	2	2	2
	H_2	2	2	2
	H_3	4	3.5	3.5
	H_{4-6}	$\approx$ 8	$\approx$ 8	$\approx$ 8-10
^{13}C	C_1	6.3	7.7	8.2
	C_2	$\approx$17.4	$\approx$20.4	$\approx$18.6
	$C_{(OEt)}$	$\approx$17.4	$\approx$20.4	$\approx$18.6
	C_3	48.8	50.8	50.8
	$C_{4,5}$	121.2	122.9	122.4
	C_6	133.7	135.5	135.5
	$C_{6'}$	-	178.6	-
	$C_{6''}$	-	-	178.2
	C_{7-11}	148.7	151	148.2
	C_{TMS}	0	0	0
^{29}Si	TMS	0	0	0
	T_3	-80	-81.2	-80.4
	Q_4	-121	-121.4	-121.8
	$Q_{4'}$	-115	-115.6	-115.1
^{15}N	N_1	184.9	185.5	184.9
	$N_{1'}$	-	197.6	-
	$N_{1''}$	-	-	187.7
	N_2	193.64	194	194.5
	$N_{2'}$	-	206.1	-
	$N_{2''}$	-	-	197.9

Table 4.1: ^{1}H, ^{13}C, ^{29}Si and ^{15}N chemical shift assignments for material Mat-Im, Mat-NHC-Ag and Mat-NHC-Ir. Values are given in ppm and referenced according to the ^{13}C and ^{1}H resonances of TCE (chemical shifts of 74 and 5.8 ppm, respectively).

but also to monitor the reaction pathway. The resonance of the ^{13}C-labelled C_6 carbon in the NMR spectrum of Mat-Im can be readily identified from its huge intensity at $\sim$ 133 ppm in Figure 4.3-(a). The conversion of the imidazolium precursor to the silver complex is evidenced by the appearance of a new resonance at 178 ppm corresponding to the C_6 carbon of the Ag-NHC complex in Figure 4.3-(b). A resonance at the same chemical shift is observed on the ^{13}C spectrum of the

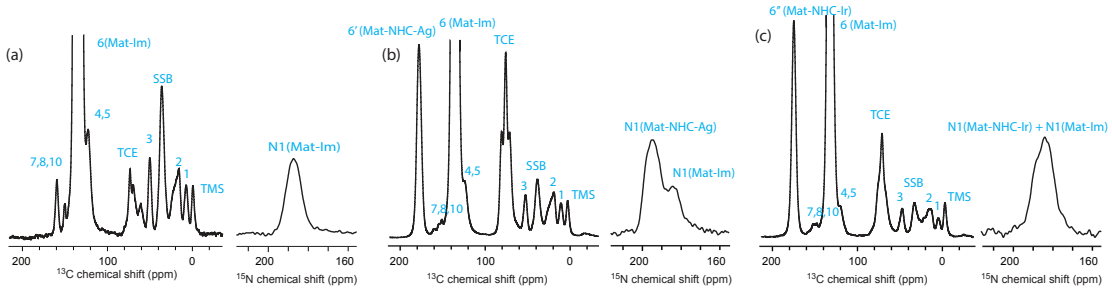

Figure 4.3: One-dimensional ^{13}C and ^{15}N DNP-enhanced NMR spectra of (a) Mat(1)-Im, (b) Mat(1)-NHC-Ag and (c) Mat(1)-NHC-Ir. The star denotes the spinning sidebands. All spectra were acquired at a MAS frequency of 10 kHz.The ^{13}C spectra were recorded with 16 scans and 3 ms of contact time. The ^{15}N spectra were recorded with 4 scans and 1 ms of contact time. The ^{13}C spectra were recorded with solvent suppression (echo delay of ms). Some residuals OEt are still presenet on the surface and the resonance overlaps with the C_2 peak.

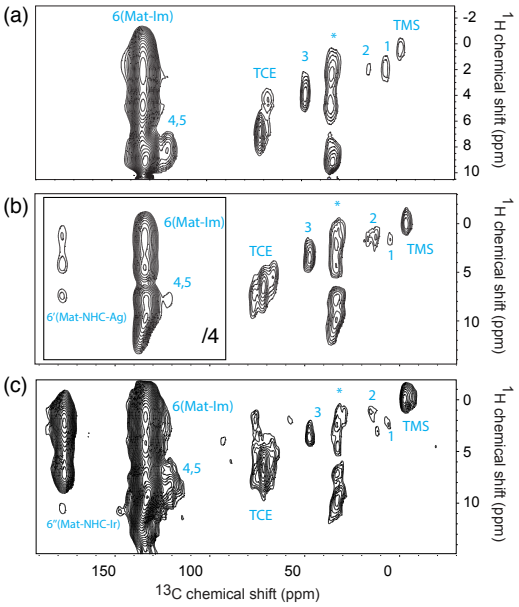

Figure 4.4: Two-dimensional ^{1}H-^{13}C HETCOR spectra of (a) Mat(1)-Im, (b) Mat(1)-NHC-Ag, (c) Mat(1)-NHC-Ir. The HETCOR experiments were recorded at 10 kHz with 64 scans and 3500 μs of contact time. DUMBO homonuclear decoupling was used at 100 kHz.

Mat(1)-NHC-Ir (Figure 4.3-(c)). The C_6 signal that corresponds to the imidazolium precursor is however still present, which indicates that the conversion from the imidazolium fragment to the intermediate silver complex is not complete, and that a significant amount of the organic precursor remains on the surface. This is corroborated by the ^{15}N NMR spectrum of Mat(1)-Ag-NHC that displays two resonances. Conversely, a single peak is observed on the ^{15}N NMR spectrum of Mat(1)-Ir-NHC, which reveals that the transmetallation is complete and the silver species are no longer present in the Mat-NHC-Ir material. In summary, the Mat(1)-NHC-Ag and Mat(1)-NHC-Ir materials are composed of a mixture of surface species, namely the imidazolium precursor in addition to the Ag-NHC or to the Ir-NHC complexes respectively. Similar observations were made with the materials having a ^{15}N- label at position 2 of the imidazole ring. We note that the spectra of Figure 4.3 were recorded using a cross-polarization step from protons, and are by

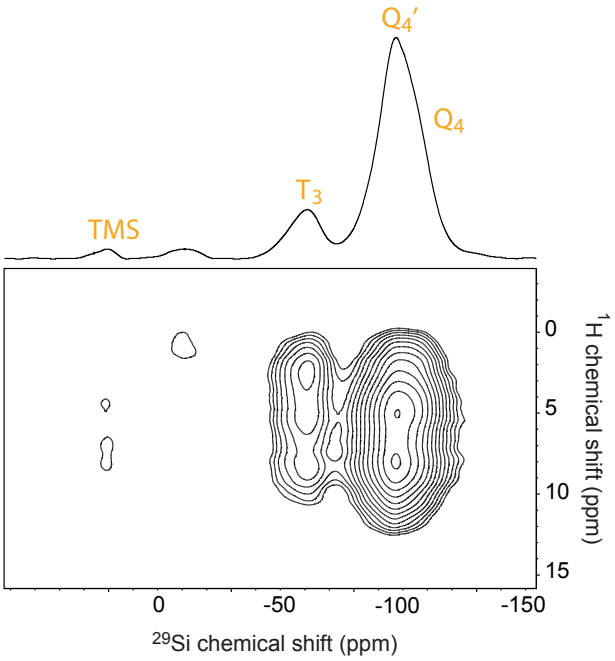

Figure 4.5: Two-dimensional ^{1}H-^{29}Si HETCOR spectrum of Mat(1)-Im. The 1D spectrum is displayed above the 2D plot. The HETCOR experiment was recorded at 10 kHz with 32 scans and 3500 μs of contact time. DUMBO homonuclear decoupling was used at 100 kHz. The additional resonance at $\sim$ -30 ppm corresponds to an unknown impurity present in all samples.

no means quantitative. Notably, long polarization build-up times will be needed to polarize the non-protonated carbene in the Ag- and Ir-NHC complexes.

In order to get quantitative estimates on the reaction yields, carbon-13 single pulse experiments were recorded on Mat(1)-NHC-Ag and Mat(1)-NHC-Im (Figure 4.6). The ratio of peak integrals gives the conversion yield from the imidazolium precursor to the silver intermediate, and from this latter to the Ir complex, in the fraction of surface species observed by DNP SENS. Similar experiments were conducted on the Mat(2) materials, and the reaction yields, as seen from NMR spectroscopy, are summarized in Figure 4.7.

Here, we note that, except for the C_6 resonances, all the other carbon resonances of the imidazolium precursor, of the silver and of the Ir complexes have identical chemical shifts. The proton chemical shifts were obtained from 2D ^{1}H-^{13}C HETCOR spectra that display all the expected correlations (Figure 4.4. In particular, the silver and iridium carbenes are polarized from both the aliphatic protons of the propyl chain and from aromatic protons of the imidazole ring. The ^{29}Si NMR spectrum of all materials display three resonances that are assigned to the TMS groups at 14.9 ppm, to the T_3 sites at -66 ppm and to the Q_4 and $Q_{4'}$ sites at respectively -106 and -100 ppm. These two latter signals were deconvoluted for the analysis of the REDOR curves. The $Q_{4'}$ sites correspond to silicon atoms of the matrix directly bound to the TMS groups. An additional unassigned peak at -30 ppm was observed in all samples. The 2D ^{1}H-^{29}Si spectra display correlations with the aliphatic and aromatic protons of the organic or organometallic ligands as illustrated in Figure 4.5 for the Mat(1)-Im material.

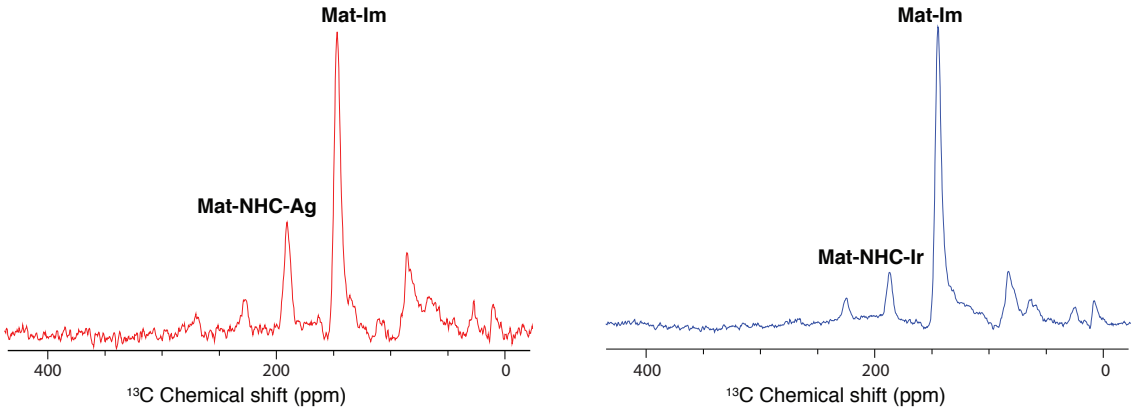

Figure 4.6: One-dimensional single pulse carbon-13 NMR spectra of Mat(1)-NHC-Ag (a) and Mat(1)-NHC-Ir (b). The spectra were acquired under 10 kHz MAS in the absence of microwave irradiation. A total of 250 scans with an interscan delay of 300 s were used. SPINAL-64 decoupling at a RF power of 100 kHz was applied during signal acquisition.

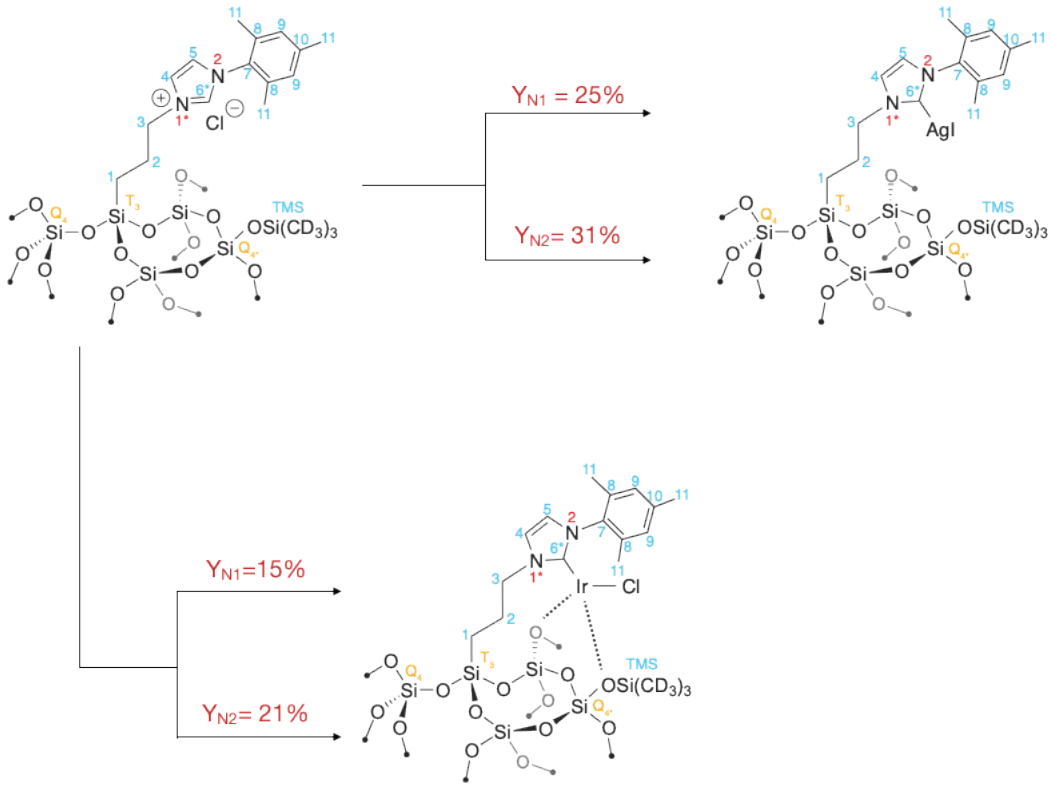

Figure 4.7: Yields for the different synthesis steps as observed by single-pulse carbon-13 NMR experiments.

4.4 Structure determination

4.4.1 REDOR and selective REDOR pulse sequences

A suite of ^{13}C-{^{15}N$_1$}, ^{13}C-{^{15}N$_2$}, ^{29}Si-{^{15}N$_1$}, ^{29}Si-{^{15}N$_1$} and ^{29}Si-{^{13}C$_6$} (conventional or selective) Rotational Echo DOuble Resonance (REDOR) experiments [225, 226] were implemented to obtain structural restraints. In the following, we briefly describe the pulse sequences that were

used. Figure 4.8-(a) shows the pulse sequence for the conventional REDOR experiment.

The conventional REDOR experiment: It relies on the reintroduction of the (MAS-averaged) heteronuclear dipolar coupling between two isolated spins X and Y. The strength of this dipolar coupling is directly related to the internuclear distance (proportional to inverse of the internuclear distance to the third). Restoring the dipolar interaction is achieved by applying a series of rotor-synchronized π-pulses on the Y channel [226,227]. While the spatial part of the dipolar interaction is modulated by $\cos(\omega_r t)$ and $\cos(2\omega_r t)$ functions (where ω_r is the spinning frequency), its spin part $X_z Y_z$ is reversed after each half-rotor period by the application of the π pulse on X. The modulation of the amplitude of the non-vanishing term of the dipolar coupling interaction is represented schematically as a sine function in Figure 4.8-(a). A π pulse is applied in the middle of the evolution period on the X spin to refocus the isotropic chemical shift. As a result, the transverse magnetization of the X spin undergoes a dipolar dephasing that leads to a signal attenuation. This signal intensity S of the X spin decreases with increasing dephasing periods. A control experiment is recorded, in the absence of π-pulses on the Y channel. In this case, the X spin experiences no dipolar dephasing and the intensity S_0 accounts only for T_2' losses (relaxation, imperfect dipolar decoupling from protons, imperfect averaging of the CSA terms...). Thus, the ratio S/S_0 as a function of the dephasing time provides a curve independent from T_2' attenuation and from which the dipolar coupling can be extracted.

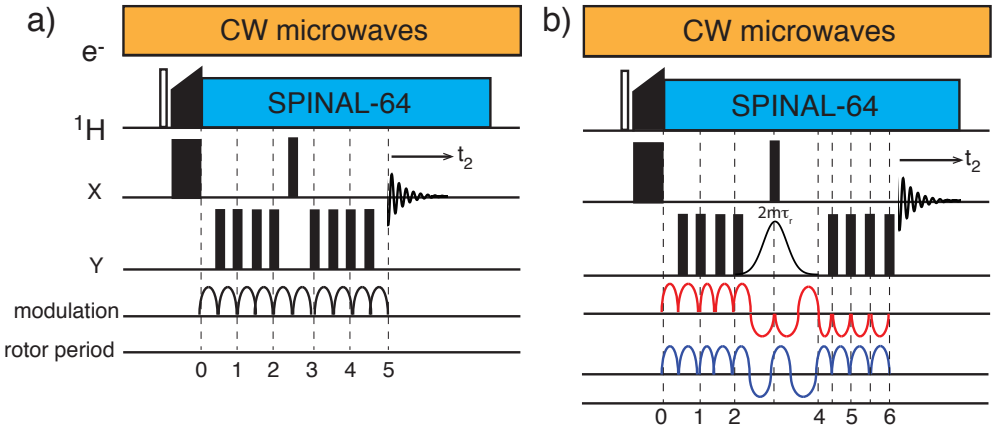

Figure 4.8: (a)X-{Y} REDOR pulse sequence used in this work, together with the schematic illustration of the modulation of the dipolar coupling interaction. (b) X-{Y} Frequency-Selective REDOR pulse sequence used in this work. The modulation of the dipolar coupling interaction is represented schematically for a spin X coupled to a non specific spin Y (in red) and for a spin X coupled to a spin Y on which the selective pulse will be applied (in blue). For simplicity, m was set to 1.

The analytical expression: An exact analytical expression from the literature can be expressed for an isolated two-spin system [226]. The expression is :

$$(\frac{S}{S_0})(t) = \frac{1}{2\pi}\int_{\alpha=0}^{\pi}\int_{\beta=0}^{\pi} cos(\frac{\gamma_X\gamma_Y\hbar}{2r^3}t\sqrt{2}sin2\beta sin\alpha)sin\beta d\alpha d\beta \tag{4.1}$$

where r is the distance between the two spins, t is the dephasing time that is an integer number of the rotor cycle, α and β are the azimuthal and polar angles of the internuclear vector for the spinning axis. γX and γY are the gyromagnetic ratios of X and Y respectively.

This analytical expression can be expanded as a series of Bessel function and then truncated at the fifth-order with a decent numerical precision as proposed by Mueller: [228]

$$(\frac{S}{S_0})(t) = (J_0(\sqrt{2}t\frac{\gamma_X\gamma_Y\hbar}{2r^3})^2 + 2\Sigma_{k=1}^{5}\frac{1}{16k^2-1}(J_k(\sqrt{2}t\frac{\gamma_X\gamma_Y\hbar}{2r^3})^2) \tag{4.2}$$

where J_k is the k^{th} Bessel function.
A scaling factor, ζ can be added to the analytical function to account for the isotopic abundance of the Y spins, the decay of coherences because of imperfect heteronuclear ^{1}H decoupling or imperfect inversion pulses on X and Y [229]. The scaling factor ζ also accounts for the fraction of X spins that are not in proximity of a Y spin and therefore are not dephased during the REDOR recoupling. We note here that this analytical expression was used only to extract the scaling factors ζ from REDOR data corresponding to fixed distances in the molecular geometry of the surface species, as will be detailed below.

$$(\frac{S}{S_0})(t) = (1-\zeta) + \zeta[(J_0(\sqrt{2}t\frac{\gamma_X\gamma_Y\hbar}{2r^3})^2 + 2\Sigma_{k=1}^{5}\frac{1}{16k^2-1}(J_k(\sqrt{2}t\frac{\gamma_X\gamma_Y\hbar}{2r^3})^2)] \tag{4.3}$$

Frequency-Selective REDOR: As discussed previously, the Mat-NHC-Ag and Mat-NHC-Ir are composed of a mixture of surface sites, namely the imidazolium precursor and the silver or iridium complex respectively. The C_6 carbene signal has a different chemical shift in the organic ligand and in the metallic complexes. In order to selectively measure structural constraints in these latter fragments, Frequency-Selective (FS) REDOR experiments were implemented where a selective pulse was applied on the C_6 resonance of the silver or iridium complex [229]. Figure 4.8-(b) shows the corresponding pulse sequence. A frequency-selective pulse is applied on the Y channel to selectively inverse a subset of spins Y, which ensures that the dipolar coupling between X and these selected Y spins will be effectively reintroduced. The X spins that are coupled to Y spins that are not affected by the selective pulse will experience no dipolar dephasing. The modulation of dipolar interaction is represented schematically for the 2 cases. The length of the selective pulse is set to a multiple of two rotor periods so as to also refocus the chemical shift anisotropy of the X spin. The FS-REDOR was used to probe distances between the C_6 carbon and the surface silicon atoms in Mat-NHC-Ag and Mat-NHC-Ir materials. The ^{15}N chemical shift differences between the imidazole precursor and the metallic complexes were too small to allow the implementation of ^{13}C-{^{15}N} or ^{29}Si-{^{15}N} FS-REDOR experiments. Nevertheless, conventional ^{29}Si-{^{15}N} REDOR experiments were carried out on the Mat(1)-NHC-Ag, Mat(2)-NHC-Ag, Mat(1)-NHC-Ir and Mat(2)-NHC-Ir materials and analyzed from the knowledge of the dipolar dephasing curve measured on the Mat(1)-Im and Mat(2)-Im materials, as explained below.

4.4.2 DNP SENS REDOR data

As the nitrogens are ^{15}N-labelled, distances can in principle be probed between these latter nuclei and the 3 types of silicon atoms of the silica matrix that yield distinct NMR resonances, as well as with the C_1 carbon. Similarly, as the carbene is ^{13}C-labelled, long-range proximities can be evaluated between this carbon atom and the surface silicons. Overall, the conventional REDOR experiment was implemented on the material containing the imidazolium precursor alone to obtain a set of 10 dipolar dephasing curves corresponding to long-range distances, as detailed in Figure 4.9-(a) and (b). We note here that some of the distances could not be probed because the signal-to-noise ratio was insufficient, as is the case for the Si_{TMS}-N_2 or C_2-N_2 proximity.

The Mat-NHC-Ag and Mat-NHC-Ir materials contain mixtures of surface species. In addition

(a)

Species	Pair of Spins	Total
Mat(1)-Im	N_1-C_1, C_6-Si(T), C_6-Si($Q_{4'}$), C_6-Si(TMS) N_1-Si(T), N_1-Si($Q_{4'}$), N_1-Si(TMS)	7
Mat(2)-Im	N_2-C_1, N_2-Si(T), N_2-Si($Q_{4'}$)	3
Mat(1)-NHC-Ag	C_6-Si(T), C_6-Si($Q_{4'}$), C_6-Si(TMS) N_1-Si(T), N_1-Si($Q_{4'}$)	5
Mat(2)-NHC-Ag	N_2-Si(T), N_2-Si($Q_{4'}$)	2
Mat(1)-NHC-Ir	C_6-Si(T), C_6-Si($Q_{4'}$), C_6-Si(TMS) N_1-Si(T), N_1-Si($Q_{4'}$)	5
Mat(2)-NHC-Ir	N_2-Si(T), N_2-Si($Q_{4'}$)	2

(b)

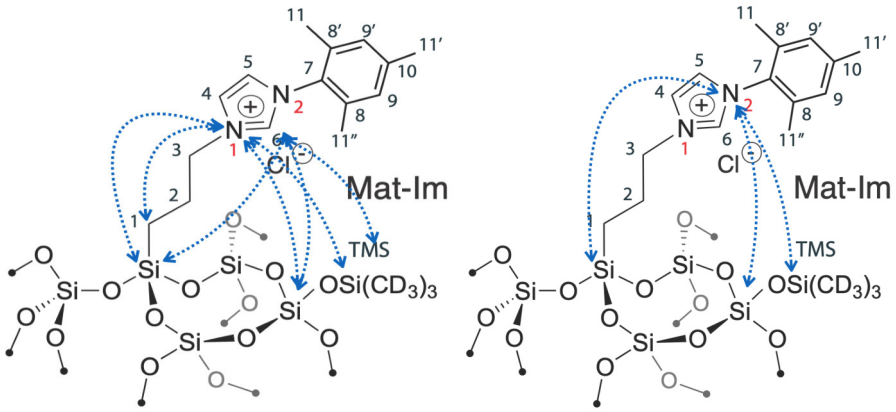

Figure 4.9: (a)List of non-trivial constraints that were measured for the three different species. The red color corresponds to the use of the FS-REDOR and the blue color for the conventional REDOR experiments.(b) Visualization of the distances that were probed on the Mat(1)-Im material.

to the organometallic complexes, the 1D carbon-13 spectra unambiguously show evidence for the residual presence of the imidazolium precursor in significant proportions. Determining the 3D structure of the supported silver and iridium sites while these spectator species still co-exit, thus represents a significant challenge. FS-REDOR experiments were implemented, which allowed one to selectively probe 3 long-range distances between the surface silicon atoms and the carbene carbon in both the Ag and Ir fragments. As the ^{15}N resonances of the imidazole ligand and those of the organometallic complexes are extremely close, if not degenerate, ^{29}Si-{^{15}N} FS REDOR could not be carried out to measure proximities between the silica matrix and the specific ^{15}N probe nuclei of the organometallic species. Nevertheless, conventional ^{29}Si-{$^{15}N_1$} REDOR experiments were carried out on the Mat(1)-NHC-Ag, Mat(2)-NHC-Ag, Mat(1)-NHC-Ir and Mat(2)-NHC-Ir materials and analyzed from the knowledge of the dipolar dephasing curve measured on the Mat(1)-Im and Mat(2)-Im materials, as detailed below. Figure 4.17 shows the experimental REDOR curves for all the constraints listed in Figure 4.9 for the three species : Mat-Im, Mat-NHC-Ag and Mat-NHC-Ir.

All the experimental details for the REDOR experiments are shown in Tables S1 and S2 in the Appendix.

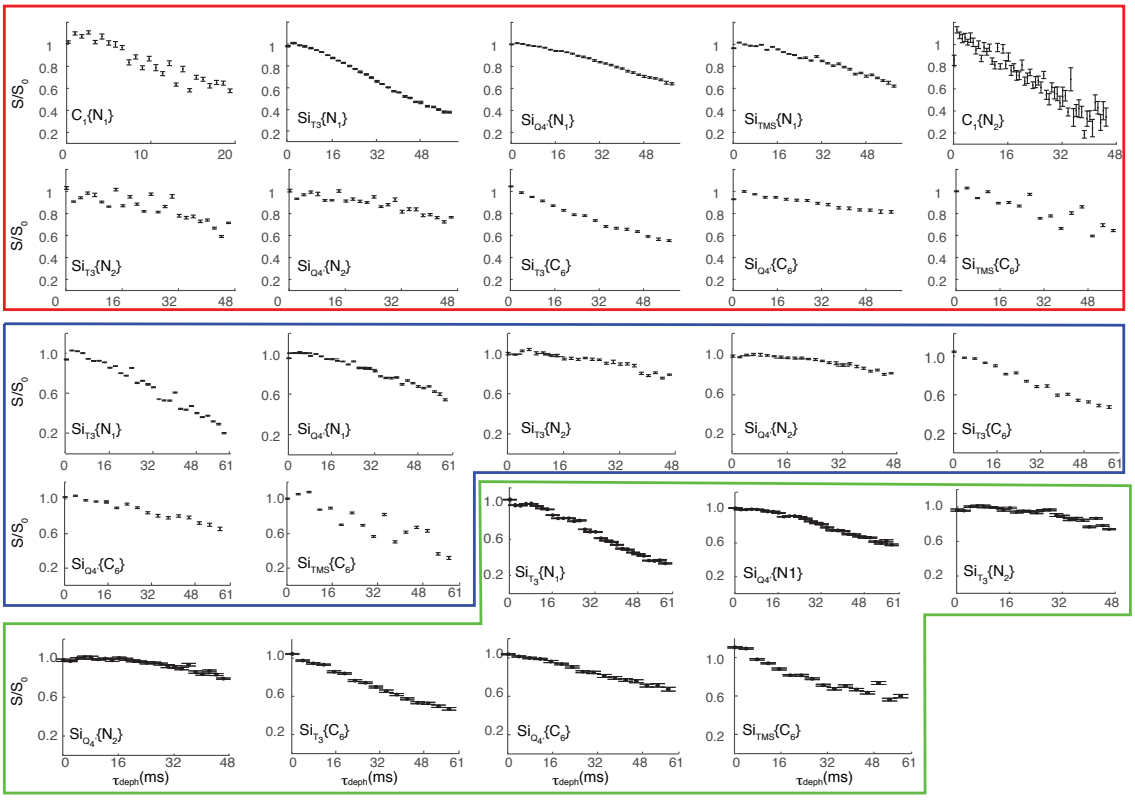

Figure 4.10: Experimental REDOR dipolar dephasing curves measured on the Mat-Im materials (red box), Mat-NHC-Ag (green box) and Mat-NHC-Ir materials (blue box). The Si-C_6 curves reported here were measured on the Mat(1)-Im, Mat(1)-NHC-Ag and Mat(1)-NHC-Ir materials.

4.4.3 Procedure for structure calculation

General protocol: The three-dimensional structures of the three types of surface species, the imidazolium precursor, the silver-based intermediate complex and the iridium-based catalysts were determined by applying the protocol initially developed for the Pt-NHC complex by Berruyer *et al.* [42], and adapted to the specificities of the systems investigated here. The overall procedure is detailed in Figure 4.11. As the molecular structure of the three surface species is of small size and in addition, anchored to a solid support, the number of conformational degrees of freedom is limited. These latter are shown in Figure 4.11 as α angles, with α varying from 1 to 7. The distance between the Si_{T3} and $Si_{Q4'}$ atoms is an additional parameter that can adopt discrete values. On the basis of previously developed models of silica surfaces [230, 231], three representative values of 4.50 Å, 5.59 Å and 5.83 Å were investigated. The rotation around α_2 within the TMS group was set to an arbitrary value since a low barrier to rotation is expected (as for the methyl groups). Moreover, the rotation around α_7 was set to the value (namely 120°) found from the X-ray data set on the homogeneous analog of this catalyst [162]. The conformational space was sampled by allowing the α_1, α_3, α_4, α_5, and α_6 angles to rotate by increments of 15°. Physically impossible structures, i.e. those which are in collusion with the surface or with other nuclei were eliminated. For a given $d_{Si_{T3}}$-$Si_{Q4'}$, a total number of 7 962 624 structures were generated, leading to an ensemble of 3 767 040 possible structures. For each structure of this pool of possible structures, a set of REDOR curves were calculated using the analytical expression 4.1. The deviation between the predicted data for a given structure k and the experimental data was then computed by calculating the sum

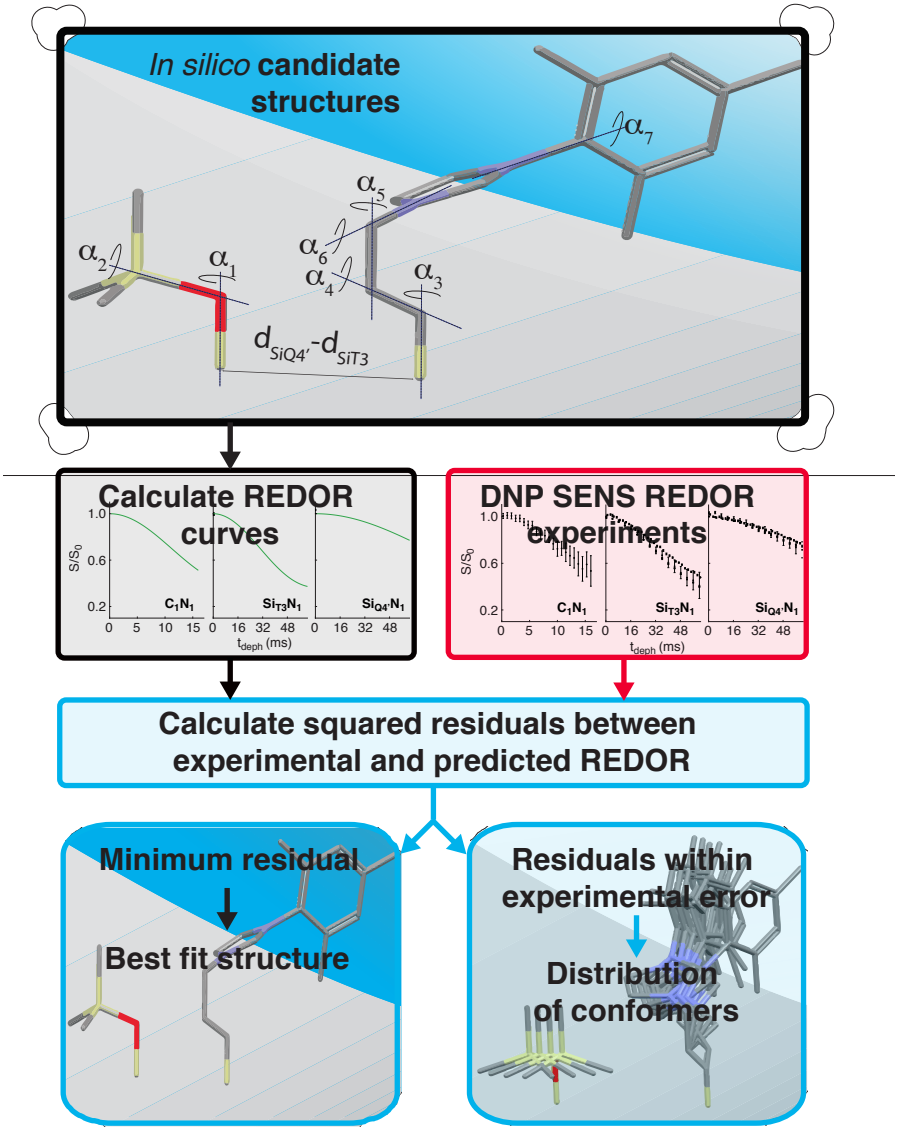

Figure 4.11: Three-dimensional structure determination protocol used here. A large set of possible structures were first generated in silico with by rotating the 5 axes (α_1, α_3, α_4, α_5, and α_6) by steps of 15°. This was done for three representative values for the $Si_{Q4'}$-Si_{T_3} distance, namely: 4.50 Å, 5.59 Å and 5.83 Å. Analytical REDOR curves were calculated for each structure and compared to the whole experimental data set. This enables the determination of a single 3D structure in best agreement with the experimental data as well as the distribution of conformers that agree with the data for an estimated experimental error. This protocol was adapted from the one implemented by Berruyer *et al.* in reference [42].

of squared residuals for all the REDOR curves, normalized by the number of REDOR points in each curve, to give the structural constraints the same weight in the determination. The structure in best agreement with the experimental data is defined as the one with the lowest value of (R). As mentioned above, for the Mat-Im material, a set of 10 REDOR curves were jointly analyzed, while only 7 curves were considered for the Mat-NHC-Ag and Mat-NHC-Ir materials. The protocol used for the structural determination can be summarized as shown in Figure 4.11.

Cross validation was applied using random sub-sampling of experimental data to determine the ensemble of structures. This method is also known as the Monte-Carlo cross-validation method.

First, a sub-set of the experimental data is generated by removing 10 % of the experimental points from each of the 10 or 7 REDOR curves. The structure determination protocol described previously is then re-applied, yielding a new best fit structure. This process is repeated 200 times and for each calculation, the best-fit structure is stored. The ensemble of best fit structures yields the distribution of possible structures at the surface.

Determination of the scaling factors: Before structure calculation, the scaling factor (or one minus the plateau value) of each REDOR curve was determined from REDOR data corresponding to internuclear distances that are fixed in the molecular geometry. The standard least squares approach was used to fit these REDOR dephasing curves. The data were fitted with two parameters, the scaling factor ζ and the distance r between the two nuclei. Fitting errors were estimated according to the following procedure: a first fit of the experimental data was performed giving a value for the distance and the scaling factor. A REDOR curve was then computed with these parameters, and a new set of points was generated by adding random noise on the calculated curves. This new set of points is then fitted according to the REDOR analytical expression. The process was repeated 20 000 times to obtain a distribution of distances and of scaling factor values from which the error was estimated. The same protocol was applied to all others fixed distances. The distances found are in good agreement with canonical distances.

Scaling factors measured on the Mat(1)-Im and Mat(2)-Im materials Figure 4.12-(a) and (b) show the REDOR data as well as the result of the fitting procedure for the C_3-N_1 and C_3-N_2 spin pairs. From the $^{13}C_3$-$\{^{15}N_1\}$ REDOR curve, a scaling factor $\zeta(^{13}C_3\text{-}\{^{15}N_1\})$ of 0.6 was found and then used as a fixed parameter for the spin pairs: ^{29}Si-$\{^{15}N_1\}$ and ^{13}C-$\{^{15}N_1\}$. From the $^{13}C_3$-$\{^{15}N_2\}$ REDOR curve, a scaling factor $\zeta(^{13}C_3\text{-}\{^{15}N_2\})$ of 0.64 was found and then used as a fixed parameter for the spin pairs: ^{29}Si-$\{^{15}N_2\}$ and ^{13}C-$\{^{15}N_2\}$. We note here that ζ counts (among other factors mentioned above) for the fraction of $^{13}C_3$ spins that are not in proximity to a ^{15}N nucleus (for example it might correspond to a fraction of the propyl iodine fragment that did not react to form the ^{15}N-labelled imidazolium precursor). Figure 4.12-(c) and (d) show the REDOR data that were used to determine the scaling factor of ^{29}Si-$\{^{13}C_6\}$ experiments recorded on Mat(1)-Im. The $^{13}C_6$-$\{^{15}N_1\}$ dephasing curve (Figure 4.12-(c)) shows a complete dephasing (with a scaling factor of 0.96), as expected since both labelled spins are introduced from fully-labelled precursors used to prepare the molecular ^{2}H-mesityl-$^{15}N_1$,$^{13}C_6$-imidazole group. From a ^{15}N-$\{^{13}$C$\}$ REDOR experiment and the N_1 dephasing curve, a scaling factor $\zeta(^{15}\text{N-}\{^{13}C_6\})$ of 0.89 was obtained (Figure 4.12-(d)). This scaling factor was combined with the one measured in the ^{13}C-$\{^{15}N_1\}$ experiment to get access to the value of the scaling factor in ^{29}Si-$\{^{13}C_6\}$ experiments. As all the C_6 carbons are linked to an isotopically labelled N_1, the scaling factor for ^{29}Si-$\{^{13}C_6\}$ experiments was simply calculated as the product of the scaling factor measured for $^{13}C_3$-$\{^{15}N_1\}$ and the scaling factor measured for ^{15}N-$\{^{13}C_6\}$:

$$\zeta(^{29}Si - \{^{13}C_6\}) = \zeta(^{13}C_3 - \{^{15}N_1\} * \zeta(^{15}N - \{^{13}C_6\}) \tag{4.4}$$

A value of 0.53 was therefore considered.

Scaling factors measured on the Mat-NHC-Ag and Mat-NHC-Ir materials The same procedure was applied to calculate the scaling factors $\zeta(^{29}\text{Si-}\{^{13}C_6\})$ and analyze REDOR data recorded on the Mat(1)-NHC-Ag and Mat(1)-NHC-Ir materials. In these cases, selective

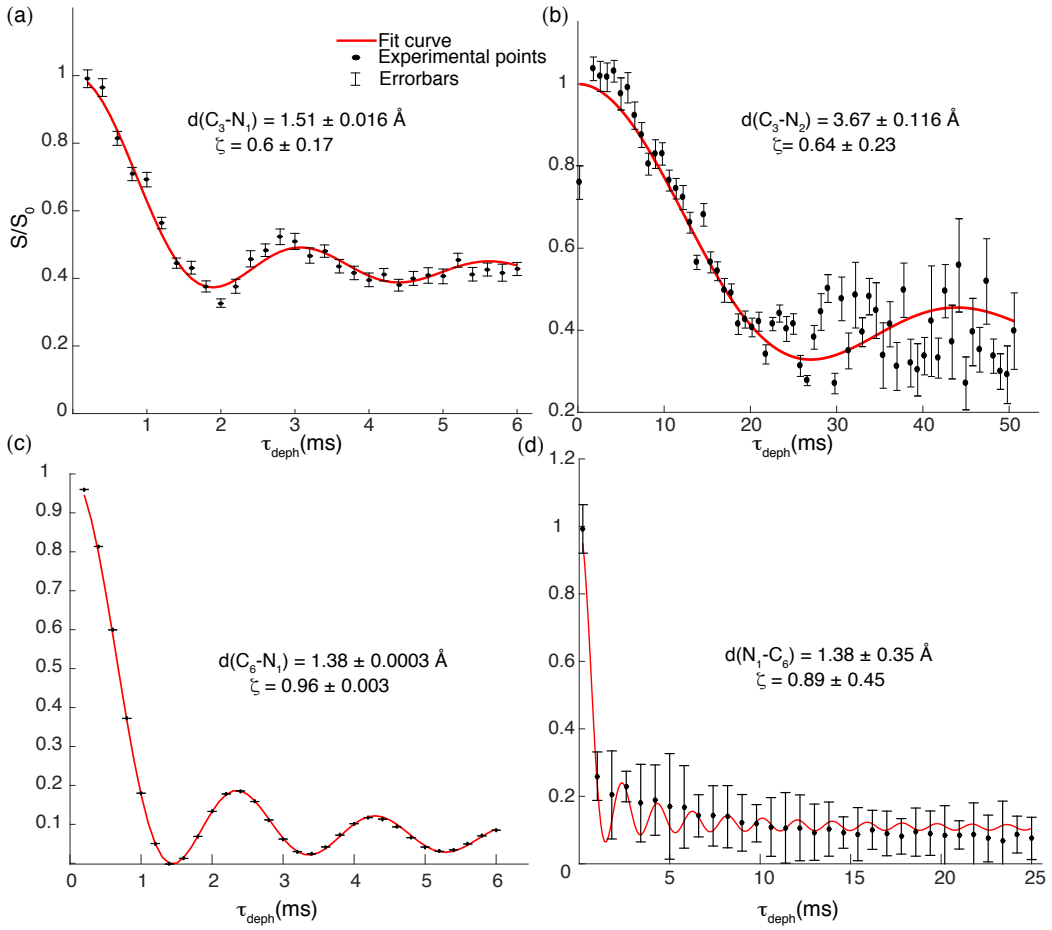

Figure 4.12: (a) C_3 dephasing curve extracted from a DNP SENS $^{13}C_3$-$\{^{15}N_1\}$ REDOR experiment recorded on Mat(1)-Im as well as values of distance and scaling factor extracted from the fitting procedure. (b) C_3 dephasing curve extracted from a DNP SENS $^{13}C_3$-$\{^{15}N_2\}$ REDOR experiment recorded on Mat(2)-Im. (c) C_6 dephasing curve extracted from a DNP SENS $^{13}C_6$-$\{^{15}N_1\}$ REDOR experiment recorded on Mat(1)-Im. (d) N_1 dephasing curve extracted from a DNP SENS ^{15}N-$\{^{13}C_6\}$ REDOR experiment recorded on Mat(1)-Im.

REDOR experiments were implemented to determine. Figure 4.13-(a) and (b) shows the N_1 dephasing curve from ^{15}N-$\{^{13}C\}$ REDOR experiments carried out on the two materials. The scaling factors were then calculated as :

$$\zeta(^{29}Si - \{^{13}C_6\}) = \zeta(^{13}C_3 - \{^{15}N_1\} * \zeta(^{15}N - \{^{13}C_6\}) \tag{4.5}$$

where $\zeta(^{15}N$-$\{^{13}C_6\})$ is the value determined from FS REDOR experiments on Mat(1)-NH-Ag (a) or on Mat(1)-NHC-Ir, and $\zeta(^{13}C_3$-$\{^{15}N_1\}$ is the value determined from REDOR experiments on Mat(1)-Im. Values of 0.46 and 0.41 were considered for the scaling factor of ^{29}Si-$\{^{13}C\}$ REDOR experiments on the silver and iridium materials respectively. As mentioned already, all these scaling factors were considered as fixed values for the structural analysis.

Treatment of the ambiguous structural constraints: Conventional (i.e. non-selective) ^{29}Si-$\{^{15}N\}$ REDOR experiments were recorded on the Mat-NHC-Ag and Mat-NHC-Ir materials. In this case, the dipolar dephasing curves are a sum of two decays, corresponding to ^{29}Si sites that are close to the imidazolium precursor as well as to sites near the silver or iridium complex. The

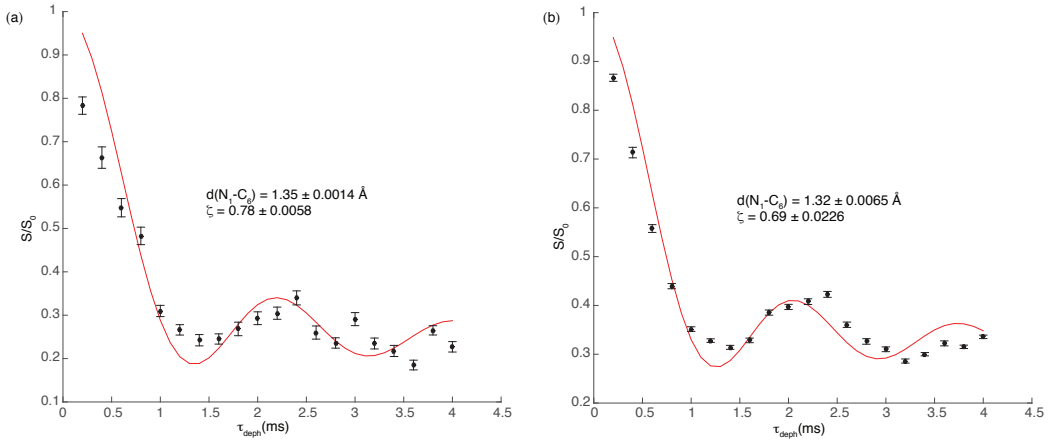

Figure 4.13: N_1 dephasing curve extracted from a DNP SENS ^{15}N-{^{13}C} REDOR experiment recorded on Mat(1)-NCH-Ag (a) and on Mat(1)-NHC-Ir (b), as well as values of distance and scaling factor extracted from the fitting procedure described above.

weight of each fraction in this sum will correspond to the relative quantity of species present at the surface of the silica matrix. The ^{29}Si-{^{15}N} dephasing curves measured on the Mat-Im, Mat-NHC-

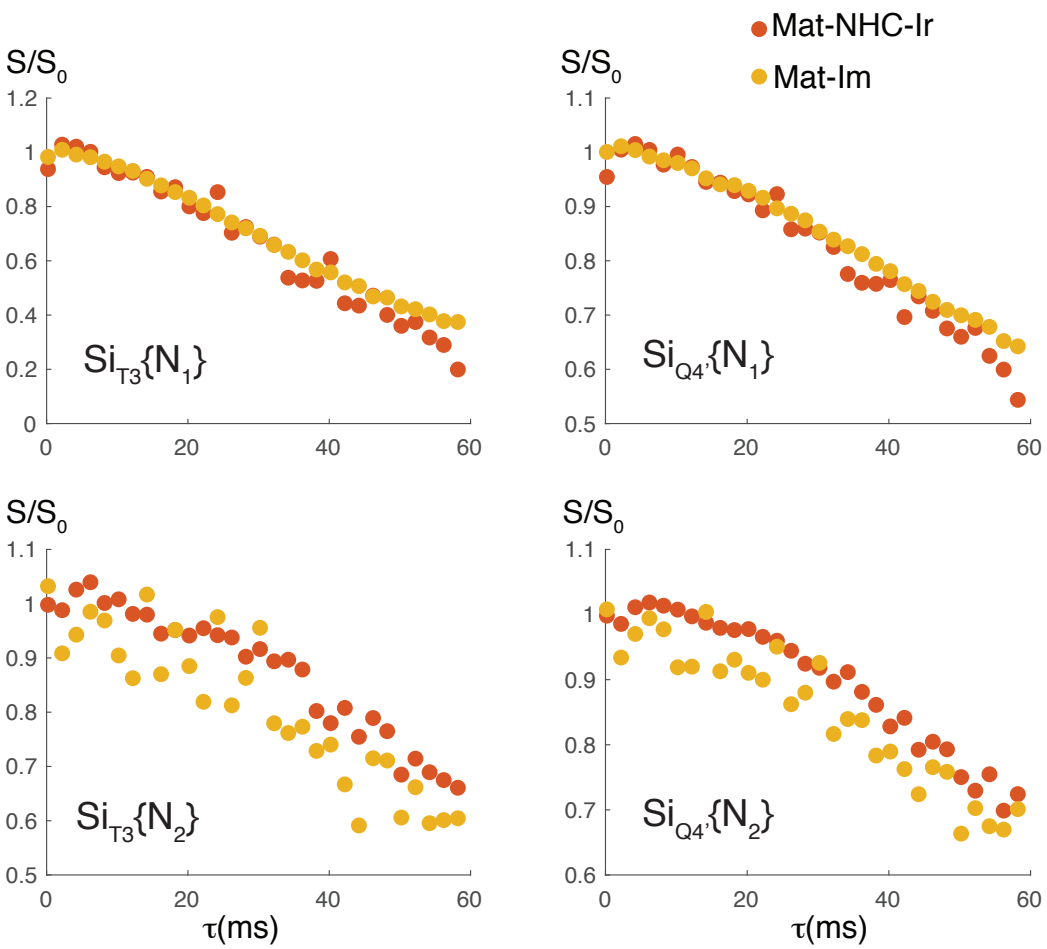

Figure 4.14: REDOR dephasing curves for the Mat-Im and Mat-NHC-Ir on four different sites $Q_{4'}$-N_1, $Q_{4'}$-N_2, T_3-N_1, and T_3-N_2

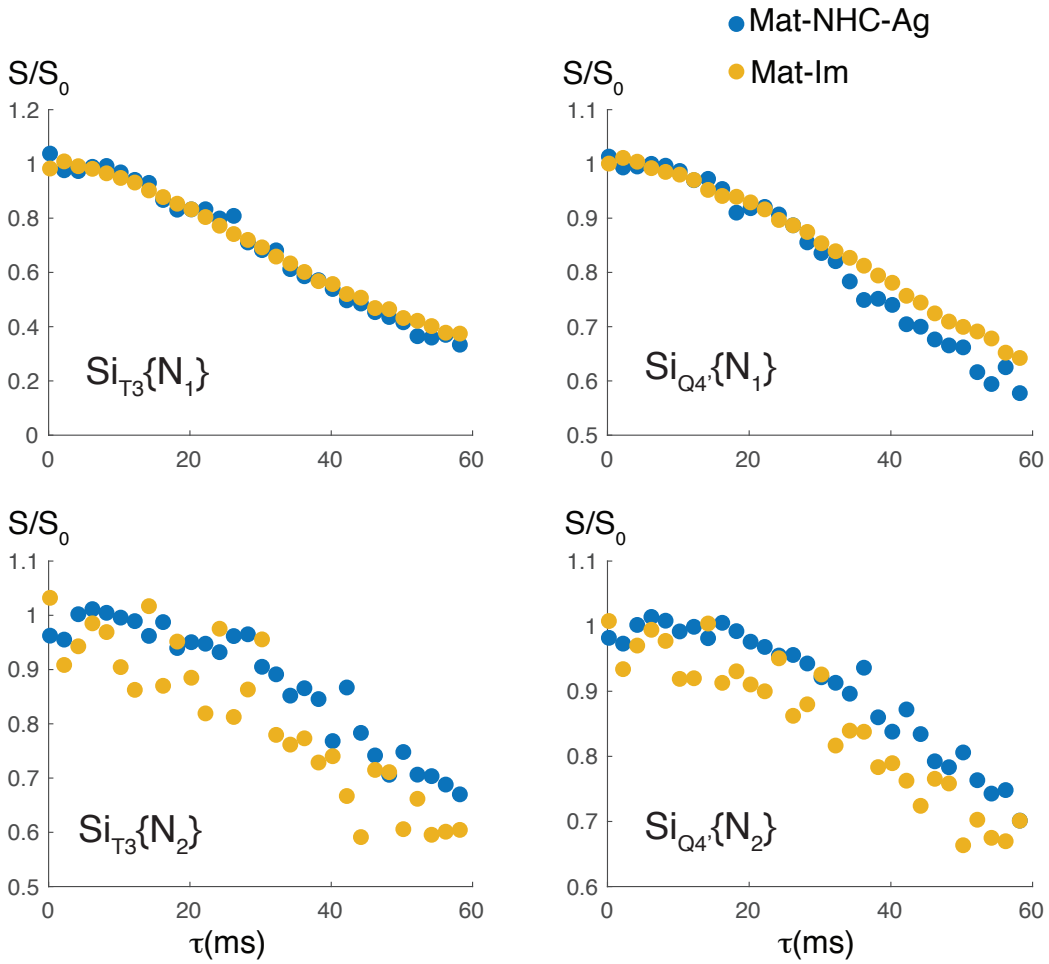

Figure 4.15: REDOR dephasing curves for the Mat-Im and Mat-NHC-Ag on four different sites $Q_{4'}$-N_1, $Q_{4'}$-N_2, T_3-N_1, and T_3-N_2

Ir and Mat-NHC-Ag materials were carefully compared, as shown in Figures 4.14 and 4.15. As the REDOR curves exhibit a relatively similar dephasing for the imidazole precursor material on one hand and the Mat-NHC-Ag or the Mat-NHC-Ir materials on the other hand, we considered that, independently of the surface species, the decay was the same. In other words, the non-selective ^{29}Si-{^{15}N} REDOR curves recorded on the Mat-NHC-Ag or the Mat-NHC-Ir materials were used in the structure calculation protocol of the Ag-NHC and Ir-NHC complexes.

4.4.4 Three-dimensional surface structures

The single 3D structures in best agreement with the experimental data, i.e. the structures of the imidazolium precursor, of the Ag-NHC and Ir-NHC complexes having the lowest value of the the sum of squared residuals (R), are shown in Figure 4.16. The corresponding REDOR curves (calculated from these structures and the analytical expression of S/S_0) are superimposed on the experimental REDOR data in Figure 4.17. Figure 4.18 shows the ensemble of the structures for the three different surface species obtained using the cross-validation protocol described above.

To validate the structure of the imidazolium precursor, the cross-validation process was repeated 200 times. Two distinct and symmetric sets of ensembles were found where the α_1 and α_3 angles differ by around $\sim 180°$. Within these two sets of ensembles, only 7 (for the left set) and

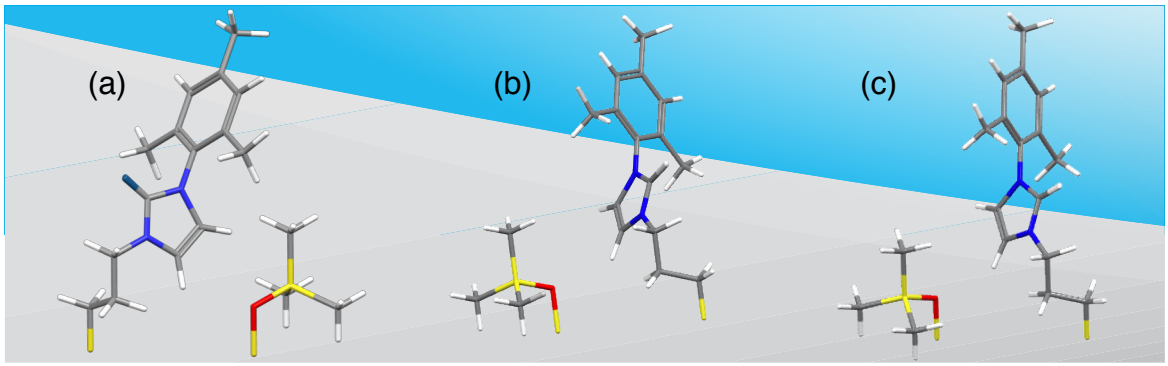

Figure 4.16: Best fit three-dimensional structures obtained for (a) the Ir-NHC complex, (b) the Mat-Im precursor, and (c) the Ag-NHC catalytic complex. The structures were obtained using the protocol detailed in Figure 4.11, using respectively 10, 7 and 7 long-range, non-trivial distance constraints. A distance between the $Si_{Q4'}$ and the Si_{T_3} sites of 5.59 Å was considered.

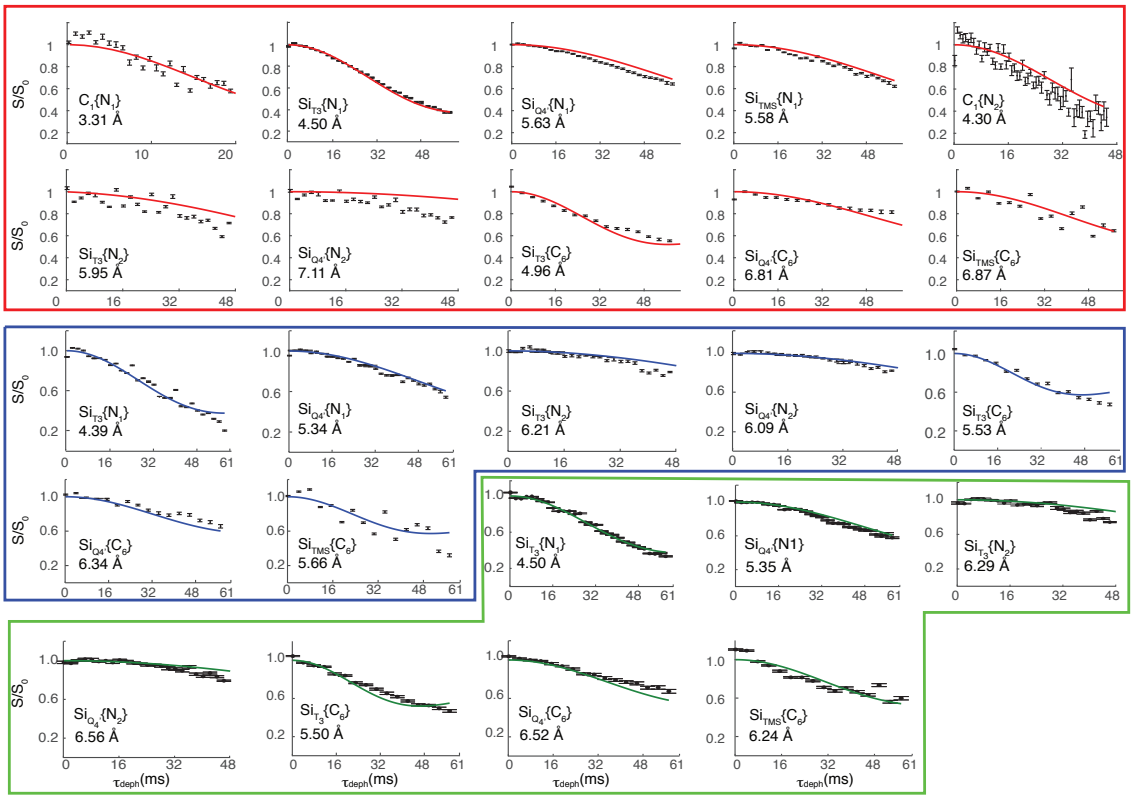

Figure 4.17: Calculated REDOR curves for the three structures in best agreement with the experimental data (plain lines) superimposed with the REDOR experimental data, for the for (red box) the imidazolium precursor, (green box) the Ag-NHC intermediate complex, and (blue box) the Ir-NHC catalytic complex.

8 (for the right set) different structures were found. The best fit structure corresponds α_1 and α_3 angles and belongs to the left ensemble in Figure 4.18-(a). Similar conclusions were drawn for the other ensemble of structures.

To validate the structure of silver complex, the cross-validation process was also repeated 200 times. 54 times out of 200, we found that the structure in best agreement with the experimental data was the exact same one as the one determined using all experimental data. A total of 11

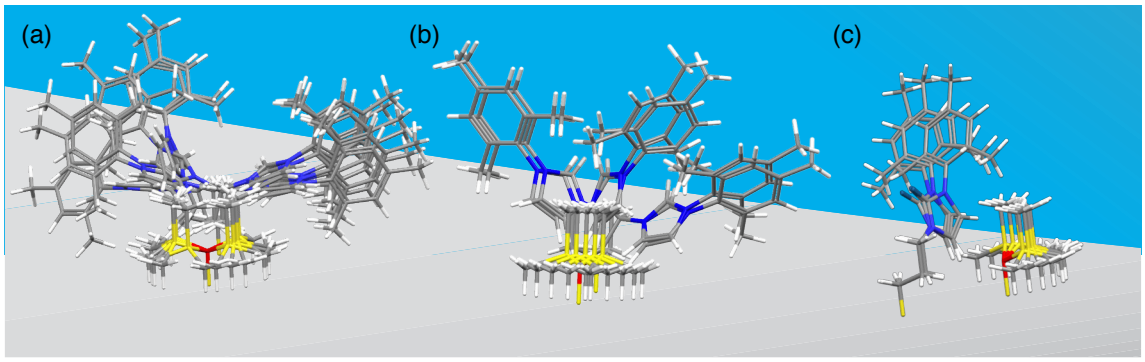

Figure 4.18: Ensemble of conformers obtained for the three species, the imidazolium precursor (a), the Ag-NHC intermediate complex (b), and the Ir-NHC catalytic complex (c). The structures were superimposed by aligning the Si_{T_3}, $Si_{Q4'}$ and O attached to the $Si_{Q4'}$.

structures were found for the silver complex.

To validate the structure of iridium complex, the cross-validation process was also repeated 200 times. 80 times out of 200, we found that the structure in best agreement with the experimental data was the exact same one as the one determined using all experimental data. In addition, we found 50 structures that differed by only 15° rotation. A total of 14 structures were found for the silver complex.

The width of each ensemble is characterized by a root-mean-square deviation (RMSD). The RMSD was calculated by generating an average structure from each ensemble. The RMSD between each structure from the ensemble and the average structure was then calculated. RMSD values of 4.33, 3.49 and 0.89 Å were respectively obtained for the imidazolium precursor, the Ag-NHC and the Ir-NHC complexes. The structures of Figure 4.16 and 4.18 were calculated with a distance of 5.59 Å between the $Si_{Q4'}$ and the Si_{T_3} sites. Calculations were also done for two other distances 4.50 Å and 5.83 Å that were derived from the amorphous silica surface model by Ugliengo *et al.* [230]. In all the three cases, the best fit structure was the same as that determined for a 5.59 Å distance. No further exploration was done on these two distances.
Table 4.2 shows a few characteristic distances measured in the 3 best fit structures. Distances are also included that correspond to the structure proposed by Berruyer *et al.* for the Pt-NHC complex.

	Mat-Im	NHC-Ag	NHC-Ir	NHC-Pt
C_6-Si_{T_3}	4.9 Å	5.5 Å	5.9 Å	4.7 Å
C_6-Si_{TMS}	6.8 Å	6.2 Å	5.6 Å	5.4 Å
C_7-Si_{T_3}	6.9 Å	7.6 Å	7.9 Å	6.7 Å
C_7-Si_{TMS}	8.6 Å	7.4 Å	5.6 Å	6.2 Å
N_1-Si_{T_3}	4.5 Å	4.5 Å	4.7 Å	4.4 Å
N_1-Si_{TMS}	5.5 Å	5.3 Å	5.1 Å	6.2 Å
Metal-O-Si_{TMS}	7.6 Å	6.3 Å	6.8 Å	2.6 Å

Table 4.2: Table summarizing some relevant distances for the three different species and the NHC-Pt determined by Berruyer *et al.* in [42]

The imidazole precursor shows two distinct and symmetric ensembles of structures as de-

scribed previously, with a relatively narrow distribution within each set. These structures appear to be folded towards the surface. Thus, although anchored to the silica matrix via a flexible propyl tether, the organometallic precursor adopts a relatively well-defined conformation. While the ensemble of structures obtained the silver complex is significantly broad with a RMSD value of 3.49 Å, a much more limited set of conformations were derived from the calculation protocol for the Ir-NHC fragment. Although only 7 structural constraints were used in the calculation versus 10 for the organic imidazolium precursor, a well-defined structure (RMSD of 0.89 Å) emerges for the iridium complex. However, unlike our initial expectations and in contrast to what had been postulated for the Pt-NHC complex, the structure clearly shows that the organometallic fragment is not folded back onto the surface but rather points outward into the porous cavity.

Figure 4.19 shows the experimental ^{29}Si-{$^{13}C_6$} FS REDOR curves measured for the Mat(1)-

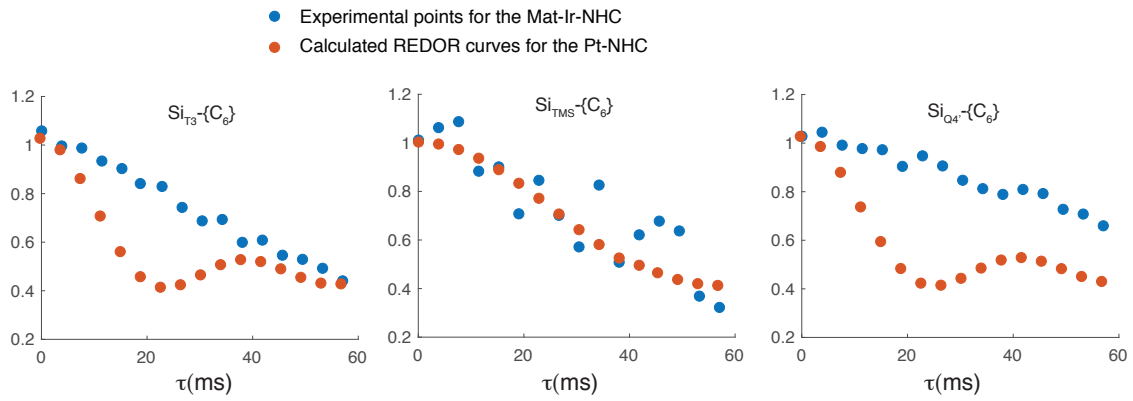

Figure 4.19: ^{29}Si- {$^{13}C_6$} DNP SENS FS REDOR data measured on the Mat(1)-NHC-Ir materials and comparisons with REDOR points (in red) calculated from the structure of the Pt-NHC complex published in reference [42].

NHC-Ir material superimposed with REDOR curves calculated from the proposed structure of the Pt-NHC complex. The two sets of curves clearly differ. In particular the modulation observed for the platinum complex that reflects the proximity of the metal center to the silicon surface atoms is absent from the data points measured for the Ir-NHC complex. In agreement with these observations, the distance between the iridium and the oxygen atom that resides between the $Si_{Q4'}$ and Si_{TMS} is 7 Å versus 2.68 Å in the Pt-NHC complex. Thus, in the 3D structure derived from the DNP SENS data, the iridium metal center is clearly not coordinated by this surface oxygen, nor by any other oxygen atoms.

Input from EXAFS analysis: As already mentioned in his manuscript, EXAFS is a well-established technique to probe the local environment of metal centers. Figure 4.20 shows the EXAFS data measured on the Mat-NHC-Ir material as well as the number and nature of nuclei surrounding the iridium center. This measurement was performed in the group of C. Copéret at ETH Zürich. EXAFS fitting analysis of the first coordination sphere of Mat-NHC-Ir suggests that the number of carbon neighbors around the Ir center is 3 +/- 1 at 2.11 +/- 0.02 Å. In addition, one Cl atom is present around the Ir centers at 2.39 +/- 0.02 Å. Thus, the EXAFS data also suggest the absence of oxygen atom in the coordination sphere, and in this respect agree with the NMR data and the proposed 3D structure. However, only one carbon atom is coordinating the Ir metal center in the NMR structure determined so far. As mentioned in section 4.2, the iridium center is

(a)

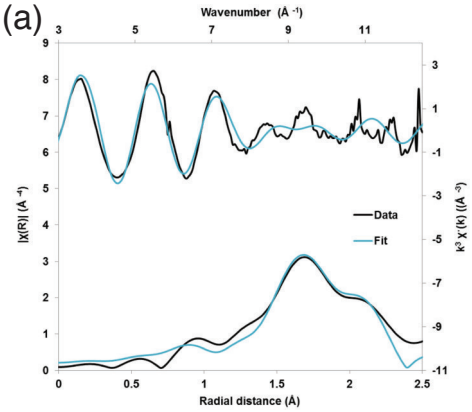

(b)

neighbor	N[a]	σ² (Å²)[b]	R (Å)[c]
C	3 (1)	0.006 (2)	2.11 (2)
Cl	1*	0.007 (2)	2.39 (2)

Figure 4.20: (a) EXAFS data (in black) and fits (in blue) in k-space (upper; top and right axes) and R-space (lower; bottom and left axes) of Mat-NHC-Ir in Ir L3 edge. (b) EXAFS fit parameters for the Ir L3-edge spectrum of Mat-NHC-Ir. [a]Number of specified neighbors. [b]Debye-Waller factor. [c]Distance between Ir metal center to the specified neighbors. *Fixed parameters in the fit.

introduced via the $[Ir(COD)Cl]_2$ molecular complex, where COD stands for a 1,5-CycloOctaDiene ligand. We therefore postulate that, in the structure derived from the NMR data, the COD ligand is still present in the surrounding of Ir metal center, stabilizing the whole organometallic edifice.

Input from chemical analysis: No evidence for the presence of a COD ligand around the Ir center was found in the study performed by Romanenko *et al.* in 2015 [162]. However, we note here that, as already mentioned, the concentration of surface sites differs in the two studies (ratio TEOS:organosilane = 30 in reference [162], versus 19 in this work). In order to quantify the amount of COD coordinated to the Ir centers in the Mat-NHC-Ir materials investigated here, the Mat-NHC-Ir material was put in contact with dry toluene (over weekend at 60 °C inside a Fisher-Porter tube under 3 bars of H_2), and the amount of cyclooctane released after hydrogenation was quantified in the group of C. Thieuleux at C2P2 Lyon. The residual presence of COD ligands at the surface of the material was confirmed, and the data suggest that 45 % of the Ir sites are still coordinated by COD ligands. This chemical analysis therefore confirms the presence of COD ligands in the Mat-NHC-Ir material prepared with a high concentration of surface sites.

Three-dimensional structure of the Ir-NHC organometallic complex with the COD ligand: A density functional theory (DFT) geometry optimization, starting from the experimentally determined best fit structure of the Ir-NHC complex and in the presence of the COD ligand was performed in collaboration with Prof. C. Widdifield from Oakland University. The resulting structure is shown in Figure 4.21. Notably, the orientation of the C_6-Ir bound pointing outwards from the silica surface is compatible with the presence of a COD ligand in the coordination sphere of the metal center. Here we note however two critical points. The EXAFS data points out to the presence of 3 ± 1 coordinating carbons (while 5 would be expected if all Ir sites were surrounded by a COD ligand). The chemical analysis also indicates that this COD ligand is absent for about half of the Ir complexes. Overall, this suggests that the iridium center is coordinated by a carbene along with a COD ligand for half of the sites. The 3D structure determined from the experimental DNP SENS REDOR data would correspond to these later sites. Thus, questions remain regarding why the sites where the COD ligand is absent had been invisible from our NMR

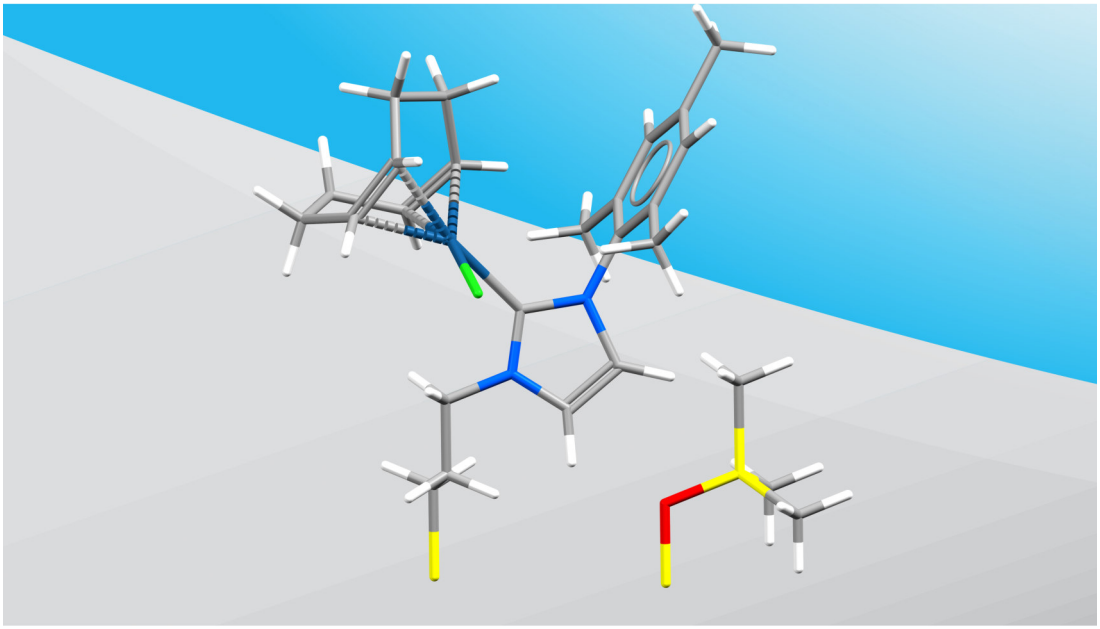

Figure 4.21: Three-dimensional structure of Ir-NHC complex obtain from the DNP SENS data in the presence of the COD ligand.

study. One hypothesis could be that such sites could lie at the entrance of the pores where the high concentration of radical would lead to strong signal attenuation by paramagnetic relaxation effects (or "bleaching" effects). Nevertheless, important structural features could be derived from our analysis. In particular, our study highlighted the fact, while the silver intermediate adopts a rather ill-defined structure, the iridium catalytic material displays an extremely narrow bundle of conformations. While the presence of the COD ligand was not postulated a priori in the calculation, the protocol converged to an atomic-scale structure where the Ir center is pointing away from the silica surface, and therefore to a structure not in line with the presence of coordinating oxygen atoms. The EXAFS and chemical analysis data allowed one to confirm the presence of the COD ligand. Finally we note that the carbon-13 NMR resonances of the COD ligand (expected at around 30 ppm for the methylene signals, and at around 50 ppm and 80 ppm for the sp^2 carbon atoms trans to respectively Cl and NHC groups [232]), could not be unambiguously observed, likely because they are masked by the huge resonance of the solvent and by the aliphatic resonances of the propyl tether of the organic and organometallic ligands.

4.5 Proton NMR spectroscopy

Proton NMR spectroscopy under very fast MAS was applied to observe the presence of COD ligands in the Mat-NHC-Ir samples. Figure 4.22 shows as a series of 1D spectra recorded at 23.1 T under 60 kHz MAS 1.3 mm rotors. Four samples were investigated: the iodopropyl precursor, the imidazolium precursor Mat(2)-Im, the unlabeled Mat-NHC-Ir material at a 1/30 dilution, and the Mat(2)-NHC-Ir. As expected the aromatic resonance appears only for Mat(2)-Im and for the iridium materials. The resonance of the methyl protons of the mesityl group is visible on the Mat-NHC-Ir (1/30) but is absent in Mat(2)-Im as they were deuterated in this latter material. Interestingly, a new resonance clearly appears at 4.5 ppm for the material with the higher concentration of surface sites, which can be assigned to the CH groups of the COD ligand. This

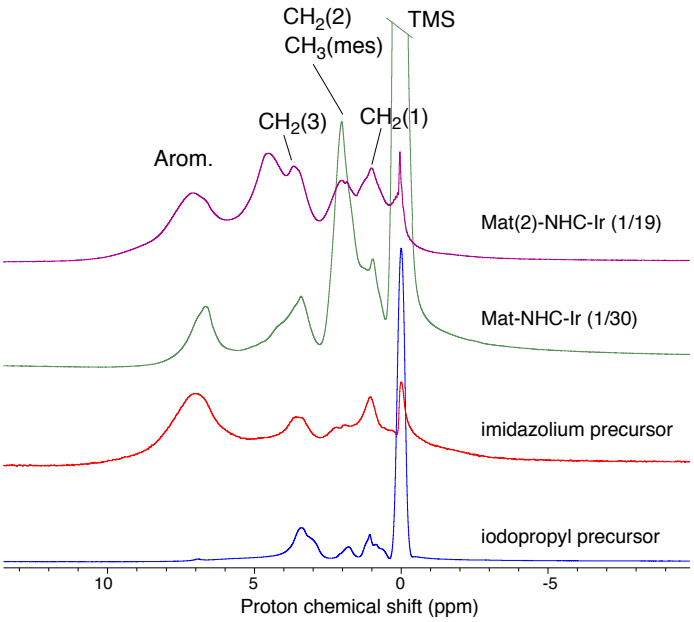

Figure 4.22: 1D ^{1}H spectra of the Iodopropyl, Mat(2)-Im, Mat-NHC-Ir (unlabeled) at 1/30 dilution and Mat(2)-NHC-Ir at 1/19 dilution. The spectra were recorded on a 23.1 T at room temperature at 60 kHz MAS rate in a 1.3 mm rotor. 64 scans were used with a recycle delay of 2 s for the four spectra.

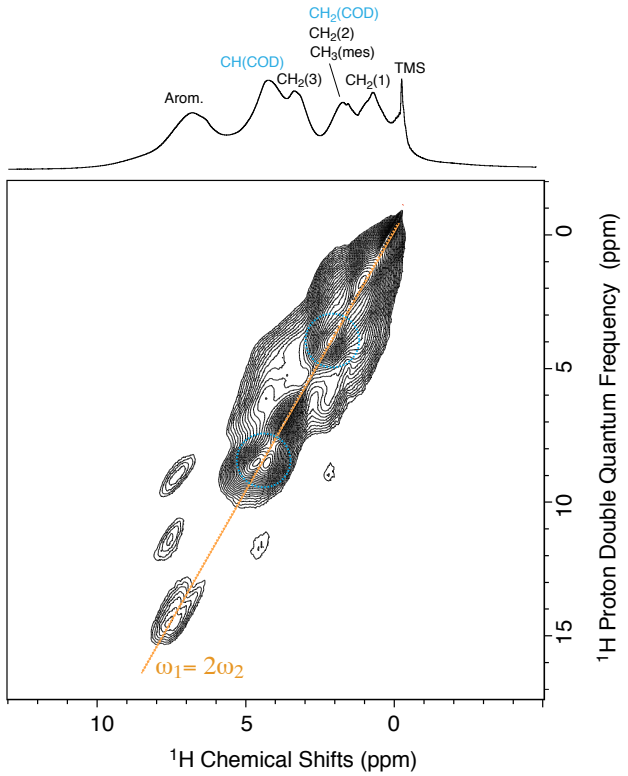

Figure 4.23: 2D ^{1}H double quantum BABA spectrum of the Mat(2)-NHC-Ir at 1/19 dilution. The spectra were recorded on a 23.1 T at room temperature at 60 kHz MAS rate in a 1.3 mm rotor. 80 scans were used with a recycle delay of 2 s. The dotted orange line corresponds to $\omega_1 = 2\omega_2$.

resonance correlates with protons at around 2.5 ppm in the 2D BAck-to-BAck (BABA) spectrum that could correspond to the CH_2 protons of the COD ligand.

4.6 Structural investigation after catalytic reaction

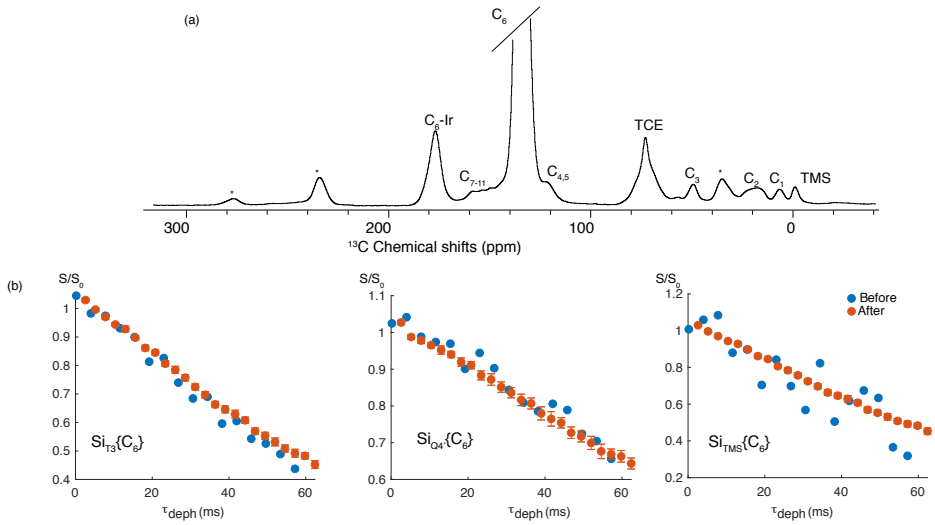

Figure 4.24: 1D ^{13}C CPMAS spectrum of post-catalysis Mat(1)-NHC-Ir material. No solvent suppression was applied. (b)^{29}Si-{^{13}C$_6$} FS-REDOR experimental data and the error bars measured on this material (red dots). The data measured on the same material prior to catalysis are superimposed for comparison (blue dots).

The Mat-NHC-Ir material was investigated by DNP SENS after the catalytic conversion of trans-stilbene under hydrogenation conditions. The COD ligand, when present, is expected to detach during the first catalytic cycle, and to transform in presence of H_2 into cyclooctane, so as the Ir metal center is able to coordinate the reagents that undergo the catalytic transformation. Thus, the COD ligand should be absent from the coordination sphere of the Ir center after catalytic reaction. Figure 4.24 shows DNP SENS data recorded on the Mat-NHC-Ir material recovered after the catalytic cycle, supposedly free of COD ligands. Figure 4.24-(a) shows the 1D ^{13}C spectrum of the post-catalysis Mat(1)-NHC-Ir material. A proton enhancement of 15 was achieved. The overall slope of the ^{29}Si-{^{13}C$_6$} FS-REDOR curves is very similar to those recorded on the same material before the catalytic reaction. In particular no modulation is observed that would suggest a close proximity between the C_6 carbene and the Q_4' site, and thus between the C_6 carbene and the oxygen atom of the $Si_{Q4'}$-O-Si_{TMS} bond. Thus, after the catalytic reaction, the iridium center must be coordinated by other oxygen atoms or by the residual olefin introduced in excess to make sure we detach all the COD ligands from the metal center. EXAFS data would be useful to get more insights into the coordination sphere of the reacted material. Experimental details on the FS-REDOR can be found in Table S3 in the Appendix.

4.7 Additional (inconclusive) experimental DNP SENS data

4.7.1 DNP SENS of a C_6 ^{13}C-labelled Pt-NHC material

DNP SENS studies were performed on a Pt-NHC material, where a ^{13}C probe nuclei had been introduced at the C_6 carbene position. The material was provided by the group of C. Copéret.

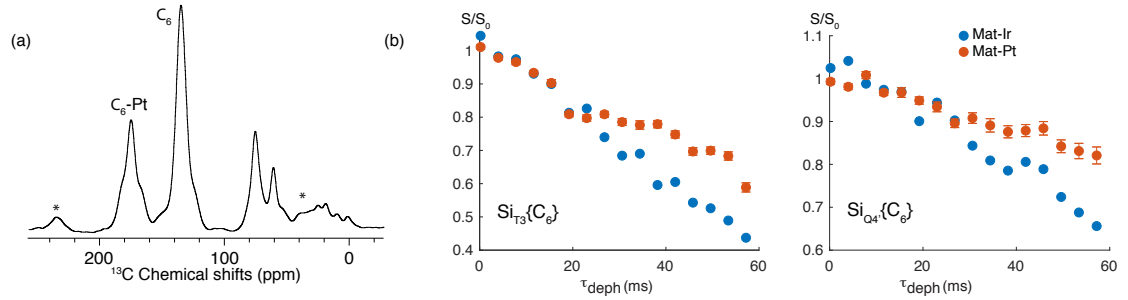

Figure 4.25: (a) 1D ^{13}C CPMAS spectrum of Mat-NHC-Pt material. Solvent suppression was applied. (b) ^{29}Si- $\{^{13}C_6\}$ FS-REDOR experimental data and the corresponding error bars measured on this material (red dots). The data measured on the Mat(1)-NHC-Ir material are superimposed for comparison (blue dots).

This study was intended to confirm the presence or not in the metal coordination sphere of the oxygen atom lying between the Si_{TMS} and $Si_{Q4'}$ silicons, as suggested by the structural model published by Berruyer *et al.* Such a labeling did not exist in this former investigation, and no structural constraint existed to orient the imidazole ring. Although we did not carry out a full 3D structure determination, the ^{29}Si-$\{^{13}C_6\}$ FS-REDOR experiments (Figure 4.25-(b)) suggest that the platinum atom is stabilized by other surface oxygens as described below.

Figure 4.25-(a) shows the 1D ^{13}C spectrum that clearly highlights the fact that the conversion from the imidazolium precursor to the iridium complex is not complete, a fact that was not taken into account in the structural study by Berruyer *et al.* The dephasing for the Pt-NHC complex is slower than for the Ir-NHC and does not agree with a structure where the Pt would be coordinated by the oxygen between Si_{TMS} and $Si_{Q4'}$. We note that this material is also prepared from a $Pt(COD)Cl_2$ and that, therefore, the presence of residual COD ligands cannot be excluded. An EXAFS study was not carried out on this new material. Experimental details on the FS-REDOR can be found in Table S3 in the Appendix.

4.7.2 DNP SENS of Mat(1)-NHC-Ir formulated with bCTbK

Finally, in order to evaluate the influence of the radical penetration into the porous channels, the FS REDOR experiments were carried out on the Mat(1)-NHC-Ir material impregnated with a solution of bCTbK [51]. This polarizing agent is of significantly smaller size than TEKPol and as discussed in section 4.2, is expected to penetrate the channels, leading to a strong but uniform paramagnetic bleaching along the length or the pore. Berruyer *et al.* estimated that around 80 % of the surface species were invisible with this radical [223]. We previously made the hypothesis that the Ir species without the COD ligand could possibly escape detection if they were located at the pore entrance where the concentration of TEKPol is expected to be high. Such species could be possibly detected with a small-sized radical. Figure 4.26 shows FS-REDOR experiments conducted on a Mat(1)-NHC-Ir sample formulated with a polarizing solution containing 16 mM of bCTbK. However, no major difference was observed with respect to experiments carried out on the same material impregnated with the TEKPol solution. Experimental details on the FS-REDOR can be found in Table S3 in the Appendix.

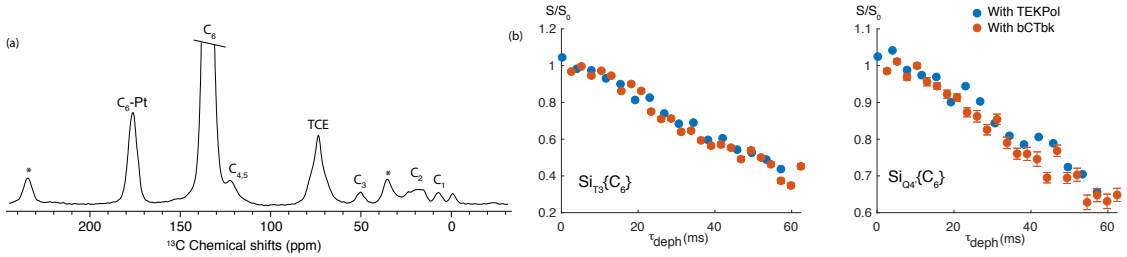

Figure 4.26: (a) 1D ^{13}C CPMAS spectrum of Mat-NHC-Ir material with bCTbK as a polarizing agent. No Solvent suppression was applied. (b) ^{29}Si- $\{^{13}C_6\}$ FS-REDOR experimental data measured on the Mat(1)-NHC-Ir material impregnated with a bCTbK solution(red dots). The data measured on the same Mat(1)-NHC-Ir material impregnated with a TEKPol solution are superimposed for comparison (blue dots).

4.8 Conclusion

In conclusion, we have shown that the imidazolium precursor ligand was only partially converted into the Ag-NHC intermediate and to the Ir-NHC complex, which resulted in a mixture of different surface species. Dedicated NMR strategies, combined with specific ^{15}N and ^{13}C labeling schemes, were implemented to overcome this challenge and get access to targeted structural insights on a surface containing multiple well-defined sites. In particular, the implementation of conventional and selective REDOR experiments allowed the measurement of a set of long-range structural constraints, namely 10 for the imidazolium precursor, and 7 for the Ag-NHC and Ir-NHC complexes, that were used to reconstruct their 3D structure. The results showed that while the precursor is folded back onto the surface and the silver intermediate exhibits a rather large distribution of conformations, the Ir-NHC complex adopts a well-defined structure, with an average RMSD in the positions of the ligand of 0.89 Å. While we were expecting to prove the presence of secondary interactions with the surface that would stabilize the complex (i.e. demonstrate the presence of surface oxygen atoms in the coordination sphere of the iridium site), we obtained a 3D where the Ir atom is pointing towards the interior of the porous channel. In agreement with EXAFS data and chemical analysis that clearly suggest the presence of residual cyclooctadiene (COD) ligands in the hybrid material, a structure was proposed where the Ir metal center is still stabilized by this latter group. Data recorded after the catalytic reaction did not allow one to evidence the presence of surface-metal interactions.

Chapter 5

Surface Structure of Platinum Single-Sites Determined by ^{195}Pt DNP-SENS and Fast MAS Solid-State NMR Spectroscopy

5.1 Introduction

In the previous chapter, the surface structure of an Iridium-based catalyst was investigated by probing the conformation of the organic ligands surrounding the metal center and their proximity to the surface. The NMR signature of the metal center itself, if it was accessible, would also represent a valuable structural probe to characterize single-site organometallic catalysts, providing access to the electronic environment and molecular symmetry of the immobilized complex from the perspective of the metal center. NMR studies of metal centers in heterogeneous catalysts remain however scarce [233–235]. This is because the NMR-active isotopes of metal nuclei (e.g., ^{183}W, ^{95}Mo, ^{91}Zr, ^{195}Pt, ^{93}Nb ...) are often challenging NMR probes (very low sensitivity and/or natural abundance, of significant chemical shift anisotropy and/or of large quadrupolar moment), which adds to the low concentration of active sites. The sensitivity gain provided by DNP opens new windows of opportunities to observe the NMR signals of some of these metal centers when diluted on a surface. Pruski and co-workers reported DNP enhanced ^{195}Pt NMR spectra of atomic Pt species supported within the pores of metal-organic frameworks [117] and of bipodal Pt^{4+} sites on silica stabilized by the methylcyclopentadienyl and methyl ligands [127]. More recently, Amoureux and co-workers applied DNP SENS to record the ^{95}Mo NMR signature of titania-supported MoO_3 [82].

In this chapter, we will summarize our efforts at elucidating the surface structure of well-defined platinum complex by ^{195}Pt NMR. Platinum is an important element used in catalysis, finding applications in numerous chemical processes. While typically used in the form of nanoparticles, Pt has recently been proposed to also participate in catalytic reactions when dispersed in the form of single-atom alloys or single-atom catalysts (Figure 5.1-(A)). While isolation of Pt sites may be confirmed by atomically resolved microscopy, understanding the molecular and electronic structure of such isolated sites remains a major challenge in catalysis. In this work we investigated the structure of isolated Pt sites, obtained via Surface Organometallic Chemistry (SOMC) by grafting the molecular precursor (COD)Pt[OSi(O^{t}Bu)$_3$]$_2$ (1,COD = 1,5-cyclooctadiene) on partially dehydroxylated silica at 700°C (**1@SiO$_2$**, Figure 5.1-(B)). The preparation of this complex had been previously reported in reference [236]. This material was used as a prototypical example of a highly dispersed metal site with 1 Pt site/ nm^2, relevant to single-site or single-atom catalysts.

5.2 NMR methods

^{195}Pt solid-state NMR spectroscopy provide valuable information on the local chemical environment and electronic structure of Pt centers as the parameters of the chemical shift tensor depend on the identity and symmetry of the ligands. However, the low sensitivity of ^{195}Pt NMR associated with sparse metal surface sites makes the NMR characterization of the local environment of Pt metal centers on surfaces extremely challenging. Although ^{195}Pt is a spin-1/2 nucleus with a moderate Larmor frequency (resonance frequency of 85.896 MHz at 9.4 T) and natural abundance of 33 %, ^{195}Pt SSNMR spectra are often severely broadened by chemical shift anisotropy (CSA). Thus, square planar Pt complexes usually give rise to wideline ^{195}Pt solid-state NMR spectra covering several hundreds of kHz since the span is often larger than 7000 ppm [237]. This results in poor sensitivity. Several NMR approaches have been proposed to overcome this sensitivity limitation. First, Schurko and co-workers have reported wideband excitation techniques such as BRoadband Adiabatic Inversion cross polarization (BRAIN-CP) [238] and Wideband Uniform-Rate Smooth-

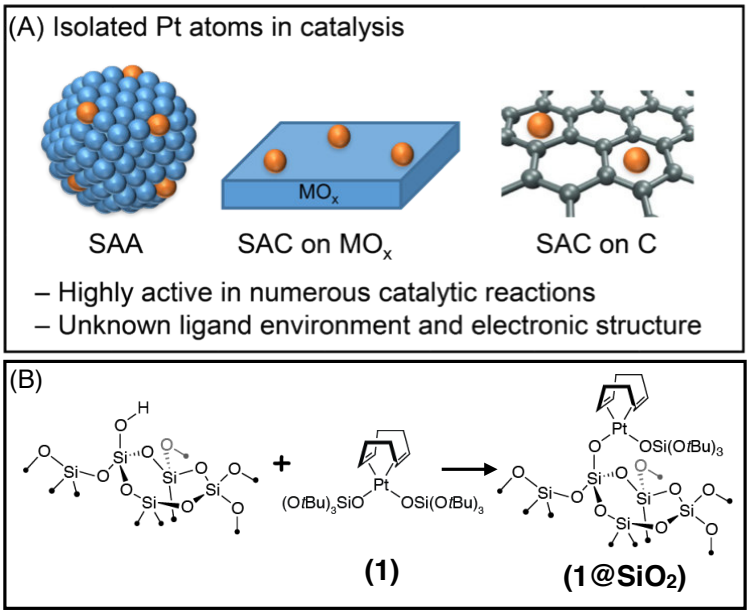

Figure 5.1: (A) Schematic representation of Pt isolated sites used in catalysis in the form of so-called single atom alloy (SAA) and single atom catalysts (SAC) on metal oxides or carbon-based materials. (B) Schematic structure of the Pt complex that will be investigated in this study. The surface complex was obtained by grafting the molecular precursor (COD)Pt[OSi(O^{t}Bu)$_3$]$_2$ on dehydroxylated silica.

Truncation (WURST) based Carr-Purcell-Meiboom-Gill echo-train acquisition (WCPMG) [239], an approach called "Ultra-Wideline NMR" that allows static wideline ^{195}Pt SSNMR spectra to be acquired with improved sensitivity. Second, the sensitivity of conventional solid-state NMR spectroscopy can also be enhanced using fast magic angle spinning (MAS) and proton detection techniques. Notably, it has been shown that fast MAS ^{1}H-^{195}Pt Dipolar Heteronuclear Multiple Quantum Coherence spectroscopy (D-HMQC) enabled the rapid determination of ^{195}Pt isotropic chemical shifts and/or acquisition of spinning sideband manifolds [240–243]. Here, we jointly applied DNP enhanced static BRAIN-CP-WCPMG methods and room temperature proton-detected NMR spectroscopy under fast MAS to obtain the ^{195}Pt solid-state NMR spectra of **1@SiO$_2$**. In this section we will review the different NMR techniques that were implemented.

5.2.1 Static Ultra-Wideline solid-state NMR spectroscopy

Conventional NMR experiments based on hard rectangular pulses cannot detect wideline patterns ranging from 250 kHz to tens of MHz, due to limited bandwidth. These wideline patterns are found for nuclei having extremely large CSA and/or quadrupolar interactions, or experiencing hyperfine couplings with unpaired electrons. ^{195}Pt falls in the first category, having very large CSA parameters like other spin I = 1/2 heavy metal atoms such as ^{119}Sn, ^{199}Hg and ^{207}Pb. Several approaches were developed to acquire sensitive ultra-wideline spectra as described in a recent review by R. W. Schurko [239] and that will be briefly summarized below:

Stepped acquisitions : In order to cover the full bandwidth, a wideline spectrum can first be acquired stepwise. In the early 80s, Slichter and co-workers reported the acquisition of ^{195}Pt NMR spectra of platinum nanoparticles by varying the magnetic field [244, 244, 245]. Later, Bastow *et al.* recorded ^{91}Zr NMR by fixing the field and varying the transmitter frequency. The probe was

retuned at each step, and the intensity of spin echo experiments were plotted as a function of the transmitter frequency [246–248]. Massiot *et al.* introduced the "Variable-Offset Cumulative Spectra" (VOCS) technique in 1995 to improve spectral resolution. The transmitter frequency is also swept across the wideline pattern, but each individual FID is Fourier Transformed and the sub-spectra are co-added [249]. This approach is limited to static conditions as it leads to distorted patterns under MAS.

CPMG acquisition : In this experiment (Figure 5.2-(A)), a series of echoes are collected, and the echo train Fourier Transform yields a frequency domain spectrum. The CPMG spectrum is composed of spikelets separated in frequency by the inverse of time separating the echoes, whose envelope reflects the static line shape. This approach is effective for nuclei having long T_2' and can be applied to spin $I = 1/2$ or to quadrupolar nuclei. The first application on quadrupolar nuclei was reported by Larson *et al.* in 1997 to improve the sensitivity of ^{87}Rb and ^{59}Co NMR in molecular complexes (with enhancement factors of up to 30) [250].

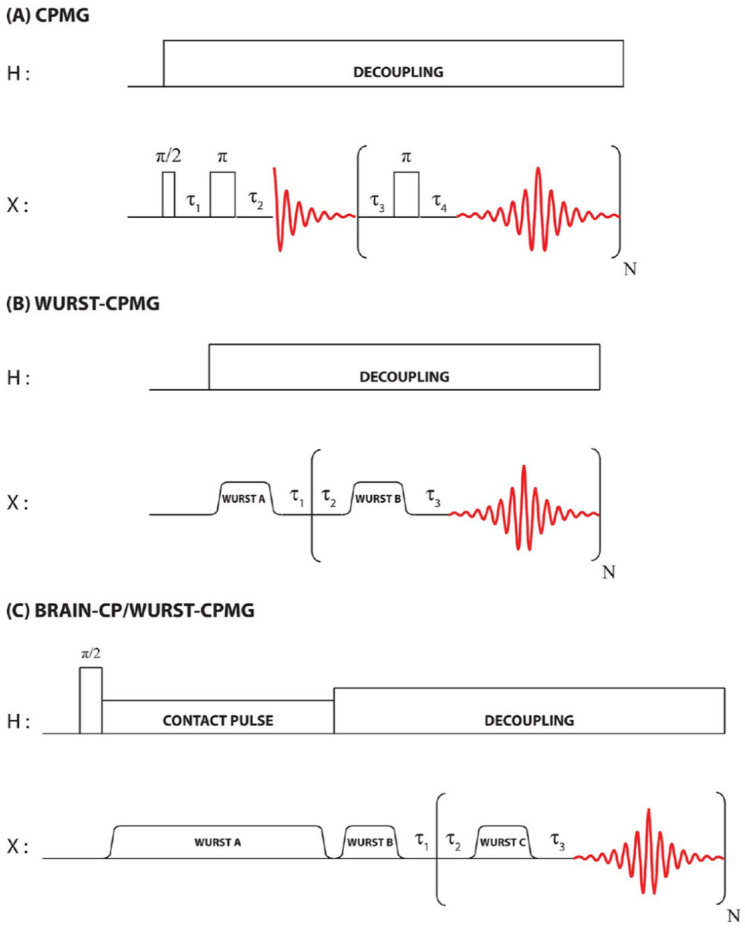

Figure 5.2: (A) CPMG pulse sequence. (B) WURST-CPMG pulse sequence for broad excitations and (C) BRAIN-CP with WURST-CPMG pulse sequence. Reprinted with permission from [239]. Copyright 2020 ACS.

WURST-CPMG experiment : In order to obtain a uniform excitation and refocusing over a broad powder pattern, CPMG acquisition can be combined with the implementation of chirp pulses, such as those belonging to the WURST (Wideband Uniform-Rate Smooth-Truncation) family. The WURST pulses display a simple amplitude and complex phase modulation that generates

an effective frequency sweep over a broad spectral range [251]. In 2008, Schurko and co-workers proposed to combine WURST pulses with CPMG acquisition (Figure 5.2-(B)) to obtain a uniform, and broadband excitation with the benefits of enhanced sensitivity [252]. This approach can be associated with the VOCS technique to observe the NMR signature of ^{35}Cl and ^{65}Cu nuclei of extremely broad powder patterns [253].

BRAIN-CP : This approach may be advantageously combined with cross-polarization (CP) from protons, in particular for nuclei having long longitudinal relaxation time T_1. Stepped CP-CPMG experiments were initially implemented to acquire UWNMR spectra of nuclei with large CSAs such as ^{109}Ag, ^{113}Cd, ^{195}Pt [254, 255]. However, due to the limited bandwidth of the CP pulses, a large number of spectra have to be collected. Schurko and co-workers introduced in 2012 a broadband version of the CP experiment called BRoadband Adiabatic INversion (BRAIN) CP (Figure 5.2-(C)) [256]. In this experiment, frequency swept WURST inversion pulse is applied on the X-channel during the CP contact time, which creates a X polarization along the -z axis. A second WURST conversion pulse is applied to rotate this polarization into the transverse plane. Finally, the acquisition is done using train WURST-CPMG pulse train. A wide range of ultra-wideline NMR nuclei were observed using this methodology, such as ^{119}Sn, ^{207}Pb, ^{119}Hg, ^{195}Pt, ^{39}K or ^{14}N [239].
All these approaches are static methods and can be combined with DNP as illustrated for example by Hirsch and co-workers with the acquisition of DNP enhanced ^{1}H-^{35}Cl BRAIN-CP spectra of active pharmaceutical ingredients [119]. Under MAS, alternative approaches must be considered.

5.2.2 Proton-detected HMQC NMR spectroscopy

Rossini and co-workers have recently shown that ^{1}H-^{195}Pt dipolar heteronuclear multiple quantum coherence spectroscopy (D-HMQC) enabled the rapid determination of ^{195}Pt isotropic chemical shifts and/or acquisition of spinning sideband manifolds [257, 258]. The pulse sequence for the D-HMQC experiment based on the classical solution NMR HMQC experiment, is depicted in Figure 5.3-(A). The sequence starts with a 90° proton pulse. During the first evolution period, the proton magnetization evolves under ^{195}Pt-^{1}H heteronuclear dipolar couplings that are reintroduced by the $SR4_2^1$ symmetry-based recoupling scheme [259]. A 90° ^{195}Pt pulse transforms the antiphase proton magnetization into multiple-quantum coherences that evolve during t_1 under the sole effect of the ^{195}Pt chemical shift. A second evolution period under $SR4_2^1$ recoupling enables to reconvert the multiple-quantum coherences into observable proton magnetization. Proton detection provides a large sensitivity gain. Two acquisition modes can be considered in the indirect dimension: i) a constant-time version where t_1 is incremented by any value during a fixed period of time equal to a multiple of the rotor period as shown in Figure 5.3-(A). This yields the spinning side-band manifold in ω_1. ii) a rotor-synchronized version, where the t_1 increment is set to the rotor period (or the indirect spectral width to the MAS frequency). All the spinning side-bands are folded onto the isotropic center-band, which provides enhanced sensitivity.

Here we used the TONE D-HMQC pulse sequence, a variant of the conventional HMQC experiment recently introduced by Venkatesh and co-workers [241] and that eliminates t_1-noise from D-HMQC spectra. This is achieved by inserting 180° ^{1}H and ^{195}Pt pulse during the excitation and reconversion periods of multiple-quantum coherences, that refocuse both CSA interactions, and by applying a Lee-Goldburg (LG) spin-lock field during the indirect evolution time. The uncorrelated proton magnetization will dephase around the LG effective field, while the correlated magnetization

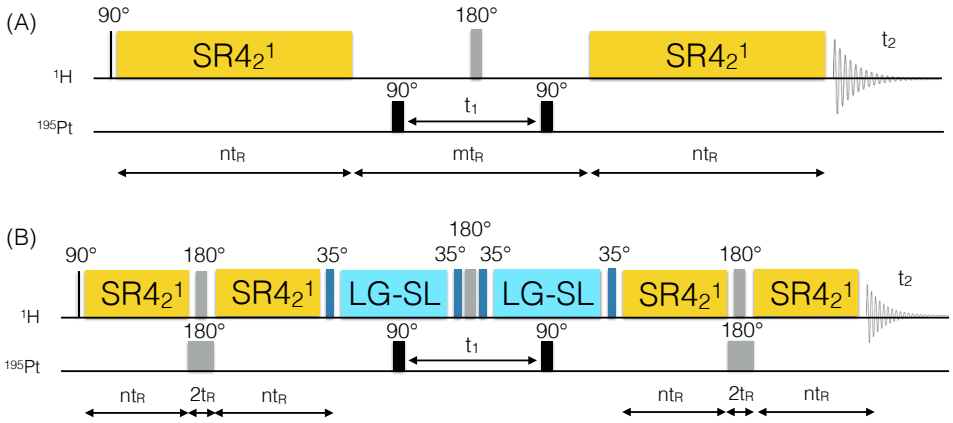

Figure 5.3: (A) Pulse scheme of the constant-time D-HMQC experiment [260]. (B) Pulse sequence of the TONE D-HMQC experiment that was used in this study [241].

will be spin-locked during the t_1 period, which additionally reduces relaxation losses. This version provides cleaner spectra, with reduced noise.

5.3 Static wide-line ^{195}Pt NMR spectra

5.3.1 Preliminary experiments on model molecular complexes

The ^{195}Pt NMR spectra of two molecular complexes were recorded as preliminary experiments to ensure that the calibration of the BRAIN-CP-WCPMG experiment was appropriate. Figure 5.4 shows the static ^{195}Pt NMR of (DMSO)$PtCl_2$ (A) and (COD)$PtCl_2$ (B). The ^{195}Pt NMR

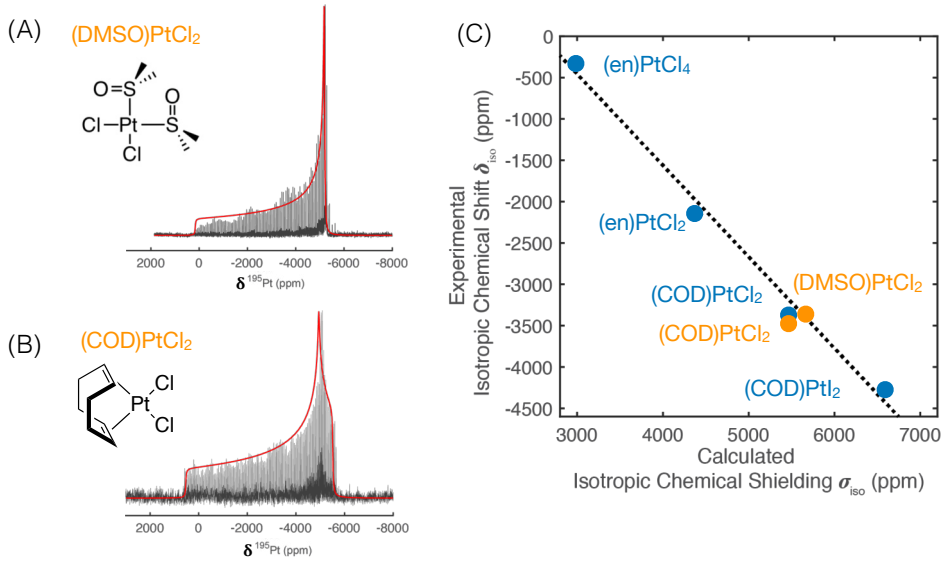

Figure 5.4: (A) and (B) Static ^{195}Pt NMR spectra of the molecular complexes (DMSO)$PtCl_2$ (A) and (COD)$PtCl_2$ (B). (C) Comparison between calculated and experimentally measure isotropic chemical shifts. The blue dots correspond a comparison with experimental values from literature (from reference [261]). The orange dots show the agreement between the measured values extracted from the NMR spectra shown in (A) and (B), and the calculations. Courtesy of Christopher Gordon.

spectra were acquired with the BRAIN-CP-WCPMG pulse sequence in combination with the VOCS technique to cover the full spectral width. These experiments were recorded on a 500 MHz wide bore Bruker AVANCE III Bruker NMR spectrometer using a 4 mm MAS probe. The samples were packed in the rotor in a glove box. In all the experiments reported here, the ^{195}Pt chemical shift has been referenced to an aqueous solution of K_2PtCl_4. In both cases, ^{1}H excitation pulse of 5 μs was used followed by a 10 ms contact time, with a WURST A swept over 400 kHz. For detection 50 μs WURST B and C pulse were swept over 500 kHz with a spikelet separation of 5 kHz. A recycle delay of 2 s was used and 2048 scans were accumulated for each slice. A total of five offsets were used for the (DMSO)$PtCl_2$ (A) and (COD)$PtCl_2$ complexes. The spectra were fitted to extract the isotropic chemical shift and CSA tensor parameters using DMfit [262].
The structure of four additional molecular complexes, whose CSA parameters were available in literature [263, 264] were also optimized by DFT calculations. The calculated isotropic shifts are plotted against the experimental values in Figure 5.4-(C) and corresponds to the blue points. The linear correlation between the experimental and calculated values allows one to validate the DFT method. For the (COD)$PtCl_2$ complex, the experimental value measured by us (-3500 ppm, orange dot) agree with previously reported data. For the (DMSO)$PtCl_2$, these values (-3400 ppm) match the calculated ones. Overall, this preliminary study allowed the validation of both the experimental and DFT calculation approaches.

5.3.2 ^{195}Pt NMR spectrum of (COD)Pt[OSi(O^{t}Bu)$_3$]$_2$

The static ^{195}Pt NMR spectrum of the molecular complex COD)Pt[OSi(O^{t}Bu)$_3$]$_2$ is presented in Figure 5.5. It was acquired with the same experimental conditions as the spectra of Figure 5.4.

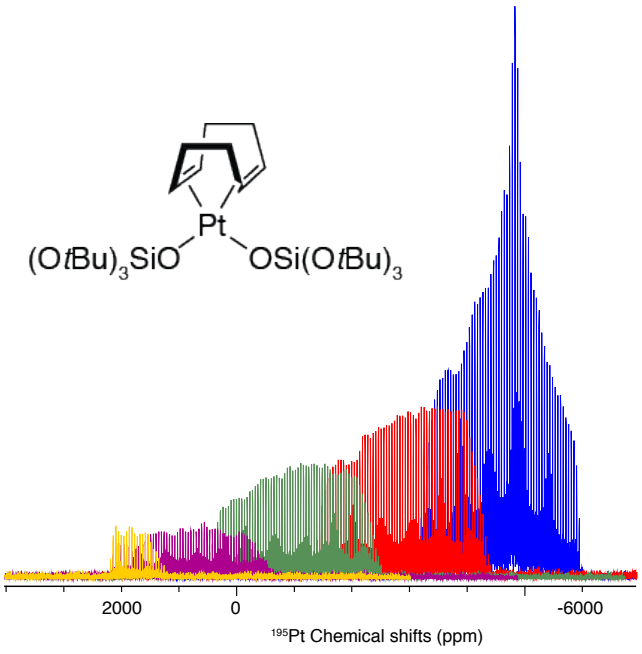

Figure 5.5: One-dimensional ^{195}Pt UWNMR spectrum of (COD)Pt[OSi(O^{t}Bu)$_3$]$_2$. A recycle delay of 2 s was used and 35840 scans were accumulated for each of the individual spectrum.

5.3.3 ^{195}Pt NMR spectrum of (COD)Pt[OSi(O^{t}Bu)$_3$]$_2$@SiO$_2$

The structure of the (COD)Pt[OSi(O^{t}Bu)$_3$]$_2$@SiO$_2$ surface complex was probed by DNP SENS. The complex is supported on silica nanoparticles of relatively low surface area (200 m^2/g) and the loading is lower than 3 %. A ^{1}95Pt NMR spectrum could by no case be obtained by conventional NMR. The sample was impregnated with 16 mM of TEKPol in TCE, and packed into a 3.2 mm sapphire rotor. The one-dimensional ^{29}Si and ^{13}C spectra were first recorded under MAS as shown

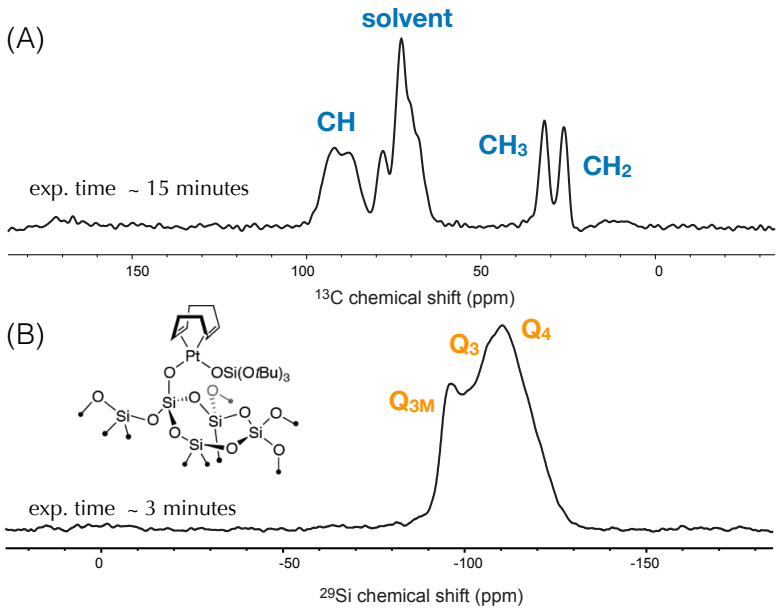

Figure 5.6: One-dimensional ^{1}3C (A) and ^{2}9Si (B) DNP SENS spectra of (COD)Pt[OSi(O^{t}Bu)$_3$]$_2$@SiO$_2$. The spectra were recorded at 9.4 T at a spinning frequency of 8 kHz. A solvent suppression method was applied for the carbon-13 spectrum. The total number of scans were 128 in (A) and (B) respectively.

in Figure 5.6. A ^{29}Si enhancement of 80 was measured. All the expected resonances could be observed. The presence of two resonances for the CH carbons suggests that the four CH groups of the COD ligand are not fully equivalent.

Figure 5.7 shows the static DNP enhanced ^{195}Pt spectrum of (COD)Pt[OSi(O^{t}Bu)$_3$]$_2$@SiO$_2$ with the BRAIN-CP-WCPMG pulse sequence described previously. A static proton enhancement of 110 was measured. The ^{1}H excitation pulse of 2.5 us was used followed by with a 10 ms contact time, with a WURST-A pulse swept over 400 kHz on ^{195}Pt. For detection 50 us WURST B and C pulses were swept over 500 kHz with a spikelet separation of 5 kHz. Variable offset accumulation was used and seven different offset frequencies were acquired. The total acquisition time was over 5 days. We note that the static ^{195}Pt spectra of the molecular and surface complexes have a similar span (of around 8000 ppm). We also note here that the interpretation of static spectra of powdered samples is challenging if there are overlapping powder patterns arising from multiple sites. We know from the crystal structure of the molecular complex that two molecules are present per unit cell. However, two distinct CSA patterns cannot be distinguished from the stationary spectrum of Figure 5.5. Similarly, the interpretation of the static spectrum of the grafted complex is difficult if we want to consider any distribution of surface structures. In that sense, MAS experiments that resolve chemical shifts would be preferable, if amenable for surface complexes. As will be described in the following, a quantitative analysis of the static ^{195}Pt spectra was done using the isotropic chemical shift values extracted from proton-detected MAS NMR experiments.

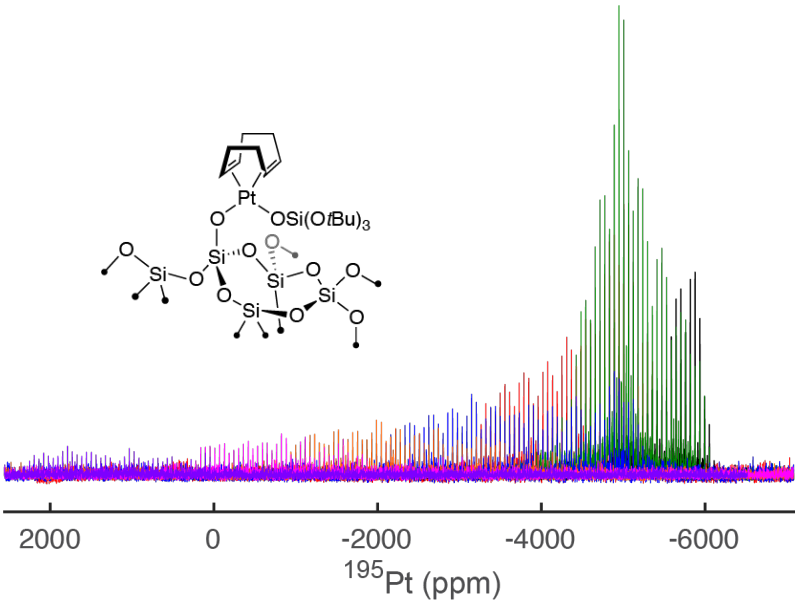

Figure 5.7: One-dimensional ^{195}Pt UWNMR spectrum of (COD)Pt[OSi(O^{t}Bu)$_3$]$_2$@SiO$_2$. A recycle delay of 7 s was used.

5.4 Proton detected ^{195}Pt NMR spectra under fast MAS

Short ^{1}H T$_1$ of 0.7 and 1.1 s in **1** and **1@SiO$_2$**, respectively, make D-HMQC experiments favorable for the indirect detection of ^{195}Pt solid-state NMR spectra. Although constant-time ^{1}H-^{195}Pt D-HMQC can be utilized to obtain the full sideband manifold of the ^{195}Pt CSA pattern. The sensitivity of ^{1}H-^{195}Pt D-HMQC spectra obtained with rotor-synchronous t$_1$-intervals is approximately 10-20 times higher because of spectral aliasing of all intensity into a single sideband. The isotropic ^{195}Pt chemical shift can be precisely determined by obtaining rotor-synchronized 2D ^{1}H-^{195}Pt D-HMQC spectra with different MAS frequencies.

Figures 5.8 (A) and (B) show the 2D rotor-synchronized ^{1}H-{^{195}Pt} TONE D-HMQC spectra of **1** and **1@SiO$_2$** respectively recorded at two different spinning frequencies, while Figures 5.8 (C) and (D) show the corresponding ^{195}Pt traces extracted along the indirect dimension. The 2D spectra were obtained within reasonable experimental times of ca. 13 minutes and 10.5 hours for **1** and **1@SiO$_2$**, respectively. The presence of two signals in the ^{195}Pt spectra of **1** (Figure 5.8 (A) and (C) is consistent with the presence of two molecules in the asymmetric unit of its crystal structure. The difference in isotropic shifts between the two sites likely arises from slight differences in local bond angles. Upon varying the MAS frequency from 50 to 51 kHz, it is observed that both signals shift positively by 2 kHz. This must mean that the observed peaks correspond to the second spinning sidebands from the isotropic shift in the positive direction. Since spinning sidebands appear exactly at integer multiples of the MAS frequency, the positions of other sidebands or center band are easily calculated. In case of **1**, the isotropic shifts of the two ^{195}Pt signals are precisely determined to be -2867 and -2838 ppm. Figure 5.8-(D) shows ^{195}Pt SSNMR spectra of **1@SiO$_2$** extracted from 2D ^{1}H-{^{195}Pt} TONE D-HMQC spectra obtained at 55 and 45 kHz MAS frequencies. The ^{195}Pt SSNMR spectra of **1@SiO$_2$** show broad peaks that can be fit to Gaussian functions, indicating there is a distribution of ^{195}Pt isotropic chemical shifts. The distribution in isotropic shifts is not surprising and likely reflects the inherently disordered nature

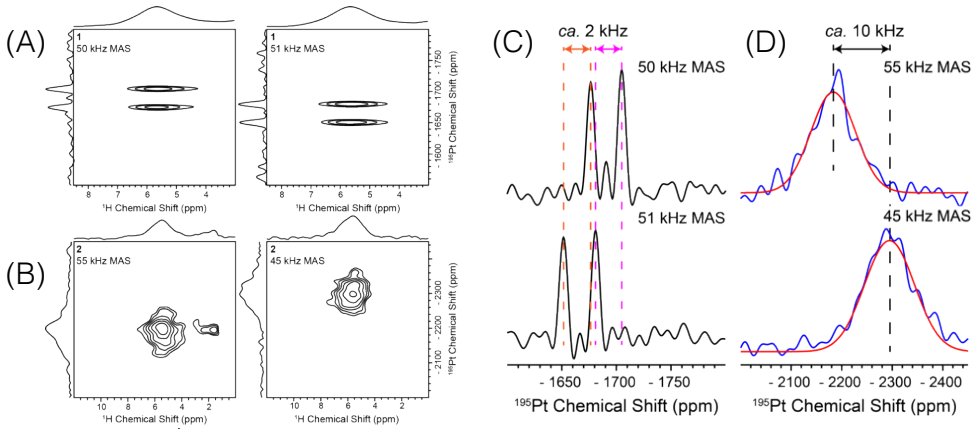

Figure 5.8: 2D ^{1}H-{^{195}Pt} HETCOR spectra of **1** (A) and **1@SiO$_2$** (B) acquired with TONE D-HMQC-4. ^{195}Pt SSNMR spectra extracted from rotor-synchronized 2D ^{1}H-{^{195}Pt} TONE D-HMQC-4 spectra of (C) **1** and (D) **1@SiO$_2$**.

of the silica surface, which will result in a range of bond lengths and angles. As the ^{195}Pt signal of **1@SiO$_2$** moved by 10 kHz frequency upon varying MAS from 55 to 45 kHz, the observed signal must correspond to the first sideband and the center of the Gaussian isotropic shift distribution is determined to be -2819 ppm.

Using the ^{195}Pt isotropic shifts of **1@SiO$_2$** from the fast MAS measurements and the observed span (Ω) of the static spectrum (ca. 8150 ppm), the skew of the CS tensor (κ) was determined to be -0.73 for both ^{195}Pt sites in **1** (green and brown traces, Figure 5.9-(A)). The sum of the two simulations is shown to fit the experimental spectrum accurately (red trace, Figure 5.9-(A)). The Ω and κ values derived from this fitting procedure were further confirmed by comparing a simulation of the sideband manifold obtained with a constant-time TONE D-HMQC experiment recorded at 50 kHz MAS. Indeed, fast MAS enables the resolution of the two sets of sidebands and confirms that the two ^{195}Pt sites with isotropic shifts of -2867 and -2838 ppm display the same CSA parameters (Ω = 8150 ppm and κ = -0.73) as shown n Figure 5.9-(B). Figure 5.9-(C) shows a DFT calculated structure of **1** and the predicted ^{195}Pt CS tensor; simulations based on the DFT parameters (δ_{iso} = -2959 ppm, Ω = 6703 ppm and κ = -0.96) agree reasonably with the experimental ^{195}Pt NMR spectra (pink traces, Figure 5.9-(A) and (B)), considering the large CSA and the high sensitivity of ^{195}Pt chemical shift to the ligand environment. Extracting the mean isotropic chemical shift of the Gaussian distribution of ^{195}Pt isotropic shifts measured for **1@SiO$_2$** (-2819 ppm) and using the width of the distribution as a starting parameter, fitting of the static DNP-SENS spectrum with 8 kHz of Gaussian broadening gave Ω and κ values of 8412 ppm and -0.77, respectively. The similarity of the fitted CSA parameters of **1@SiO$_2$** to those of **1** is consistent with a similar Pt chemical environment and with the proposed structure of the surface-bound Pt(II) complex (Figure 5.1).

Finally, although I was not involved in this part of the work, I briefly mentioned that ^{1}H-{^{195}Pt} Symmetry-based REDOR experiments [265] with SR4$^{1}_{2}$ heteronuclear dipolar recoupling were applied by the group of A. Rossini to measure the ^{1}H-^{195}Pt dipolar coupling constants and internuclear distances between the vinyl protons of the COD ligand and the Pt center in both **1** and **1@SiO$_2$**. The S-REDOR curve for **1** (Figure 5.10-(A)) was fit to a dipolar coupling of 1.4 kHz and a distance of 2.65 Å by minimizing the root mean square deviation (RMSD) between the

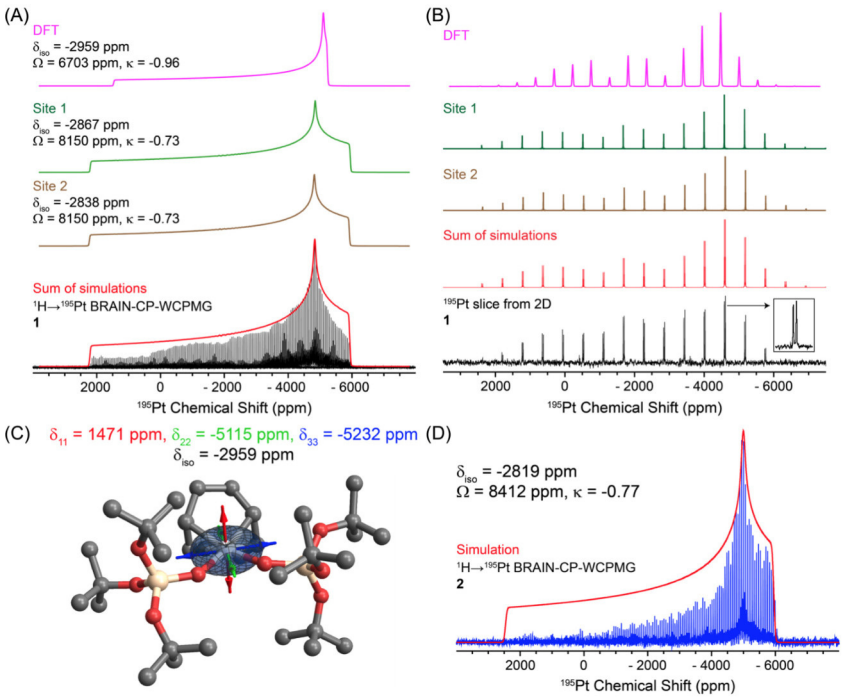

Figure 5.9: (A, black trace) Conventional ^{1}H-^{195}Pt BRAIN-CP-WCPMG spectrum of **1** at B_0 = 11.7 T. (B, black trace) ^{195}Pt MAS NMR spectra extracted from constant-time 2D ^{1}H-^{195}Pt TONE D-HMQC spectrum; inset shows the resolution of two signals. Analytical simulations (green and brown traces) corresponding to the two ^{195}Pt sites in **1** and (pink trace) a spectrum simulated with CSA parameters from the DFT calculation. (C) DFT optimized structure of **1** showing the principal components of the ^{195}Pt CS tensor; hydrogens are omitted for clarity. (D) DNP enhanced ^{1}H-^{195}Pt BRAIN-CP-WCPMG spectrum of **1@SiO$_2$** at B_0 = 9.4 T together with a single-site simulation was performed with Gaussian broadening to model the distribution in isotropic shifts observed in the synchronized TONE-D-HMQC experiment reported in Figure 5.3. A single-site simulation was performed with Gaussian broadening to model the distribution in isotropic shifts (red trace). Fitted CS tensor parameters are indicated.

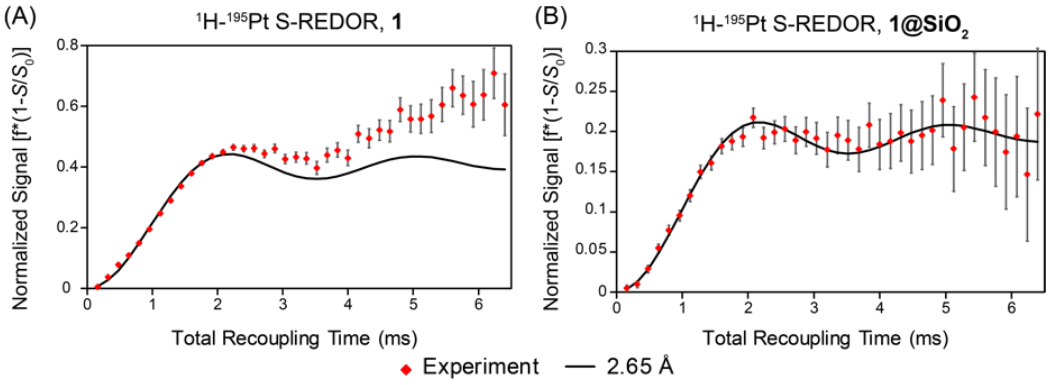

Figure 5.10: ^{1}H-^{195}Pt S-REDOR measurements on samples (A) **1** and (B) **1@SiO$_2$**. Experimental data points are plotted as red diamonds and SIMPSON numerical simulations as black lines. Experiments were performed at 50 kHz MAS and B_0 = 9.4 T.

fitted and experimental data points. Note that only experimental data up to 2 ms of recoupling were considered as additional dephasing of the ^{1}H signal is observed at longer recoupling durations

due to long-distance Pt-H contacts with Pt atoms in the adjacent molecules in the crystal lattice. However, the experimental S-REDOR curve for **1@SiO$_2$** (Figure 5.10-(B))can be fit precisely to a 2.65 Å with data points up to 6.4 ms of recoupling included in the RMSD analysis. The observation that the S-REDOR curve for **1@SiO$_2$** does not show increased dephasing at longer recoupling times is consistent with isolation of Pt sites on the silica surface; there should be a low probability of a second ^{195}Pt spin being found within a 5 Å radius from the vinyl hydrogen atom due to the 1 Pt site/nm^2 surface coverage. The measured Pt-H distances are in good agreement with the average Pt-H distance of 2.63 Å predicted for the DFT optimized structure of **1**. In both **1** and **1@SiO$_2$**, slower dephasing was also observed for the methyl groups at 1.2-1.4 ppm due to weaker Pt-H dipolar couplings. These measurements also confirm that the model proposed for the grafted complex in Figure 5.1 is the correct surface structure.

5.5 Conclusion

In conclusion, we reported the DNP-enhanced ^{195}Pt BRAIN-CP-WCPMG spectrum of a well-defined platinum complex grafted on a low-surface area material at low concentration. Fast MAS, proton-detected experiments were used to determine the isotropic shift of the ^{195}Pt surface complex and its distribution. These data were crucial to constrain the fit of ^{195}Pt static CSA pattern. The observation of a single Pt site in **1@SiO$_2$** with CSA parameters similar to the molecular precursor 1 suggests that the Pt site is well-defined in **1@SiO$_2$**, where the relatively narrow distribution of isotropic shifts is likely due to small variations in local bond angles associated with the presence of different local environments arising because of the amorphous surface structure of silica. This conclusion was validated by Pt-H distance measurements, which indicate that the local geometry of the Pt metal center is unchanged in the precursor and on the silica surface.

Importantly, while proton-detected experiments allowed one to record the spinning side-band manifold of the molecular precursor, this was not the case for the surface complex due to poor sensitivity. This highlights the relevance of the DNP-SENS approach applied here to overcome the issue of surface dilution, which in combination fast MAS proton-detected experiments, yielded here a quite detailed characterization of system that is a prototypical example of highly dispersed and isolated Pt sites. Other complexes are currently being investigated.

The longer-term perspective would consist in extracting structural features from surface ^{195}Pt spectra in combination with DFT calculations. An effort along these lines was done during my PhD thesis with the investigation by ^{195}Pt NMR of the Pt-NHC complex, previously mentioned in chapter 4 and whose structure was published by Berruyer *et al.* [42]. Figure 5.11-(A) shows the DNP-SENS ^{195}Pt BRAIN-CP-WCPMG spectrum of this surface complex. The sample was impregnated with 16 mM TEKPol in TCE and a static proton enhancement of 90 on the solvent was measured. The full UWNMR spectrum was acquired using 3 offsets over 2 days. Calculations of ^{195}Pt CSA parameters were performed by C. Gordon in Copéret's group on two model molecular complexes. A good agreement could not be achieved so far as shown in Figure 5.11-(B). However, we note that the agreement improves (reduced span) when including an oxygen atom in the coordination sphere of the Pt center. This would tend to confirm that the Pt is coordinated by oxygen atoms of the surface as suggested previously by Berruyer *et al.* [42]. Additional work is still needed to conclude this study.

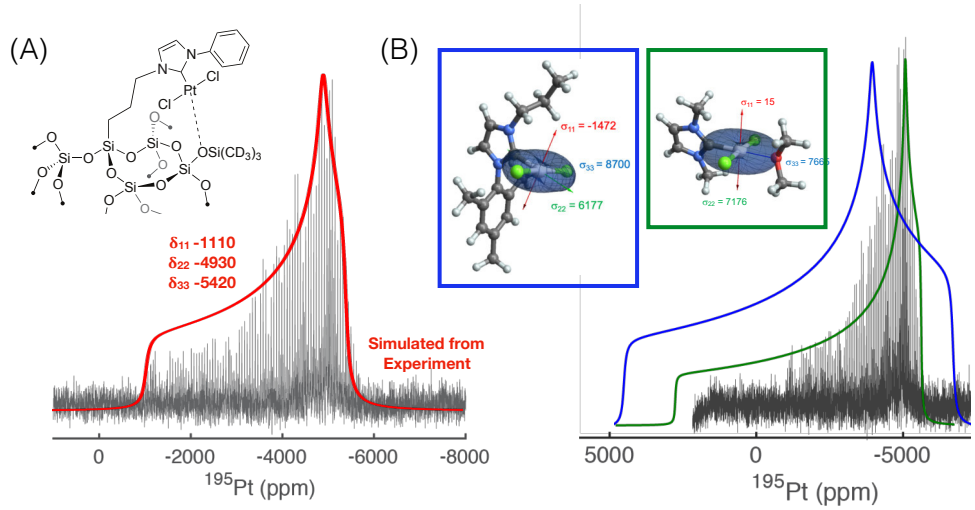

Figure 5.11: (A) ^{195}Pt UWNMR spectrum of the Pt-NHC surface complex obtained in 3 slices. A recycle delay of 4 s was used with 256 scans. The experimental conditions for the BRAIN-CP and the WURST shapes are the same as described in 5.3.1 . The red line corresponds to the simulated spectrum. (B) Results from DFT calculations performed in Copéret's group for two Pt molecular models. The blue and green lines correspond to calculated spectra from the models shown as insets.

Chapter 6

Structure Elucidation of Well-Defined Heterobimetallic Catalysts

6.1 Introduction

In previous chapters, we showed that solid-state NMR spectroscopy in combination with DNP is a unique tool to elucidate the three-dimensional structure of organometallic fragments anchored at the surface of a solid support. We implemented a methodology where internuclear distances were measured between pairs of low-gamma nuclei (^{13}C, ^{15}N and ^{29}Si) in chapter 4 and a strategy where the NMR signature of the metal center was directly probed in chapter 5. However, when the metal center is surrounded by hydrides as is the case in a variety of heterogeneous catalysts and catalytic intermediates, the NMR spectral signature of these nuclei also holds key structural information. In particular, as mentioned in the Chapter 3, proton multiple-quantum (MQ) NMR spectroscopy is a unique experimental approach that can be implemented to determine ("count") the number of hydrides around the metal. As proton has a high gyromagnetic ratio and is 100 % abundant, ^{1}H MQ spectra of dilute surface species including hydrides can be recorded in reasonable experimental times using conventional NMR, i.e. without the need of the amplification power provided by DNP. Several studies that exploit proton MQ NMR have been reported on a series of well-defined organometallic complexes as described in chapter 3. While proton ^{1}H DQ NMR spectroscopy has been employed to discriminate between mono- and di-hydride species [212], there is so far no example to our best knowledge where ^{1}H TQ spectroscopy has been constructively used to estimate the number of hydrides directly bound to the metal center. In this chapter, we will describe our efforts at implementing proton MQ NMR experiments on highly reactive multi-heteronuclear metallic complexes. We applied this methodology on Ta-Ir complexes that were the object of the PhD thesis of Sébastien Lasalle at C2P2 under the supervision of Dr Clément Camp and of Dr Chloé Thieuleux. Several complexes were investigated that were obtained from different synthetic routes. This approach was also applied for the structural characterization of new Hf complexes.

6.2 Tantalum/iridium hydrido complexes: a new class of active heterogeneous catalysts

A current frontier in organometallic chemistry is the cooperative activity between two distinct metal centers so as to induce new reactivity pathways and original transformations that would not be possible with monometallic species. [266–268] In particular, molecular edifices associating early (such as Ta) and late (such as Ir) transition metals and featuring a polar metal-metal interaction are particularly promising to promote the heterolytic cleavage of strong, unactivated apolar bonds (H-H, C-H, N≡N ...) and could open attractive opportunities for unprecedented reactivity in catalysis. [269–271] Catalytic applications of early/late hetero-binuclear metal complexes are however very limited to date, due to the difficulty of stabilizing the resulting edifices without using bulky ligands that will prevent a close approach of the substrates and in turn make catalysis inefficient. One strategy to overcome this limitation is to target early/late heterobimetallic systems with simple ligands, assembled through metal-metal bonds, in combination with Surface OrganoMetallic Chemistry (SOMC). Preparing such supported assemblies in a controlled manner requires however smart and targeted synthetic strategies so as to efficiently combine the two metal centers of different chemical properties on a single solid support. The methodologies classically employed for immobilizing Ta and Ir metals are indeed orthogonal. While Ta can be grafted directly onto the surface of an oxide material (e.g., for silica) via reaction with surface hydroxyl groups (e.g., the

silanols ≡Si-O-H), Ir atoms are generally grafted onto hybrid functionalized supports because the Ir-O bond weaker and leads to incomplete grafting or the formation of undesired metal nanoparticles. Thus, the type of supports conventionally used for iridium and tantalum are different, and as a result these metals cannot be easily combined using two independent monometallic precursors on a single support. To overcome this limitation, Lassalle and co-workers developed innovative modular synthetic approaches that are described below [272].

6.2.1 One-step synthesis

In the one-step synthesis approach described in this section, a robust molecular precursor featuring a Ta=Ir double bond to ensure proximity between the two metals is firstly prepared. Then Ta chemistry is applied to establish strong Ta-siloxide bonds with silicon oxide materials in order to anchor the Ta/Ir species at the silica surface and to ultimately obtain well-defined early/late heterobimetallic supported catalysts. This approach will be referred to as the one-step synthesis approach, since the bimetallic complex is introduced as one single molecular precursor. The one-step synthesis of the Ta-Ir bi-metallic complex is shown in Figure 6.1. One advantage of the approach implemented here is not only the possibility to access organometallic species with unprecedented structures that cannot be stabilized in solution, but also to prepare by surface chemistry new edifices that cannot be reached otherwise (here the bimetallic molecular complex leads to unwanted dimerization in solution, which prevents any subsequent chemical modification). Thus, Lassalle and co-workers explored the reactivity of the bimetallic Ta-Ir complex toward H_2 to prepare a new surface structure as shown in Figure 6.1-(b).

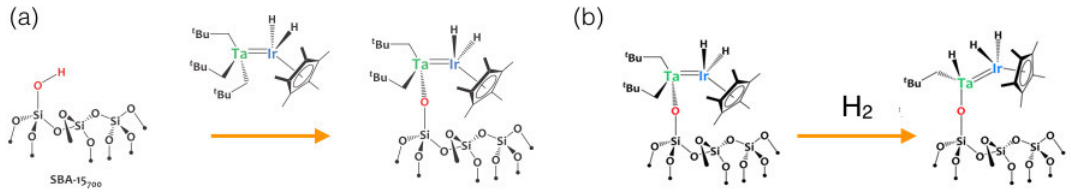

Figure 6.1: (a) One-step synthesis of the grafted Ta=Ir catalyst. A SBA-15 silica support is dehydroxylated under high-vacuum at 700 °C to yield a material featuring a low density of isolated surface hydroxyl groups (ca. 0.5 OH group per nm^2), required to ensure sites-isolation. The material is then treated with a pentane solution containing the molecular complex [$(CH_2^t$ Bu$)_3$Ta(Cp*IrH_2)]. (b) Hydrogenation and conversion of the bimetallic complex [≡SiOTa-$(CH_2^t$Bu$)_2$IrH_2(Cp*)] to [≡SiOTa$(CH_2^t$ Bu)H-IrH_2(Cp*)]. All the experimental details on the synthesis of these materials are reported in reference [272].

Characterization by IR spectroscopy

The two grafted materials before and after hydrogenation were characterized by Lassalle and co-workers using IR spectroscopy prior to the NMR experiments. Upon treatment of SBA-15 with a solution of the molecular complex, the characteristic sharp IR band at 3747 cm^{-1} corresponding to isolated surface silanols (data not reported here) disappears while new signals attributed to ν(C-H) stretches of the neopentyl and Cp* ligands at 2960-2860 cm^{-1} and signals assigned to ν(Ir-H) stretches at 2064 and 2037 cm^{-1} appear (Figure 6.2-(a), red spectrum). These analyses are consistent with the chemical grafting of the precursor onto silica to yield the monopodal [≡SiOTa-$(CH_2^t$Bu$)_2$IrH_2(Cp*)]. After hydrogenation, IR monitoring of the solid shows a decrease in intensity

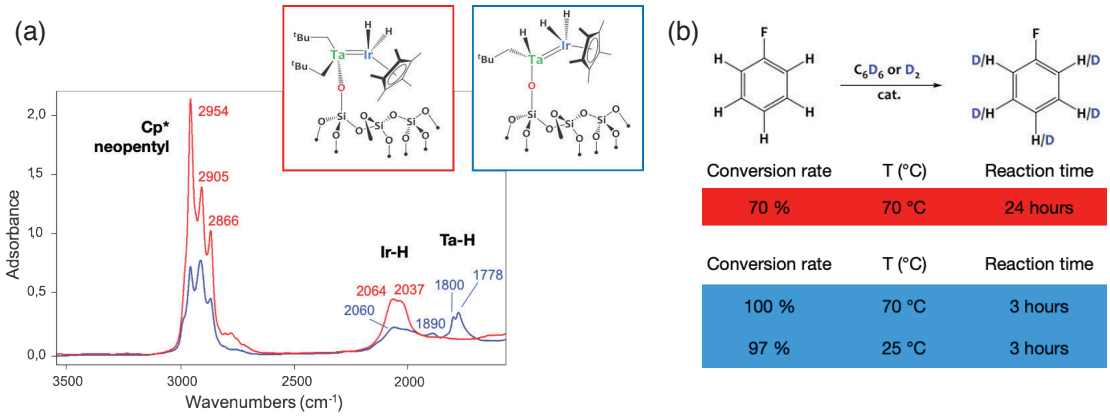

Figure 6.2: (a) DRIFT spectra of [≡SiOTa-$(CH_2^tBu)_2IrH_2(Cp^*)$] and [≡SiOTa(CH_2^tBu)H-$IrH_2(Cp^*)$] after hydrogenation. A new band corresponding to Ta-H appears in the product after hydrogenation, validating the reaction pathway.(b) Comparison of reactivity between [≡SiOTa-$(CH_2^tBu)_2IrH_2(Cp^*)$] and [≡SiOTa(CH_2^tBu)H-$IrH_2(Cp^*)$] for the deuteration of fluorobenzene under different conditions. A 97% conversion rate can be achieved in 3 hours at room temperature by using the complex [≡SiOTa(CH_2^tBu)H-$IrH_2(Cp^*)$].

of the neopentane ligand, and the appearance of new bands around 1800 cm^{-1} attributed to a ν(Ta-H) vibration mode issuing from tantalum hydride species (Figure 6.2-(a), blue spectrum).

Catatytic activity of the materials

The activity of the two materials was evaluated in the context of the catalytic H/D exchange reactions by Lassalle and co-workers. It was shown that the supported Ta/Ir species exhibit drastically increased catalytic performances in H/D catalytic exchange reactions with respect to monometallic analogues as well as homogeneous systems. In particular, the material obtained after reaction with H_2 promotes much more efficiently H/D exchange between fluorobenzene and C_6D_6 or D_2 as deuterium sources with excellent productivity under mild conditions as reported in Figure 6.2-(b).

6.2.2 Two-step synthesis

To prepare supported heterobimetallic species, another synthetic methodology has been envisioned that consists first in grafting the Ta monometallic complex onto the oxide support and then, in a second step, in using this supported organometallic species as a reactive center to introduce the second metal, as summarized in Figure 6.3.

Characterization by IR spectroscopy

The IR spectroscopy analysis of [(≡SiO)Ta$(CH_2^tBu)(CH_2^tBu)_2$] obtained after reaction with a solution containing the iridium molecular precursor Cp^*IrH_4 shows the appearance of a new set of bands, assigned to ν(Ir-H) stretches, in the 2080-1940 cm^{-1} region as shown in Figure 6.4-(a). These data in combination with elemental analysis suggest that one iridium center has reacted with one tantalum center in this two-step synthesis route. However this is not sufficient to claim that the one and two-steps routes are equivalent on a molecular level, and a first hint of the dissimilarities between the one-step and two-steps synthesis were gained through the analysis of their catalytic performances.

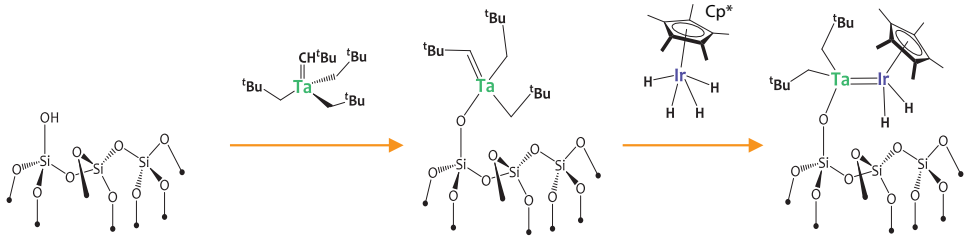

Figure 6.3: Two-step synthesis of the grafted Ta=Ir catalyst. The monometallic monopodal silica-supported tantalum species $[(\equiv SiO)Ta(CH^tBu)(CH_2^tBu)_2]$ was first prepared by grafting the molecular complex $Ta(CH^tBu)(CH_2^tBu)_3$ onto dehydroxylated SBA-15 at 700 °C. The bimetallic complex was subsequently formed after treatment with a pentane solution of Cp^*IrH_4.

Catatytic activity of the materials

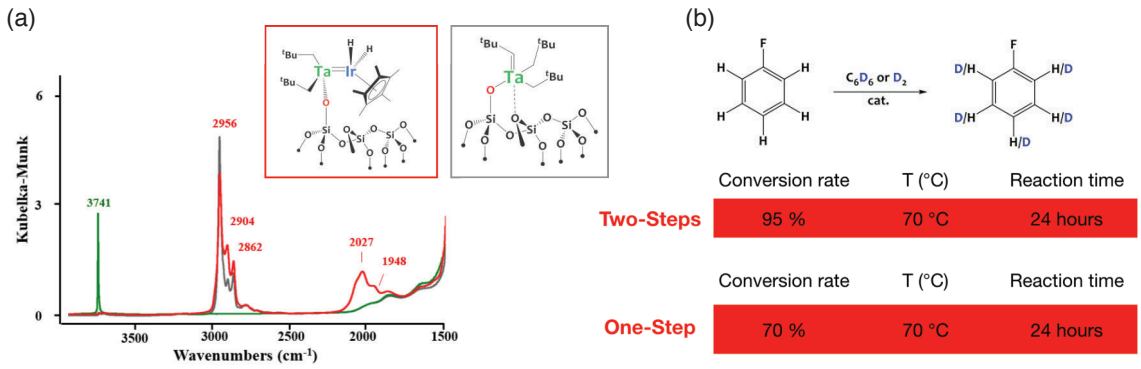

Figure 6.4: DRIFT spectra of the species formed after two steps synthesis bimetallic complex (red box) and the tantalum complex before reaction (grey box). New set of bands, assigned to ν(Ir-H) stretches, in the 2080-1940 cm^{-1} region.(b) Comparison of reactivity between materials for the deuteration of fluorobenzene under different conditions. A 95% conversion rate can be achieved in 24 hours at 70 °C by using the complex from the two-steps route compared to 70% with $[\equiv SiOTa\text{-}(CH_2^tBu)2IrH_2(Cp^*)]$. The green spectrum corresponds to the silica surface alone.

Lassalle and co-workers compared the catalytic activity of the materials formed in the one-step and two- steps synthesis in the reaction of H/D exchange in the benchmark H/D with the conversion of C_6D_6 to C_6H_5F at 70 °C. As reported in Figure 6.4-(b), the surface species obtained with the two-step synthesis exhibits a significant increase in activity compared to the previously reported material, thereby suggesting the existence of different active species in both materials. Similar observations were made in propane metathesis. Overall the catalytic results suggest that the actives sites in the materials prepared by the one- and two-synthesis approaches are different. Experiments carried out on molecular models by our collaborators, and that will not be detailed here suggested the presence of trimetallic supported complexes in the materials prepared by the two-step method. Additional surface species were postulated as described in Figure 6.5.

6.2.3 Synthesis of heterotrimetallic Ta/Ir_2 surface species

To confirm this hypothesis, Lasalle and co-workers prepared the pure trimetallic complex grafted on SBA-15 as shown in Figure 6.6. The IR and elemental analyses were consistent with the chemical grafting of the precursor onto silica via protonolysis of one Ta-Np bond by a surface silanol group,

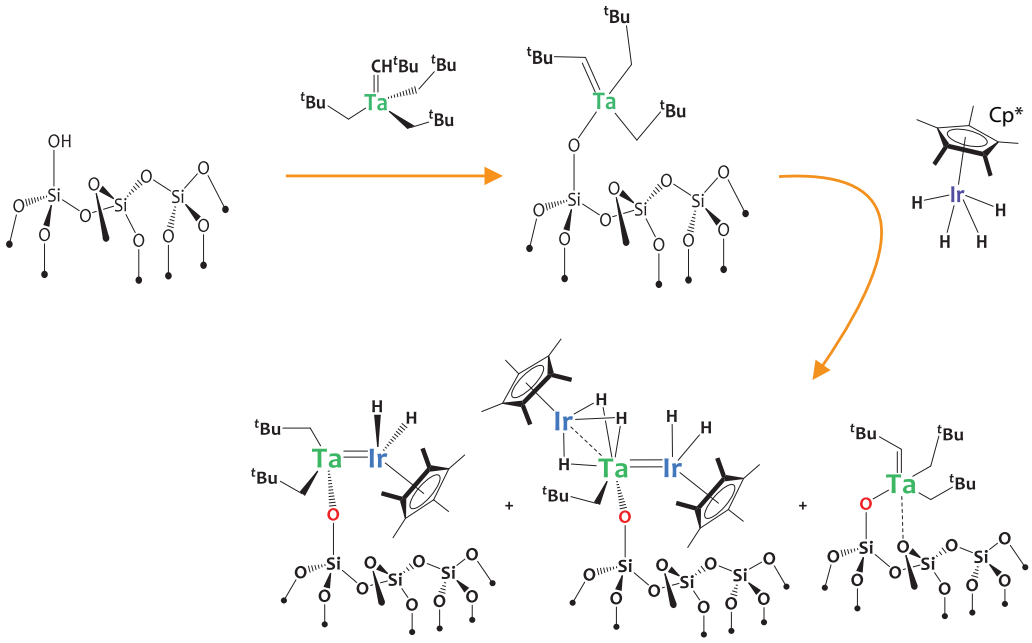

Figure 6.5: Mixture of species that are formed during the two-steps synthesis. The new postulated products of the two-step synthesis are mono-, bi-, and trimetallic species.

yielding a monopodal well-defined trimetallic surface species. Its catatylic activity was much lower than that of the other materials. Importantly, the IR analysis confirmed that the material prepared by the two-step synthesis routes was a mixture of heterobimetallic (as obtained in the one-step synthetic approach) and heterotrimetallic surface species.

In the following sections, we describe how the use proton MQ NMR spectroscopy enables to unambiguously identify the species formed during each synthesis pathway, and notably to further corroborate the assumption that the two routes yield different active sites.

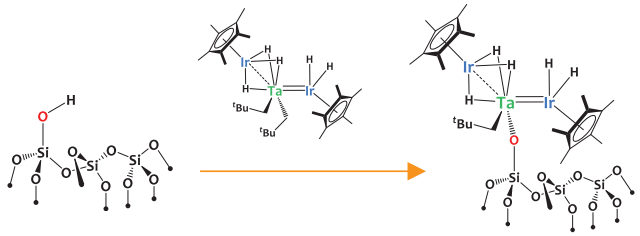

Figure 6.6: Synthesis of the isolated supported trimetallic species. The reaction is carried out in a 1:1 stoechiometric ratio in pentane at room temperature and affords exclusively the monosiloxy heterotrimetallic complex $[IrH_3(Cp^*)Ta(CH^t_2Bu)(OSi(O^tBu)_3)_2IrH_2(Cp^*)]$.

6.3 Proton MQ NMR spectroscopy of Ta-Ir complexes obtained through the one-step synthesis route

6.3.1 Experimental details

Proton solid-state NMR spectroscopy was carried out to confirm the structure of the surface complexes. In particular, multiple-quantum (MQ) experiments were applied to determine the number of hydrides around the metal centers. The proton solid-state NMR spectra were obtained on a Bruker 700 MHz narrow-bore spectrometer using a double resonance 2.5 mm MAS probe. The samples were introduced under argon (in a glove-box) in a zirconia rotor, which was then tightly closed. Ultra-dry nitrogen gas directly produced from the evaporation of liquid nitrogen was used to spin the samples to avoid their degradation. As all materials were extremely sensitive to traces of water or oxygen, working under ultra-dry gas was mandatory to ensure the stability of the complexes in the course of the NMR experiments. For all the proton multiple-quantum experiments, the spinning frequency was set to 18 kHz. The 2D proton DQ-SQ correlation spectra were recorded according to the following general scheme: excitation of DQ coherences, t_1 evolution and reconversion into observable magnetization, Z-filter, and detection. DQ excitation and reconversion were achieved using the POST-C7 [200] pulse sequence. The length of the POST-C7 excitation and reconversion block was set to 160 μs (corresponding to seven basic POST-C7 cycles). Quadrature detection in $\omega 1$ was achieved using the States-TPPI method [273]. TQ excitation was achieved by the sequential application of first a 90° proton pulse followed by a DQ POST-C7 pulse sequence as previously described in the literature. The length of the POST-C7 excitation and reconversion block was set to 160 μs (corresponding to seven basic POST-C7 cycles). Quadrature detection in $\omega 1$ was achieved using the States-TPPI method [273]. Although less informative, carbon-13 solid-state NMR spectra were also recorded. They were obtained on a Bruker 500 MHz wide-bore spectrometer using a double resonance 4 mm MAS probe from cross-polarization (CP) from protons, using a linear ramped CP to optimize the magnetization transfer efficiency. A proton radio frequency (RF) field of 70 kHz in the center of the ramp was applied, while the RF field on carbon-13 was adjusted for optimal sensitivity. The same experimental conditions were used for all the MQ spectra reported in this section, and therefore the experimental details are not repeated for the characterization of the other set of compounds. These experiments enable the detection of spatial proximities between pairs (DQ) or triplets (TQ) of dipolar-coupled protons, with correlations at the sum of the individual frequencies in the indirect dimension. For hydrides with degenerate chemical shifts, auto-correlation peaks along the $\omega_1 = 2\omega_2$ (DQ) or $\omega_1 = 3\omega_2$ (TQ) diagonal reveal the presence of pools of (at least) two or three protons respectively.

6.3.2 Characterization of the [≡SiOTa(CH_2^tBu)$_2$IrH_2(Cp*)] complex

The DQ and TQ solid-state NMR spectrum of [≡SiOTa(CH_2^tBu)$_2$IrH_2(Cp*)] are shown in Figure 6.8 and 6.7. The one-dimensional proton spectrum is shown above these 2 spectra. It shows two main intense signals at 2.06 and 0.96 ppm assigned to the CH_3 groups of the Cp* and Np moieties, respectively, along with a broad signal at -11 ppm corresponding to the iridium hydrides. The peak at 2.06 ppm also includes the resonance of the CH_2 protons of the Np moiety. The ^{13}C CP MAS NMR spectrum (shown in Appendix S2) displays four resonances at 107.5, 93.9, 33.5, and 9.1 ppm, assigned to the CH_2(Np), C(Cp*), CH_3(Np), and CH_3(Cp*) carbons, respectively, in agreement with the proposed structure. The DQ spectrum (Figure 6.8) shows an autocorrelation along the $\omega_1 = 2\omega_2$ line at around (ω_1, ω_2) = (-11 ppm, -22 ppm) confirming the presence of two hydrides. Conversely, the TQ correlation spectrum (Figure 6.7) does not display any autocorrelation for the

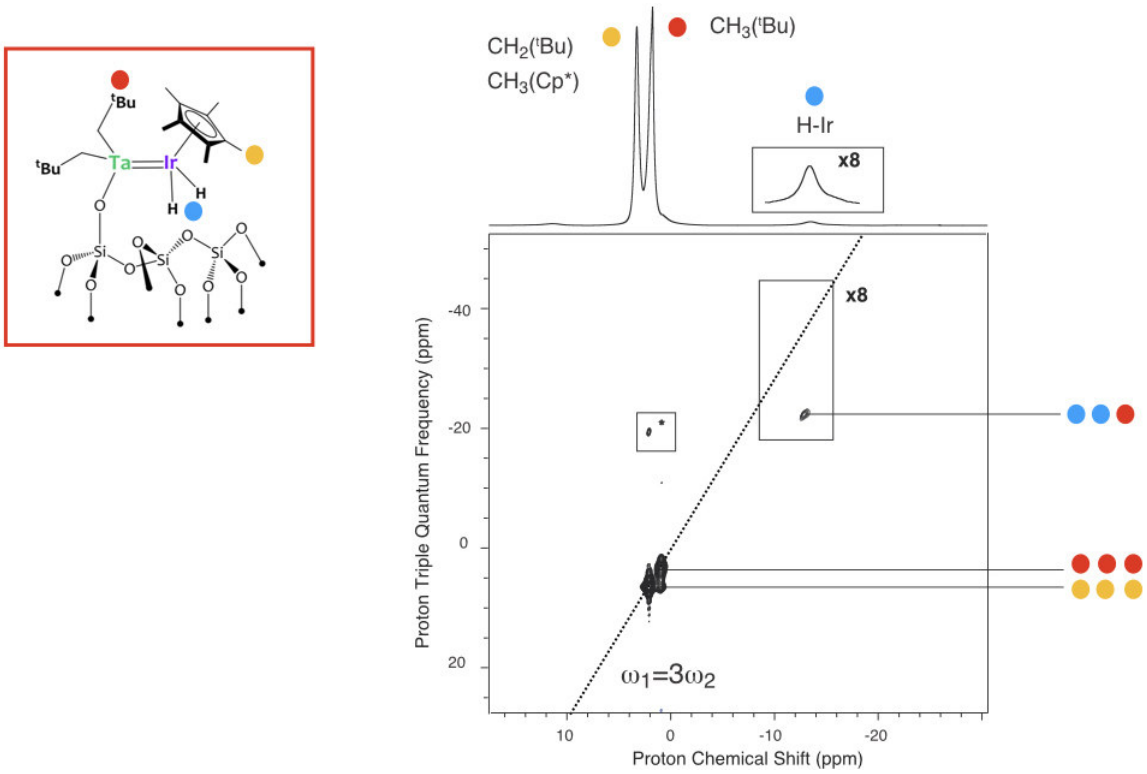

Figure 6.7: Proton SQ-TQ NMR spectrum of [≡SiOTa(CH_2^tBu)$_2$IrH_2(Cp*)] (700 MHz, 2.5 mm probe, 18 kHz MAS frequency). The spectrum has been zoomed by a factor 8 in the hydride region to clearly show the absence of autocorrelation for the hydride proton at around (-11 ppm, -33 ppm). A total of 300 t_1 increments of 8.3 μs with 96 scans each were recorded. The total experimental time was 16 hours. The dotted line corresponds to the $\omega_1 = 3\omega_2$ diagonal.

hydride resonance along the $\omega_1 = 3\omega_2$ line, as expected for a set of two isolated coupled protons. The DQ-SQ and TQ-SQ correlation spectra have in addition the expected autocorrelations for the CH_3 groups of the Cp* and Np moieties, as well as the expected off-diagonal correlations with the hydrides.

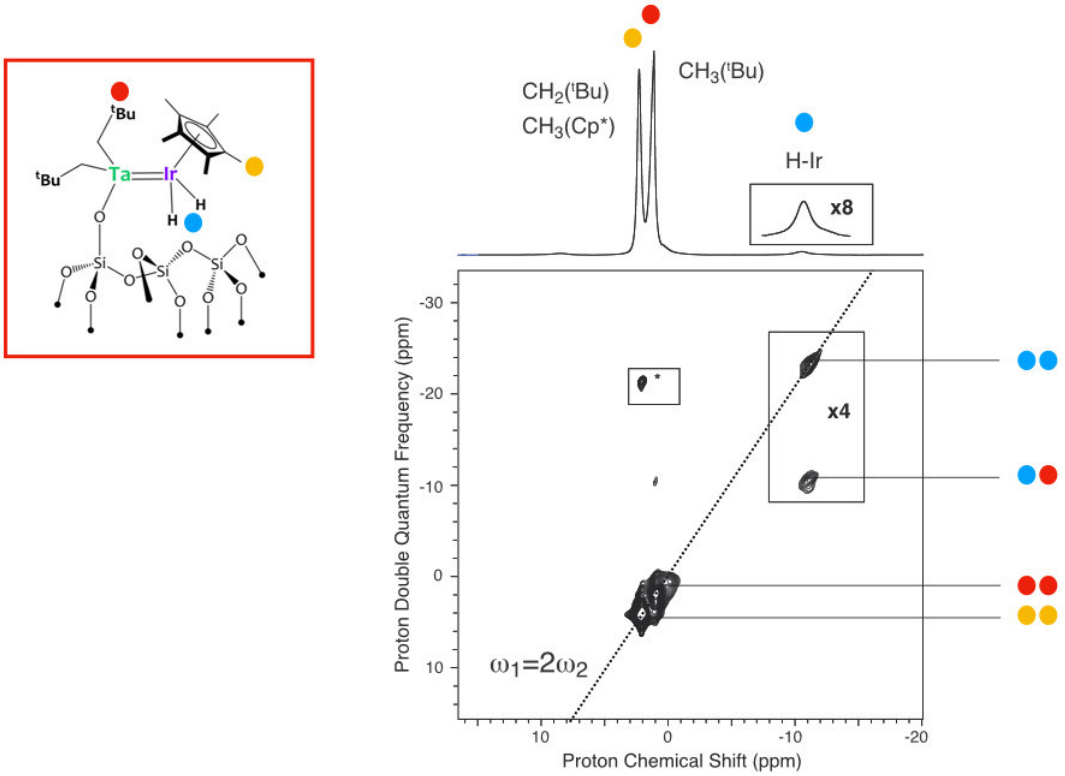

Figure 6.8: Proton SQ-DQ NMR spectrum of [≡SiOTa(CH_2^tBu)$_2$IrH_2(Cp*)] (700 MHz, 2.5 mm probe, 18 kHz MAS frequency). The trace above the 2D plot corresponds to the one-dimensional ^{1}H NMR spectrum. The dotted line corresponds to the $\omega_1 = 2\omega_2$ diagonal. The spectrum has been zoomed by a factor 4 in the hydride region to clearly show the autocorrelation at around (-11 ppm, -22 ppm) and the correlation between the hydrides and the neopentyl CH_3 protons at around (-11 ppm, -10 ppm). A total of 300 t_1 increments of 14.3 μs with 32 scans each were recorded. The total experimental time was 5 hours and 20 minutes.

6.3.3 Characterization of the [≡SiOTa(CH_2^tBu)H-IrH_2(Cp*)] complex

The DQ and TQ solid-state NMR spectrum of [≡SiOTa(CH_2^tBu)H-IrH_2(Cp*)] obtained after the hydrogenation are shown in Figure 6.9 and 6.10. The one-dimensional proton spectrum is shown above these 2 spectra. The ^{1}H solid-state NMR spectrum is similar to the one of [≡SiOTa(CH_2^tBu)$_2$IrH_2(Cp*)]. It displays two intense signals at 2.06 and 0.96 ppm assigned as previously to the CH_3(Cp*) and CH_2(Np), and to the CH_3(Np) moieties, respectively. We note that their intensity ratio is different, because the hydrogenation reaction leads to the release of some of the neopentyl ligands. The hydride signal appears as a broad resonance ranging from -11 to -15 ppm. The ^{13}C CP MAS NMR spectrum (shown in Appendix S2) also displays four resonances at 106.9, 93.9, 33.3, and 8.9 ppm, assigned to the CH_2(Np), C(Cp*), CH_3(Np), and CH_3(Cp*) carbons, respectively, which agrees with the proposed structure. The proton DQ and TQ spectra show elongated autocorrelations along respectively the $\omega_1 = 2\omega_2$ and $\omega_1 = 3\omega_2$ diagonals, at -22 ppm and -33 ppm respectively. Additional off-diagonal correlations with the aliphatic resonances are observed as well as their auto-correlations. In particular a correlation between one hydride proton and the ^{t}Bu at -10 ppm for the DQ and two hydride and the ^{t}Bu at -21 ppm for the TQ. Thus, the proposed structure of the trihydride species is confirmed by proton multiple-quantum NMR experiments. The elongated shapes of the autocorrelations observed for the hydride resonances in both DQ and TQ correlation spectra reflect the inhomogeneous nature of the line broadening

due to slight surface heterogeneity, as well as the presence of correlated chemical shift distributions. [274, 275] We note that fast exchange on the NMR time scale between Ta-H/Ir-H hydrides is very likely to occur, which would lead to the observation of a distribution of average chemical shifts.

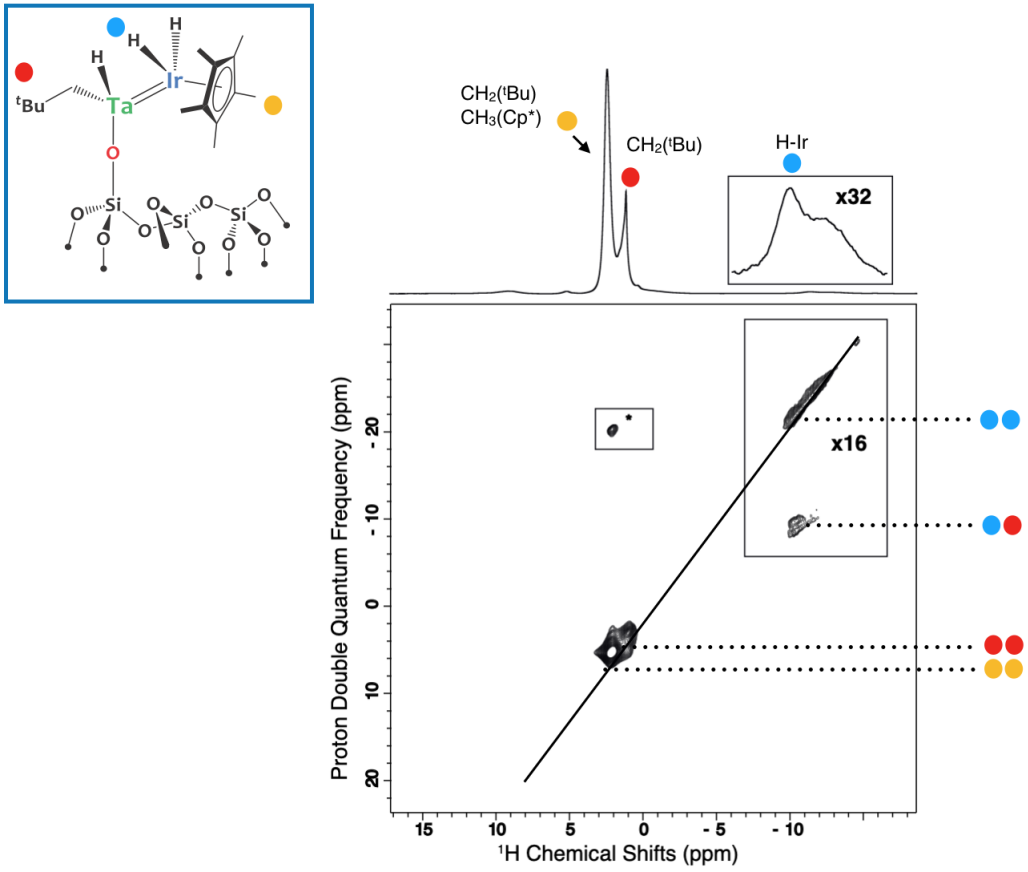

Figure 6.9: Proton SQ-DQ NMR spectrum of [≡SiOTa(CH_2^tBu)H-IrH_2(Cp*)] (700 MHz, 2.5 mm probe, 18 kHz MAS frequency). The trace above the 2D plot corresponds to the one-dimensional ^{1}H NMR spectrum. The dotted line corresponds to the $\omega_1 = 2\omega_2$ diagonal. The spectrum has been zoomed by a factor 16 in the hydride region to clearly show the autocorrelation at around (-11 ppm, -22 ppm) and the correlation between the hydrides and the neopentyl CH_3 protons at around (-11 ppm, -10 ppm). A total of 300 t_1 increments of 14.3 μs with 32 scans each were recorded. The total experimental time was 5 hours and 20 minutes.

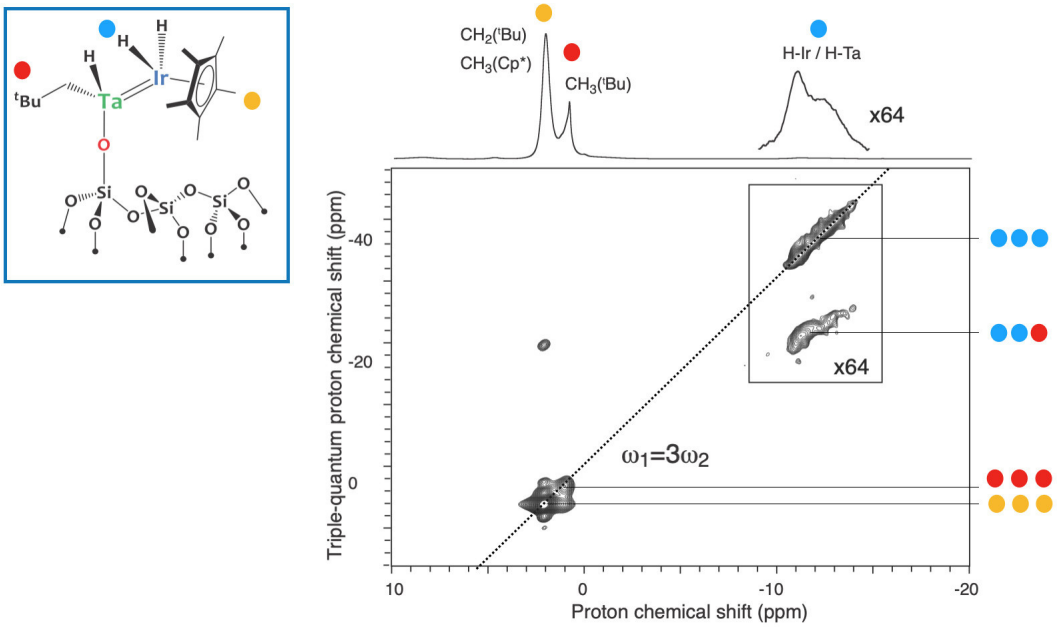

Figure 6.10: Proton SQ-TQ NMR spectrum of [≡SiOTa(CH_2^tBu)H-IrH_2(Cp*)] (700 MHz, 2.5 mm probe, 18 kHz MAS frequency). The spectrum has been zoomed by a factor 64 in the hydride region to clearly show the autocorrelation for the hydride proton (-11 ppm, -33 ppm). A total of 300 t_1 increments of 8.3 μs with 96 scans each were recorded. The total experimental time was 16 hours. The dotted line corresponds to the $\omega_1 = 3\omega_2$ diagonal.

6.3.4 DFT calculations of the surface structures

Periodic DFT calculations were done by our collaborators to gain further insights into the structures of the silica-supported species [≡SiOTa(CH_2^tBu)$_2$$IrH_2$(Cp*)] and the complex [≡SiOTa(CH_2^tBu)H-IrH_2(Cp*)] formed after exposure to H_2. Figure 6.11-(a) shows the most stable structure for

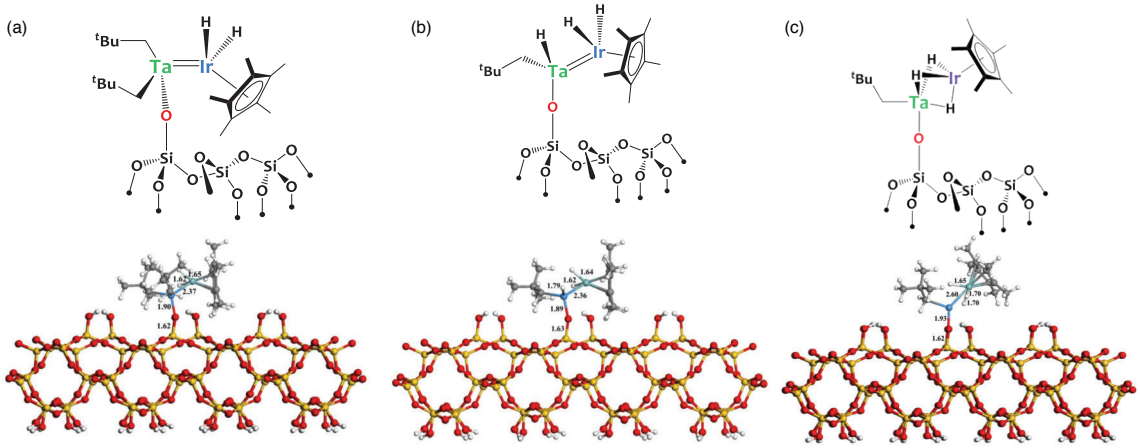

Figure 6.11: DFT optimized structures of the silica-supported complexes (a) [≡SiOTa-(CH_2^tBu)$_2$$IrH_2$(Cp*)] and [≡SiOTa($CH_2^tBu$)H-$IrH_2$(Cp*)] ((b)-model A composed of one Ta-H terminal hydride and two Ir-H terminal hydrides and (c)-model B composed of three hydrides bridging the two metals). Selected bond distances are given in Å. Ta is represented in blue, Ir in green, Si in yellow, O in red, C in grey and H in white.

[≡SiOTa(CH_2^tBu)$_2$$IrH_2$(Cp*)]. The details are provided in the corresponding publication [272]. The Ta/Ir complex is anchored to the silica support through one Ta-O-Si interface bond (Ta-O

bond is 1.90 Å, Si-O bond is 1.62 Å). The Ta=Ir bond distance remains virtually unchanged upon deposition on silica. Interestingly, two putative structures were obtained for the trihydride species [≡SiOTa(CH_2^tBu)H-IrH_2(Cp*)]. Model A (Figure 6.11-(b)) has one terminal Ta-H hydride bond and two Ir-H terminal hydride bonds. Model B (Figure 6.11-(c)) contains three bridging Ir-H-Ta hydrides and a longer Ta-Ir distance (2.59 Å versus 2.36 Å in A), and is 29.3 kcal/mol^{-1} less stable than model A. We note that the NMR experiments are compatible with these two structures and that they cannot be discriminated as the hydrides are likely in fast chemical exchange at ambient temperatures. Experiments at lower temperature could be envisioned to potentially discriminate between the two structures.

6.4 Proton MQ NMR spectroscopy of Ta-Ir complexes obtained through the two-steps synthesis route

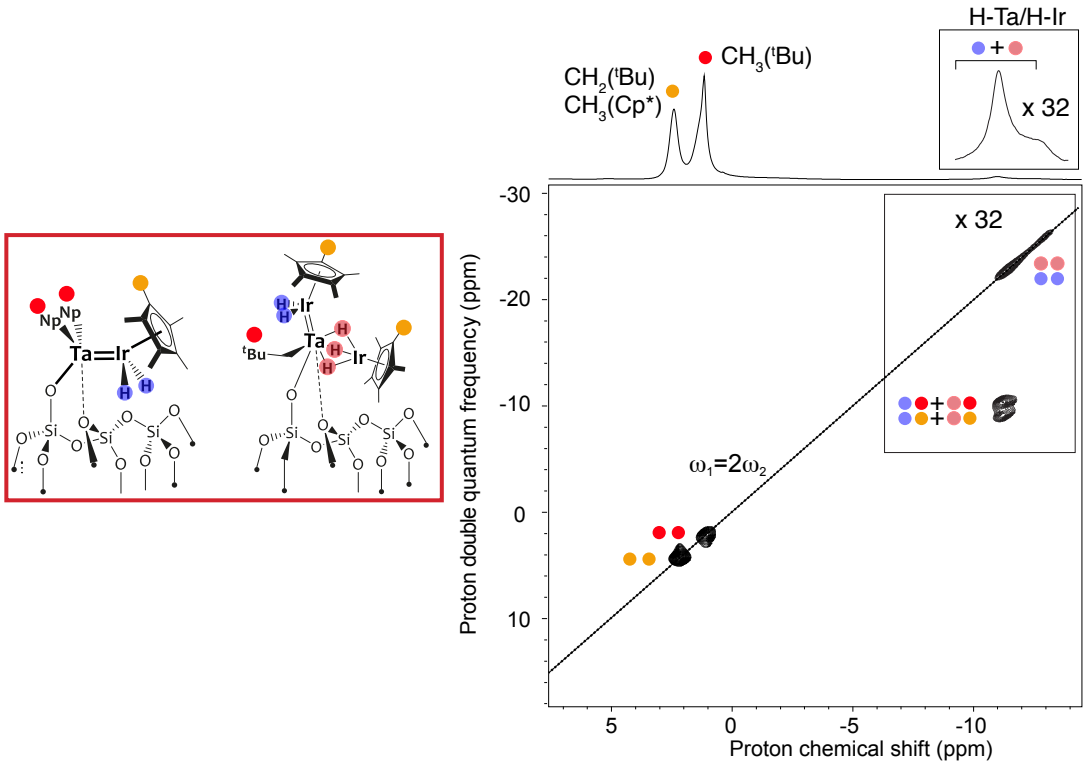

Figure 6.12: Proton SQ-DQ NMR spectrum of the material obtained by the two-steps synthesis (700 MHz, 2.5 mm probe, 18 kHz MAS frequency). The trace above the 2D plot corresponds to the one-dimensional ^{1}H NMR spectrum. The spectrum has been zoomed by a factor 32 in the hydride region to clearly show the autocorrelation at around (-11 ppm, -22 ppm). A total of 300 t_1 increments of 14.3 μs with 32 scans each were recorded. The total experimental time was 5 hours and 20 minutes. The dotted line corresponds to the $\omega_1 = 2\omega_2$ diagonal.

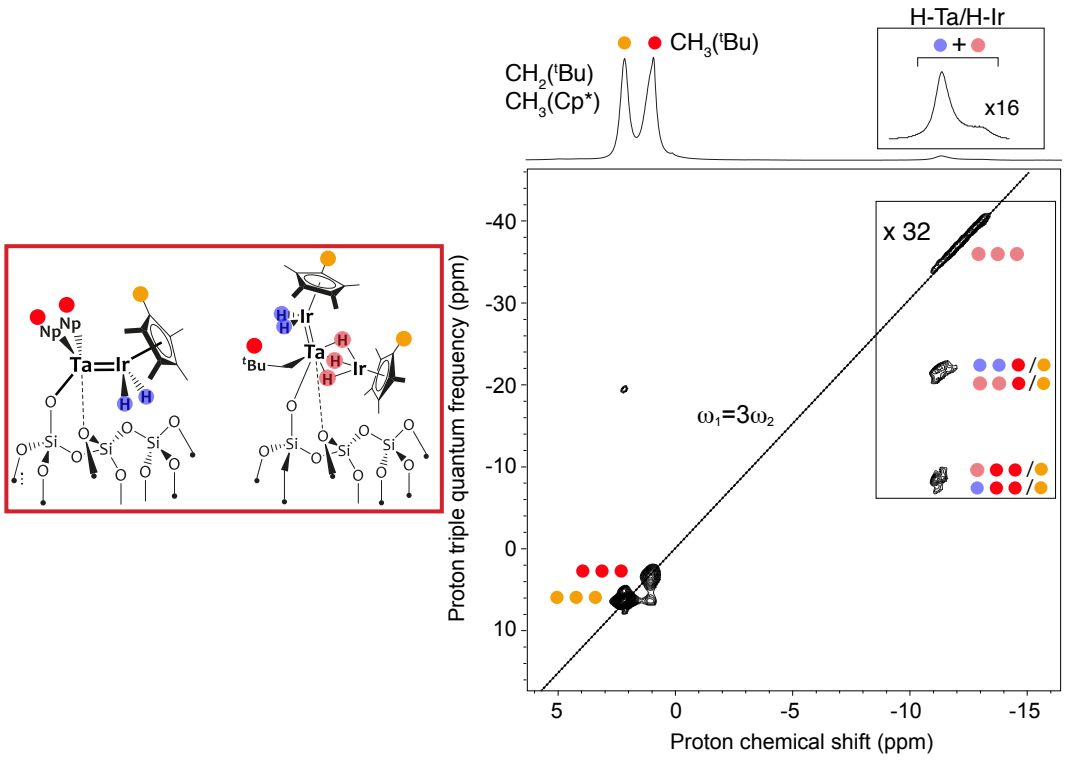

Figure 6.13: Proton SQ-TQ NMR spectrum of the complexes obtained by the two-steps synthesis (700 MHz, 2.5 mm probe, 18 kHz MAS frequency). The trace above the 2D plot corresponds to the one-dimensional ^{1}H NMR spectrum. The dotted line corresponds to the $\omega_1 = 3\omega_2$ diagonal. The spectrum has been zoomed by a factor 32 in the hydride region to clearly show the autocorrelation at around (-11 ppm, -33 ppm). A total of 300 t_1 increments of 8.3 μs with 96 scans each were recorded. The total experimental time was 16 hours.

The experimental details are similar to the ones described for the characterization of the previous complexes and therefore are not repeated here (section 6.3.1). The DQ and TQ solid-state NMR spectra of the material prepared by the two-steps synthesis are shown in Figure 6.12 and 6.13. The one-dimensional proton spectrum is shown above these 2 spectra. The ^{1}H solid-state NMR spectrum is very similar to the one of [≡SiOTa(CH_2^tBu)$_2$IrH_2(Cp*)]. It displays two intense signals at 2.2 and 0.9 ppm assigned as previously to the CH_3(Cp*), and to the CH_3(Np) moieties, respectively. The hydride signal (Figure 6.12) appears as a broad resonance ranging from -10 to -15 ppm.The proton DQ spectrum is similar to the one of the [≡SiOTa(CH_2^tBu)$_2$IrH_2(Cp*)] material obtained with the one-step approach, with auto-correlations for the CH_3(Cp*), CH_3(Np) and hydride protons. Off-diagonal correlations between the CH_3 and hydride protons are also observed. Therefore, this spectrum does not allow one to confirm that the two synthesis routes yield different surface species. The evidence is clearly provided by proton TQ NMR spectroscopy. The SQ-TQ spectrum of the material obtained with the two-steps process is shown in Figure 6.13. The observation of an auto-correlation along the diagonal at (-11 ppm, -33 ppm) demonstrate unambiguously that [≡SiOTa(CH_2^tBu)$_2$IrH_2(Cp*)] is not the only species to be formed during the two-step route, and that additional organometallic complexes bearing a higher number of hydrides are present. While this correlation was absent from the SQ-TQ spectrum of the material resulting from the one-step route, it is clearly visible in the spectrum of heterotrimetallic Ta/Ir2 surface species as described below. This confirms that the trimetallic species is formed during the two-

steps synthesis.

6.5 Proton MQ NMR Spectroscopy of $[Ta(CH_2^tBu)_2Ir_2H_5(Cp^*)_2]$

6.5.1 Proton DQ and TQ NMR spectroscopy

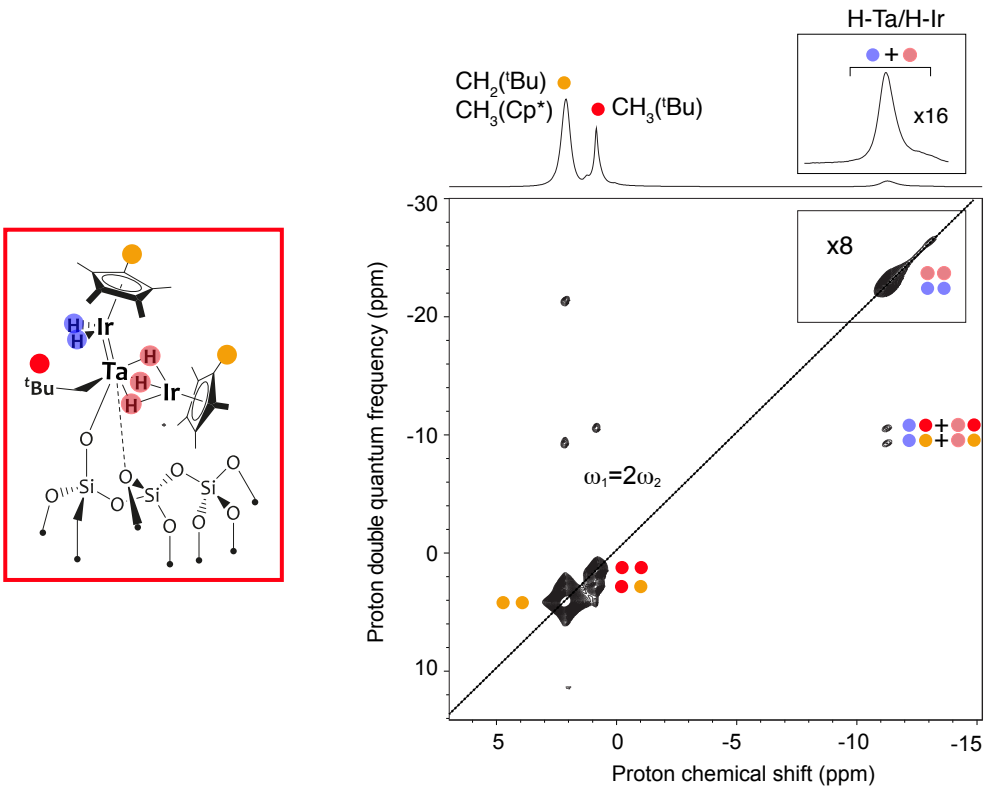

Figure 6.14: Proton SQ-DQ NMR spectrum of $[Ta(CH_2^tBu)_2Ir_2H_5(Cp^*)_2]$ (700 MHz, 2.5 mm probe, 18 kHz MAS frequency). The trace above the 2D plot corresponds to the one-dimensional ^{1}H NMR spectrum. The spectrum has been zoomed by a factor 8 in the hydride region to clearly show the autocorrelation at around (-11 ppm, -22 ppm). A total of 300 t_1 increments of 14.3 μs with 32 scans each were recorded. The total experimental time was 5 hours and 20 minutes. The dotted line corresponds to the $\omega_1 = 2\omega_2$ diagonal.

The experimental details are similar to the ones described for the characterization of the previous complexes (section 6.3.1), expect for the sample temperature. The temperature was set to 235 K (versus 293 K in the previous characterization) to increase the stability of the surface species. Indeed, we observed a rapid evolution of the proton spectra of the trimetallic complex during the course of the NMR experiments when these latter were carried out at ambiant temperature (293 K), indicating the degradation of the complex. The DQ and TQ solid-state NMR spectra of $[Ta(CH_2^tBu)_2Ir_2H_5(Cp^*)_2]$ are shown in Figure 6.14 and 6.15 respectively. The one-dimensional proton spectrum is shown above these 2 spectra. Again, the 1D proton spectrum shows the expected resonances of the Cp*, neopentyl and hydride protons resonances at around 2.2, 0.9 and -11 ppm. The SQ-DQ spectrum is similar to the one recorded on the bimetallic complexes obtained by the two synthetic methods and displays all the expected correlations. The SQ-TQ spectrum also yields the expected cross-peaks, and notably a strong auto-correlation peak along the diagonal for the hydride protons. The elongated shape of the autocorrelation indicates that the broadening of the hydride resonance is inhomogeneous, i.e. corresponds to a distribution of chemical shifts

due to slight structural heterogeneity likely originating from the support. [274, 275] We also note that fast exchange on the NMR time scale between hydrides is very likely to occur, leading to the observation of a distribution of average chemical shifts, and that the two types of hydrides can't be distinguished at the temperature of the experiments.

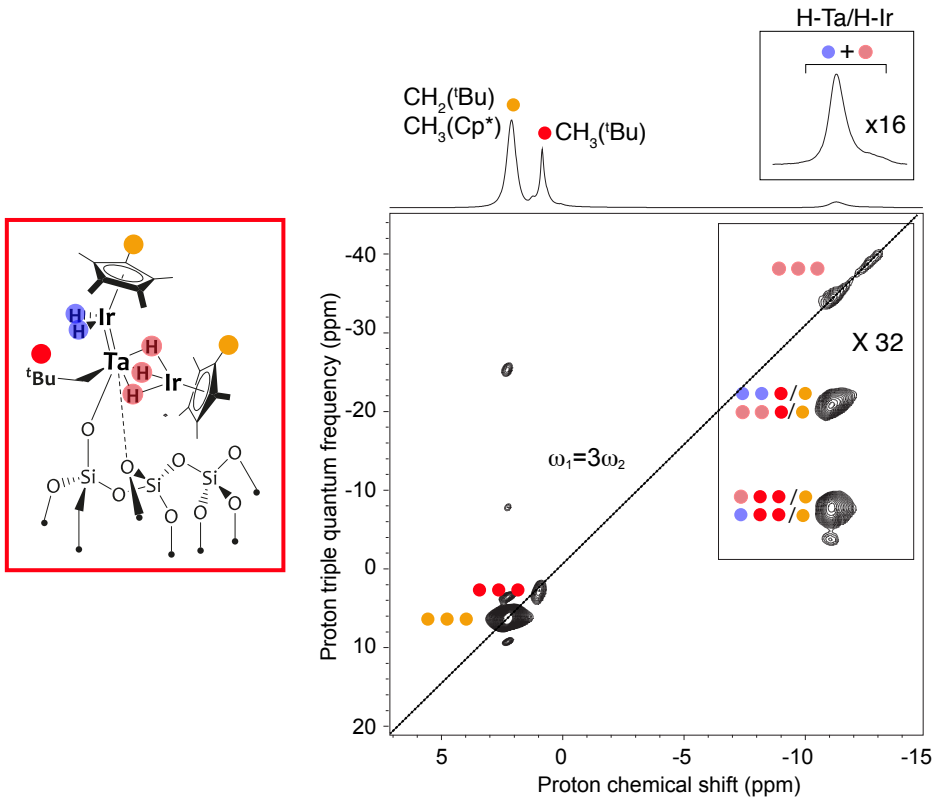

Figure 6.15: Proton SQ-TQ NMR spectrum of $[Ta(CH_2^tBu)_2Ir_2H_5(Cp^*)_2]$ (700 MHz, 2.5 mm probe, 18 kHz MAS frequency). The trace above the 2D plot corresponds to the one-dimensional ^{1}H NMR spectrum. The dotted line corresponds to the $\omega_1 = 3\omega_2$ diagonal. The spectrum has been zoomed by a factor 32 in the hydride region to clearly show the autocorrelation at around (-11 ppm, -33 ppm). A total of 300 t_1 increments of 8.3 μs with 96 scans each were recorded. The total experimental time was 16 hours.

6.5.2 Proton MQ NMR spectroscopy of higher coherences

The structure of the trimetallic complex has five hydride protons. Multiple-quantum experiments with higher coherences were implemented in order to confirm the number of hydrides surrounding the three metal centers. Figure 6.16-(a) shows the SQ-4Q spectrum recorded on $[Ta(CH_2^tBu)_2Ir_2H_5(Cp^*)_2]$. To record this spectrum, the phase cycling of the SQ-DQ pulse sequence was modified. Namely, the phase cycling of the POST-C7 reconversion block was set to select coherence jumps of 4 (increments of $\pi/4$), and the quadrature detection was ensured by incrementing the phases of the POST-C7 excitation block by $\pi/8$. The 4Q correlation spectrum does not display an auto-correlation along the line ω_1=4ω_2, at around (-11 ppm, -44 ppm). However, a set of 4Q correlations are observed among the CH_3 protons, and between these CH_3 proton and the hydrides. As stated in chapter 3, going to higher coherences affect drastically the sensitivity. Figure 6.16-(b) shows the efficiency of one-dimensional MQ experiments, recorded on the $[Ta(CH_2^tBu)_2Ir_2H_5(Cp^*)_2]$ for coherence numbers ranging from 2 to 5. For the 5Q experiment, the

phase cycling of the SQ-TQ pulse sequence was modified so as to enable coherence jumps of 5. The phase cycling of POST-C7 reconversion block and of the 90° were simultaneously incremented by $\pi/5$. Efficiencies of 27 %, 7.7 %, 0.12%, and $\sim$ 0.05% were measured for the DQ, TQ, 4Q and 5Q experiments respectively on the resonances of the CH_3 groups. The extremely severe drop in efficiency may explain the absence of a 4Q correlation among the hydride protons in the spectrum of Figure 6.16-(a).

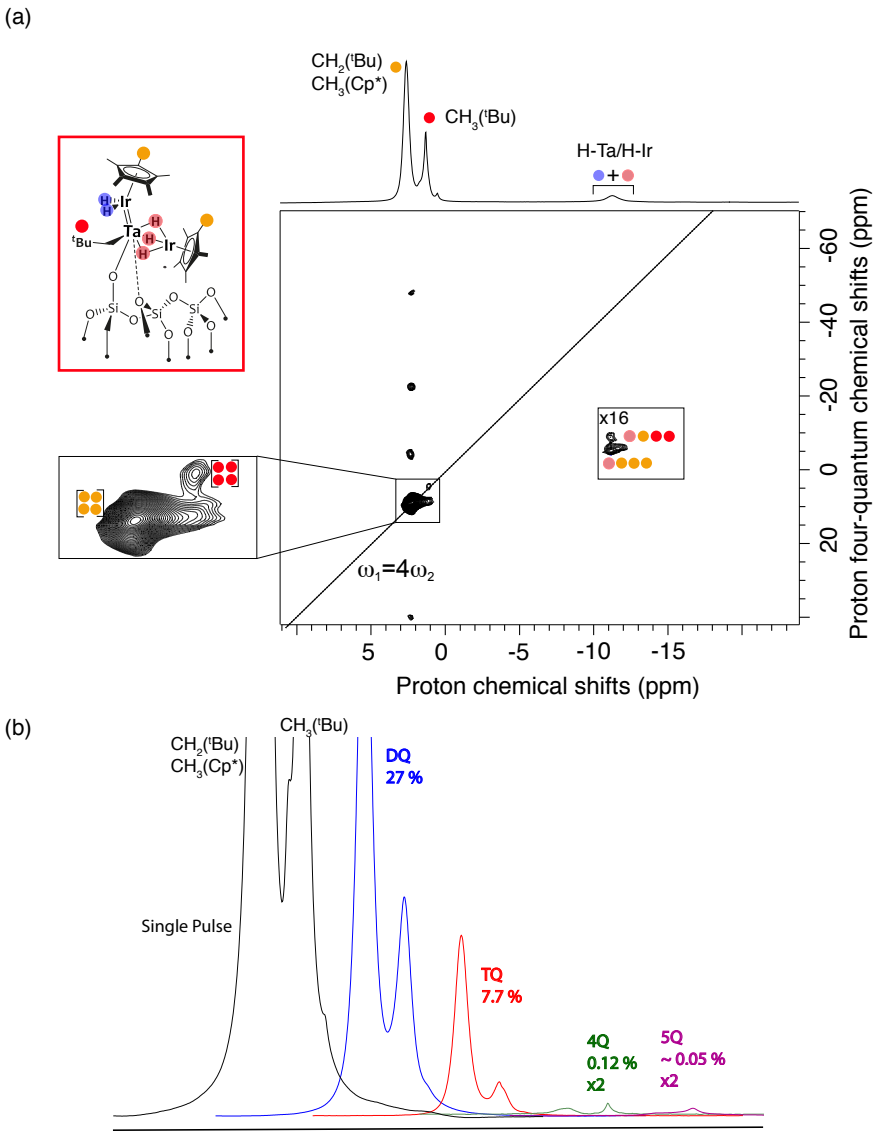

Figure 6.16: (a) Proton SQ-4Q NMR spectrum of $[Ta(CH_2^tBu)_2Ir_2H_5(Cp^*)_2]$ (700 MHz, 2.5 mm probe, 22 kHz MAS frequency). The direct dimension corresponds to the ^{1}H-NMR spectrum (700 MHz, 2.5 mm probe, 22 kHz MAS frequency. The spectrum has been zoomed by a factor 32 in the hydride region to clearly show the absence of autocorrelation at around (-11 ppm, -44 ppm) and a zoom on the CH_3 protons of the Cp* and neopentyl ligand to show the auto-correlations at (2.2 ppm, 8.8 ppm and 0.9 ppm, 3.6 ppm) respectively. A total of 300 t_1 increments of 6.25 μs with 96 scans each were recorded. The total experimental time was 16 hours. The dotted line corresponds to the ω_1=4ω_2 diagonal. (b) Proton MQ efficiency for the tri-metallic compound. A recycle delay of 2 s was used with 1920 scans for each 1D experiment. The two resonances correspond to the CH_3 protons of the Cp* and neopentyl ligand.

6.6 Proton MQ NMR Spectroscopy of a Hf=Ir complex

The methodology described for the bi- and trimetallic Ta-Ir complexes was extended to the characterization of Hafnium-Iridium heteronuclear complexes, also prepared by Lassalle and co-workers. The one-step synthesis route was applied to prepare this material, in analogy to the protocol developed for the Ta-Ir complex. A structure with three bridging hydrides was postulated by our collaborators from FTIR analysis. The DQ and TQ solid-state NMR spectra of the Hf=Ir complex are shown in Figure 6.17 and 6.18 respectively. The one-dimensional proton spectrum

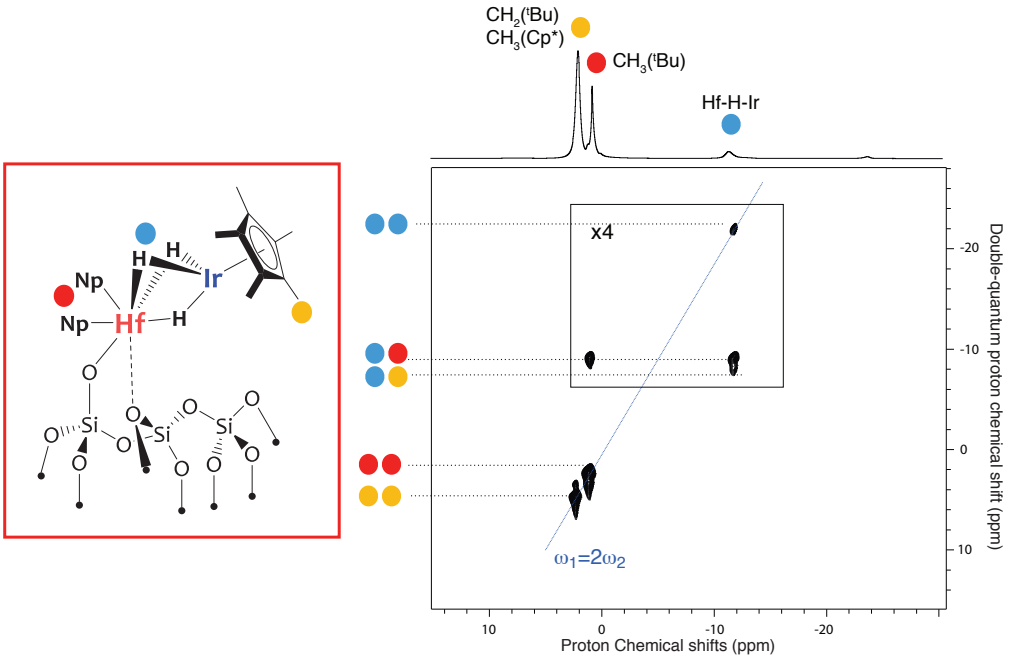

Figure 6.17: Proton SQ-DQ-(a) of a Hf=Ir complex (700 MHz, 2.5 mm probe, 18 kHz MAS frequency). The direct dimension corresponds to the ^{1}H-NMR spectrum (700 MHz, 2.5 mm probe, 18 kHz MAS frequency. The SQ-DQ spectrum has been zoomed by a factor 4 in the hydride region to clearly show the presence of autocorrelation at around (-11.5 ppm, -23 ppm). A total of 350 t_1 increments of 14.3 μs with 80 scans each were recorded. The total experimental time was 15 hours and 33 minutes. The dotted line corresponds to ω_1=2ω_2.

is shown above these 2 spectra. The ^{1}H solid-state NMR spectrum is very similar to the one of [≡SiOTa(CH_2^tBu)$_2$IrH_2(Cp*)] with two intense signals at 2.2 and 0.9 ppm assigned as previously to the CH_3(Cp*)) and to the CH_3(Np) moieties, respectively. The hydride signal appears again as a broad resonance at around -11 ppm. The DQ and TQ spectra show clear autocorrelations along respectively the ω_1=2ω_2 and ω_1=3ω_2 diagonals at around (-11.5 ppm, -23 ppm) and (-11.5 ppm, -34.5 ppm), indicating the presence of three dipolar-coupled hydride protons. As was the case for the other complexes, DQ and TQ correlations are also observed between the hydrides and the CH_3 group of the Cp* and neopentyl ligands, highlighted in the Figure by the color code. Therefore, the NMR analysis confirms that, unlike the Ta=Ir complex, the Hf=Ir bimetallic species has bridging hydrides between the two metal centers.

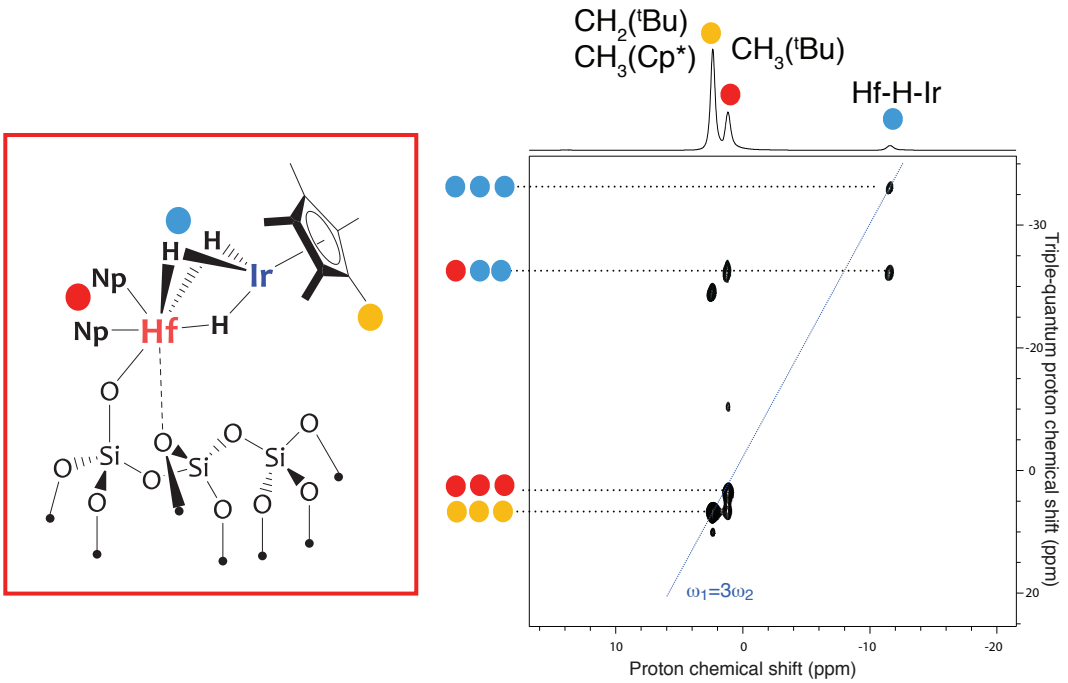

Figure 6.18: Proton SQ-TQ of a Hf=Ir complex (700 MHz, 2.5 mm probe, 18 kHz MAS frequency). The direct dimension corresponds to the ^{1}H-NMR spectrum (700 MHz, 2.5 mm probe, 18 kHz MAS frequency. The TQ experiment was recorded with a total of 300 t_1 increments of 8.3 μs with 72 scans each. The total experimental time was 12 hours. The dotted line corresponds to ω_1=3ω_2.

6.7 Conclusion

To summarize, we have shown that proton multiple-quantum NMR spetroscopy in combination with IR analysis and DFT calculations was a unique tool to characterize heteronuclear metallic grafted hydride complexes. In particular, this kind of spectroscopy enables the monitoring of the number of hydrides surrounding the metal centers. We have characterized bi- and tri-metallic Ta-Ir complexes and demonstrated that the surface species obtained using two different preparation protocols were different. Their structures could be unambiguously identified. As illustrated for the Hf=Ir complex, this robust methodology could be applied to a large set of multi-metallic hydride complexes.

Chapter 7

Conclusions and perspectives

"Each person does see the world in a different way. There is not a single, unifying, objective truth. We're all limited by our perspective."

-Siri Hustvedt-

Over the last three years, I have been working on the implementation and development of advanced NMR methods to characterize the atomic-scale structure of supported, well-defined organometallic catalysts, prepared by our collaborators, the groups of C. Thieuleux at C2P2 Lyon and of C. Copéret at ETH Zürich, using state-of-the art, controlled synthetic procedures. Three types of systems were investigated: an iridium N-heterocyclic carbene (NHC) material of high catalytic hydrogenation performance, tantalum-iridium heterobimetallic catalysts for H/D Exchange reactions and a single-site platinum complex, a prototypical example of highly dispersed isolated metal sites in single-atom catalysis. Two NMR approaches of high sensitivity were considered to overcome the sensitivity issue associated to the extreme dilution of the surface species of interest, namely Dynamic Nuclear Polarization (DNP) and proton NMR spectroscopy.

In chapter 4, we first extended the DNP Surface Enhanced NMR Spectroscopy (DNP SENS) approach proposed by Berruyer *et al.* in 2018 to investigate the 3D structure of the Ir-NHC catalytic site. We faced many unexpected difficulties during this project. The first one was related to the clear-cut observation of the NMR resonances of the imidazolium precursor in both the silver- and iridium-NHC materials. This forces us to implement NMR strategies that selectively probed long-range distances in the metallic complexes. The second difficulty was related to the interpretation of the 3D structure of the Ir-NHC catalytic site itself. Indeed, while we were expecting a structure that would have been folded back to the surface, with oxygen atoms stabilizing the overall molecular edifice, a set of conformations pointing to the porous cavity was instead obtained. We have been puzzled by this result for many months, working hard on improving and repeating the analysis of our NMR data, before postulating the presence of residual COD ligands, which could indeed be confirmed by EXAFS and chemical analysis. Overall our work demonstrated that DNP SENS can deal with multiple-site surfaces (or "dirty" surfaces where spectator and active species are jointly present), and be applied in many modern catalytic materials, where the series of surface chemical post-reactions leading to the preparation of the active site are not often incomplete. The DNP SENS analysis was done on a material of higher concentration of active sites than that published by Romanenko *et al.* in 2015. This modification was introduced in order to further improve the sensitivity of the NMR experiments (relatively low signal-to-noise ratio were observed in early DNP NMR studies carried out on the initial material). The higher loading likely hampers the removal of the COD ligand, though without changing the catalytic activity of the hybrid material. The COD ligand is released after the first catalytic cycle. A set of preliminary DNP SENS experiments were carried out on the material after reaction, which could not provide evidence for the presence of surface-metal interactions. However, the absence of such evidence does not imply that these latter do not exist. The systems that were investigated in this PhD are obviously extremely complex, and alternative strategies should be conceived to have direct experimental evidence for the stabilization of the immobilized species by the support, and demonstrate unambiguously that the silica matrix is not a simply passive carrier. Our work has been based on the implementation of REDOR experiments to probe long-range proximities. Alternative strategies could be introduced allowing for the quantitative measurement of additional inter-atomic distances and dihedral angles in order to further constrain the three-dimensional structure of the organometallic fragments. This could concern for example the implementation of dipolar-based double-quantum (DQ) ^{13}C filters. Taking advantage of the ^{13}C-label at the carbene position and of different chemical shifts for the carbene resonance in NHC- and Ir-NHC ligands, the possibility of selectively editing the sub-spectrum of the Ir-NHC complex could be envisaged. ^{13}C-^{13}C distances could then be measured, by recording DQ build-up curves under DNP conditions. Dihe-

dral angles could also be possibly measured via a new family of experiments that would correlate a recoupled chemical shift anisotropy (CSA) pattern with the neighboring CH dipolar couplings along the alkyl chain. However, it is highly probable that all these experiments would be extremely challenging sensitivity-wise. We also note that in case the silica support is replaced by an alumina or aluminosilicate matrix, the implementation of ^{27}Al-^{13}C or ^{27}Al-^{15}N Rotational Echo Adiabatic Passage DOuble Resonance (REAPDOR) experiments would allow one to measure inter-nuclear distances with surface aluminum sites, which could provide clear-cut structural information into the 3D fold of the same NHC ligands immobilized on a radically different type of solid support. The spectral signature of halogen atoms (here chlorine, but other atoms could be considered like boron or iodine) could also be possibly examined, as they play an important role in the catalytic activity, to decipher the nature of their interaction with the metal center.

In chapter 5, DNP SENS was combined with proton-detected experiments under very fast MAS to unravel the surface structure of isolated Pt sites. In particular, Ultra-Wideline NMR spectroscopy was applied under DNP conditions to get access to the extremely broad chemical shift anisotropy tensor of the surface Pt complex, while proton-detected heteronuclear multiple-quantum coherences (HMQC) pulse schemes provided information on isotropic chemical shift. The strategy implemented in this project was extremely innovative, as it was based on the joint application of two recent developments in MAS NMR, namely ^{1}H-detection at increased magic-angle spinning (MAS) frequencies and DNP to successfully tackle the sensitivity limitation associated with dilute species. We anticipate that the approach demonstrated here on a model platinum surface site could be widely applied to a variety of other Pt-based supported materials including recently described single atom Pt-catalysts. The static ^{195}Pt NMR experiments carried out on the surface complex required long experimental times (several days) despite the signal amplification provided by DNP. An obvious development of this project concerns the implementation of DNP enhanced non-synchronized proton-detected HMQC experiments, where the ^{195}Pt CSA spinning side-band manifold will appear in the indirect dimension. This could be done in 1.3 mm probes, spinning stably at 40 kHz and 100 K. We anticipate that such experiments could be recorded in a few hours. This remains however to be experimentally demonstrated. A few challenges are associated with the DNP formulation of the sample. In particular the presence of the radical will induce a shortening of the proton transverse coherence lifetimes, which will in turn affect the overall efficiency of the experiment.

Finally, a significant part of my PhD thesis was focused on the implementation of multiple-quantum proton NMR spectroscopy for the characterization of a new family of organometallic catalysts, namely hetero-bimetallic complexes (Chapter 6). Although this work does not represent a novel NMR strategy, we believe that triple-quantum experiments were applied here for the first time to "count" the number of hydrides around metal centres in highly reactive systems. This approach appeared extremely efficient to differentiate between surface species prepared using different synthetic methodologies, and for which the one-dimensional proton and carbon-13 spectra are identical. Proton multiple coherences of higher order could in principle be generated to characterize complexes bearing more than 3 protons, such as the Ta-Ir_2 complex investigated during this project. This approach however is hampered by the very low sensitivity of the creation of high order coherences. Combining this methodology with the amplification power of DNP could be a way to go, if it were not the extreme reactivity of the surface complexes that prevent the use of conventional impregnation methods. These systems are indeed highly reactive to solvents, probably to radicals, and in addition highly pyrophoric when in contact with oxygen and degrade

rapidly upon contact with air as shown in Figure S5 in the Appendix. The development of alternative and targeted solutions to hyperpolarize these complexes would be necessary.

In conclusion, a set of state-of-the art NMR methods have been implemented during this PhD to provide unique atomic-level information on the structure of support catalysts. While I encountered several unexpected problems all along this three-year work, several key achievements were made. Several questions are still open and new developments are foreseen, which will likely be solved / made in the near future by the ongoing and hard work of the CRMN members and their collaborators.

Abbreviations

AFM	Atomic Force Microscopy
BABA	BAck-to-BAck
BDPA	1,3-BisDiphenylene-2-PhenylAllyl
bTbK	bis-TEMPO-bis-Ketal
CE	Cross-Effect
COD	CycloOcta-1,5-Diene
CP	Cross-Polarization
CPMG	Carr-Purcell-Meiboom-Gill
CSA	Chemical Shift Anisotropy
CW	Continous Waves
DFT	Density Functional Theory
DMSO	DiMethylSulfOxide
DNP	Dynamic Nuclear Polarization
EPR	Electron Paramagnetic Resonance
EXAFS	Extended X-Ray Absorption Fine Structure
FS-REDOR	Frequency Selective Rotational Echo-DOuble Resonance
FTIR	Fourier Transform InfraRed
HETCOR	HETeronuclear CORrelation
HMQC	Heteronuclear Multiple Quantum Coherence
IR	InfraRed Spectroscopy
IWI	Incipient Wetness Impregnation
LAC	Level Anti -Crossings
LT	Low Temprature
MAS	Magic Angle Spinning
MOF	Metal-Organic Frameworks
MOP	Mesoporous Organic Polymers
MQ	Multiple Quantum
NHC	N-Heterocyclic Carbene
NMR	Nuclear Magnetic Resonance
NP	Nanoparticles

Np	Neopentyl
OE	Overhauser Effect
PA	Polarizing Agent
QC	Quantum Coherences
REDOR	Rotational Echo-DOuble Resonance
SABRE	Signal Amplification By Reversible Exchange
SE	Solid effect
SENS	Surface Enhanced NMR Spectroscopy
SOMC	Surface OrganoMetallic Chemistry
SSNMR	Solid-State NMR
STM	Scanning Tunneling Microscopy
TCE	1,1,2,2-TetraChloroEthane
TEMPO	(2,2,6,6-TEtraMethylPiperidin-1-yl)Oxyl
UWNMR	UltraWideline-NMR
VOCS	Variable Offset Cumulative Spectrum
WURST	Wideband Uniform-Rate Smooth-Truncation
XPS	X-Ray Photoelectron Spectroscopy

Bibliography

[1] Hugh S. Taylor. *Encyclopædia Britannica, inc.*, 2018.

[2] Humphry Davy. "The Bakerian Lecture". *Phil Trans Royal Soc (London)*, 1806.

[3] American Chemical Society Report, Technology Vision 2020: The Chemical Industry, December 1996.

[4] Ioana Fechete, Ye Wang, and Jacques C. Védrine. The past, present and future of heterogeneous catalysis. *Catal. Today*, 189(1):2–27, 2012.

[5] Noritaka Mizuno and Makoto Misono. Heterogeneous catalysis. *Chem. Rev.*, 98(1):199–217, 1998.

[6] Wolfgang Hölderich, Michael Hesse, and Fritz Näumann. Zeolites: Catalysts for Organic Syntheses. *Angew. Chem., Int. Ed.*, 27(2):226–246, 1988.

[7] Stephen T Wilson, Brent M Lok, Celeste A Messina, Thomas R Cannan, and Edith M Flanigen. Aluminophosphate molecular sieves: a new class of microporous crystalline inorganic solids. *J. Am. Chem. Soc.*, 104(4):1146–1147, 1982.

[8] Soofin Cheng. From layer compounds to catalytic materials. *Catal. Today*, 49(1-3):303–312, 1999.

[9] Yoshinori Ando and Sumio Iijima. Preparation of carbon nanotubes by arc-discharge evaporation. *Jpn. J. Appl. Phys., Part 2*, 32:L107–L107, 1993.

[10] Chuan De Wu. Crystal Engineering of Metal-Organic Frameworks for Heterogeneous Catalysis. *Selective Nanocatalysts and Nanoscience: Concepts for Heterogeneous and Homogeneous Catalysis*, pages 271–298, 2011.

[11] Mika Lindén, Stefan Schacht, Ferdi Schüth, Allan Steel, and Klaus K Unger. Recent advances in nano-and macroscale control of hexagonal, mesoporous materials. *J. Porous Mater.*, 5(3-4):177–193, 1998.

[12] Dongyuan Zhao, Jianglin Feng, Qisheng Huo, Nicholas Melosh, Glenn H Fredrickson, Bradley F Chmelka, and Galen D Stucky. Triblock copolymer syntheses of mesoporous silica with periodic 50 to 300 angstrom pores. *Science*, 279(5350):548–552, 1998.

[13] Chrisophe Copéret and Jean-Marie Basset. Strategies to immobilize well-defined olefin metathesis catalysts: Supported homogeneous catalysis vs. surface organometallic chemistry. *Adv. Synth. Catal.*, 349(1-2):78–92, 2007.

[14] Avelino Corma and Hermenegildo Garcia. Crossing the borders between homogeneous and heterogeneous catalysis: developing recoverable and reusable catalytic systems. *Top. Catal.*, 48(1-4):8–31, 2008.

[15] Christophe Copéret, Florian Allouche, Ka Wing Chan, Matthew P Conley, Murielle F Delley, Alexey Fedorov, Ilia B Moroz, Victor Mougel, Margherita Pucino, Keith Searles, Keishi Yamamoto, and Pavel A Zhizhko. Bridging the gap between industrial and well-defined supported catalysts. *Angew. Chem., Int. Ed.*, 57(22):6398–6440, 2018.

[16] Christophe Copéret, Aleix Comas-Vives, Matthew P Conley, Deven P Estes, Alexey Fedorov, Victor Mougel, Haruki Nagae, Francisco Nunez-Zarur, and Pavel A Zhizhko. Surface organometallic and coordination chemistry toward single-site heterogeneous catalysts: strategies, methods, structures, and activities. *Chem. Rev.*, 116(2):323–421, 2016.

[17] Manoja K Samantaray, Eva Pump, Anissa Bendjeriou-Sedjerari, Valerio D'Elia, Jérémie DA Pelletier, Matteo Guidotti, Rinaldo Psaro, and Jean-Marie Basset. Surface organometallic chemistry in heterogeneous catalysis. *Chem. Soc. Rev.*, 47(22):8403–8437, 2018.

[18] Matthew P Conley, Christophe Coperet, and Chloe Thieuleux. Mesostructured hybrid organic–silica materials: ideal supports for well-defined heterogeneous organometallic catalysts. *ACS Catal.*, 4(5):1458–1469, 2014.

[19] Norihiro Mizoshita, Takao Tani, and Shinji Inagaki. Syntheses, properties and applications of periodic mesoporous organosilicas prepared from bridged organosilane precursors. *Chem. Soc. Rev.*, 40(2):789–800, 2011.

[20] Yugen Zhang and Jackie Y Ying. Main-chain organic frameworks with advanced catalytic functionalities. *ACS Catal.*, 5(4):2681–2691, 2015.

[21] Jérémie DA Pelletier and Jean-Marie Basset. Catalysis by design: Well-defined single-site heterogeneous catalysts. *Acc. Chem. Res.*, 49(4):664–677, 2016.

[22] Manoja K. Samantaray, Eva Pump, Anissa Bendjeriou-Sedjerari, Valerio D'Elia, Jérémie D.A. Pelletier, Matteo Guidotti, Rinaldo Psaro, and Jean Marie Basset. Surface organometallic chemistry in heterogeneous catalysis. *Chem. Soc. Rev.*, 47(22):8403–8437, 2018.

[23] Dean W. Sindorf and Gary E. Maciel. Cross-polarization/magic-angle-spinning silicon-29 nuclear magnetic resonance study of silica gel using trimethylsilane bonding as a probe of surface geometry and reactivity. *J. Phys. Chem.*, 86(26):5208–5219, 1982.

[24] Laurie Bemi, Howard C Clark, Julian A Davies, Colin A Fyfe, and Rodrick E Wasylishen. Studies of phosphorus (iii) ligands and their complexes of nickel (ii), palladium (ii), and platinum (ii) immobilized on insoluble supports by high-resolution solid-state phosphorus-31 nmr using magic-angle spinning techniques. *J. Am. Chem. Soc.*, 104(2):438–445, 1982.

[25] David Gajan, Daniel Levine, Eva Zocher, Christophe Copéret, Anne Lesage, and Lyndon Emsley. Probing surface site heterogeneity through 1d and inadequate 31 p solid state nmr spectroscopy of silica supported pme 3-au (i) adducts. *Chem. Sci.*, 2(5):928–931, 2011.

[26] Nicolas Merle, Guillaume Girard, Nicolas Popoff, Aimery De Mallmann, Yassine Bouhoute, Julien Trébosc, Elise Berrier, Jean-François Paul, Christopher P Nicholas, Iker Del Rosal, et al. On the track to silica-supported tungsten oxo metathesis catalysts: input from 17o solid-state nmr. *Inorg. Chem.*, 52(17):10119–10130, 2013.

[27] Francesca Reineri, Tommaso Boi, and Silvio Aime. Parahydrogen induced polarization of 13 c carboxylate resonance in acetate and pyruvate. *Nat. Comm.*, 6(1):1–6, 2015.

[28] Daniel Raftery, Henry Long, Thomas Meersmann, Philip J Grandinetti, Linda Reven, and Alex Pines. High-field NMR of adsorbed xenon polarized by laser pumping. *Phys. Rev. lett.*, 66(5):584, 1991.

[29] Heiko G Niessen, Dana Schleyer, Sabine Wiemann, Joachim Bargon, Stephan Steines, and Birgit Driessen-Hoelscher. In situ PHIP-NMR studies during the stereoselective hydrogenation of sorbic acid with a [Cp* Ru]+ catalyst. *Mag. Res. Chem.*, 38(9):747–750, 2000.

[30] Andrei Nossov, Flavien Guenneau, Marie-Anne Springuel-Huet, Elias Haddad, Valérie Montouillout, Benno Knott, Frank Engelke, Christian Fernandez, and Antoine Gédéon. Continuous flow hyperpolarized ^{129}Xe-MAS NMR studies of microporous materials. *Phys. Chem. Chem. Phys.*, 5(20):4479–4483, 2003.

[31] Dudari B Burueva, Larisa M Kovtunova, Valerii I Bukhtiyarov, Kirill V Kovtunov, and Igor V Koptyug. Single-site heterogeneous catalysts: From synthesis to NMR signal enhancement. *Chem. - Eur. J.*, 25(6):1420–1431, 2019.

[32] Erika Weiland, Marie-Anne Springuel-Huet, Andrei Nossov, and Antoine Gedeon. ^{129}Xenon nmr: Review of recent insights into porous materials. *Microporous Mesoporous Mater.*, 225:41–65, 2016.

[33] Lars T Kuhn and Ü Akbey. *Hyperpolarization methods in NMR spectroscopy*, volume 338. Springer, 2013.

[34] Albert W. Overhauser. Polarization of nuclei in metals. *Phys. Rev.*, 92(2):411–415, 1953.

[35] T. R. Carver and C. P. Slichter. Polarization of nuclear spins in metals [15]. *Phys. Rev.*, 92(1):212–213, 1953.

[36] Anatole Abragam and Warren G Proctor. Une nouvelle méthode de polarisation dynamique des noyaux atomiques dans les solides. *Comptes Rendus Hebdomadaires Des Seances De L Academie Des Sciences*, 246(15):2253–2256, 1958.

[37] AV Kessenikh, VI Lushchikov, AA Manenkov, and Yu V Taran. Proton polarization in irradiated polyethylenes. *Soviet Phys.-Solid State (English Transl.)*, 5, 1963.

[38] Tim R Eichhorn, Ben van den Brandt, Patrick Hautle, Anne Henstra, and Tom W Wenckebach. Dynamic nuclear polarisation via the integrated solid effect ii: experiments on naphthalene-h 8 doped with pentacene-d 14. *Mol.Phys.*, 112(13):1773–1782, 2014.

[39] Guinevere Mathies, Sheetal Jain, Marcel Reese, and Robert G Griffin. Pulsed dynamic nuclear polarization with trityl radicals. *J. Phys. Chem. Lett.*, 7(1):111–116, 2016.

[40] Thach V Can, Joseph J Walish, Timothy M Swager, and Robert G Griffin. Time domain dnp with the NOVEL sequence. *J. Chem. Phys.*, 143(5):054201, 2015.

[41] Kong Ooi Tan, Chen Yang, Ralph T Weber, Guinevere Mathies, and Robert G Griffin. Time-optimized pulsed dynamic nuclear polarization. *Sci. adv.*, 5(1):eaav6909, 2019.

[42] Pierrick Berruyer, Moreno Lelli, Matthew P Conley, Daniel L Silverio, Cory M Widdifield, Georges Siddiqi, David Gajan, Anne Lesage, Christophe Copéret, and Lyndon Emsley. Three-dimensional structure determination of surface sites. *J. Am. Chem. Soc.*, 139(2):849–855, 2017.

[43] Kent R Thurber and Robert Tycko. Theory for cross effect dynamic nuclear polarization under magic-angle spinning in solid state nuclear magnetic resonance: the importance of level crossings. *J. Phys. Chem.*, 137(8):084508, 2012.

[44] Frederic Mentink-Vigier, Ümit Akbey, Yonatan Hovav, Shimon Vega, Hartmut Oschkinat, and Akiva Feintuch. Fast passage dynamic nuclear polarization on rotating solids. *J. Magn. Res.*, 224:13–21, 2012.

[45] Björn Corzilius. Theory of solid effect and cross effect dynamic nuclear polarization with half-integer high-spin metal polarizing agents in rotating solids. *Phys. Chem. Chem. Phys.*, 18(39):27190–27204, 2016.

[46] Thach V Can, Marc A Caporini, Frédéric Mentink-Vigier, Bjorn Corzilius, Joseph J Walish, Mélanie Rosay, Werner E Maas, Marc Baldus, Shimon Vega, Timothy M Swager, and Robert G Griffin. Overhauser effects in insulating solids. *J. Chem. Phys.*, 141(6):064202, 2014.

[47] Gary J Gerfen, Lino R Becerra, Dennis A Hall, Robert G Griffin, Richard J Temkin, and David J Singel. High frequency (140 ghz) dynamic nuclear polarization: polarization transfer to a solute in frozen aqueous solution. *J. Chem. Phys.*, 102(24):9494–9497, 1995.

[48] Kan-Nian Hu, Hsiao-hua Yu, Timothy M Swager, and Robert G Griffin. Dynamic nuclear polarization with biradicals. *J. Am. Chem. Soc.*, 126(35):10844–10845, 2004.

[49] Changsik Song, Kan-Nian Hu, Chan-Gyu Joo, Timothy M Swager, and Robert G Griffin. Totapol: a biradical polarizing agent for dynamic nuclear polarization experiments in aqueous media. *J. Am. Chem. Soc.*, 128(35):11385–11390, 2006.

[50] Yoh Matsuki, Thorsten Maly, Olivier Ouari, Hakim Karoui, François Le Moigne, Egon Rizzato, Sevdalina Lyubenova, Judith Herzfeld, Thomas Prisner, Paul Tordo, et al. Dynamic nuclear polarization with a rigid biradical. *Angew. Chem., Int. Ed.*, 48(27):4996–5000, 2009.

[51] Alexandre Zagdoun, Gilles Casano, Olivier Ouari, Giuseppe Lapadula, Aaron J Rossini, Moreno Lelli, Mathieu Baffert, David Gajan, Laurent Veyre, Werner E Maas, Melanie Rosay, Ralph T Weber, Chloé Thieuleux, Christophe Copéret, Anne Lesage, Paul Tordo, and Lyndon Emsley. A slowly relaxing rigid biradical for efficient dynamic nuclear polarization surface-enhanced nmr spectroscopy: Expeditious characterization of functional group manipulation in hybrid materials. *J. Am. Chem. Soc.*, 134(4):2284–2291, 2012.

[52] Alexandre Zagdoun, Gilles Casano, Olivier Ouari, Martin Schwarzwälder, Aaron J Rossini, Fabien Aussenac, Maxim Yulikov, Gunnar Jeschke, Christophe Copéret, Anne Lesage, Paul

Tordo, and Lyndon Emsley. Large molecular weight nitroxide biradicals providing efficient dynamic nuclear polarization at temperatures up to 200 K. *J. Am. Chem. Soc.*, 135(34):12790–12797, 2013.

[53] Claire Sauvée, Melanie Rosay, Gilles Casano, Fabien Aussenac, Ralph T Weber, Olivier Ouari, and Paul Tordo. Highly efficient, water-soluble polarizing agents for dynamic nuclear polarization at high frequency. *Angew. Chem., Int. Ed.*, 52(41):10858–10861, 2013.

[54] Hideo Sato, Velavan Kathirvelu, Alistair Fielding, James P Blinco, AS Micallef, Steven E Bottle, Sandra S Eaton, and Gareth R Eaton. Impact of molecular size on electron spin relaxation rates of nitroxyl radicals in glassy solvents between 100 and 300 K. *Mol. Phys.*, 105(15-16):2137–2151, 2007.

[55] Dominik J Kubicki, Gilles Casano, Martin Schwarzwälder, Sébastien Abel, Claire Sauvée, Karthikeyan Ganesan, Maxim Yulikov, Aaron J Rossini, Gunnar Jeschke, Christophe Copéret, Anne Lesage, Paul Tordo, Olivier Ouari, and Lyndon Emsley. Rational design of dinitroxide biradicals for efficient cross-effect dynamic nuclear polarization. *Chem. Sci.*, 7(1):550–558, 2016.

[56] Anil P Jagtap, Michel-Andreas Geiger, Daniel Stöppler, Marcella Orwick-Rydmark, Hartmut Oschkinat, and Snorri Th Sigurdsson. bcTol: a highly water-soluble biradical for efficient dynamic nuclear polarization of biomolecules. *Chem. Comm.*, 52(43):7020–7023, 2016.

[57] Vladimir K Michaelis, Albert A Smith, Björn Corzilius, Olesya Haze, Timothy M Swager, and Robert G Griffin. High-field ^{13}C dynamic nuclear polarization with a radical mixture. *J. Am. Chem. Soc.*, 135(8):2935–2938, 2013.

[58] Guinevere Mathies, Marc A Caporini, Vladimir K Michaelis, Yangping Liu, Kan-Nian Hu, Deni Mance, Jay L Zweier, Melanie Rosay, Marc Baldus, and Robert G Griffin. Efficient dynamic nuclear polarization at 800 MHz/527 GHz with trityl-nitroxide biradicals. *Angew. Chem., Int. Ed.*, 54(40):11770–11774, 2015.

[59] Dorothea Wisser, Ganesan Karthikeyan, Alicia Lund, Gilles Casano, Hakim Karoui, Maxim Yulikov, Georges Menzildjian, Arthur C Pinon, Armin Purea, Frank Engelke, Sachin R Chaudhari, Dominik Kubicki, Aaron J Rossini, Ilia B Moroz, David Gajan, Jeschke Gunnar Copéret, Christophe, Moreno Lelli, Lyndon Emsley, Anne Lesage, and Olivier Ouari. BDPA-nitroxide biradicals tailored for efficient dynamic nuclear polarization enhanced solid-state NMR at magnetic fields up to 21.1 T. *J. Am. Chem. Soc.*, 140(41):13340–13349, 2018.

[60] Frédéric Mentink-Vigier, Ildefonso Marin-Montesinos, Anil P Jagtap, Thomas Halbritter, Johan Van Tol, Sabine Hediger, Daniel Lee, Snorri Th Sigurdsson, and Gaël De Paëpe. Computationally assisted design of polarizing agents for dynamic nuclear polarization enhanced NMR: the AsymPol family. *J. Am. Chem. Soc.*, 140(35):11013–11019, 2018.

[61] Alicia Lund, Gilles Casano, Georges Menzildjian, Monu Kaushik, Gabriele Stevanato, Maxim Yulikov, Ribal Jabbour, Dorothea Wisser, Marc Renom-Carrasco, Chloé Thieuleux, Florian Bernada, Hakim Karoui, Didier Siri, Melanie Rosay, Ivan V Sergeyev, David Gajan, Moreno Lelli, Lyndon Emsley, Olivier Ouari, and Anne Lesage. TinyPols: a family of water-soluble binitroxides tailored for dynamic nuclear polarization enhanced nmr spectroscopy at 18.8 and 21.1 T. *Chem. Sci.*, 2020.

[62] Moreno Lelli, Sachin R Chaudhari, David Gajan, Gilles Casano, Aaron J Rossini, Olivier Ouari, Paul Tordo, Anne Lesage, and Lyndon Emsley. Solid-state dynamic nuclear polarization at 9.4 and 18.8 T from 100 K to room temperature. *J. Am. Chem. Soc.*, 137(46):14558–14561, 2015.

[63] Sachin Rama Chaudhari, John M Griffin, Moreno Lelli, Katharina Broch, Vincent Lemaur, Yoann Olivier, Henning Sirringhaus, Clare P Grey, Anne Lessage, and Lyndon Emsley. New developments in surface-enhanced solid-state nmr spectroscopy and their applications. *Found. Crystallogr.*, 70:C321, 2017.

[64] Monu Kaushik, Mian Qi, Adelheid Godt, and Björn Corzilius. Bis-gadolinium complexes for solid effect and cross effect dynamic nuclear polarization. *Angew. Chem.*, 129(15):4359–4363, 2017.

[65] Tanmoy Chakrabrty, Nir Goldin, Akiva Feintuch, Lothar Houben, and Michal Leskes. Paramagnetic metal ion dopants as polarization agents for DNP NMR spectroscopy in inorganic solids. *Chem. Phys. Chem.*, 5:644–656, 2018.

[66] Daniel Jardon-Alvarez, Guy Reuveni, Adi Harchol, and Michal Leskes. Enabling natural abundance ^{17}O solid state nmr by direct polarization from paramagnetic metal ions. *J. Phys. Chem. Lett.*, 2020.

[67] Björn Corzilius. Paramagnetic metal ions for dynamic nuclear polarization. *EMagRes*, pages 179–194, 2007.

[68] Grzegorz Kwiatkowski, Yevhen Polyhach, Fabian Jähnig, Toni Shiroka, Fabian HL Starsich, Matthias Ernst, and Sebastian Kozerke. Exploiting endogenous surface defects for dynamic nuclear polarization of silicon micro-and nanoparticles. *J. Phys. Chem., C*, 122(44):25668–25680, 2018.

[69] Scott L Carnahan, Amrit Venkatesh, Frederic A Perras, James F Wishart, and Aaron J Rossini. High-field magic angle spinning dynamic nuclear polarization using radicals created by γ-irradiation. *J. Phys. Chem. Lett.*, 10(17):4770–4776, 2019.

[70] Lino R Becerra, Gary J Gerfen, Brenden F Bellew, Jeff A Bryant, Dennis A Hall, Souheil J Inati, Ralph T Weber, Sun Un, Thomas F Prisner, Ann E Mcdermott, Kenneth W Fishbein, Kenneth E Kreischer, Richard J Temkin, David J Singel, and Robert G Griffin. A spectrometer for dynamic nuclear polarization and electron paramagnetic resonance at high frequencies. *J. Magn. Res., Series A*, 117(1):28–40, 1995.

[71] Gary J Gerfen, Lino R Becerra, Dennis A Hall, Robert G Griffin, Richard J Temkin, and David J Singel. High frequency (140 Ghz) dynamic nuclear polarization: polarization transfer to a solute in frozen aqueous solution. *J. Chem. Phys.*, 102(24):9494–9497, 1995.

[72] Melanie Rosay, Leo Tometich, Shane Pawsey, Reto Bader, Robert Schauwecker, Monica Blank, Philipp M Borchard, Stephen R Cauffman, Kevin L Felch, Ralph T Weber, Richard J Temkin, Robert G Griffin, and Werner E Maas. Solid-state dynamic nuclear polarization at 263 GHz: spectrometer design and experimental results. *Phys. Chem. Chem. Phys.*, 12(22):5850–5860, 2010.

[73] Melanie Rosay, Monica Blank, and Frank Engelke. Instrumentation for solid-state dynamic nuclear polarization with magic angle spinning NMR. *J. Magn. Res.*, 264:88–98, 2016.

[74] Yoh Matsuki, Keisuke Ueda, Toshitaka Idehara, Ryosuke Ikeda, Isamu Ogawa, Shinji Nakamura, Mitsuru Toda, Takahiro Anai, and Toshimichi Fujiwara. Helium-cooling and-spinning dynamic nuclear polarization for sensitivity-enhanced solid-state NMR at 14 T and 30 K. *J. Mag. Res.*, 225:1–9, 2012.

[75] Daniel Lee, Eric Bouleau, Pierre Saint-Bonnet, Sabine Hediger, and Gaël De Paëpe. Ultra-low temperature mas-dnp. *J. Mag. Res.*, 264:116–124, 2016.

[76] Aaron J Rossini, Alexandre Zagdoun, Moreno Lelli, Anne Lesage, Christophe Coperet, and Lyndon Emsley. Dynamic nuclear polarization surface enhanced NMR spectroscopy. *Acc. Chem. Res.*, 46(9):1942–1951, 2013.

[77] Wei-Chih Liao, Behnaz Ghaffari, Christopher P Gordon, Jun Xu, and Christophe Copéret. Dynamic nuclear polarization surface enhanced nmr spectroscopy (DNP SENS): principles, protocols, and practice. *Curr. Opin. Colloid Interface Sci.*, 33:63–71, 2018.

[78] Pierrick Berruyer, Lyndon Emsley, and Anne Lesage. DNP in materials science: Touching the surface. *eMagRes*, 7(4):93–104, 2018.

[79] Anne Lesage, Moreno Lelli, David Gajan, Marc A Caporini, Veronika Vitzthum, Pascal Miéville, Johan Alauzun, Arthur Roussey, Chloé Thieuleux, Ahmad Mehdi, Geoffrey Bodenhausen, Christophe Copéret, and Lyndon Emsley. Surface enhanced nmr spectroscopy by dynamic nuclear polarization. *J. Am. Chem. Soc.*, 132(44):15459–15461, 2010.

[80] Moreno Lelli, David Gajan, Anne Lesage, Marc A Caporini, Veronika Vitzthum, Pascal Miéville, Florent Héroguel, Fernando Rascón, Arthur Roussey, Chloé Thieuleux, et al. Fast characterization of functionalized silica materials by silicon-29 surface-enhanced nmr spectroscopy using dynamic nuclear polarization. *J. Am. Chem. Soc.*, 133(7):2104–2107, 2011.

[81] Bénédicte Elena, Gaël de Paëpe, and Lyndon Emsley. Direct spectral optimisation of proton–proton homonuclear dipolar decoupling in solid-state NMR. *Chem. Phys. Lett.*, 398(4-6):532–538, 2004.

[82] Hiroki Nagashima, Julien Trebosc, Yoshihiro Kon, Kazuhiko Sato, Olivier Lafon, and Jean-Paul Amoureux. Observation of low-γ quadrupolar nuclei by surface-enhanced NMR spectroscopy. *J. Am. Chem. Soc.*, 2020.

[83] Raynald Giovine, Julien Trébosc, Frédérique Pourpoint, Olivier Lafon, and Jean-Paul Amoureux. Magnetization transfer from protons to quadrupolar nuclei in solid-state NMR using PRESTO or dipolar-mediated refocused INEPT methods. *J. Mag. Res.*, 299:109–123, 2019.

[84] Xin Zhao, Wilfried Hoffbauer, Jörn Schmedt auf der Günne, and Malcolm H Levitt. Heteronuclear polarization transfer by symmetry-based recoupling sequences in solid-state NMR. *Solid State Nucl. Magn. Reson.*, 26(2):57–64, 2004.

[85] Jacco D van Beek, Ray Dupree, and Malcolm H Levitt. Symmetry-based recoupling of ^{17}O-^{1}H spin pairs in magic-angle spinning NMR. *J. Mag. Res.*, 179(1):38–48, 2006.

[86] Snædís Björgvinsdóttir, Brennan J Walder, Arthur C Pinon, and Lyndon Emsley. Bulk nuclear hyperpolarization of inorganic solids by relay from the surface. *J. Am. Chem. Soc.*, 140(25):7946–7951, 2018.

[87] Snædís Björgvinsdóttir, Brennan J Walder, Nicolas Matthey, and Lyndon Emsley. Maximizing nuclear hyperpolarization in pulse cooling under MAS. *J. Mag. Res.*, 300:142–148, 2019.

[88] Krijn P De Jong. *Synthesis of solid catalysts*. John Wiley & Sons, 2009.

[89] Alexandre Zagdoun, Aaron J. Rossini, David Gajan, Adrien Bourdolle, Olivier Ouari, Melanie Rosay, Werner E. Maas, Paul Tordo, Moreno Lelli, Lyndon Emsley, Anne Lesage, and Christophe Copéret. Non-aqueous solvents for DNP surface enhanced NMR spectroscopy. *Chem. Comm.*, 48(5):654–656, 2012.

[90] Akinori Kagawa, Yu Murokawa, Kazuyuki Takeda, and Masahiro Kitagawa. Optimization of ^{1}H spin density for dynamic nuclear polarization using photo-excited triplet electron spins. *J. Mag. Res.*, 197(1):9–13, 2009.

[91] Ümit Akbey, W Trent Franks, Arne Linden, Sascha Lange, Robert G Griffin, Barth-Jan van Rossum, and Hartmut Oschkinat. Dynamic nuclear polarization of deuterated proteins. *Angew. Chem., Int. Ed.*, 49(42):7803–7806, 2010.

[92] Lloyd Lumata, Matthew E Merritt, and Zoltan Kovacs. Influence of deuteration in the glassing matrix on ^{13}C dynamic nuclear polarization. *Phys. Chem. Chem. Phys.*, 15(19):7032–7035, 2013.

[93] Frédéric A Perras, Regina R Reinig, Igor I Slowing, Aaron D Sadow, and Marek Pruski. Effects of biradical deuteration on the performance of DNP: towards better performing polarizing agents. *Phys. Chem. Chem. Phys.*, 18(1):65–69, 2016.

[94] Ta-Chung Ong, Melody L Mak-Jurkauskas, Joseph J Walish, Vladimir K Michaelis, Björn Corzilius, Albert A Smith, Andrew M Clausen, Janet C Cheetham, Timothy M Swager, and Robert G Griffin. Solvent-free dynamic nuclear polarization of amorphous and crystalline ortho-terphenyl. *J. Phys. Chem., B*, 117(10):3040–3046, 2013.

[95] Jasmine Viger-Gravel, Pierrick Berruyer, David Gajan, Jean-Marie Basset, Anne Lesage, Paul Tordo, Olivier Ouari, and Lyndon Emsley. Frozen acrylamide gels as dynamic nuclear polarization matrices. *Angew. Chem., Int. Ed.*, 56(30):8726–8730, 2017.

[96] Michael P Hanrahan, Yunhua Chen, Rafael Blome-Fernández, Jennifer L Stein, Gregory F Pach, Marquix AS Adamson, Nathan R Neale, Brandi M Cossairt, Javier Vela, and Aaron J Rossini. Probing the surface structure of semiconductor nanoparticles by DNP SENS with Dielectric Support Materials. *J. Am. Chem. Soc.*, 141(39):15532–15546, 2019.

[97] Frédéric A Perras, Lin-Lin Wang, J Sebastian Manzano, Umesh Chaudhary, Naftali N Opembe, Duane D Johnson, Igor I Slowing, and Marek Pruski. Optimal sample formulations for DNP SENS: The importance of radical-surface interactions. *Curr. Opin. Colloid Interface Sci.*, 33:9–18, 2018.

[98] Alexandre Zagdoun, Aaron J Rossini, Matthew P Conley, Wolfram R Grüning, Martin Schwarzwälder, Moreno Lelli, W Trent Franks, Hartmut Oschkinat, Christophe Copéret, Lyndon Emsley, and Anne Lesage. Improved dynamic nuclear polarization surface-enhanced NMR spectroscopy through controlled incorporation of deuterated functional groups. *Angew. Chem., Int. Ed.*, 52(4):1222–1225, 2013.

[99] Sachin R Chaudhari, Dorothea Wisser, Arthur C Pinon, Pierrick Berruyer, David Gajan, Paul Tordo, Olivier Ouari, Christian Reiter, Frank Engelke, Christophe Copéret, Moreno Lelli, Anne Lesage, and Lyndon Emsley. Dynamic nuclear polarization efficiency increased by very fast magic angle spinning. *J. Am. Chem. Soc.*, 139(31):10609–10612, 2017.

[100] Eva Pump, Jasmine Viger-Gravel, Edy Abou-Hamad, Manoja K Samantaray, Bilel Hamzaoui, Andrei Gurinov, Dalaver H Anjum, David Gajan, Anne Lesage, Anissa Bendjeriou-Sedjerari, Lyndon Emsley, and Jean-Marie Basset. Reactive surface organometallic complexes observed using dynamic nuclear polarization surface enhanced nmr spectroscopy. *Chem. Sci.*, 8(1):284–290, 2017.

[101] Wei-Chih Liao, Ta-Chung Ong, David Gajan, Florian Bernada, Claire Sauvée, Maxim Yulikov, Margherita Pucino, Roman Schowner, Martin Schwarzwälder, Michael R Buchmeiser, Gunnar Jeschke, Paul Tordo, Olivier Ouari, Anne Lesage, Lyndon Emsley, and Christophe Copéret. Dendritic polarizing agents for dnp sens. *Chem. Sci.*, 8(1):416–422, 2017.

[102] Eva Pump, Anissa Bendjeriou-Sedjerari, Jasmine Viger-Gravel, David Gajan, Baptiste Scotto, Manoja K Samantaray, Edy Abou-Hamad, Andrei Gurinov, Walid Almaksoud, Zhen Cao, Anne Lesage, Luigi Cavallo, Lyndon Emsley, and Jean-Marie Basset. Predicting the DNP-SENS efficiency in reactive heterogeneous catalysts from hydrophilicity. *Chem. Sci.*, 9(21):4866–4872, 2018.

[103] Alexander Yakimov, Deni Mance, Keith Searles, and Christophe Copéret. A formulation protocol with pyridine to enable DNP-SENS on reactive surface sites: Case study with olefin polymerization and metathesis catalysts. 2020.

[104] Moreno Lelli, Aaron J Rossini, Gilles Casano, Olivier Ouari, Paul Tordo, Anne Lesage, and Lyndon Emsley. Hydrophobic radicals embedded in neutral surfactants for dynamic nuclear polarization of aqueous environments at 9.4 T. *Chem. Comm.*, 50(71):10198–10201, 2014.

[105] Michelle Ha, Alyxandra N Thiessen, Ivan V Sergeyev, Jonathan GC Veinot, and Vladimir K Michaelis. Endogenous dynamic nuclear polarization nmr of hydride-terminated silicon nanoparticles. *Solid State Nucl. Magn. Reson.*, 100:77–84, 2019.

[106] Evan R McCarney and Songi Han. Spin-labeled gel for the production of radical-free dynamic nuclear polarization enhanced molecules for nmr spectroscopy and imaging. *J. Magn. Res.*, 190(2):307–315, 2008.

[107] Veronika Vitzthum, Françoise Borcard, Sami Jannin, Mylène Morin, Pascal Miéville, Marc A Caporini, Andrzej Sienkiewicz, Sandrine Gerber-Lemaire, and Geoffrey Bodenhausen. Fractional spin-labeling of polymers for enhancing NMR sensitivity by solvent-free dynamic nuclear polarization. *CPCHFT*, 12(16):2929–2932, 2011.

[108] Aany Sofia Lilly Thankamony, Olivier Lafon, Xingyu Lu, Fabien Aussenac, Melanie Rosay, Julien Trébosc, Hervé Vezin, and Jean-Paul Amoureux. Solvent-free high-field dynamic nuclear polarization of mesoporous silica functionalized with TEMPO. *Appl. Magn. Reson.*, 43(1-2):237–250, 2012.

[109] Vladimir K Michaelis, Evgeny Markhasin, Eugenio Daviso, Judith Herzfeld, and Robert G Griffin. Dynamic nuclear polarization of oxygen-17. *J. Phys. Chem. Lett.*, 3(15):2030–2034, 2012.

[110] Frederic Blanc, Samantha Y Chong, Tom O McDonald, Dave J Adams, Shane Pawsey, Marc A Caporini, and Andrew I Cooper. Dynamic nuclear polarization NMR spectroscopy allows high-throughput characterization of microporous organic polymers. *J. Am. Chem. Soc.*, 135(41):15290–15293, 2013.

[111] Frédéric A Perras, Takeshi Kobayashi, and Marek Pruski. Natural abundance 17o dnp two-dimensional and surface-enhanced nmr spectroscopy. *J. Am. Chem. Soc.*, 137(26):8336–8339, 2015.

[112] Frédéric A Perras, Zhuoran Wang, Pranjali Naik, Igor I Slowing, and Marek Pruski. Natural abundance 17o dnp nmr provides precise o- h distances and insights into the brønsted acidity of heterogeneous catalysts. *Angew. Chem.*, 129(31):9293–9297, 2017.

[113] Junchao Chen, Michael A Hope, Zhiye Lin, Meng Wang, Tao Liu, David M Halat, Yujie Wen, Teng Chen, Xiaokang Ke, Pieter CMM Magusin, Weiping Ding, Xifeng Xia, Xin-Ping Wu, Xue-Qing Gong, Clare P Grey, and Luming Peng. Interactions of oxide surfaces with water revealed with solid-state NMR spectroscopy. *J. Am. Chem. Soc.*, 2020.

[114] Nick J Brownbill, David Gajan, Anne Lesage, Lyndon Emsley, and Frédéric Blanc. Oxygen-17 dynamic nuclear polarisation enhanced solid-state NMR spectroscopy at 18.8 T. *Chem. Comm.*, 53(17):2563–2566, 2017.

[115] Daniel Lee, César Leroy, Charlene Crevant, Laure Bonhomme-Coury, Florence Babonneau, Danielle Laurencin, Christian Bonhomme, and Gaël De Paëpe. Interfacial Ca^{2+} environments in nanocrystalline apatites revealed by dynamic nuclear polarization enhanced ^{43}Ca NMR spectroscopy. *Nat. Comm.*, 8:14104, 2017.

[116] Frédéric Blanc, Luke Sperrin, Daniel Lee, Rıza Dervişoğlu, Yoshihiro Yamazaki, Sossina M Haile, Gaël De Paëpe, and Clare P Grey. Dynamic nuclear polarization NMR of low-γ nuclei: structural insights into hydrated yttrium-doped $BaZrO_3$. *J. Phys. Chem. Lett.*, 5(14):2431–2436, 2014.

[117] Takeshi Kobayashi, Frédéric A Perras, Tian Wei Goh, Tanner L Metz, Wenyu Huang, and Marek Pruski. DNP-enhanced ultrawideline solid-state NMR spectroscopy: studies of platinum in metal-organic frameworks. *J. Phys. Chem. Lett.*, 7(13):2322–2327, 2016.

[118] Frédéric A Perras, Takeshi Kobayashi, and Marek Pruski. Growing signals from the noise: Challenging nuclei in materials DNP. *eMagRes*, pages 35–50, 2007.

[119] David A Hirsh, Aaron J Rossini, Lyndon Emsley, and Robert W Schurko. 35 cl dynamic nuclear polarization solid-state nmr of active pharmaceutical ingredients. *Phys. Chem. Chem. Phys.*, 18(37):25893–25904, 2016.

[120] Hiyam Hamaed, Jenna M Pawlowski, Benjamin FT Cooper, Riqiang Fu, S Holger Eichhorn, and Robert W Schurko. Application of solid-state 35cl nmr to the structural characterization of hydrochloride pharmaceuticals and their polymorphs. *J. Am. Chem. Soc.*, 130(33):11056–11065, 2008.

[121] Takeshi Kobayashi, Frédéric A. Perras, Igor I. Slowing, Aaron D. Sadow, and Marek Pruski. Dynamic nuclear polarization solid-state NMR in heterogeneous catalysis research. *ACS Catal.*, 5(12):7055–7062, 2015.

[122] Torsten Gutmann, Jiquan Liu, Niels Rothermel, Yeping Xu, Eva Jaumann, Mayke Werner, Hergen Breitzke, Snorri T Sigurdsson, and Gerd Buntkowsky. Natural abundance 15n nmr by dynamic nuclear polarization: Fast analysis of binding sites of a novel amine-carboxyl-linked immobilized dirhodium catalyst. *Chem. - Eur. J.*, 21(9):3798–3805, 2015.

[123] Naresh Eedugurala, Zhuoran Wang, Umesh Chaudhary, Nicholas Nelson, Kapil Kandel, Takeshi Kobayashi, Igor I Slowing, Marek Pruski, and Aaron D Sadow. Mesoporous silica-supported amidozirconium-catalyzed carbonyl hydroboration. *ACS Catal.*, 5(12):7399–7414, 2015.

[124] Matthew P Conley, Aaron J Rossini, Aleix Comas-Vives, Maxence Valla, Gilles Casano, Olivier Ouari, Paul Tordo, Anne Lesage, Lyndon Emsley, and Christophe Copéret. Silica-surface reorganization during organotin grafting evidenced by ^{119}Sn DNP SENS: a tandem reaction of gem-silanols and strained siloxane bridges. *Phys. Chem. Chem. Phys.*, 16(33):17822–17827, 2014.

[125] Maha A Aljuhani, Jérémie DA Pelletier, and Jean-Marie Basset. Imine metathesis by silica-supported catalysts using the methodology of surface organometallic chemistry. *JoVE*, (152):e59409, 2019.

[126] Ta-Chung Ong, Wei-Chih Liao, Victor Mougel, David Gajan, Anne Lesage, Lyndon Emsley, and Christophe Copéret. Atomistic description of reaction intermediates for supported metathesis catalysts enabled by dnp sens. *Angew. Chem., Int. Ed.*, 55(15):4743–4747, 2016.

[127] Jeffrey Camacho-Bunquin, Magali Ferrandon, Hyuntae Sohn, Dali Yang, Cong Liu, Patricia Anne Ignacio-de Leon, Frédéric A Perras, Marek Pruski, Peter C Stair, and Massimiliano Delferro. Chemoselective hydrogenation with supported organoplatinum (IV) catalyst on Zn (II)-modified silica. *J. Am. Chem. Soc.*, 140(11):3940–3951, 2018.

[128] Vlad Pascanu, Greco González Miera, A Ken Inge, and Belén Martín-Matute. Metal–organic frameworks as catalysts for organic synthesis: A critical perspective. *J. Am. Chem. Soc.*, 141(18):7223–7234, 2019.

[129] Aaron J Rossini, Alexandre Zagdoun, Moreno Lelli, Jérôme Canivet, Sonia Aguado, Olivier Ouari, Paul Tordo, Melanie Rosay, Werner E Maas, Christophe Copéret, David Farrusseng, Lyndon Emsley, and Anne Lesage. Dynamic nuclear polarization enhanced solid-state NMR spectroscopy of functionalized metal–organic frameworks. *Angew. Chem. Int. Ed.*, 51(1):123–127, 2012.

[130] Frédérique Pourpoint, Aany Sofia Lilly Thankamony, Christophe Volkringer, Thierry Loiseau, Julien Trébosc, Fabien Aussenac, Diego Carnevale, Geoffrey Bodenhausen, Hervé Vezin, Olivier Lafon, and Jean Paul Amoureux. Probing 27Al–13C proximities in metal–organic frameworks using dynamic nuclear polarization enhanced NMR spectroscopy. *Chem. Comm.*, 50(8):933–935, 2014.

[131] Nick J Brownbill, Reiner Sebastian Sprick, Baltasar Bonillo, Shane Pawsey, Fabien Aussenac, Alistair J Fielding, Andrew I Cooper, and Frédéric Blanc. Structural elucidation of amorphous photocatalytic polymers from dynamic nuclear polarization enhanced solid state NMR. *Macromolecules*, 51(8):3088–3096, 2018.

[132] Florian M Wisser, Pierrick Berruyer, Luis Cardenas, Yorck Mohr, Elsje Alessandra Quadrelli, Anne Lesage, David Farrusseng, and Jérôme Canivet. Hammett parameter in microporous solids as macroligands for heterogenized photocatalysts. *ACS Catal.*, 8(3):1653–1661, 2018.

[133] Veronika Vitzthum, Pascal Miéville, Diego Carnevale, Marc A. Caporini, David Gajan, Christophe Copéret, Moreno Lelli, Alexandre Zagdoun, Aaron J. Rossini, Anne Lesage, Lyndon Emsley, and Geoffrey Bodenhausen. Dynamic nuclear polarization of quadrupolar nuclei using cross polarization from protons: Surface-enhanced aluminium-27 NMR. *Chem. Comm.*, 48(14):1988–1990, 2012.

[134] Daniel Lee, Nghia Tuan Duong, Olivier Lafon, and Gaël De Paëpe. Primostrato solid-state NMR enhanced by dynamic nuclear polarization: Pentacoordinated Al^{3+} ions are only located at the surface of hydrated γ-alumina. *J. Phys. Chem. C*, 118(43):25065–25076, 2014.

[135] Maxence Valla, Aaron J. Rossini, Maxime Caillot, Céline Chizallet, Pascal Raybaud, Mathieu Digne, Alexandra Chaumonnot, Anne Lesage, Lyndon Emsley, Jeroen A. Van Bokhoven, and Christophe Copéret. Atomic Description of the Interface between Silica and Alumina in Aluminosilicates through Dynamic Nuclear Polarization Surface-Enhanced NMR Spectroscopy and First-Principles Calculations. *J. Am. Chem. Soc.*, 137(33):10710–10719, 2015.

[136] Dong Xiao, Shutao Xu, Xiuwen Han, Xinhe Bao, Zhongmin Liu, and Frédéric Blanc. Direct structural identification of carbenium ions and investigation of host–guest interaction in the methanol to olefins reaction obtained by multinuclear nmr correlations. *Chem. Sci.*, 8(12):8309–8314, 2017.

[137] Dong Xiao, Shutao Xu, Nick J Brownbill, Subhradip Paul, Li-Hua Chen, Shane Pawsey, Fabien Aussenac, Bao-Lian Su, Xiuwen Han, Xinhe Bao, Zhongmin Liu, and Frédéric Blanc. Fast detection and structural identification of carbocations on zeolites by dynamic nuclear polarization enhanced solid-state NMR. *Chem. Sci.*, 9(43):8184–8193, 2018.

[138] Abhishek Dutta Chowdhury, Irina Yarulina, Edy Abou-Hamad, Andrei Gurinov, and Jorge Gascon. Surface enhanced dynamic nuclear polarization solid-state nmr spectroscopy sheds light on brønsted–lewis acid synergy during the zeolite catalyzed methanol-to-hydrocarbon process. *Chem. Sci.*, 10(39):8946–8954, 2019.

[139] Stef Smeets, Zachariah J Berkson, Dan Xie, Stacey I Zones, Wei Wan, Xiaodong Zou, Ming-Feng Hsieh, Bradley F Chmelka, Lynne B McCusker, and Christian Baerlocher. Well-defined silanols in the structure of the calcined high-silica zeolite SSZ-70: New understanding of a successful catalytic material. *J. Am. Chem. Soc.*, 139(46):16803–16812, 2017.

[140] William R Gunther, Vladimir K Michaelis, Marc A Caporini, Robert G Griffin, and Yuriy Román-Leshkov. Dynamic nuclear polarization NMR enables the analysis of sn-β zeolite prepared with natural abundance ^{119}Sn precursors. *J. Am. Chem. Soc.*, 136(17):6219–6222, 2014.

[141] Patrick Wolf, Maxence Valla, Aaron J Rossini, Aleix Comas-Vives, Francisco Núñez-Zarur, Bernard Malaman, Anne Lesage, Lyndon Emsley, Christophe Copéret, and Ive Hermans. NMR signatures of the active sites in Sn-β zeolite. *Angew. Chem.*, 126(38):10343–10347, 2014.

[142] Patrick Wolf, Wei-Chih Liao, Ta-Chung Ong, Maxence Valla, James W Harris, Rajamani Gounder, William NP van der Graaff, Evgeny A Pidko, Emiel JM Hensen, Paola Ferrini, Jan Dijkmans, Bert Sels, Ive Hermans, and Christophe Copéret. Identifying Sn site heterogeneities prevalent among Sn-β zeolites. *Helv. Chim. Acta*, 99(12):916–927, 2016.

[143] James W Harris, Wei-Chih Liao, John R Di Iorio, Alisa M Henry, Ta-Chung Ong, Aleix Comas-Vives, Christophe Coperet, and Rajamani Gounder. Molecular structure and confining environment of sn sites in single-site chabazite zeolites. *Chem. Mat.*, 29(20):8824–8837, 2017.

[144] Ina Vollmer, Irina Yarulina, Freek Kapteijn, and Jorge Gascon. Progress in developing a structure-activity relationship for the direct aromatization of methane. *ChemCatChem*, 11(1):39–52, 2019.

[145] Maher Ben Abda, Olivier Schäf, Fabio Ziarelli, Hélène Pizzala, Renaud Denoyel, Stéphane Viel, and Yves Zerega. Investigating the interaction of two asymmetric dioxins with FAU 13X zeolites using calorimetry and solid-state NMR. *Microporous Mesoporous Mater.*, 234:200–206, 2016.

[146] Robert L Johnson, Frédéric A Perras, Takeshi Kobayashi, Thomas J Schwartz, James A Dumesic, Brent H Shanks, and Marek Pruski. Identifying low-coverage surface species on supported noble metal nanoparticle catalysts by dnp-nmr. *Chem. Comm.*, 52(9):1859–1862, 2016.

[147] Laura Piveteau, Ta Chung Ong, Aaron J. Rossini, Lyndon Emsley, Christophe Copéret, and Maksym V. Kovalenko. Structure of Colloidal Quantum Dots from Dynamic Nuclear Polarization Surface Enhanced NMR Spectroscopy. *J. Am. Chem. Soc.*, 137(43):13964–13971, 2015.

[148] Laura Piveteau, Dmitry Dirin, Christopher P. Gordon, Brennan J Walder, Ta-Chung Ong, Lyndon Emsley, Christophe Copéret, and Maksym V. Kovalenko. Colloidal-ALD-grown core/shell CdSe/CdS nanoplatelets as seen by DNP enhanced PASS-PIETA NMR spectroscopy. *Nano Lett.*, 2020.

[149] Leah B Casabianca. Solid-state nuclear magnetic resonance studies of nanoparticles. *Solid State Nuc. Mag. Res.*, page 101664, 2020.

[150] Michael A Hope, David M Halat, Pieter CMM Magusin, Subhradip Paul, Luming Peng, and Clare P Grey. Surface-selective direct ^{17}O DNP NMR of CeO_2 nanoparticles. *Chem. Comm.*, 53(13):2142–2145, 2017.

[151] Hans Werner Wanzlick. Aspects of nucleophilic carbene chemistry. *Angew. Chem., Int. Ed.*, 1(2):75–80, 1962.

[152] Hans Werner Wanzlick and Hans Jürgen Schönherr. Direct synthesis of a mercury salt-carbene complex. *Angew. Chem., Int. Ed.*, 7(2):141–142, 1968.

[153] Anthony J Arduengo III, Richard L Harlow, and Michael Kline. A stable crystalline carbene. *J. Am. Chem. Soc.*, 113(1):361–363, 1991.

[154] Kalluri VS Ranganath, Satoaki Onitsuka, A Kiran Kumar, and Junji Inanaga. Recent progress of N-heterocyclic carbenes in heterogeneous catalysis. *Catal. Sci. Technol.*, 3(9):2161–2181, 2013.

[155] Manoja K Samantaray, Johan Alauzun, David Gajan, Santosh Kavitake, Ahmad Mehdi, Laurent Veyre, Moreno Lelli, Anne Lesage, Lyndon Emsley, Christophe Copéret, and Chloé Thieuleux. Evidence for metal–surface interactions and their role in stabilizing well-defined immobilized Ru–NHC alkene metathesis catalysts. *J. Am. Chem. Soc.*, 135(8):3193–3199, 2013.

[156] Mathieu Baffert, Tarun K Maishal, Laurent Mathey, Christophe Coperet, and Chloé Thieuleux. Tailored ruthenium–n-heterocyclic carbene hybrid catalytic materials for the hydrogenation of carbon dioxide in the presence of amine. *ChemSusChem*, 4(12):1762–1765, 2011.

[157] Tarun K Maishal, Johan Alauzun, Jean-Marie Basset, Christophe Copéret, Robert JP Corriu, Erwan Jeanneau, Ahmad Mehdi, Catherine Reyé, Laurent Veyre, and Chloé Thieuleux. A Tailored Organometallic–Inorganic Hybrid Mesostructured Material: A Route to a Well-Defined, Active, and Reusable Heterogeneous Iridium-NHC Catalyst for H/D Exchange. *Angew. Chem.*, 120(45):8782–8784, 2008.

[158] Julia Wappel, César A Urbina-Blanco, Mudassar Abbas, Jörg H Albering, Robert Saf, Steven P Nolan, and Christian Slugovc. Halide exchanged hoveyda-type complexes in olefin metathesis. *Beilstein J. Org. Chem.*, 6(1):1091–1098, 2010.

[159] Iyad Karamé, Malika Boualleg, Jean-Michel Camus, Tarun K Maishal, Johan Alauzun, Jean-Marie Basset, Christophe Copéret, Robert JP Corriu, Erwan Jeanneau, Ahmad Mehdi, et al. Tailored Ru-NHC Heterogeneous Catalysts for Alkene Metathesis. *Chem. - Eur. J.*, 15(44):11820–11823, 2009.

[160] Matthew P Conley, Ruben M Drost, Mathieu Baffert, David Gajan, Cornelis Elsevier, W Trent Franks, Hartmut Oschkinat, Laurent Veyre, Alexandre Zagdoun, Aaron Rossini, Moreno Lelli, Anne Lesage, Gilles Casano, Olivier Ouari, Paul Tordo, Lyndon Emsley, Christophe Copéret, and Chloé Thieuleux. A Well-Defined Pd Hybrid Material for the Z-Selective Semihydrogenation of Alkynes Characterized at the Molecular Level by DNP SENS. *Chem. - Eur. J.*, 19(37):12234–12238, 2013.

[161] Manoja K Samantaray, Johan Alauzun, David Gajan, Santosh Kavitake, Ahmad Mehdi, Laurent Veyre, Moreno Lelli, Anne Lesage, Lyndon Emsley, Christophe Copéret, et al. Evidence for metal–surface interactions and their role in stabilizing well-defined immobilized ru–nhc alkene metathesis catalysts. *J. Am. Chem. Soc.*, 135(8):3193–3199, 2013.

[162] Iuliia Romanenko, David Gajan, Reine Sayah, Delphine Crozet, Erwan Jeanneau, Christine Lucas, Lénaic Leroux, Laurent Veyre, Anne Lesage, Lyndon Emsley, Emmanuel Lacôte, and journal=*Angew. Chem.* volume=127 number=44 pages=13129–13133 year=2015 publisher=Wiley Online Library Thieuleux, Chloé. Iridium (I)/N-Heterocyclic Carbene Hybrid Materials: Surface Stabilization of Low-Valent Iridium Species for High Catalytic Hydrogenation Performance.

[163] Pierrick Berruyer, Moreno Lelli, Matthew P Conley, Daniel L Silverio, Cory M Widdifield, Georges Siddiqi, David Gajan, Anne Lesage, Christophe Copéret, and Lyndon Emsley. Three-Dimensional Structure Determination of Surface Sites. *J. Am. Chem. Soc.*, 139(2):849–855, jan 2017.

[164] Anatole Abragam. *The principles of nuclear magnetism*. Number 32. Oxford university press, 1961.

[165] M Matti Maricq and JS Waugh. Nmr in rotating solids. *J. Chem. Phys.*, 70(7):3300–3316, 1979.

[166] Susanne Penzel, Andres Oss, Mai-Liis Org, Ago Samoson, Anja Böckmann, Matthias Ernst, and Beat H Meier. Spinning faster: protein NMR at MAS frequencies up to 126 kHz. *J. Biomol. NMR*, 73(1-2):19–29, 2019.

[167] Ulrich Sternberg, Raiker Witter, Ilya Kuprov, Jonathan M Lamley, Andres Oss, Józef R Lewandowski, and Ago Samoson. 1h line width dependence on mas speed in solid state nmr–comparison of experiment and simulation. *J. Mag. Res.*, 291:32–39, 2018.

[168] Elodie Salager, Robin S Stein, Stefan Steuernagel, Anne Lesage, Bénédicte Elena, and Lyndon Emsley. Enhanced sensitivity in high-resolution 1H solid-state NMR spectroscopy with DUMBO dipolar decoupling under ultra-fast MAS. *Chem. Phys. Lett.*, 469(4-6):336–341, 2009.

[169] John S Waugh, Lee M Huber, and Ulrich Haeberlen. Approach to high-resolution nmr in solids. *Phys. Rev. Lett.*, 20(5):180, 1968.

[170] Elena Vinogradov, Perunthiruthy K Madhu, and Shimon Vega. Strategies for high-resolution proton spectroscopy in solid-state NMR. In *New Techniques in Solid-State NMR*, pages 33–90. Springer, 2005.

[171] Dimitris Sakellariou, Anne Lesage, Paul Hodgkinson, and Lyndon Emsley. Homonuclear dipolar decoupling in solid-state NMR using continuous phase modulation. *Chem. Phys. Lett.*, 319(3-4):253–260, 2000.

[172] Anne Lesage, Dimitris Sakellariou, Sabine Hediger, Bénédicte Eléna, Patrick Charmont, Stefan Steuernagel, and Lyndon Emsley. Experimental aspects of proton NMR spectroscopy in solids using phase-modulated homonuclear dipolar decoupling. *J. Mag. Res.*, 163(1):105–113, 2003.

[173] Elena Vinogradov, Perunthiruthy K Madhu, and Shimon Vega. High-resolution proton solid-state NMR spectroscopy by phase-modulated Lee–Goldburg experiment. *Chem. Phys. Lett.*, 314(5-6):443–450, 1999.

[174] Elena Vinogradov, Perunthiruthy K Madhu, and Shimon Vega. Phase modulated lee–goldburg magic angle spinning proton nuclear magnetic resonance experiments in the solid state: a bimodal floquet theoretical treatment. *J. Chem. Phys.*, 115(19):8983–9000, 2001.

[175] Elena Vinogradov, Perunthiruthy K Madhu, and Shimon Vega. Proton spectroscopy in solid state nuclear magnetic resonance with windowed phase modulated lee–goldburg decoupling sequences. *Chem. Phys. Lett.*, 354(3-4):193–202, 2002.

[176] Leon Bosman, Perunthiruthy K Madhu, Shimon Vega, and Elena Vinogradov. Improvement of homonuclear dipolar decoupling sequences in solid-state nuclear magnetic resonance utilising radiofrequency imperfections. *J. Mag. Res.*, 169(1):39–48, 2004.

[177] Michal Leskes, Perunthiruthy K Madhu, and Shimon Vega. Proton line narrowing in solid-state nuclear magnetic resonance: New insights from windowed phase-modulated Lee-Goldburg sequence. *J. Chem. Phys.*, 125(12):124506, 2006.

[178] Michal Leskes, Perunthiruthy K Madhu, and Shimon Vega. A broad-banded z-rotation windowed phase-modulated Lee–Goldburg pulse sequence for ^{1}H spectroscopy in solid-state NMR. *Chem. Phys. Lett.*, 447(4-6):370–374, 2007.

[179] Michal Leskes, Perunthiruthy K Madhu, and Shimon Vega. Supercycled homonuclear dipolar decoupling in solid-state NMR: Toward cleaner ^{1}H spectrum and higher spinning rates. *J. Chem. Phys.*, 128(5):052309, 2008.

[180] Federico M Paruzzo and Lyndon Emsley. High-resolution ^{1}H NMR of powdered solids by homonuclear dipolar decoupling. *J. Mag. Res.*, 309:106598, 2019.

[181] Jean Baum and Alex Pines. NMR Studies of Clustering in Solids. *J. Am. Chem. Soc.*, 108(24):7447–7454, 1986.

[182] Jean Baum, Michael Munowitz, Allen N Garroway, and Alex Pines. Multiple-quantum dynamics in solid state nmr. *J. Chem. Phys.*, 83(5):2015–2025, 1985.

[183] Yu-Sze Yen and A Pines. Multiple-quantum nmr in solids. *J. Chem. Phys.*, 78(6):3579–3582, 1983.

[184] Jean Baum, Karen K Gleason, Alex Pines, Allen N Garroway, and Jeffrey A Reimer. Multiple-quantum nmr study of clustering in hydrogenated amorphous silicon. *Phys. Rev. Lett.*, 56(13):1377, 1986.

[185] David N Shykind, Jean Baum, Shang-Bin Liu, Alex Pines, and Allen N Garroway. Phase-incremented multiple-quantum nmr experiments. *J. Mag. Res.*, 76(1):149–154, 1988.

[186] Bernard C Gerstein, Marek Pruski, and Son-Jong Hwang. Determination of proton densities on silica gel catalyst supports by n-quantum coherence in NMR. *Anal. Chim. Acta*, 283(3):1059–1079, 1993.

[187] Beat H Meier and William L Earl. Excitation of multiple quantum transitions under magic angle spinning conditions: Adamantane. *J. Chem. Phys.*, 85(9):4905–4911, 1986.

[188] Beat H Meier and William L Earl. Double-quantum filter for rotating solids. *J. Am. Chem. Soc.*, 109(26):7937–7942, 1987.

[189] Robert Tycko and Gary Dabbagh. Double-quantum filtering in magic-angle-spinning nmr spectroscopy: an approach to spectral simplification and molecular structure determination. *J. Am. Chem. Soc.*, 113(25):9444–9448, 1991.

[190] Ingo Schnell. Dipolar recoupling in fast-mas solid-state nmr spectroscopy. *Prog. Nucl. Magn. Reson. Spectrosc.*, 1(45):145–207, 2004.

[191] Gaël De Paëpe. Dipolar recoupling in magic angle spinning solid-state nuclear magnetic resonance. *Annu. Rev. Phys. Chem.*, 63:661–684, 2012.

[192] W Sommer, Johannes Gottwald, Dan E Demco, and Hans W Spiess. Dipolar heteronuclear multiple-quantum NMR spectroscopy in rotating solids. *J. Magn. Res., Series A*, 113(1):131–134, 1995.

[193] Ingo Schnell, Adonis Lupulescu, Siegfried Hafner, Dan E Demco, and Hans W Spiess. Resolution enhancement in multiple-quantum mas nmr spectroscopy. *J. Magn. Res.*, 133(1):61–69, 1998.

[194] David J States, Ronald A Haberkorn, and David J Ruben. A two-dimensional nuclear overhauser experiment with pure absorption phase in four quadrants. *J. Magn. Res.*, 48(2):286–292, 1982.

[195] Robert Graf, Dan E Demco, Johannes Gottwald, Siegfried Hafner, and Hans W Spiess. Dipolar couplings and internuclear distances by double-quantum nuclear magnetic resonance spectroscopy of solids. *J. Chem. Phys.*, 106(3):885–895, 1997.

[196] Helen Geen, Jeremy J Titman, Johannes Gottwald, and Hans W Spiess. Spinning sidebands in the fast-mas multiple-quantum spectra of protons in solids. *J. Mag. Res.*, 114:264–267, 1995.

[197] Ulli Friedrich, Ingo Schnell, Steven P Brown, Adonis Lupulescu, Dan E Demco, and Hans W Spiess. Spinning-sideband patterns in multiple-quantum magic-angle spinning nmr spectroscopy. *Mol. Phys.*, 95(6):1209–1227, 1998.

[198] Steven P Brown and Hans W Spiess. Advanced solid-state NMR methods for the elucidation of structure and dynamics of molecular, macromolecular, and supramolecular systems. *Chem. Rev.*, 101(12):4125–4155, 2001.

[199] Young K Lee, Narayanan D Kurur, Michael Helmle, Ole G Johannessen, Niels C Nielsen, and Malcolm H Levitt. Efficient dipolar recoupling in the NMR of rotating solids. A sevenfold symmetric radiofrequency pulse sequence. *Chem. Phys. Lett.*, 242(3):304–309, 1995.

[200] Morten Hohwy, Hans Jørgen Jakobsen, Mattias Eden, Malcolm H Levitt, and Niels C Nielsen. Broadband dipolar recoupling in the nuclear magnetic resonance of rotating solids: A compensated C7 pulse sequence. *J. Chem. Phys.*, 108(7):2686–2694, 1998.

[201] Per Eugen Kristiansen, Marina Carravetta, Jacco D Van Beek, Wai Cheu Lai, and Malcolm H Levitt. Theory and applications of supercycled symmetry-based recoupling sequences in solid-state nuclear magnetic resonance. *J. Chem. Phys.*, 124(23):234510, 2006.

[202] Rongchun Zhang, You-lee Hong, Thirupathi Ravula, Yusuke Nishiyama, and Ayyalusamy Ramamoorthy. High-resolution proton-detected MAS experiments on self-assembled diphenylalanine nanotubes enabled by fast MAS and high magnetic field. *J. Mag. Res.*, page 106717, 2020.

[203] Ravi Shankar Palani. Pulse Design in Solid-State Nuclear Magnetic Resonance: Study and Design of Dipolar Recoupling Experiments in Spin-1/2 Nuclei. *arXiv*, 2017.

[204] Ingo Schnell, Adonis Lupulescu, Siegfried Hafner, Dan E. Demco, and Hans W. Spiess. Resolution Enhancement in Multiple-Quantum MAS NMR Spectroscopy. *J. Magn. Res.*, 133(1):61–69, jul 1998.

[205] Ulli Friedrich, Ingo Schnell, Dan E. Demco, and Hans W. Spiess. Triple-quantum NMR spectroscopy in dipolar solids. *Chem. Phys. Lett.*, 285(1-2):49–58, 1998.

[206] Mattias Edén and Malcolm H Levitt. Excitation of carbon-13 triple quantum coherence in magic-angle-spinning nmr. *Chem. Phys. Lett.*, 293(3-4):173–179, 1998.

[207] Andreas Brinkmann and Mattias Edén. Second order average hamiltonian theory of symmetry-based pulse schemes in the nuclear magnetic resonance of rotating solids: application to triple-quantum dipolar recoupling. *J. Chem. Phys.*, 120(24):11726–11745, 2004.

[208] Mattias Edén and Andreas Brinkmann. Triple-quantum dynamics in multiple-spin systems undergoing magic-angle spinning: application to ^{13}C homonuclear correlation spectroscopy. *J. Mag. Res.*, 173(2):259–279, 2005.

[209] Michal Leskes and Shimon Vega. Design of a triple quantum coherence excitation scheme for protons in solid state nmr. *J. Chem. Phys.*, 130(12):03B620, 2009.

[210] Franck Rataboul, Anne Baudouin, Chloé Thieuleux, Laurent Veyre, Christophe Copéret, Jean Thivolle-Cazat, Jean-Marie Basset, Anne Lesage, and Lyndon Emsley. Molecular Understanding of the Formation of Surface Zirconium Hydrides upon Thermal Treatment under Hydrogen of [(≡ SiO)Zr(CH_2^tBu)$_3$] by Using Advanced Solid-State NMR Techniques. *J. Am. Chem. Soc.*, 126(39):12541–12550, 2004.

[211] Manoja K Samantaray, Emmanuel Callens, Edy Abou-Hamad, Aaron J Rossini, Cory M Widdifield, Raju Dey, Lyndon Emsley, and Jean-Marie Basset. WMe_6 Tamed by Silica:≡Si–O–WMe5 as an Efficient, Well-Defined Species for Alkane Metathesis, Leading to the Observation of a Supported W–Methyl/Methylidyne Species. *J. Am. Chem. Soc.*, 136(3):1054–1061, 2014.

[212] Steven P Brown. Applications of high-resolution ^{1}H solid-state NMR. *Solid State Nucl. Magn. Reson.*, 41:1–27, 2012.

[213] Géraldine Tosin, Marco Delgado, Anne Baudouin, Catherine C Santini, François Bayard, and Jean-Marie Basset. Surface Organometallic Chemistry of Hf(CH_2^tBu)$_4$ on Silica and Silica- Alumina: Reaction of the Resulting Grafted Hafnium Neopentyl with Dihydrogen. *Organometallics*, 29(6):1312–1322, 2010.

[214] Géraldine Tosin, Catherine C Santini, Anne Baudouin, Aimery De Mallman, Steven Fiddy, Céline Dablemont, and Jean-Marie Basset. Reactivity of silica-supported hafnium trisneopentyl with dihydrogen: formation and characterization of silica surface hafnium hydrides and alkyl hydride. *Organometallics*, 26(17):4118–4127, 2007.

[215] Marco Delgado, Catherine C Santini, Françoise Delbecq, Anne Baudouin, Aimery De Mallmann, Carmello Prestipino, S Norsic, Philippe Sautet, and Jean-Marie Basset. Characterization of surface hydride hafnium complexes on alumina by a combination of experiments and dft calculations. *J. Phys. Chem., C*, 115(14):6757–6763, 2011.

[216] Cherif Larabi, Nicolas Merle, Sébastien Norsic, Mostafa Taoufik, Anne Baudouin, Christine Lucas, Jean Thivolle-Cazat, Aimery de Mallmann, and Jean-Marie Basset. Surface organometallic chemistry of titanium on silica- alumina and catalytic hydrogenolysis of waxes at low temperature. *Organometallics*, 28(19):5647–5655, 2009.

[217] Priscilla Avenier, Anne Lesage, Mostafa Taoufik, Anne Baudouin, Aimery De Mallmann, Steven Fiddy, Manon Vautier, Laurent Veyre, Jean-Marie Basset, Lyndon Emsley, and Elsje Alessandra Quadrelli. Well-defined surface imido amido tantalum (V) species from ammonia and silica-supported tantalum hydrides. *J. Am. Chem. Soc.*, 129(1):176–186, 2007.

[218] Priscilla Avenier, Mostafa Taoufik, Anne Lesage, Xavier Solans-Monfort, Anne Baudouin, Aimery De Mallmann, Laurent Veyre, Jean-Marie Basset, Odile Eisenstein, Lyndon Emsley, and Elsje Alessandra Quadrelli. Dinitrogen dissociation on an isolated surface tantalum atom. *Science*, 317(5841):1056–1060, 2007.

[219] Pedro Serna and Bruce C Gates. Molecular metal catalysts on supports: organometallic chemistry meets surface science. *Acc. Chem. Res.*, 47(8):2612–2620, 2014.

[220] Sandra Huebner, Johannes G de Vries, and Vittorio Farina. Why does industry not use immobilized transition metal complexes as catalysts? *Adv. Synth. Catal.*, 358(1):3–25, 2016.

[221] Iuliia Romanenko, David Gajan, Reine Sayah, Delphine Crozet, Erwan Jeanneau, Christine Lucas, Lénaic Leroux, Laurent Veyre, Anne Lesage, Lyndon Emsley, Emmanuel Lacôte, and Chloé Thieuleux. Iridium(I)/N-heterocyclic carbene hybrid materials: Surface stabilization of low-valent iridium species for high catalytic hydrogenation performance. *Angew. Chem., Int. Ed.*, (44):12937–12941, oct.

[222] Aaron J Rossini, Alexandre Zagdoun, Moreno Lelli, David Gajan, Fernando Rascón, Melanie Rosay, Werner E Maas, Christophe Copéret, Anne Lesage, and Lyndon Emsley. One hundred fold overall sensitivity enhancements for silicon-29 nmr spectroscopy of surfaces by dynamic nuclear polarization with cpmg acquisition. *Chem. Sci.*, 3(1):108–115, 2012.

[223] Pierrick Berruyer. *Three-Dimensional Structure Determination of Surface Sites with Dynamic Nuclear Polarization Surface Enhanced NMR Spectroscopy.* PhD thesis, 2017.

[224] Jayasubba Reddy Yarava, Sachin Rama Chaudhari, Aaron J Rossini, Anne Lesage, and Lyndon Emsley. Solvent suppression in DNP enhanced solid state NMR. *J. Mag. Res.*, 277:149–153, 2017.

[225] Terry Gullion and Jacob Schaefer. Detection of weak heteronuclear dipolar coupling by rotational-echo double-resonance nuclear magnetic resonance. In *Adv. Mag. and Opt. Res.*, volume 13, pages 57–83. Elsevier, 1989.

[226] Terry Gullion. Introduction to rotational-echo, double-resonance NMR. *Concepts Magn. Reson.*, 10(5):277–289, 1998.

[227] Janet M Griffiths and Robert G Griffin. Nuclear magnetic resonance methods for measuring dipolar couplings in rotating solids. *Analytica chimica acta*, 283(3):1081–1101, 1993.

[228] Karl Todd Mueller. Analytic solutions for the time evolution of dipolar-dephasing NMR signals. *J. Mag. Res. A*, 113(1):81–93, 1995.

[229] Christopher P Jaroniec, Brett A Tounge, Judith Herzfeld, and Robert G Griffin. Frequency selective heteronuclear dipolar recoupling in rotating solids: accurate ^{13}C- ^{15}N distance measurements in uniformly ^{13}C, ^{15}N-labeled peptides. *J. Am. Chem. Soc.*, 123(15):3507–3519, 2001.

[230] Piero Ugliengo, M Sodupe, F Musso, IJ Bush, Roberto Orlando, and Roberto Dovesi. Realistic models of hydroxylated amorphous silica surfaces and MCM-41 mesoporous material simulated by large-scale periodic B3LYP calculations. *Adv. Mater.*, 20(23):4579–4583, 2008.

[231] Aleix Comas-Vives. Amorphous sio 2 surface models: energetics of the dehydroxylation process, strain, ab initio atomistic thermodynamics and ir spectroscopic signatures. *Phys. Chem. Chem. Phy.*, 18(10):7475–7482, 2016.

[232] Brian E Mann. ^{13}c nmr chemical shifts and coupling constants of organometallic compounds. *Advances in Organometallic Chemistry', Eds. FGA Stone and R. West, Academic Press, New York*, 12:135, 1974.

[233] Denys Grekov, Tom Vancompernolle, Mostafa Taoufik, Laurent Delevoye, and Regis M Gauvin. Solid-state NMR of quadrupolar nuclei for investigations into supported organometallic catalysts: scope and frontiers. *Chem. Soc. Rev.*, 47(8):2572–2590, 2018.

[234] Tom Vancompernolle, Xavier Trivelli, Laurent Delevoye, Frédérique Pourpoint, and RM Gauvin. On the use of solid-state ^{45}Sc NMR for structural investigations of molecular and silica-supported scandium amide catalysts. *Dalton Trans.*, 46(39):13176–13179, 2017.

[235] Valerio D'Elia, Hailin Dong, Aaron J Rossini, Cory M Widdifield, Sai VC Vummaleti, Yury Minenkov, Albert Poater, Edy Abou-Hamad, Jeremie DA Pelletier, Luigi Cavallo, Lyndon Emsley, and Jean-Marie Basset. Cooperative effect of monopodal silica-supported niobium complex pairs enhancing catalytic cyclic carbonate production. *J. Am. Chem. Soc.*, 137(24):7728–7739, 2015.

[236] Pierre Laurent, Laurent Veyre, Chloé Thieuleux, Sébastien Donet, and Christophe Copéret. From well-defined Pt(II) surface species to the controlled growth of silica supported Pt nanoparticles. *Dalton Trans.*, 42(1):238–248, 2013.

[237] Bryan EG Lucier, Alex R Reidel, and Robert W Schurko. Multinuclear solid-state NMR of square-planar platinum complexes—Cisplatin and related systems. *Can. J. Chem.*, 89(7):919–937, 2011.

[238] Sungsool Wi, Robert W Schurko, and Lucio Frydman. Broadband adiabatic inversion cross-polarization phenomena in the NMR of rotating solids. *Solid State Nucl. Mag. Res.*, 94:31–53, 2018.

[239] Robert W Schurko. Ultra-wideline solid-state NMR spectroscopy. *Acc. Chem. Res.*, 46(9):1985–1995, 2013.

[240] Yixuan Li, Julien Trébosc, Bingwen Hu, Ming Shen, Jean-Paul Amoureux, and Olivier Lafon. Indirect detection of broad spectra in solid-state NMR using interleaved DANTE trains. *J. Mag. Res.*, 294:101–114, 2018.

[241] Amrit Venkatesh, Xuechen Luan, Frederic A Perras, Ivan Hung, Wenyu Huang, and Aaron Rossini. t1-Noise Eliminated Dipolar Heteronuclear Multiple-Quantum Coherence Solid-State NMR Spectroscopy. *ChemRxiv*, 2020.

[242] Gwendal Kervern, Guido Pintacuda, and Lyndon Emsley. Fast adiabatic pulses for solid-state NMR of paramagnetic systems. *Chem. Phys. Lett.*, 435(1-3):157–162, 2007.

[243] Kevin J Sanders, Andrew J Pell, Sebastian Wegner, Clare P Grey, and Guido Pintacuda. Broadband MAS NMR spectroscopy in the low-power limit. *Chem. Phys. Lett.*, 697:29–37, 2018.

[244] Howard E Rhodes, Po-Kang Wang, Harold T Stokes, Charles P Slichter, and John H Sinfelt. NMR of platinum catalysts. I. Line shapes. *Phys. Rev. B*, 26(7):3559, 1982.

[245] Harold T Stokes, Howard E Rhodes, Po-Kang Wang, Charles P Slichter, and John H Sinfelt. NMR of platinum catalysts. III. Microscopic variation of the Knight shifts. *Phys. Rev. B*, 26(7):3575, 1982.

[246] Timothy J Bastow, Mark E Smith, and Simon N Stuart. Observation of ^{91}Zr NMR in zirconium-based metals and oxides. *Chem. phys. lett.*, 191(1-2):125–129, 1992.

[247] Timothy J Bastow and Mark E Smith. ^{91}Zr NMR characterisation of phases in transformation toughened zirconia. *Solid State Nucl. Magn. Reson.*, 1(4):165–174, 1992.

[248] Timothy J Bastow, Mark E Smith, and Simon N Stuart. A Novel Characterisation of Phases in Zirconia-Based Ceramics-^{91}Zr NMR. *Science and Technology of Zirconia V*, page 171, 1993.

[249] Dominique Massiot, Ian Farnan, Nathalie Gautier, Dominique Trumeau, Arlette Trokiner, and Jean Pierre Coutures. ^{71}Ga and ^{69}Ga nuclear magnetic resonance study of β-Ga_2O_3: resolution of four-and six-fold coordinated Ga sites in static conditions. *Solid State Nucl. Magn. Reson.*, 4(4):241–248, 1995.

[250] Flemming H Larsen, Hans J Jakobsen, Paul D Ellis, and Niels C Nielsen. Sensitivity-enhanced quadrupolar-echo NMR of half-integer quadrupolar nuclei. Magnitudes and relative orientation of chemical shielding and quadrupolar coupling tensors. *J. Phys. Chem. A*, 101(46):8597–8606, 1997.

[251] Jean-Marc Bohlen and Geoffrey Bodenhausen. Experimental aspects of chirp NMR spectroscopy. *J. Mag. Res., Series A*, 102(3):293–301, 1993.

[252] Luke A O'Dell and Robert W Schurko. QCPMG using adiabatic pulses for faster acquisition of ultra-wideline NMR spectra. *Chem. Phys. Lett.*, 464(1-3):97–102, 2008.

[253] Luke A O'Dell, Aaron J Rossini, and Robert W Schurko. Acquisition of ultra-wideline NMR spectra from quadrupolar nuclei by frequency stepped WURST–QCPMG. *Chem. phys. lett.*, 468(4-6):330–335, 2009.

[254] Renée Siegel, Thomas T Nakashima, and Roderick E Wasylishen. Application of multiple-pulse experiments to characterize broad NMR chemical-shift powder patterns from spin-1/2 nuclei in the solid state. *J. Phys. Chem. B*, 108(7):2218–2226, 2004.

[255] Ivan Hung, Aaron J Rossini, and Robert W Schurko. Application of the Carr- Purcell Meiboom- Gill pulse sequence for the acquisition of solid-state NMR spectra of spin-1/2 nuclei. *J. Phys. Chem. A*, 108(34):7112–7120, 2004.

[256] Kristopher J Harris, Adonis Lupulescu, Bryan EG Lucier, Lucio Frydman, and Robert W Schurko. Broadband adiabatic inversion pulses for cross polarization in wideline solid-state NMR spectroscopy. *J. Mag. Res.*, 224:38–47, 2012.

[257] Aaron J Rossini, Michael P Hanrahan, and Martin Thuo. Rapid acquisition of wideline MAS solid-state NMR spectra with fast MAS, proton detection, and dipolar HMQC pulse sequences. *Phys. Chem. Chem. Phys.*, 18(36):25284–25295, 2016.

[258] Frédéric A Perras, Amrit Venkatesh, Michael P Hanrahan, Tian Wei Goh, Wenyu Huang, Aaron J Rossini, and Marek Pruski. Indirect detection of infinite-speed mas solid-state nmr spectra. *J. Mag. Res.*, 276:95–102, 2017.

[259] Andreas Brinkmann and Arno PM Kentgens. Proton-Selective ^{17}O-H Distance Measurements in Fast Magic-Angle-Spinning Solid-State NMR Spectroscopy for the Determination of Hydrogen Bond Lengths. *J. Am. Chem. Soc.*, 128(46):14758–14759, 2006.

[260] Amrit Venkatesh, Michael P Hanrahan, and Aaron J Rossini. Proton detection of MAS solid-state NMR spectra of half-integer quadrupolar nuclei. *Solid state Nucl. Mag. Res.*, 84:171–181, 2017.

[261] Elliot JW Austin, Patrick J Barrie, and Robin JH Clark. Solid-state ^{195}Pt NMR studies of the complexes Pt(en)Cl$_x$ (en= 1, 2-diaminoethane; x= 2, 3 or 4). *J. Chem. Soc., Chem. Commun.*, (18):1404–1405, 1993.

[262] Dominique Massiot, Franck Fayon, Mickael Capron, Ian King, Stéphanie Le Calvé, Bruno Alonso, Jean-Olivier Durand, Bruno Bujoli, Zhehong Gan, and Gina Hoatson. Modelling one-and two-dimensional solid-state nmr spectra. *Mag. Res. Chem.*, 40(1):70–76, 2002.

[263] Bryan EG Lucier, Karen E Johnston, Wenqian Xu, Jonathan C Hanson, Sanjaya D Senanayake, Siyu Yao, Megan W Bourassa, Monika Srebro, Jochen Autschbach, and Robert W Schurko. Unravelling the structure of magnus' pink salt. *J. Am. Chem. Soc.*, 136(4):1333–1351, 2014.

[264] Bryan Lucier. New Directions for Solid-State NMR of Insensitive Nuclei: Applications to Metal Nuclei in Inorganic Materials. 2013.

[265] Lei Chen, Qiang Wang, Bingwen Hu, Olivier Lafon, Julien Trébosc, Feng Deng, and Jean-Paul Amoureux. Measurement of hetero-nuclear distances using a symmetry-based pulse sequence in solid-state NMR. *Phys. Chem. Chem. Phys.*, 12(32):9395–9405, 2010.

[266] Paulin Buchwalter, Jacky Rosé, and Pierre Braunstein. Multimetallic catalysis based on heterometallic complexes and clusters. *Chem. rev.*, 115(1):28–126, 2015.

[267] Neal P Mankad. Diverse bimetallic mechanisms emerging from transition metal lewis acid/base pairs: development of co-catalysis with metal carbenes and metal carbonyl anions. *Chem. Comm.*, 54(11):1291–1302, 2018.

[268] Ian G Powers and Christopher Uyeda. Metal–metal bonds in catalysis. *ACS Catal.*, 7(2):936–958, 2017.

[269] Benjamin G Cooper, Wesley J Napoline, and Christine M Thomas. Catalytic applications of early/late heterobimetallic complexes. *Cat. Rev.*, 54(1):1–40, 2012.

[270] Ewen Bodio, Michel Picquet, and Pierre Le Gendre. "Early–Late" Heterobimetallic Catalysis and Beyond. In *Homo-and Heterobimetallic Complexes in Catalysis*, pages 139–186. Springer, 2015.

[271] Lutz H Gade. Highly polar metal–metal bonds in "early–late" heterodimetallic complexes. *Angew.Chem., Int. Ed.*, 39(15):2658–2678, 2000.

[272] Sébastien Lassalle, Ribal Jabbour, Pauline Schiltz, Pierrick Berruyer, Tanya K Todorova, Laurent Veyre, David Gajan, Anne Lesage, Chloé Thieuleux, and Clément Camp. Metal–Metal Synergy in Well-Defined Surface Tantalum–Iridium Heterobimetallic Catalysts for H/D Exchange Reactions. *J. Am. Chem. Soc.*, 141(49):19321–19335, 2019.

[273] Dominique Marion, Mitsuhiko Ikura, Rolf Tschudin, and Ad Bax. Rapid recording of 2D NMR spectra without phase cycling. Application to the study of hydrogen exchange in proteins. *J. Mag. Res.*, 85(2):393–399, 1989.

[274] Sylvian Cadars, Anne Lesage, and Lyndon Emsley. Chemical shift correlations in disordered solids. *J. Am. Chem. Soc.*, 127(12):4466–4476, 2005.

[275] Dimitris Sakellariou, Steven P Brown, Anne Lesage, Sabine Hediger, Michel Bardet, Carlos A Meriles, Alexander Pines, and Lyndon Emsley. High-resolution nmr correlation spectra of disordered solids. *J. Am. Chem. Soc.*, 125(14):4376–4380, 2003.

[276] Timothy M Hayes and James B. Boyce. *Extended X-Ray Absorption Fine Structure Spectroscopy*, volume 37. 1983.

[277] Christopher R Brundle. In *Encyclopedia of Materials Characterization*, pages 282–299. Elsevier, 1992.

[278] Diek C Koningsberger and Robert Prins. X-ray absorption: principles, applications, techniques of EXAFS, SEXAFS, and XANES, 1988.

[279] Boon K Teo. *EXAFS: basic principles and data analysis*, volume 9. Springer Science & Business Media, 2012.

[280] B. M. Fung, A. K. Khitrin, and Konstantin Ermolaev. An Improved Broadband Decoupling Sequence for Liquid Crystals and Solids. *J. Mag. Res.*, 142(1):97–101, 2000.

[281] Lyndon Emsley and Geoffrey Bodenhausen. Optimization of shaped selective pulses for nmr using a quaternion description of their overall propagators. *J. Mag. Res.*, 97(1):135–148, 1992.

[282] SGJ Van Meerten, WMJ Franssen, and APM Kentgens. ssnake: A cross-platform open-source nmr data processing and fitting application. *J. Mag. Res.*, 301:56–66, 2019.

[283] Dominique Massiot, Franck Fayon, Mickael Capron, Ian King, Stéphanie Le Calvé, Bruno Alonso, Jean Olivier Durand, Bruno Bujoli, Zhehong Gan, and Gina Hoatson. Modelling one- and two-dimensional solid-state NMR spectra. *Magnetic Resonance in Chemistry*, 40(1):70–76, 2002.

List of Publications

Sébastien Lassalle, Ribal Jabbour, Pauline Schiltz, Pierrick Berruyer, Tanya K. Todorova, Laurent Veyre, David Gajan, Anne Lesage, Chloé Thieuleux, and Clément Camp. Metal–Metal Synergy in Well-Defined Surface Tantalum–Iridium Heterobimetallic Catalysts for H/D Exchange Reactions. *J. Am. Chem. Soc.* **2019**,141,19321–19335.

Alicia Lund, Gilles Casano, Georges Menzildjian, Monu Kaushik, Gabriele Stevanato, Maxim Yulikov, Ribal Jabbour, Dorothea Wisser, Marc Renom-Carrasco, Chloé Thieuleux, Florian Bernada, Hakim Karoui, Didier Siri, Gunnar Jeschke, David Gajan, Moreno Lelli, Lyndon Emsley, Olivier Ouari, and Anne Lesage. TinyPols: a family of water-soluble binitroxides tailored for dynamic nuclear polarization enhanced NMR spectroscopy at 18.8 and 21.1 T. *Chem. Sci.* **2020**, 11, 2810–2818.

Jasmine Viger-Gravel, Federico M. Paruzzo, Corine Cazaux, Ribal Jabbour, Amandine Leleu, Françoise Canini, Pierre Florian, Frédéric Ronzon, David Gajan, and Anne Lesage. Atomic-Scale Description of Interfaces between Antigen and Aluminum-Based Adjuvants Used in Vaccines by Dynamic Nuclear Polarization (DNP) Enhanced NMR Spectroscopy. *Chem. - Eur. J.* **2020**, 26, 8976–8982.

Sébastien Lassalle, Ribal Jabbour, Iker Del Rosal, Laurent Maron, Emiliano Fonda, Laurent Veyre, David Gajan, Anne Lesage, Chloé Thieuleux and Clément Camp. Stepwise Construction of Silica-supported Tantalum/Iridium Heteropolymetallic Catalysts Using Surface Organometallic Chemistry. *Submitted.*

Amrit Venkatesh, Alicia Lund, Lukas Rochlitz, Ribal Jabbour, Christopher P. Gordon, Georges Menzildjian, Jasmine Viger-Gravel, Pierrick Berruyer, David Gajan, Christophe Copéret, Anne Lesage, Aaron J. Rossini. *Submitted.*

Ribal Jabbour, Christopher Ashling, Dorothea Wisser, Pierrck Berruyer, Ashta C. Ghosh, Yorck Mohr, Jérôme Canivet, Thomas D. Bennett, Caroline Mellot-Draznieks, Anne Lesage, Florian M. Wisser. Unveiling the molecular environment of an organometallic catalyst heterogenized within an amorphous porous macroligand. *In preparation.*

Ribal Jabbour, Marc Renom-Carrasco, Pierrick Berruyer, David Gajan, Cory Widdifield, Chan Ka Wing, Moreno Lelli, Lyndon Emsley, Christophe Copéret, Chloé Thieuleux, Anne Lesage. Atomic-Scale Surface Structure of a Highly Active Iridium N-Heterocyclic Carbene Catalyst. *In preparation*

Appendix

Extended X-Ray Absorption Fine Structure (EXAFS):

Discovered in the 1920s, the first explanation and practice was done in 1970 in two parts. [276] The first one explained the mathematical algorithms for analyzing EXAFS data and the second one was generating the irradiation with a synchrotron for acquisition of the data. EXAFS refers to the oscillations of X-Ray on the high energy of an absorption edge. The signal measured is the attenuation of the latter upon passage through a material. EXAFS is non-destructive and element specific technique used to probe the atomic environment of an absorbent material and thus provide bonding information. The inner and outer shells of electrons (K, L, M, N ...) can be excited by X-rays. At a certain binding energy for a certain element in a sample, absorption can occur and rising edge absorption is observed. The absorption process excites the core of the electron leading to its ionization and the photoelectron wave will propagate from the atom and will be scattered by neighboring atoms. The EXAFS spectrum is a result of the constructive and destructive interference between the outgoing and incoming photoelectron waves at the absorbing atom. [277] The experiment involves the measurement of the incident and transmitted X-ray intensities, I_0 ad I_t. EXAFS can probe structural distributions and identity of atoms in the vicinity ($\sim$5 Å) of the absorbing atom. It usually refers to the region 40-1000 eV above the absorption edge. The pre-edge and edge absorption are referred to as XANES or NEXAFS and can probe the site symmetry and valence (more details are depicted in [277]). More detailed information on the principle and theory of EXAFS will not be discussed any further and can be found in [277] and [276]. Since its discovery, EXAFS have been used to determine structure of adsorbed atoms, moieties on surfaces, small molecules, metals, semi-conductors, insulators and lot more. [277–279] Although EXAFS is widely used for lots of applications, it faces its own challenges and limitations. One limitation lies within samples with absorbing elements in multiple environments. In this case, the EXAFS signal will be for an average environment for all the absorbing atoms. Under favorable circumstances and since the EXAFS is sensitive to short range distances, stereochemical details can be determined. [279] On a logistical point of view, the EXAFS presents one major drawback which is the necessity of conducting the experiments in a synchrotron facility. Getting the time needed to do the experiments is difficult, and if one gets the time it will be a short one let alone all the logistical problems that might appear along the way. Finally, since the EXAFS is element dependent, it relies on the weight of the atoms in question. For heavy atoms, this is not a problem and the measurement can provide useful information. However, for atoms with close weight (typically C,N,O) fitting the EXAFS curves is not so straightforward, and one can find different solutions or interpretation by finding different fits that correlates with the experimental data.

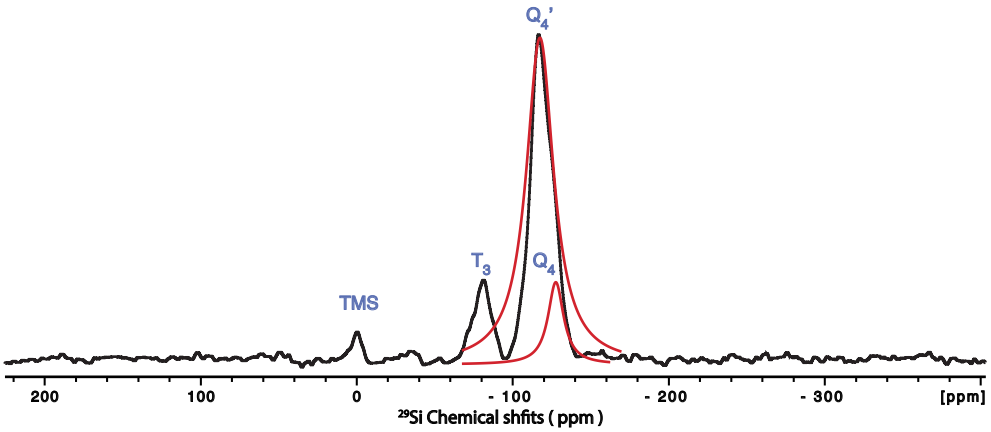

Figure S1: Silicon-29 spectrum of Mat-Im. The spectrum was recorded on a 400 MHz with a 3.2 mm rotor at an MAS rate of 10 kHz. A delay of 2 s was used with 256 scans. The ^{29}Si CP MAS NMR spectrum displays four resonances at -121.9.3, -115.2, -80, and ppm, assigned to the $Q_{4'}$, Q_4, T_3, and TMS sites, respectively. The $Q_{4'}$ and Q_4 were deconvoluted using a matlab script. The same spectrum was recorded for the Mat-NHC-Ag and Mat-NHC-Ir.

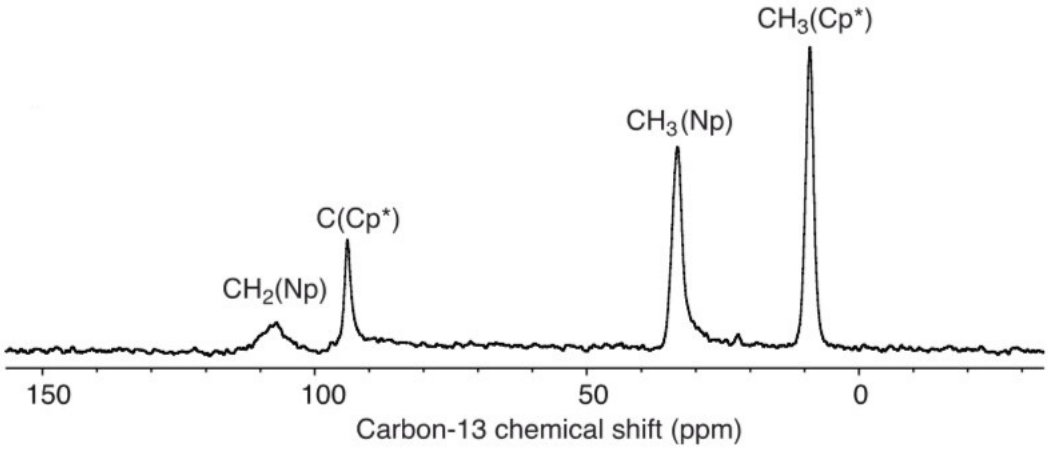

Figure S2: Carbon-13 spectrum of [≡SiOTa(CH_2^tBu)$_2$IrH_2(Cp*)]. The spectrum was recorded on a 500 MHz with a 4 mm rotor at an MAS rate of 5 kHz. A delay of 2 s was used with 61440 scans. The ^{13}C CP MAS NMR spectrum displays four resonances at 107.5, 93.9, 33.5, and 9.1 ppm, assigned to the CH_2(Np), C(Cp*), CH_3(Np), and CH_3(Cp*) carbons, respectively.

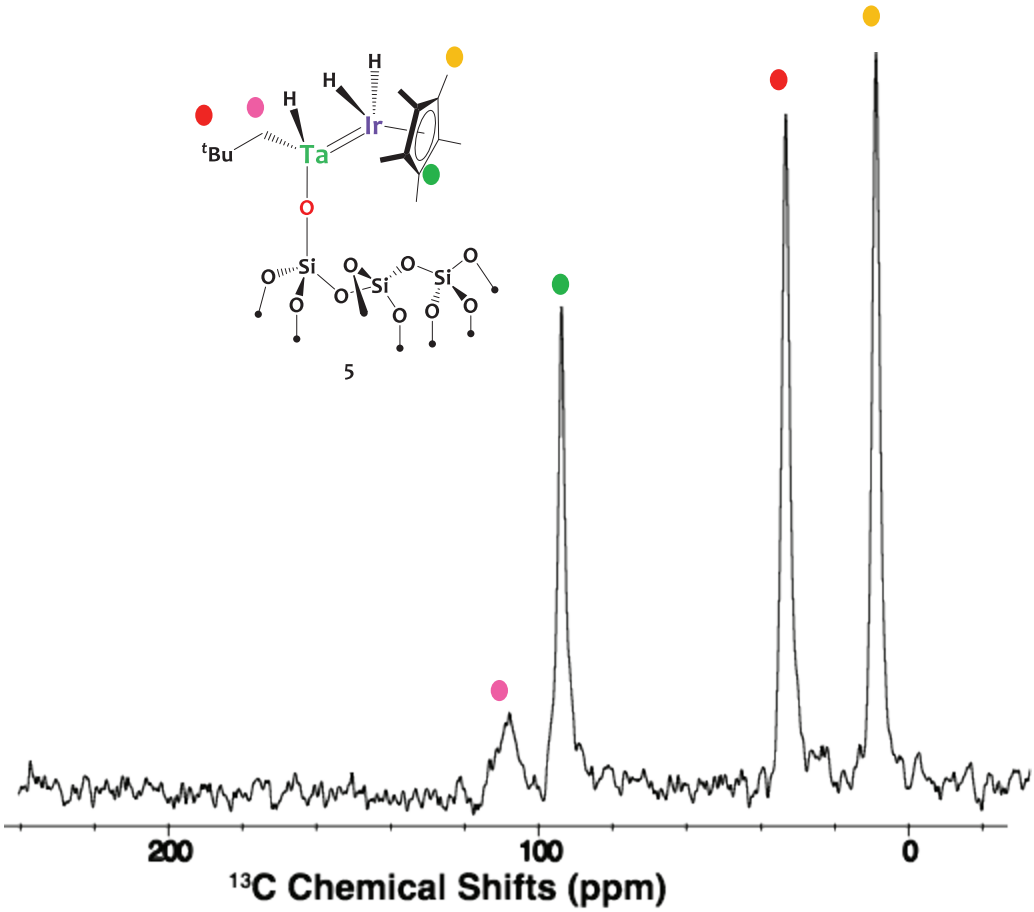

Figure S3: Carbon-13 spectrum of [≡SiOTa(CH_2^tBu)H-IrH_2(Cp*)]. The spectrum was recorded on a 500 MHz with a 4 mm rotor at an MAS rate of 5 kHz. A delay of 2 s was used with 61440 scans. The ^{13}C CP MAS NMR spectrum displays four resonances at 107.5, 93.9, 33.5, and 9.1 ppm, assigned to the CH_2(Np), C(Cp*), CH_3(Np), and CH_3(Cp*) carbons, respectively.

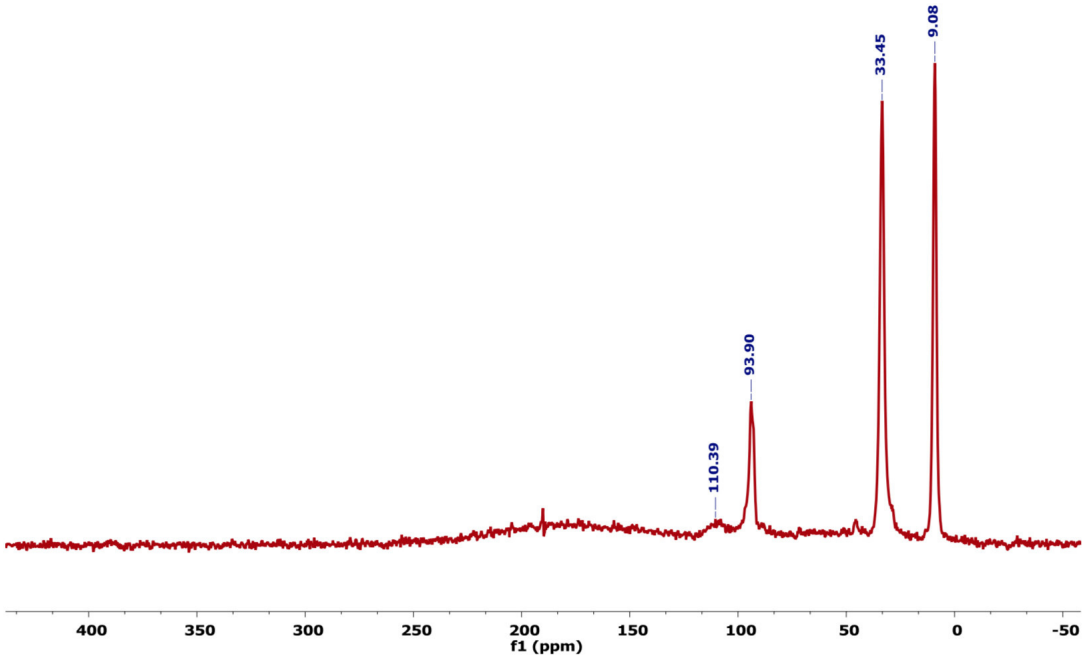

Figure S4: Carbon-13 spectrum of product of the two step synthesis route. The spectrum was recorded on a 125 MHz with a 4 mm probe at an MAS rate of 10 kHz. The ^{13}C CP MAS NMR spectrum displays four resonances at 110.39, 93.9, 33.45, and 9.08 ppm, assigned to the CH_2(Np), C(Cp*), CH_3(Np), and CH_3(Cp*) carbons, respectively.

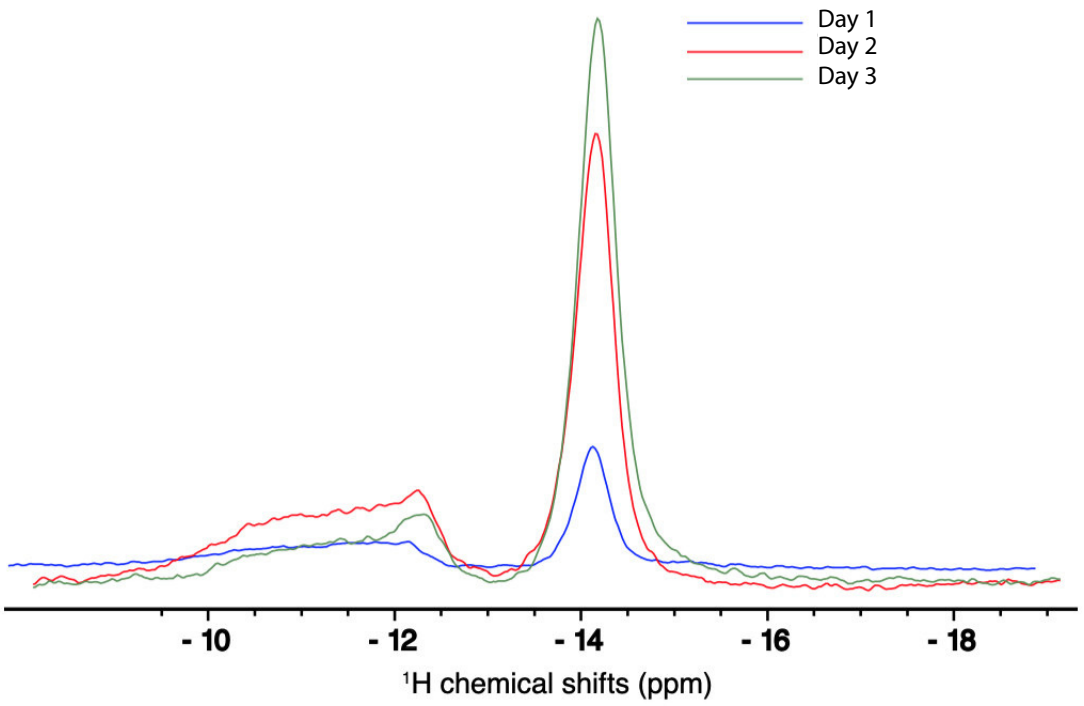

Figure S5: ^{1}H spectrum of $\equiv$SiOTa(CH_2^tBu)$_2$IrH_2(Cp*)] on three successive days. The spectrum was recorded on a 700 MHz with a 2.5 mm rotor at an MAS rate of 18 kHz. A delay of 2 s was used with 4 scans.The ^{1}H MAS NMR spectrum displays the hydrides resonances around -11 pm. It also displays the degradation and the appearance of a new resonance around -14 ppm that increases over a period of 72 hrs.

	^{29}Si-{^{15}N} REDOR					
	Mat(1)-Im	Mat(1)-NHC-Ag	Mat(1)-NHC-Ir	Mat(2)-Im	Mat(2)-NHC-Ag	Mat(2)-NHC-Ir
Scans	1280	1280	1920	384	896	896
Acquisition Time	9.9 ms	9.9 ms	9.9 ms	9.9 ms	9.9 ms	9.9 ms
REDOR points	60	60	60	60	60	60
Recycle delays	3 s	3 s	3 s	3 s	3 s	3 s
Depahsing time	60 ms	60 ms	60 ms	60 ms	60 ms	60 ms
CP contact time	3.5 ms	3.5 ms	3.5 ms	3.5 ms	5 ms	5 ms

Table S1: ^{29}Si-{^{15}N} REDOR experimental details used for the different surface species.

	^{29}Si-{^{13}C} REDOR		
	Mat(1)-Im	Mat(1)-NHC-Ag	Mat(1)-NHC-Ir
Scans	896	1152	768
Acquisition Time	9.9 ms	9.9 ms	9.9 ms
REDOR points	32	32	32
Recycle delays	3 s	3 s	3 s
Depahsing time	48 ms	48 ms	48 ms
CP contact time	3.5 ms	3.5 ms	3.5 ms

Table S2: ^{29}Si-{^{13}C} REDOR experimental details used for the different surface species.

	^{29}Si-{^{13}C} REDOR		
	Mat-Im post reaction	Mat(1)-Im with bCTbk	Mat-NHC-Pt
Scans	1536	768	1280
Acquisition Time	9.9 ms	9.9 ms	9.9 ms
REDOR points	48	48	32
Recycle delays	3 s	3 s	3 s
Depahsing time	62.4 ms	62.4 ms	49.4 ms
CP contact time	3.75 ms	3.75 ms	3.75 ms

Table S3: ^{29}Si-{^{13}C} REDOR experimental details used for the Mat-Im post reaction, Mat(1)-Im impregnated with bCTbk and the Mat-NHC-Pt.

Experimental details for chapter 6 The carbon-13 solid-state NMR spectra were obtained on a Bruker 500 MHz wide-bore spectrometer using a double resonance 4 mm MAS probe, while the proton solid-state NMR spectra were obtained on a Bruker 700 MHz narrow-bore spectrometer using a double resonance 2.5 mm MAS probe. The samples were introduced under argon in a zirconia rotor, which was then tightly closed. Dry nitrogen gas was used to spin the samples to avoid sample degradation. The ^{13}C spectra were obtained from cross-polarization (CP) from protons using a linear ramped CP to optimize the magnetization transfer efficiency. A proton radio frequency (RF) field of 70 kHz in the center of the ramp was applied, while the RF field on carbon-13 was adjusted for optimal sensitivity. For all the proton multiple-quantum experiments, the spinning frequency was set to 18 kHz. The 2D proton DQ-SQ correlation spectra were recorded according to the following general scheme: excitation of DQ coherences, t_1 evolution and reconversion into observable magnetization, Z-filter, and detection. DQ excitation and reconversion were achieved using the POST-C7 pulse sequence. The length of the POST-C7 excitation and reconversion block was set to 160 μs (corresponding to seven basic POST-C7 cycles). Quadrature detection in ω_1 was achieved using the States-TPPI method. A recycle delay of 1.5 s was used. A total of 80 t_1 increments of 96 μs with 384 scans each were recorded. The total experimental time for the DQexperiments was 12 h. The 2D proton TQ-SQ correlation spectra were recorded according to the following general scheme: excitation of TQ coherences, t_1 evolution, reconversion into observable magnetization, Z-filter, and detection. TQ excitation was achieved by the sequential application

of first a 90° proton pulse followed by a DQ POST-C7 pulse sequence as previously described in the literature. The length of the POST-C7 excitation and reconversion block was set to 160 μs (corresponding to seven basic POST-C7 cycles). Quadrature detection in ω_1 was achieved using the States-TPPI method. A recycle delay of 1.5 s was used. A total of 128 t_1 increments of 32 μs with 288 scans each were recorded. The total experimental time for the TQ experiment was 15 h.

Experimental details for chapter 4 All DNP SENS experiments were conducted on a solid-state DNP NMR Bruker spectrometer. It consists of a wide-bore 9.4 T magnet ($\omega_{^1H}/(2\pi)$) = 400 MHz, $\omega_{^{29}Si}/(2\pi)$) = 79.5 MHz, $\omega_{^{13}C}/(2\pi)$) = 100 MHz, $\omega_{^{15}N}/(2\pi)$) = 40.5 MHz) equipped with an Avance III HD console and a triple resonance 3.2 mm low-temperature CPMAS probe. The probe was used in three different configurations, ^{1}H-^{13}C-^{15}N, ^{1}H-^{29}Si-^{15}N, and ^{1}H-^{13}C-^{29}Si with the appropriate insert for each configuration. DNP was achieved by irradiating the sample with microwaves (mw) generated by a fixed frequency gyrotron (263 GHz) and delivered to the probe by a corrugated wave-guide. [73] Sapphire rotors were used (with vespel caps) for optimal microwave penetration and resistance to low temperatures. The cross-effect matching condition was set to the maximum positive enhancement of TEKPOL by sweeping the coil of the spectrometer mag-net. The microwave power was optimized to get the highest proton enhancement on the solvent for each sample (≈22 W of power reaching the sample). The REDOR DNP SENS data were acquired with a spinning frequency of 10 kHz at sample temperature of approximately 110 K. SPINAL64 [280] was used for ^{1}H heteronuclear decoupling with 100 kHz ^{1}H nutation frequencies. Experimental details for the ^{13}C-^{15N} ^{29}Si-^{13}C, ^{29}Si-^{15}N REDOR and for ^{29}Si-13C FS-REDOR experiments (number of scans, experimental times, number of points in each curve...) are summarized in Table S2, S1. For FS-REDOR, selective inversion of the C_6 resonance was achieved using a Gaussian cascade Q_3 shaped excitation pulse [281] of 0.8 ms. Before structure calculation, the scaling factor of each REDOR curve was determined from REDOR and FS-REDOR data corresponding to internuclear distances that are fixed in the molecular geometry. TEKPOL radical was provided by Prof. Olivier Ouari (Aix-Marseille University) and prepared according to the synthesis reported in [52].

Experimetal details for chapter 5

Static ^{195}Pt Experiments of 1 at 11.7 T. Static experiments were performed on compound **1** using a Bruker 4 mm double resonance MAS probe on a 500 MHz wide bore Bruker AVANCE III Bruker NMR spectrometer. [73] The sample was packed into a 4 mm zirconia rotor in a glovebox. The ^{195}Pt chemical shift was referenced to an aqueous solution of K_2PtCl_4. The BRAIN-CP-WCPMG pulse sequence was performed using the variable offset cumulative spectrum (VOCS) procedure. [249] A ^{1}H excitation pulse of 5 μs was used followed by a 10 ms contact time, with WURST A swept over 400 kHz applied to ^{195}Pt. For detection 50 μs WURST B and C pulse were swept over 500 kHz with a spikelet separation of 5 kHz. A recycle delay of 1.5 s was used and 2048 scans were accumulated. The transmitter offset between subspectra was 200 kHz. Analytical simulation of the static ^{195}Pt spectrum was performed using a two-site model on ssNAKEsoftware. [282] The isotropic shifts determined from the MAS experiments was fixed for the two sites. The span (Ω) of both CS tensors was fixed to 8150 ppm and the skew (κ) was adjusted to -0.73 to yield the best fit.

Static DNP-SENS ^{195}Pt Experiments of 1@SiO2 at 9.4 T. The static DNP SENS experiments were performed using a Bruker AVANCE III wide bore 400 MHz/263 GHz DNP spectrometer. [73] The ^{195}Pt chemical shift was referenced to an aqueous solution of K_2PtCl_4. The DNP sample of compound **1@SiO2** was prepared in a glovebox and impregnated with a solution of 16 mM TEKPol [52] radical in 1,1,2,2-tetrachloroethane (TCE) via the incipient wetness method and packed into a 3.2 mm sapphire rotor. The DNP sample was immediately inserted into a Bruker 3.2 mm low-temperature MAS DNP probe pre-cooled to 100 K. The static DNP ^{195}Pt spectra were acquired using the BRAIN-CP-WCPMG pulse sequence [256] with microwave irradiation. Continuous microwave irradiation was generated by a gyrotron operating at a frequency of 263 GHz and with an approximate power of 40 W. A ^{1}H excitation pulse of 2.5 us was used followed by a 10 ms contact time, with WURST A swept over 400 kHz applied to ^{195}Pt. For detection 50 μs WURST B and C pulse were swept over 500 kHz with a spikelet separation of 5 kHz. A recycle delay of 7 s was used and 4096 scans were accumulated. Variable offset accumulation was used, and seven different offset frequencies were acquired by stepping the transmitter by 100 kHz. The line shape fitting was carried out using the software package DMFIT [283] using a static CSA model parametrized in the Herzfeld-Berger convention. The isotropic chemical shift was fixed to the values determined with MAS TONE D-HMQC experiments under fast MAS and the other parameters were optimized. A Gaussian line broadening of ca. 8 kHz was necessary to obtain a satisfying fit, in good agreement with the data.